University of Alberta

Library Release Form

Name of Author: Lara De Nardo

Title of Thesis: Measurement of the Structure Function g_1^d at HERMES and Extraction of Polarized Parton Distributions

Degree: Doctor of Philosophy

Year this Degree Granted: 2002

Lara De Nardo
11121-82 Avenue
Edmonton, Alberta
Canada, T6G-0T4

Date: ____________________

Se non puoi essere un pino sul monte
sii una saggina nella valle,
ma sii la migliore:
piccola sponda del ruscello.
Se non puoi essere un albero
sii un cespuglio.
Se non puoi essere un'autostrada
sii un sentiero.
Se non puoi essere il sole
sii una stella.
Sii sempre il meglio di cio' che sei.
Cerca di scoprire il disegno che sei chiamato ad essere
poi mettiti con passione a realizzarlo nella vita.
Martin Luther King

University of Alberta

MEASUREMENT OF THE STRUCTURE FUNCTION g_1^d AT HERMES AND EXTRACTION OF POLARIZED PARTON DISTRIBUTIONS

by

Lara De Nardo

A thesis submitted to the Faculty of Graduate Studies and Research in partial fulfillment of the requirements for the degree of **Doctor of Philosophy**.

Department of Physics

Edmonton, Alberta
Fall 2002

University of Alberta

Faculty of Graduate Studies and Research

The undersigned certify that they have read, and recommend to the Faculty of Graduate Studies and Research for acceptance, a thesis entitled **Measurement of the Structure Function g_1^d at HERMES and Extraction of Polarized Parton Distributions** submitted by Lara De Nardo in partial fulfillment of the requirements for the degree of **Doctor of Philosophy**.

Dr. M. Vincter (Supervisor)

Dr. M. de Montigny

Dr. G. Greeniaus

Dr. F. Marsiglio

Dr. S. Bhadra (External Examiner)

Dr. H. Sherif (Chair)

Date: ____________

To my family

Abstract

HERMES is a Deep Inelastic Scattering experiment located at the DESY facility in Hamburg, Germany, and uses longitudinally polarized 27.5 GeV electrons or positrons from the HERA storage ring to scatter off fixed, polarized nucleon targets. From the rate of detected scattered beam leptons it is possible to measure the *structure function* g_1 which enters the cross section as an unknown, given the lack of knowledge of the internal structure of the nucleons. This function is in turn dependent on the distribution of spin inside the nucleons. This field of research was triggered by the discovery, in the late 1980's by the EMC experiment, that the total spin 1/2 of nucleons did not come entirely from the contribution of quarks, as expected.

The deuteron structure function g_1^d has been measured with unprecedented precision in this thesis from 10 million DIS events collected by the HERMES experiment during the years 1998 and 2000. The data cover the kinematic range 0.0041< x <0.81 and 0.21< Q^2 <7.3 GeV^2, and have been divided into 49 x and Q^2 bins, where x is the fraction of nucleon's momentum carried by the struck quark and Q^2 is the negative four-momentum transfer to the nucleon. The extraction of g_1^d from data requires a deep knowledge of the detector performance for the dis-entanglement of effects possibly due to malfunctions. Statistical tests were performed on the data to study possible unwanted dependencies.

QCD fits at next-to-leading order have been performed to world data on the structure functions $\mathrm{g}_1^{p,n,d}(x, Q^2)$. They have in turn been used to extract the polarized distributions $\Delta q_{NS}^{p,n}(x, Q^2)$, $\Delta\Sigma(x, Q^2)$ and $\Delta G(x, Q^2)$. A method has been developed to propagate the statistical and systematic uncertainties on $\mathrm{g}_1^{p,n,d}$ to the extracted distributions. The integrals of these distributions over the measured range of the variable x have been obtained

for four Q^2 reference values and also from the HERMES data alone.

The results in this thesis clearly demonstrate that in the measured x range gluons are positively polarized, which may explain the spin deficit in the nucleon known as the *spin puzzle*.

Acknowledgements

First and foremost, I would like to thank my supervisor, Dr. Manuella Vincter, for her outstanding guidance and mentor-ship.

This thesis would have not been possible without my co-workers in the g_1 group: Uta Stösslein and Christoph Weiskopf. Christoph was the one I worked in closer contact, and we were able to carry on the analysis even if separated by eight time zones. He has always been very helpful and a great working companion.

Special thanks go to Helmuth Böttcher with whom I had long and fruitful discussions on the QCD fits. Thank you Helmut, for your patience!

I am very grateful to Dr. Gordon Greeniaus for proof-reading this thesis and for his valuable suggestions.

I would like to thank all the colleagues in the HERMES collaboration. Elke Aschenauer and Andy Miller contributed to the analysis with their suggestions. Their deep knowledge of the technical and physical aspects of the experiment was extremely helpful.

The *delta-q* group collaborated with the g_1 group, and I would like to thank Juergen Wendland and Chiara Simani in a special way for the nice discussions we had. Thanks go to Matthias Hartig who, from my first days at HERMES, has always been ready to help me whatever problem I had. He earned his ice-creams! The same is true for Bjoern Seitz and Larry Felawka.

With the Italians in HERMES I enjoyed not only working but also going out at night, especially with Erika Garutti who has become one of my best friends. I will never forget the great time drinking glühwein and eating schmalzkuchen at the DOM!

Friends played a special role in my life in the past few years, and many of them are now scattered around the globe. Since my first days in Edmonton, Massimo and Paolo helped me with their humor and positive attitude. My roommates Lourdes, Simona and especially Veronica were like a family to me.

My friends in Napoli contributed to make me feel like I had never left home, making me still part of their lives, Ida and Valentina most of all. It helped me a lot, being so far away from Italy.

Thanks to Henning, for understanding and always encouraging me.

My love goes to my father, my mother and my sister, who have always been my inspiration.

Contents

List of Tables

List of Figures

List of Symbols

Quantity	Description
M	Nucleon's mass
x	Nucleon's momentum fraction carried by the struck parton
y	Energy fraction transferred to the virtual photon γ^*
$q^2 = -Q^2$	Virtual photon's four-momentum squared
W	Invariant mass of the $\gamma^* p$ system
θ	Lepton scattering angle
ϕ	Lepton azimuthal angle
F_1, F_2	Unpolarized structure functions
g_1, g_2	Polarized structure functions
R	Longitudinal to transverse virtual photon cross section ratio
$k = (E, p)$	Initial lepton four-momentum
$k' = (E', p')$	Final lepton four-momentum
$A^d_{\parallel}$	Deuterium longitudinal experimental asymmetry
D	Virtual photon depolarization factor
$N^{(\overset{\Leftarrow}{\rightarrow})\overset{\Rightarrow}{\rightarrow}}$	Number of DIS events with target and beam polarized in (anti)parallel direction
$L^{(\overset{\Leftarrow}{\rightarrow})\overset{\Rightarrow}{\rightarrow}}$	Integrated luminosity for target and beam polarized in (anti)parallel direction
P_b	Beam polarization
P_t	Target polarization
z_v	Vertex position of DIS event in the target along the z axis
a_0, a_3, a_8	Matrix elements of axial currents on nucleon states
F, D	Constants appearing in the β decays matrix elements
$\Gamma_1^{p,d,n}$	Integrals of $\mathrm{g}_1^{p,d,n}$ over x
$\Delta\Sigma(x, Q^2)$	Singlet polarized quark distribution
$\Delta q^{NS}(x, Q^2)$	Non singlet polarized quark distribution

Chapter 1

Introduction

The structure of nucleons can be studied with experiments analogous to Rutherford's, where in this case particles scatter off target nucleons rather than the nucleus. From the distribution of scattered particles it is possible to gain information on the nucleon's constituents.

At very low beam energies, the *constituent model* describes the static properties of nucleons like their masses, spins and magnetic moments in terms of *quarks* constituents. The nucleons are seen as irreducible representations of the SU(3) symmetry group.

In Deep Inelastic Scattering (DIS) ([1]) a lepton beam scatters off target nucleons with the exchange of a virtual probe, such as a photon. If the virtual photon four-momentum Q^2 is large enough, the photon interacts directly with a quark carrying a fraction x of the nucleon's momentum. The nucleon breaks up, and the fragments recombine into hadrons, which are then detected. Since the lepton is a point-like particle, the distribution of scattered particles directly depends only on the nucleon's internal structure.

At very high Q^2 nucleons appear to be made of free or quasi-free quarks, because the strong coupling constant decreases asymptotically: quarks interact with the exchange of *gluons*, the carriers of the strong interaction. The nucleon is thus seen as an extremely active environment, where quark-antiquark pairs (the *sea*) are continuously created and destroyed.

When target and/or beam are not polarized, then the distribution of momentum carried by quarks and gluons can be studied by DIS, and very precise data is available, with high statistics, of which Ref. [2] and Ref. [3] are only a few examples. For photon exchange, the differential cross section depends on two *unpolarized structure functions* $\mathrm{F}_1(x)$ and $\mathrm{F}_2(x)$, which in zero-th order QCD can be written as ([4])

$$\mathrm{F}_2(x) = \sum_i e_i^2 \, x \, q_i(x) \qquad\qquad \mathrm{F}_1(x) = \frac{1}{2x}\mathrm{F}_2(x) = \frac{1}{2}\sum_i e_i^2 \, q_i(x), \tag{1.1}$$

where q_i denotes the distribution of quark i with charge e_i, and the sum runs over quarks and antiquarks.

When both target and beam are polarized, the distribution of spin inside the nucleon can be studied. The differential cross section acquires a dependence on *polarized structure functions*. The analogue of $\mathrm{F}_1(x)$ in the polarized case is

$$\mathrm{g}_1(x) = \sum_i e_i^2 \Delta q_i(x) \; , \tag{1.2}$$

where $\Delta q_i(x) = q_i^+(x) - q_i^-(x)$ is the difference between parton distributions with polarization parallel to the nucleon's spin and the corresponding distributions with anti-parallel polarization.

Ideally quark and antiquark distributions inside the proton are not expected to depend on Q^2, but in practice they do. This can be explained when one considers that the processes that the virtual photon accesses change with the four-momentum transferred. At low Q^2 the photon is not sensitive to gluon-initiated processes, and can not distinguish the sea quarks. When Q^2 increases the photon can probe the most inner structure of nucleons, and becomes sensitive to the sea. As a result, when one considers QCD effects like *photon-gluon fusion* ($\gamma^* g \rightarrow q\bar{q}$) and *gluon radiation* ($\gamma^* q \rightarrow gq$), the structure functions acquire a dependence on Q^2.

The total spin of a nucleon is $1/2$, which must come from contributions from the total angular momentum L of quarks and gluons, and from the spin carried by gluons (ΔG) and quarks ($\Delta\Sigma$):

$$\frac{1}{2} = L + \frac{1}{2}\Delta\Sigma + \Delta G \; . \tag{1.3}$$

Naively one would expect that the static model results apply at higher energies too, and that the spin is carried by quarks for the most part.

Experiments to study the nucleon's spin are more difficult to realize than unpolarized ones, because of the necessity of both polarized target and beam. The pioneer EMC experiment ([5]) in the 1980's used polarized high energy muons incident on polarized targets to determine the polarized structure function g_1^p. From the integral of g_1^p over the whole range of the variable x (between 0 and 1), using some assumptions on SU(3), it is possible to extract $\Delta\Sigma$. The astonishing result was that the quarks inside the nucleon contributed very little ($\Delta\Sigma \simeq 4\%$) to the spin of the nucleon. Even though the interpretation of the EMC results is now different, the result remains that the angular momentum and gluon contribution to the spin may be relevant.

The EMC results generated the so called *spin puzzle* and gave way to many polarized DIS experiments, mainly concentrated at the CERN and SLAC laboratories. The most important CERN experiment was SMC, an upgrade of the EMC detector. In this experiment, 100-190 GeV muons scattered off butanol, deuterated butanol, and ammonia targets. One remarkable feature of the experiment was the simultaneous use of two polarized targets with opposite polarization. This greatly reduced systematic uncertainties related to luminosity and detector performance. Also, the high beam energy led to high $Q^2 \simeq 10$ GeV^2, and very low $x \simeq 0.003$, important to determine the behavior of g_1 at low x for the calculation of the integral of g_1. On the other hand, the SMC detector had the disadvantage of having small dilution factors: the dilution factor is the ratio of polarizable nucleons divided by the total number of nucleons in the target. In the SMC experiment this factor varied from 0.13 to 0.23. The target polarization was $\simeq$ 86% for protons and $\simeq$25-50% for deuterons.

The SLAC experiments (E142, E143, E154, E155) all used the same polarized electron beam, but they differed in the targets (E142 and E154 used ^{3}He, E143 and E155 used NH_3, ND_3 and LiD), and small changes in the spectrometers. Also these experiments had to face the problem of the small dilution factors. In the spectrometers used for E142 and E143 the electrons were detected at scattering angles of 4.5^o and 7.0^o. Electrons were identified by Cerenkov detectors and lead-glass calorimeters, and scintillator hodoscopes provided tracking. E154 and E155 used different scattering angles: 2.75^o, 5.5^o and a new spectrometer at 10^o. One obvious problem of these experiments was the low geometrical acceptance.

The HERMES experiment ([6]) studies the spin structure of the nucleon through DIS of longitudinally polarized electrons (or positrons) on longitudinally polarized nucleons.

One of the strengths of HERMES is the purity of the target: the dilution factor is 1 for hydrogen and deuterium. The polarized gas (H, D, ^{3}He) enters into a windowless storage cell located directly inside the beam pipe. Gas escapes out of the ends of the cell and is pumped away by the high speed differential pumping system. The target polarization can be as high as 92% while beam polarization can reach 55%. HERMES is a forward spectrometer divided in two symmetric top-bottom halves. Drift chambers just downstream of the target window and before and after the magnet measure the scattering angle and momentum of charged particles. The acceptance of the detector covers a large kinematic range for the scattered positron. The HERMES particle identification system (RICH, TRD, Preshower, Calorimeter) is able to identify the scattered electron and hadrons produced in coincidence.

There are many ways to access the distribution of spin among the nucleon's constituents. In *inclusive scattering* only the scattered lepton is detected, and in this way there is sensitivity on the structure function $g_1(x, Q^2)$. Even though g_1 depends on a specific combination of polarized distributions, it is possible to separate quark and gluon distributions using their different Q^2 dependence. This is theoretically a very clean way to obtain the polarized distributions. Unfortunately the relatively small amount of data available requires the use of assumptions, such as SU(3) symmetry and hypotheses on the shape of the distributions at an input scale Q_0^2.

In *semi-inclusive scattering* ([7], [8], [9]), one or more hadrons are detected in coincidence with the lepton, and the charge of the hadron, together with its valence quark composition, provide sensitivity to the flavor of the struck quark. Many assumptions are needed in order to extract the polarized quark distributions, including models on the fragmentation of nucleons. Also, experiments need to identify efficiently as many types of hadrons as possible, to be able to separate the flavors. Since this was not possible with all flavors, assumptions often had to be introduced on the sea polarizations Δq_s. For example $\Delta q_s(x)/q_s(x)$ or $\Delta q_s(x)$ were assumed to be a constant for all flavors. Recently, though, given the excellent hadron separation capabilities of the HERMES experiment, these additional assumptions could be dropped, thus allowing the extraction of the polarization distributions of u, d, $\bar{u}$, $\bar{d}$ and s quarks ([10]) in the range $0.023 \leq x \leq 0.6$ and $1 \leq Q^2 \leq 15$ GeV^2.

This thesis deals with the measurement of the deuteron polarized structure function g_1^d from data collected by the HERMES experiment in the spring of 1998 and in 2000, for a total of almost 10 millions inclusive DIS events.

The first chapter is an overview of the HERMES experiment. The detector is treated in detail, with special emphasis to the particle identification system, which is able to discriminate between hadrons and leptons, and among hadrons. For the g_1 analysis only a good separation is needed between hadrons and leptons. Studies performed on the trigger efficiency conclude the chapter. These studies were necessary to the g_1 measurements in the low momentum region. The efficiencies were found to have reached the plateau after the rise in the region of interest from lower momenta, but a new effect was found: one detector showed efficiencies as low as 90% and had to be corrected. The inefficiencies do not affect the extraction of g_1, which is obtained from ratios of cross sections, but can affect measurements of total cross-sections. For this reason correction functions were obtained.

The second chapter presents an introduction to deep inelastic scattering, and the measurement of g_1 in the kinematic region accessible by the HERMES detector $0.0041 < x < 0.81$ and $0.21 < Q^2 < 7.3$ GeV^2. Data were divided into 27 x bins, and up to 3 Q^2 bins, where allowed by enough statistics. Many statistical tests were performed to study the stability of the results, and possible dependences, like on the trigger efficiencies or on the beam helicity. The data have been corrected for charge symmetric backgrounds and hadron contaminations. For the final extraction information was needed from unpolarized data, like a parameterization on the structure function F_1. The final results on g_1^d represent the most precise measurement so far.

The third chapter introduces QCD effects: the Operator Product Expansion (OPE), which was developed explicitly to study DIS and describe structure functions in terms of matrix elements of quark and gluon operators, which become more and more important at small Q^2, where non-perturbative effects play a role. The evolution in Q^2 of parton distributions described by the Altarelli-Parisi equations is also introduced, in leading and next-to-leading-order. The effect on the structure functions is discussed.

Chapter 4 shows how the new measurements of g_1^d can be used together with world data on $g_1^{p,n,d}$ to extract fits to the polarized quark and gluon distributions as a function

of x, exploiting the Q^2 range of measurements. A method is developed to propagate the statistical and systematic uncertainties from $g_1^{p,n,d}$ data into the polarized distributions. Integrals of $g_1^{p,n,d}$ over the measured range of x are obtained for four Q^2 values.

Chapter 2

The HERMES experiment

2.1 HERMES

HERMES is a fixed-target experiment located at the east straight section of the HERA electron (positron)-proton storage ring at the DESY laboratory in Hamburg. HERMES was designed to optimize the measurement of quantities related to the nucleon's spin. For this it needs high beam current, high values of target and beam polarization, high target density, and a large detector acceptance.

One of the strengths of HERMES is the purity of its target: the dilution factor (i.e. the ratio of polarizable nucleons divided by the total number of nucleons in the target) is 1 for hydrogen and deuterium.

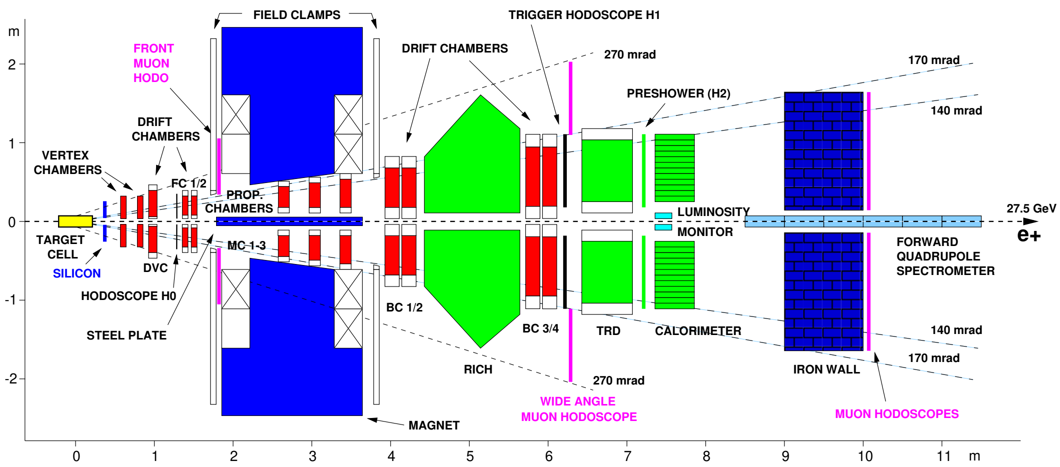

Figure 2.1: Schematic side view of the HERMES spectrometer

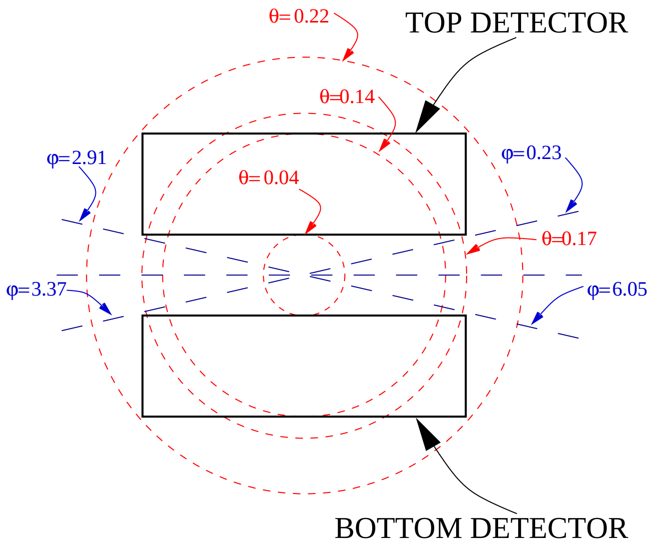

Figure 2.2: HERMES angular acceptance. The dotted lines indicate the acceptance in the polar angle θ, while the dashed circles refer to the acceptance in the azimuthal angle φ. The plot represents a scaled version of the actual acceptance.

HERMES [6] is a conventional forward spectrometer with a dipole magnet providing an integrated field of 1.3 Tm. The spectrometer is divided into two symmetric top-bottom halves by the HERA beam lines, which are shielded by a horizontal iron plate.

Fig. 2.1 shows a schematic of the detector setup. The particle acceptance in the scattering angle θ is limited at small angles to 0.04 rad by the iron plate, while the maximum angles in the horizontal and vertical directions are 0.17 and 0.14 rad, respectively (see Fig. 2.2). As is shown in Fig. 2.1, each half of the detector has a series of drift-chamber planes for tracking. An angular resolution of $\delta\theta < 0.6$ mrad and a momentum resolution of $\delta p/p \sim 1\%$ are achieved. The trigger is formed by a combination of signals from three hodoscopes and a lead-glass electromagnetic calorimeter. Particle identification is achieved by a probability analysis of the signals from the transition radiation detector, the preshower hodoscope and the calorimeter. In the results presented here the efficiency for electron identification was on average 98%, while the hadron contamination was estimated to be less than 0.5%. The luminosity was measured by two small $NaBi(WO_4)_2$ electromagnetic calorimeters [12] detecting the Møller (Bhabha) scattering of the beam electrons (positrons) off the target electrons.

Each component of the HERMES experiment will be discussed in this chapter, includ-

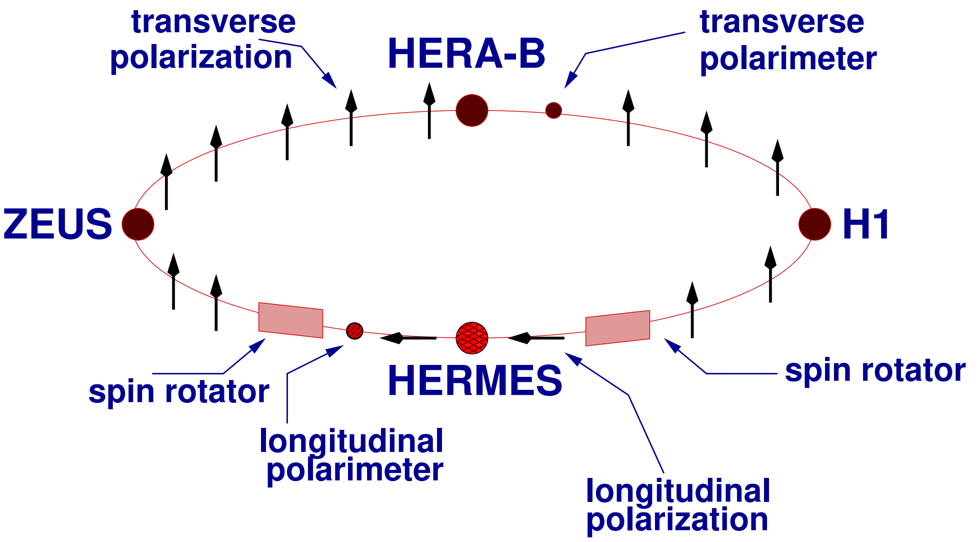

Figure 2.3: The HERA ring.

ing particle identification and trigger efficiencies.

2.2 The HERA beam

HERMES makes use only of the polarized positron or electron beam from the HERA storage ring. Since HERA is unable to provide polarized protons, HERMES uses a polarized fixed target. The electron beam is naturally highly transversely polarized due to a small asymmetry in the emission of synchrotron radiation: since the probability of spin flip to the direction parallel to the magnetic field is slightly higher than the spin-flip into the anti-parallel direction, in time there is a net polarization build up of the beam in the direction parallel to the magnetic field. This is the Solokov-Ternov effect[13]. The time dependence of the beam polarization is described by the equation:

$$P_B(t) = P_{max}(1 - e^{-t/\tau}) \ , \qquad (2.1)$$

where P_{max} is the asymptotic polarization, and τ the rise time constant. In a real machine de-polarizing effects such as orbital effects in the synchrotron radiation as well as magnetic and alignment imperfections prevent the polarization from reaching its maximum and have the net effect of lowering both the maximum polarization and the rise time from the theoretical values. These theoretical values

$$P_{max}^{THEORY} = \frac{8}{5\sqrt{3}} = 92.38\% \qquad \tau^{THEORY} = P_{max}^{THEORY}\frac{m_e^2 c^2 \rho^3}{e^2 \hbar \gamma^5} = 37 \text{ min} \tag{2.2}$$

may be compared to the experimentally determined values of $\sim 55\%$ and ~ 22 minutes. Here m_e and e are the electron mass and charge, c is the speed of light, $\hbar$ is the Planck constant, ρ is the bending radius, and $\gamma = E/m_e$, E being the electron energy.

Two polarimeters measure the polarization of the beam: the transverse polarimeter located in the western section of HERA, and the longitudinal polarimeter located in the HERMES region (see Fig. 2.3). The average beam polarization for 2000 was $< P_B >$=0.53.

2.2.1 Longitudinal polarimeter

Spin rotators are positioned upstream and downstream of the HERMES area and serve to rotate the beam polarization from transverse to longitudinal (as needed for HERMES physics) and then back again. A measurement of longitudinal polarization was necessary for HERMES, so in 1997 the longitudinal polarimeter ([14]) became operational. A schematic view of the HERA east section with the longitudinal polarimeter is shown in Fig. 2.4. A laser beam of circularly polarized light with an energy of 2.33 eV is guided by remotely controlled mirrors in a vacuum pipe for 72 m until it reaches the electron beam. It then scatters off the electron beam 52 m downstream of the HERMES interaction point. Because of the high boost of the electron beam, the resulting back-scattered Compton photons are very focused and are contained within a small region centered around the direction of the electron beam. The bending magnet BH90 bends the electron beam away from the Compton scattering, so that the Compton back-scattered light and the beam

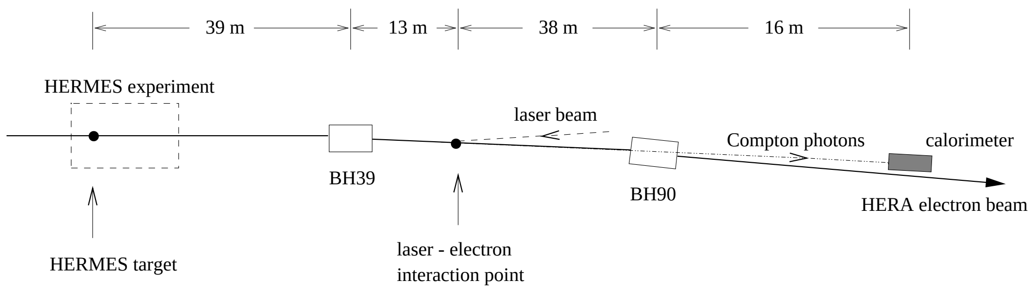

Figure 2.4: Overview of the longitudinal polarimeter.

slightly separate. A small calorimeter located 16 m downstream of BH90 measures the energy deposited by the Compton photons. The differential cross section for Compton scattering of circularly polarized light off of polarized electrons is related to the known unpolarized differential cross section $d\sigma/dE_0$ and to the photon and beam polarizations P_γ and P_b by the relation

$$\frac{d\sigma}{dE_\gamma} = \frac{d\sigma}{dE_0}\left(1 + P_\gamma P_b A_\gamma\right) \ , \tag{2.3}$$

where A_γ is an asymmetry, known exactly. The total energy deposited into the calorimeter per electron bunch is measured, thus providing the beam polarization measurement. If the measured cross sections are the same for photon helicity $\lambda = \pm 1$ then the beam is not polarized. The photon polarization is on the order of 0.999 and it is checked by means of a polarization analyzer before and after the collision with the beam.

The polarization measurement is made once every minute, and it has an absolute statistical accuracy of 0.01. Systematic uncertainties on the measurement are estimated to be of the order of 2%, and come from sources of false asymmetry that can contribute to give a wrong asymmetry measurement, the measurement of the laser light polarization, and electron beam instability.

2.2.2 Transverse polarimeter

The transverse polarimeter operates on similar principles to the longitudinal one. It uses an Argon-ion laser which produces photons with an energy of 2.41 eV. As with the longitudinal polarimeter, the beam of light is brought to interact with the electron beam by use of a series of mirrors. The backscattered Compton light is collimated both horizontally and vertically and is measured by a calorimeter about 65 m away. The TPOL calorimeter is separated into two pieces, one above and the other below the beam pipe.

The process used to recover the value of the beam polarization involves the fact that the cross section for circularly polarized light on transversely polarized leptons has a spin dependent azimuthal distribution: the asymmetry constructed from the shift in vertical direction of the two light polarization states is proportional to the electron beam polarization.

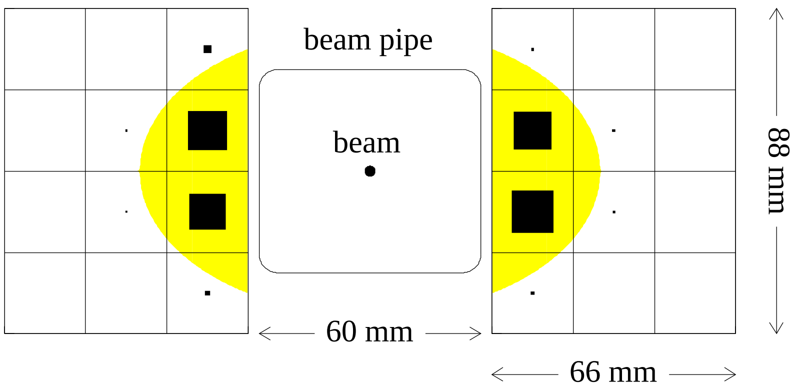

Figure 2.5: Schematic picture of the luminosity monitor, with the hit distribution (the black boxes have a size proportional to the number of hits). The shaded area corresponds to the beam acceptance.

2.3 The luminosity monitor

Since the luminosity cannot be measured by placing a detector inside the beam-pipe, an indirect measurement is obtained from the scattering rate of beam electrons (positrons) off the atomic target electrons, in the elastic Møller (Bhabha) reaction

$$e^{-(+)} + e^{-} \rightarrow e^{-(+)} + e^{-} \tag{2.4}$$

and on the annihilation

$$e^{+} + e^{-} \rightarrow 2\gamma \tag{2.5}$$

in the case of a positron beam. The kinematics of the scattering are precisely defined: the scattered particles each carrying half the beam energy exit the beam-pipe at 7.2 m from the scattering point, where two identical calorimeters are placed in order to detect the two particles in coincidence. Each calorimeter, 2.2x2.2x20 cm^3 in size, consists of 12 crystals of $NaBi(WO_4)_2$, as shown in Fig. 2.5, each coupled to a photo-multiplier. The luminosity is then obtained from the ratio of the measured rate over the cross section for the process, which is precisely known. As radiation at beam injection and dump can damage the calorimeters, they are usually moved 20 cm away horizontally from the beam-pipe at those times.

2.4 The target

One of the strengths of the HERMES experiment is its target ([6]), because of its purity and its position internal to the beam-pipe, so that the electron beam does not encounter any unpolarized material before colliding with the target atoms. A schematic of the target is shown in Fig. 2.6.

An atomic beam source (ABS) is used to create the target atoms, at a rate of approximately 6.4×10^{16} atoms/sec. The atoms are then injected from the top into the target cell. The whole system is surrounded by a solenoidal magnet providing a homogeneous field of up to 1.5 Tm parallel or anti-parallel to the HERA beam direction. The target cell is 40 cm long and 75 μm thick, with an elliptical cross section, and is made of pure aluminum. The gas is then pumped away by a differential pumping system at each end of the storage cell, giving the target density a characteristic triangular density profile. A cooling system, which brings the temperature down to 30 K decreases the velocity of the atoms, allowing them to spend more time in the cell, and increasing the target density to approximately 10^{14} atoms/cm^2.

The polarization is quickly measured by a *Breit-Rabi polarimeter* (BRP) and the polarization is reversed about every minute to reduce systematic effects. A small fraction of deuterium atoms is extracted from the target cell through a tube mounted on the target cell, where through radio frequency transitions and sextuple magnets it is possible to isolate the nuclear spin. Mass spectroscopy allows the measurement of the occupancy number of the selected state, and the atomic polarization. The *target gas analyzer* (TGA) measures the fraction of dissociated target atoms in the cell. Since the target atoms recombine into molecules in the cell, corrections have to be made to the polarization value measured by the BRP. The polarization of the gas inside the cell, P_T, can be extracted from the values measured by the TGA and BRP:

$$P_T = \alpha_0 P_{BRP}[(1-\alpha_r)\beta + \alpha_r] \; , \tag{2.6}$$

where α_0 is the initial fraction of atoms leaving the ABS, α_r is the fraction of atoms that do not recombine to molecules in the target cell, and β (assumed to be 0.5) is the nuclear polarization of the recombined molecules relative to the nuclear polarization of the atoms P_{BRP}.

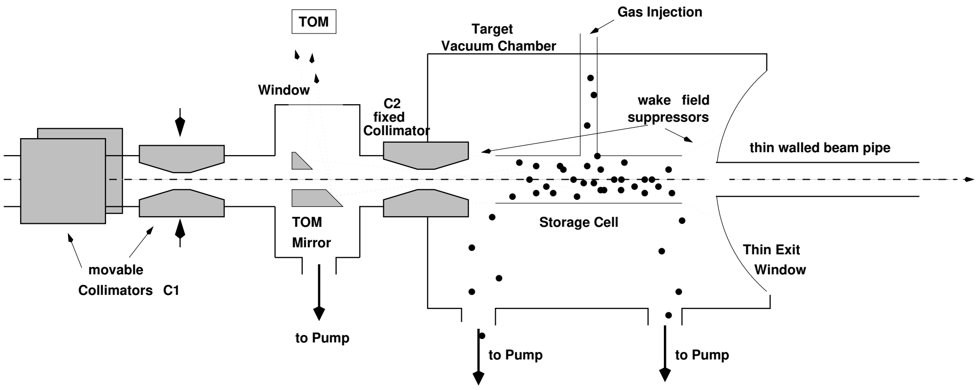

Figure 2.6: Scheme of the HERMES target.

The values of α_0 =0.934, α_r =0.957, P_{BRP} =0.81 characterize the 1998 data set. In 2000 the target conditions were extremely stable, and $P^+ = 0.851$ and $P^- = 0.840$ are the averaged constant values of target polarization in the two polarization states. They have been used in the g_1 analysis presented in this thesis, with a relative error of 8% and 4% for 1998 and 2000.

2.5 The tracking system

The Tracking System consists of a set of drift chambers DVC, two front chambers FC1/2, three magnet chambers MC1/3 and two back chambers BC1/2 per detector half. It serves many purposes. First, it has to provide a measurement of the position of the scattering vertex in the target. Second, through the bending of the track in the magnetic field, it gives the track's momentum. Third, it has to associate tracks to hits in the particle identification detectors. The overall tracking efficiency is larger than 95%, with a momentum resolution of 0.7 to 1.25% in the total kinematical range, and an angular resolution $\delta\theta$ lower than 0.6 mrad. Many tracking chambers have wires oriented along three planes, of which one is the vertical direction (X plane) to provide the x coordinate, while the other two are tilted +30^o and -30^o (U and V planes). There are no chambers with wires in the horizontal direction since they would sag, given the length of the chambers.

2.5.1 The front chambers

The DVC's were proposed in 1995 to improve the tracking in front of the magnet. They became operative in 1997. Both the FC and DVC are a set of 6 planes of alternating anode and cathode wires, separated by cathode planes. The DVC and FC are 1.1 m and 1.6 m away from the target, and their resolutions are of the order of 220 μm.

2.5.2 The back chambers

The BC's form the tracking system behind the magnet. They are arranged in four sets, two above and two below the beam-pipe, two directly behind the magnet and two downstream, after the RICH. Each chamber consists of six wire planes alternated with cathode foils. The wires in the first and last pair of planes are tilted by 30^o. They measure the track direction after the magnetic field, thus providing a measurement of momentum.

Their resolutions are approximately 210 μm for BC1/2 and 250 μm for BC3/4.

2.5.3 The magnet

The HERMES magnet provides an integrated magnetic field of 1.5 Tm, with the magnetic field in the vertical direction, so that the particles are deflected in the horizontal direction. The magnet size sets the limits on the geometrical acceptance to the spectrometer: $\pm$ 170 mrad in the horizontal direction and $\pm$ 140 mrad in the vertical direction, while the shielding plate gives the lower limit to the vertical acceptance, setting it to $\pm$ 40 mrad. The tracks are reconstructed independently in the front and back tracking system and then they are matched to the center of the magnet by a fitting procedure. Three sets of Magnet Chambers are located in the gap of the magnet, as shown in Fig. 2.1. Each chamber is made of 3 planes in the XUV orientations. They were designed to help match the front and back tracks, but they turned out to be very useful also in the detection of low energy particles that are then deflected away by the magnetic field, and are then not detected by the back chambers. Their resolution is on the order of 1 mm.

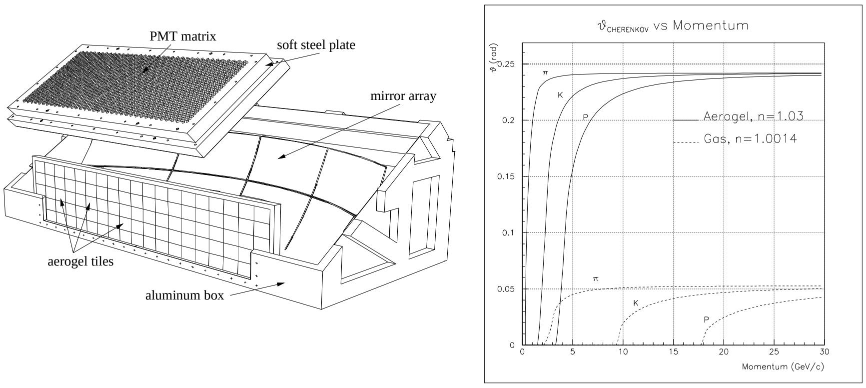

Figure 2.7: Left: the RICH detector. Right: angle of Cerenkov emission as a function of momentum for pions, kaons and protons, in aerogel and gas. At low momentum the plot shows that the aerogel gives a good discrimination among particles, while the gas is good at high momentum, where the aerogel curves tend to overlap.

2.6 The particle identification system

The HERMES spectrometer includes four particle identification detectors: a Cerenkov detector, replaced by a Ring Imaging Cerenkov detector (RICH) in 1998, a Transition Radiation Detector (TRD), a preshower (H2) and an electromagnetic calorimeter (CALO).

2.6.1 The RICH

The threshold gas Cerenkov detector present at HERMES from 1995 to 1997 was replaced in 1998 with a dual radiator Ring Imaging Cerenkov Detector (RICH), see Fig. 2.7.

The RICH is the first particle identification detector a particle meets. It is located between the drift chambers BC1/2 and BC3/4. It allows the identification of pions, kaons and protons over a large momentum range, with a low contamination and a high efficiency.

Most of the hadrons present at HERMES have a momentum between 2 and 15 GeV. The scattered particles encounter a first radiator consisting of an array of 17x5 silica aerogel tiles, followed by a 4000 l volume of C_4F_{10} radiator gas. Depending on the β of the particle, it will emit Cerenkov radiation in the aerogel, in the gas, or in both*. The light is then reflected by a mirror, and the Cerenkov ring is detected by an array of 1934 photo-

* A particle emits Cerenkov radiation in a medium if the ratio of its velocity over the speed of light in the medium is greater than 1.

multipliers per detector half. As shown in Fig. 2.7 the two radiators have a different momentum window in which they give a good separation between pions, kaons and protons: momenta lower than approximately 10 GeV are below threshold for Cerenkov radiation with a gas radiator, while in this range the aerogel has its greatest discriminating power. At higher momenta the curves for aerogel saturate and it is not possible anymore to distinguish among hadrons based on aerogel information, and the gas is used instead. In the analysis for the determination of the structure function g_1 no information is used from the RICH, as only a good discrimination is needed between hadrons and leptons. It is not important to identify the kind of hadron.

2.6.2 The transition radiation detector

The Transition Radiation Detector (TRD) (see Fig. 2.8) is a particle identification detector used for the separation of electrons from hadrons. When a relativistic particle passes through the interface between two dielectric media with dielectric constants ϵ_1 and ϵ_2, it emits radiation in the forward direction at an angle φ proportional to $1/\gamma$, where γ is the Lorentz factor E/m, and E and m being the energy and mass of the particle. The transition radiation (TR) for ultra-relativistic particles is in the X-ray region (several keV), useful for particle physics applications. In the passage from vacuum to a medium with electron density n_e, the probability of emission of a transition radiation photon in the

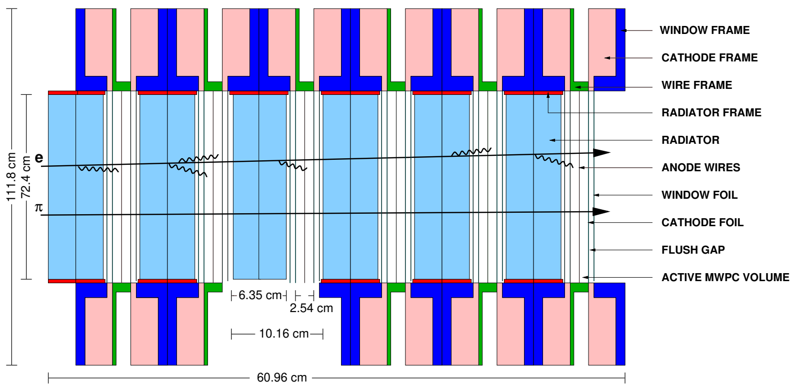

Figure 2.8: Schematic picture of the six TRD modules. Electrons and pions induce different signals in the detector since electrons emit TR photons, detected on top of the ionization dE/dx.

ultra-relativistic regime is given by

$$W_{TR} = \frac{8\pi\alpha^2\gamma n_e}{3m_e} \tag{2.7}$$

where α is the fine structure constant and m_e the electron mass. The linear dependence of W_{TR} on γ enables a separation of highly relativistic particles ($\beta \simeq 1$) in a way that would require a much longer Cerenkov detector for the same separation power. For example a 5 GeV electron has a $\gamma = 10000$ while for a pion $\gamma = 35$, so that the probability that the electron emits a TR photon will be 300 times larger than for the pion. Fig. 2.9 shows how the measurement of the TR improves the separation of electrons from pions. The dependence of W_{TR} on the square of $\alpha = 1/137$ implies that in order to achieve a considerable probability for the emission of a TR photon, many radiator layers are needed, and the dependence on n_e implies the use of a material with high electron density. The radiator also needs to be highly transparent to X rays, in order to avoid self-absorption. A polypropylene fiber radiator satisfies all requirements, while the last problem is also solved by building a sandwich structure of radiators and X-ray detectors, as shown in Fig. 2.8. The radiator is a loosely packed array of polypropylene fibers with a diameter of 17-20 μm, arranged in roughly 300 2-dimensional layers, with a total thickness of 6.35 cm.

The detector consists of 12 modules, 6 above and 6 below the beam pipe. The outer

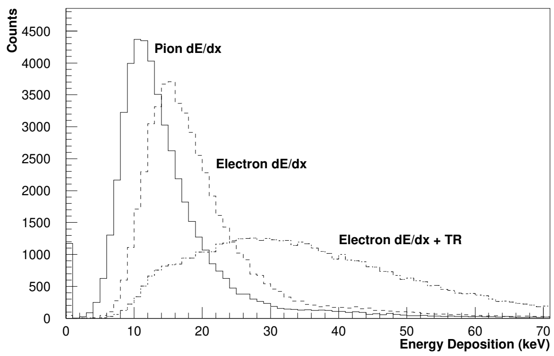

Figure 2.9: Response of a single TRD module. The energy dE/dx deposited in the TRD due to ionization is not able to provide a clear separation between pions and electrons. When the transition radiation is included, the electron peak moves to higher energies and the separation improves.

dimensions of the two halves are 401 x 112 x 61 cm^3. Each module is made of a radiator and a wire chamber, separated by a flush-gap where CO_2 circulates in order to avoid the diffusion of oxygen and nitrogen into the chambers, thus protecting them from the ambient atmosphere. The gas in the wire chambers needs to have high atomic number, in order to achieve best X-ray absorption, thus the use of a mix of 90% Xenon and 10% methane, the latter acting as a quencher to avoid the creation of electron avalanches in the chamber.

The TRD detector reaches a *hadron rejection factor* (defined as the ratio of the total number of hadrons to the number of hadrons misidentified as leptons, for a given energy cut) of 100 for 90% lepton efficiency (the number of leptons above the cut over the total number of leptons). The discrimination can be improved by a factor three with a probability analysis ([15]), whose concepts will be outlined in section 2.6.5.

2.6.3 The preshower detector

The preshower detector H2 sits in the back region (see Fig. 2.1) and it has the two functions of being both in the trigger and part of the particle identification system. The scintillators are identical to the hodoscope H1; both consist of 42 vertical 9.3 cm wide scintillator paddles overlapping each other by 1.5 mm to avoid acceptance gaps. H2 incorporates 1.1 cm of lead directly in front of the scintillators. Hadrons are minimum ionizing so they produce a very low signal in the detector, while leptons produce electromagnetic showers, triggered by the high Z of the lead, thus giving rise to a much higher signal. Hadrons deposit about 2 MeV in the detector, while the electron energy distribution varies roughly like ln E. Fig. 2.11 includes a histogram with the response of the preshower.

2.6.4 The electromagnetic calorimeter

The calorimeter is part of both the trigger and the particle identification system. It consists of two identical 42x10 arrays of 9x9x50 cm^3 blocks of radiation resistant F101 lead-glass located above and below the beam-pipe (see Fig. 2.10), each connected to a photomultiplier. As with the luminosity monitor, each half is moved away from the beam-pipe 50 cm vertically at beam injection and dump to avoid radiation damage. Leptons tend to lose all their energy by creating electromagnetic showers which start in the preshower,

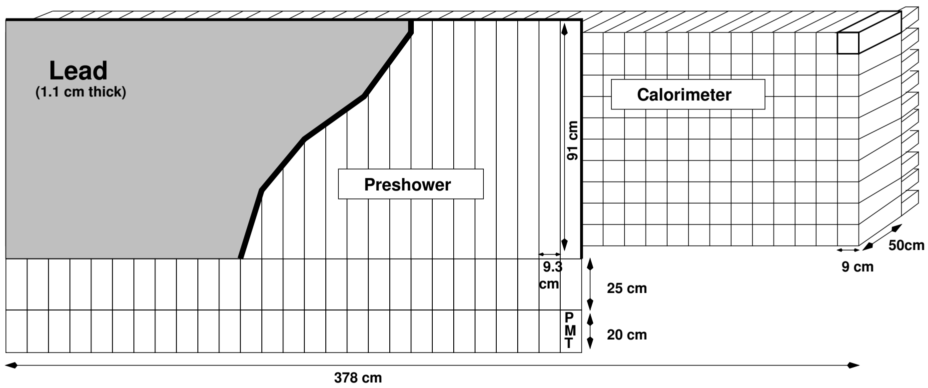

Figure 2.10: Preshower H2 and calorimeter. Particles first encounter 1.1 cm of lead, which favors the creation of electromagnetic showers, giving rise to a high signal in H2 and the calorimeter if the particle was a lepton, thus providing a discrimination with hadrons.

and are almost fully contained within the preshower and the calorimeter, since the total length of the calorimeter blocks is 18 radiation lengths. Hadrons instead tend to lose their energy by hadron interactions, processes that have a much higher characteristic length, so that a hadronic shower will not be entirely contained in the calorimeter. This proves to be a means of hadron-lepton separation. For hadrons the sum of the energies deposited in the preshower and in the calorimeter divided by the momentum measured by the tracking system will be much less than 1, while for leptons this ratio will be very close to 1. Fig. 2.11 includes a histogram with the E/p calorimeter response and the cuts used to separate leptons from hadrons. It also shows a tail with events having $E/p > 1$. Such events could come from high energy leptons that lose energy by radiating a photon before entering the magnet and the measurement of their momentum; if the emitted photon is detected in the same calorimeter cluster, this would give a measured energy greater than the momentum.

2.6.5 PID

From the response of the particle identification detectors it is possible to generate a quantity PID (Particle IDentification), that is related to the probability of a particle to be a hadron or a lepton. From the deflection of the particle in the magnet it is possible to calculate its momentum p. In each PID detector the particle will leave some energy E. The issue is then to find the probability $P(l(h)|Ep)$, given E and p, that the particle is a lepton

	1996-1997		1998-2000	
	Leptons	Hadrons	Leptons	Hadrons
CALO	0.92$< E/p <$ 1.10	0.01$< E/p <$ 0.80	0.92$< E/p <$ 1.05	0.01$< E/p <$ 0.50
PRE	$E >$ 0.025 GeV	$E <$ 0.004 GeV	$E >$ 0.03 GeV	$E <$ 0.003 GeV
TRD	$E >$26 keV	0.1$< E$(keV)$<$14	$E >$ 26 keV	0.1 $< E$(keV)$<$13

Table 2.1: Hard cuts used to identify leptons and hadrons.

l or a hadron h.

Bayes theorem relates such a probability to the observable probabilities $P(l(h)|p)$ that a particle with momentum p is a lepton (hadron), and $P(E|l(h)p)$ that a lepton (hadron) with momentum p deposits an energy E in the detector:

$$P(l(h)|Ep) = \frac{P(l(h)|p)\ P(E|l(h)p)}{P(l|p)P(E|lp) + P(h|p)P(E|hp)}\ . \tag{2.8}$$

The probability distributions $P(E|lp)$ and $P(E|hp)$, called *parent distributions*, can be measured in a test beam facility by measuring the response of the detectors to a beam of pure leptons or hadrons. Another way, commonly used in HERMES , is to place "hard" cuts on the response of the other detectors, to be sure that the response of the detector under consideration is generated by a certain type of particle. This way has the advantage of taking into account possible aging effects of the detectors. The cuts have to be hard enough to define a clean sample but also they need to have enough statistics, so the cut values vary for each data production, being tighter only for the productions with more data like 1998, 1999 and 2000, and less tight for 1996 and 1997, as is shown in Table 2.1.

Fig. 2.11 shows the response of these detectors and the cuts identifying leptons and hadrons in 1996-1997. The plots are obtained using data from 1996. A track is included if it has a good data quality, it is Trigger 21 (the DIS trigger in HERMES , see next section), and its vertex originates from the target region. From the parent distributions one can create the quantity PID. The flux ratio (ratio of hadrons over leptons) and the PID for each detector D are defined as:

$$\phi = \frac{\phi_h}{\phi_l} = \frac{P(h|p)}{P(l|p)} \qquad\qquad PID_D = \log_{10}\frac{P_D(E|lp)}{P_D(E|hp)}, \tag{2.9}$$

where P_D are the conditional probabilities for a detector D.

When one considers the response of more detectors then one gets a better discrimination between hadrons and leptons, so we can define as PID the combined PID for more

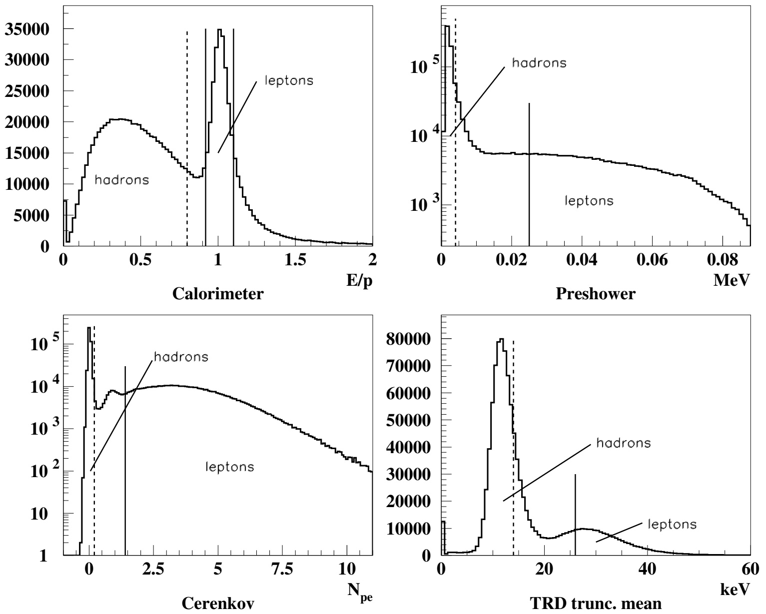

Figure 2.11: The responses of the Particle Identification Detectors. Superposed are the cuts identifying hadrons (dashed lines) and leptons (solid lines). The plots refer to the 1996 data. Since the Cerenkov detector was upgraded to a RICH, it is not included in the PID anymore. The plots are from Ref. [16].

than one detector:

$$PID' = \log_{10} \prod_D \frac{P_D(E|lp)}{P_D(E|hp)} = \sum_D PID_D \; . \tag{2.10}$$

The most common PID combinations used in HERMES are

$$\begin{aligned} PID2 &= PID_{CALO} + PID_{PRE} \\ PID3 &= PID_{CALO} + PID_{PRE} + PID_{CER} \\ PID5 &= PID_{TRD} = \sum_{i=1}^{6} PID_{TRD_i} \; , \end{aligned} \tag{2.11}$$

where the last sum runs over the 6 TRD modules per detector half.

After the 1997 production, the Cerenkov was upgraded to a RICH detector, and the information coming from it no longer enters into the PID, as now it is mainly used for hadron identification. So for the data used in this thesis PID2=PID3.

The quantity

$$PID = \log_{10} \frac{P(l|Ep)}{P(h|Ep)} \tag{2.12}$$

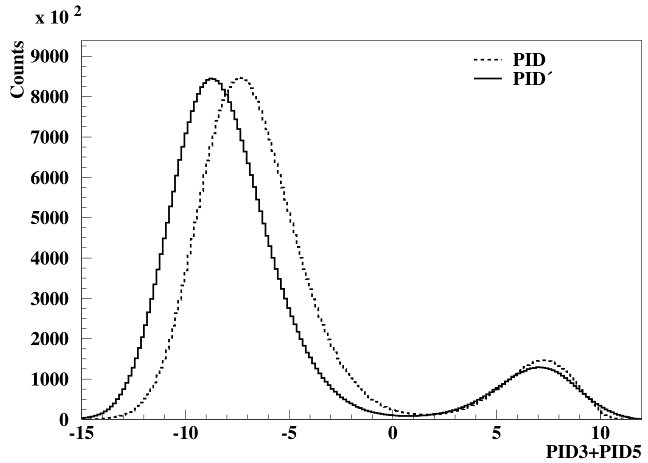

Figure 2.12: The distribution of PID values when fluxes are taken into account (dotted line) compared to the one without fluxes (solid line) (from Ref. [17]). Depending on the cut value, the inclusion of fluxes is more or less important.

is clearly positive if the probability of being a lepton is higher than that of being a hadron, and vice-versa for a hadron. In terms of flux ratio ϕ and PID, and using Eq. (2.8) it can be re-written as:

$$PID = \log_{10} \frac{P(E|lp)}{P(E|hp)} \cdot \frac{P(l|p)}{P(h|p)} = PID' - \log_{10} \phi \,. \tag{2.13}$$

In many HERMES analyses the flux ratios are often neglected, and this is clearly wrong, especially if one places a cut very close to zero, as is shown in Fig. 2.12.

The fluxes of hadrons and leptons depend both on the momentum p and on the polar angle θ, since the cross section depends on these quantities. They are not as straightforward to calculate as the PID since they require the particle identification as an input, so they are calculated using an iterative procedure giving an initial guess for the fluxes, and continuing until convergence, as is explained in section 3.2.2.

2.7 Trigger

In HERMES a number of triggers are used to extract information useful not only to physics but also for diagnostics on the functioning of the detector.

As a first level screening, many types of triggers are used to record data likely produced by different physical processes. Trigger 21 is the trigger defining a potential deep inelastic scattering event.

The trigger requirements that a track has to satisfy involve signals in the top or bottom H0, H1, H2 scintillators and the calorimeter.

The trigger requirements are briefly summarized.

- The requirement of a signal in the H0 and H1 detectors prevents showers originating from photons and resulting in high signals in H2 and the calorimeter from being accepted as DIS events.

- The signal in the preshower is required to be above the minimum ionizing level, in order to avoid background from hadronic showers.

- The calorimeter must have an energy deposition above 1.4 GeV. Since hadrons are less likely to shower in the calorimeter, the combination of a signal in the preshower H2 and the calorimeter has a high probability of coming from an electromagnetic shower rather than a hadronic one. The threshold of the calorimeter was set to 3.5 GeV until 1996, equivalent to an event selection with cut on $y = (E - E')/E < 0.87$, where E is the beam energy and E' is the energy of the scattered track.

  From 1996 the threshold was lowered to 1.4 GeV, so that the cut on y was extended to $y < 0.91$.

- The signal has to satisfy time ordering conditions: it is compared to the HERA clock, which is synchronized to the beam bunch signal, and it is accepted only if it is within some time window corresponding to the passage of the electron beam.

2.7.1 Trigger Efficiencies

Trigger efficiencies (TE's) had never been taken into account in any HERMES analysis before the studies shown in this thesis. It was always believed that the main source of inefficiency was from the tracking system, and that the trigger was highly efficient. It will be shown that this is not true, as the efficiency of Trigger 21 was as low as 90% from 1998 to 2000. Here only studies regarding 1998 and 2000 will be shown. Results on 1999 and high density unpolarised data are in Ref.[18].

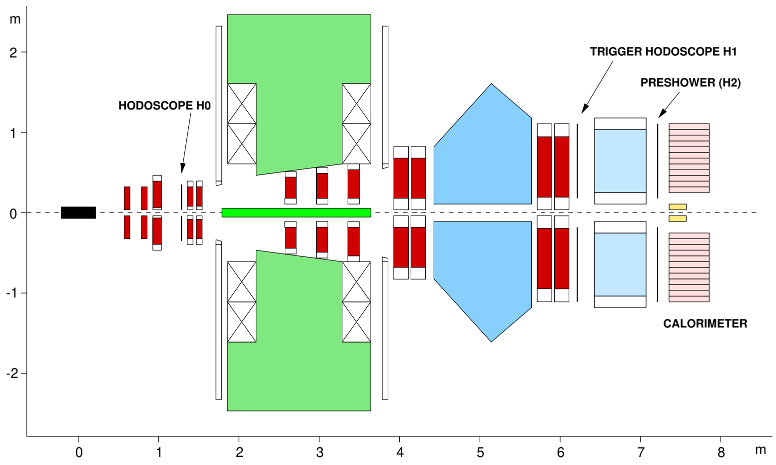

Figure 2.13: The detectors involved in the trigger study.

The detector that contributed the most to the inefficiency was H0 (see Fig. 2.13). Unfortunately this was due to many possible causes, not all well understood. One possible reason was a small misalignment found in the bottom H0. During the summer 1999 shutdown this problem was discovered and fixed, but the low efficiencies and the top-bottom difference in trigger efficiencies remained, disappearing only after various voltage increases, showing that the most probable cause for the inefficiencies was a voltage problem. In the 2000 production the H0 efficiency was again low, but this time the top efficiency was worse than the bottom one. The source of low efficiency is probably radiation damage, as it will be explained below.

2.7.2 Definitions

The efficiencies of H0, H1, H2, CALO must be determined in order to get the Trigger 21 efficiency. The main reason for this study was to find the upper y-cut to be used for the low-x and low-Q^2 g_1 analysis. After these studies it was found that the H0 efficiency was very low compared to previous years, so it was important to find the cause of this behavior. Trigger 18, 19, 20, 28 and 21 are defined as:

$$\begin{aligned}
\mathrm{Tr18} &= (H1 * H2 * (CALO > 1.4\,\mathrm{GeV}))_{\mathrm{top}} + ()_{\mathrm{bot}} \\
\mathrm{Tr19} &= (H0 * H2 * (CALO > 1.4\,\mathrm{GeV}))_{\mathrm{top}} + ()_{\mathrm{bot}} \\
\mathrm{Tr20} &= (H0 * H1 * (CALO > 1.4\,\mathrm{GeV}))_{\mathrm{top}} + ()_{\mathrm{bot}}
\end{aligned}$$

$$
\begin{aligned}
\text{Tr28} &= (H0 * H1 * H2 * BC)_{\text{top}} * ()_{\text{bot}} \\
\text{Tr21} &= (H0 * H1 * H2 * (CALO > 1.4\,\text{GeV}))_{\text{top}} + ()_{\text{bot}} \,. \qquad (2.14)
\end{aligned}
$$

The efficiency of each trigger detector and Trigger 21 are

$$
\begin{aligned}
\varepsilon(H0) &= \frac{N_{18\&21}}{N_{18}} \qquad (2.15)\\
\varepsilon(H1) &= \frac{N_{19\&21}}{N_{19}} \qquad (2.16)\\
\varepsilon(H2) &= \frac{N_{20\&21}}{N_{20}} \qquad (2.17)\\
\varepsilon(CALO) &= \frac{N_{28\&21}}{N_{28}} \qquad (2.18)\\
\varepsilon(\text{Tr21}) &= \varepsilon(H0) * \varepsilon(H1) * \varepsilon(H2) * \varepsilon(CALO) \,, \qquad (2.19)
\end{aligned}
$$

where $N_{i\&21}$ is the number of events common to Trigger i and 21, while N_i is the number of events that fired Trigger i. Clearly $N_{i\&21} < N_i$, so that their ratio is always less than or equal to one. A track satisfying all geometric and PID cuts and firing Trigger i should also fire Trigger 21, which contains a signal from the same detectors except one, so the efficiency of this one detector is determined by the number of times that the detector did not give a signal when it should have done so.

In this study an event was selected if the track with highest momentum in the event is of the same charge as the beam, if it satisfies the geometric cuts that ensure that all the track was contained within the acceptance of the HERMES detector and originated in the target and a PID5>4 cut. Such a high PID cut, together with information from the RICH, were necessary to make sure that the particle selected was an electron, since no information could be used from the preshower and calorimeter, as they enter in the study, and using information from them could bias the result. The cut applied to the RICH was

$$
\log_{10}\left(\frac{\text{g1RICH.rprob1}}{\text{g1RICHrprob3}}\right) > 0 \,, \qquad (2.20)
$$

to take into account that the electron could be a misidentified pion. The quantity in Eq. (2.20) is the logarithm of the ratio of probabilities for the RICH signal to come from an electron over the probability for the particle to be a pion. Only if Prob(e)>Prob(π) the logarithm is greater than zero.

2.7.3 Calorimeter efficiency

No specific trigger can be used to directly derive the calorimeter efficiency. Instead, Trigger 28 can be used, since it is the closest to a Trigger 21 without CALO:

$$\mathrm{Tr28} \;=\; (\; H0 \;*\; H1 \;*\; H2 \;*\; BC\;)_{\mathrm{top}} \;*\; (\;)_{\mathrm{bot}} \,. \tag{2.21}$$

The BC's are known to be very efficient, so that they can be neglected in Eq. (2.21). The presence of a logical AND instead of a logical OR in Eq. (2.21) requires that events with at least 2 tracks have to be selected, of which one has to be in the top and one in the bottom half of the detector. This fact is the cause for the (statistical) error bars being large for the calorimeter efficiencies.

2.7.4 Error calculation

The error on the trigger efficiencies is the error on quantities of the form:

$$\varepsilon = \frac{N_A}{N_B} \,. \tag{2.22}$$

The error formula used in this report is ([19])

$$\delta\varepsilon = \sqrt{\frac{(N_A+1)(N_B-N_A+1)}{(N_B+2)^2(N_B+3)}} \,. \tag{2.23}$$

The origin of this formula is not straightforward. It takes into account the fact that there are bins in which N_A and N_B are very small numbers, so that the usual error formulas may not be valid, since they usually apply in the limit of large numbers. In the limit of large numbers it takes the usual form of the binomial error:

$$\delta\varepsilon = \sqrt{\frac{(1-\varepsilon)\,\varepsilon}{N_B}} \,. \tag{2.24}$$

The errors will be plotted as asymmetric since the efficiency cannot be larger than 1.

2.7.5 Trigger efficiencies for 1998 data set

Plots of the efficiencies of the H0, H1, H2 and calorimeter detectors are shown in Fig. 2.14, as a function of θ_x and θ_y. These are the angles that the projection of the track on the

x, y plane makes with the x and y axis:

$$\begin{aligned} \tan\theta_x &= \tan\theta\cos\varphi \\ \tan\theta_y &= \tan\theta\sin\varphi \,. \end{aligned} \tag{2.25}$$

The last two variables were chosen instead of the cartesian position variables x and y because they reflect the acceptance of the HERMES detector, simplifying the comparison among plots of different detectors. They also do not require the knowledge of the exact position of the detectors on the z axis. The figures show the upper and lower detectors, and the beam line is to be imagined to be in the center, in the zero position of the (θ_x, θ_y) axis. The plots are done taking into account only events with one track, as the efficiency for the detection of more than 1 track is higher and depends on the efficiencies for 1 track in a non trivial way. For diagnosis purposes 1-track events were singled out and the efficiencies studied. The efficiencies of the H1, H2, Calo and the top H0 detector were all very close to 1, while the H0 bottom detector has a lower efficiency of the order or 90%, almost independent of the position. At high angles there are not enough statistics, so that the low values of the efficiencies in green actually have large errors.

The trigger efficiencies have to be taken into account in any measurement of absolute cross sections. The cross section σ depends on the ratio between the measured number of events N and the efficiency:

$$\sigma = \frac{N}{\varepsilon L} \,, \tag{2.26}$$

where L is the luminosity. Given the efficiency ε, this is equivalent to considering the *corrected* number of events common to Trigger 18 and 21:

$$N_{18\&21}^{\text{corr}} = \frac{N_{18\&21}^{\text{meas}}}{\varepsilon(H0)} \tag{2.27}$$

in the cross section expression, together with $\varepsilon = 1$. By correcting $N_{18\&21}$ in each bin of momentum, track multiplicity, time, etc., the efficiency in each of these bins should be 1, since:

$$\varepsilon^{\text{corr}}(H0) = \frac{N_{18\&21}^{\text{corr}}}{N_{18}} = 1 \,. \tag{2.28}$$

This correction has been done in two different ways for the years 1998 and 2000.

In the 1998 production $\varepsilon(H0)$ was very low only in the bottom detector, probably because of an incorrect voltage setting. The bad voltage gave a strong dependence of

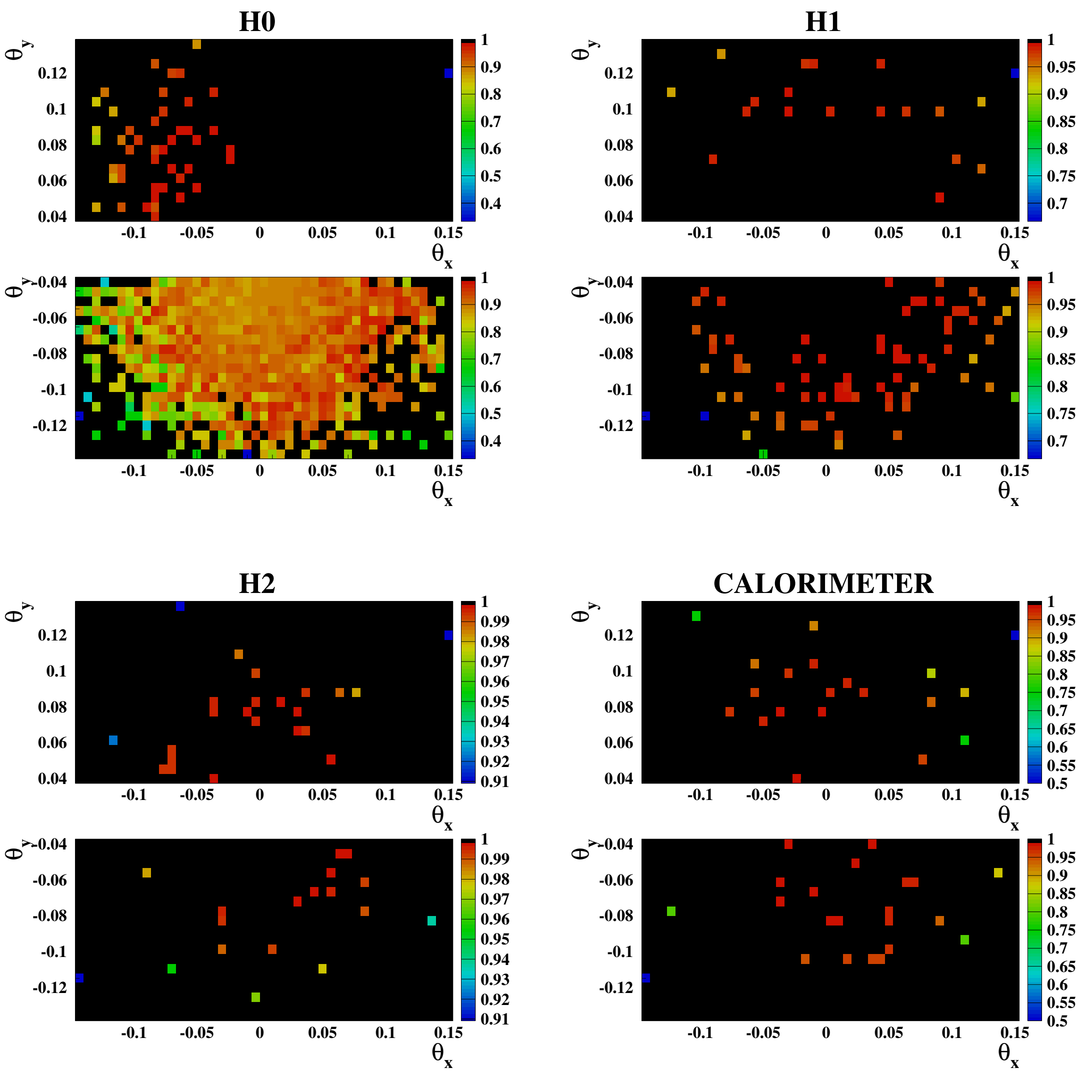

Figure 2.14: Color-coded plots of the efficiency of Trigger 18 (H0,top left), Trigger 19 (H1, top right), Trigger 20 (H2, bottom left) for 1-track events and Trigger 28 (Calorimeter, bottom right) for 2-track events, as a function of θ_x and θ_y. The efficiency for the H0 detector is low for the bottom detector, while all the other detectors show very high efficiencies.

the efficiencies on the particle's momentum, as is shown in the top plots of Fig. 2.15. The bottom plots in Fig. 2.15 show instead plots of the efficiency versus time (beam fill number) for one track events (left) and any number of tracks (right). Even though the efficiencies are not constant in time, it is not possible to separate them into different

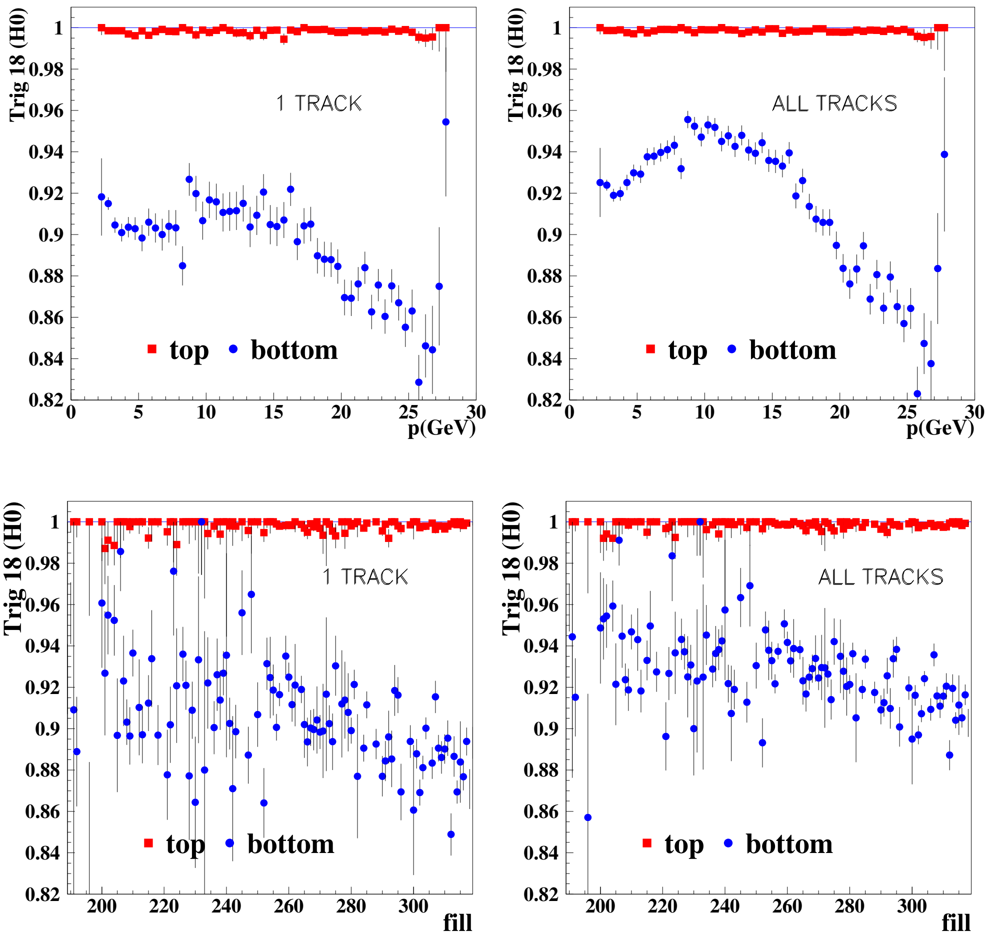

Figure 2.15: Trigger 18 efficiency (H0 detector) for 1 track events (left) and total (any number of tracks) efficiency (right), for the 1998 data set, as a function of momentum in the top plots, and of beam fill number in the bottom plots. The total efficiency is higher than the efficiency for 1 track events since events with multiple tracks have a higher probability of being detected, thus increasing the efficiency.

periods, mostly because there is not enough statistics. Since the only strong dependencies are the ones on momentum and on the number of tracks, the efficiencies for 1, 2 and 3 or more tracks were considered, and then fitted to a polynomial function of the momentum. The functions are shown in Table 2.2.

The effect of the correction on the efficiencies is shown in Fig. 2.16, where the corrected total efficiencies are plotted as a function of momentum and time. The figure

# of tracks	Correction function
1	$0.97 - 0.035p + 0.0059p^2 - 0.40 \times 10^{-3}p^3 + 0.11 \times 10^{-4}p^4 - 0.115 \times 10^{-6}p^5$
2	$0.966 + 0.00324p - 0.266 \times 10^{-3}p^2$
3 or more	$1.0003 - 0.0042p + 0.64 \times 10^{-3}p^2 - 0.28 \times 10^{-4}p^3$

Table 2.2: Correction functions for Trigger 18 efficiency as a function of the particle's momentum, where p is in GeV. The correction is valid for the bottom H0 detector, in the 1998 data set.

shows that the corrections are valid within $\simeq 2\%$.

2.7.6 Trigger efficiencies for 2000 data set

Fig. 2.17 shows the efficiencies for the H0, H1, H2 and Calorimeter detectors, as a function of θ_x and θ_y for the year 2000.

The efficiencies of the four detectors show a similar circular shape that can be easily explained as radiation damage, since the beam-pipe is in the origin of the θ_x,θ_y axis. The plots are made considering only 1-track events. The above mentioned figures also show that only the H0 detector has a very low efficiency, ranging from 94% in the top-center to less than 99% everywhere else. The other detectors show some damage and have

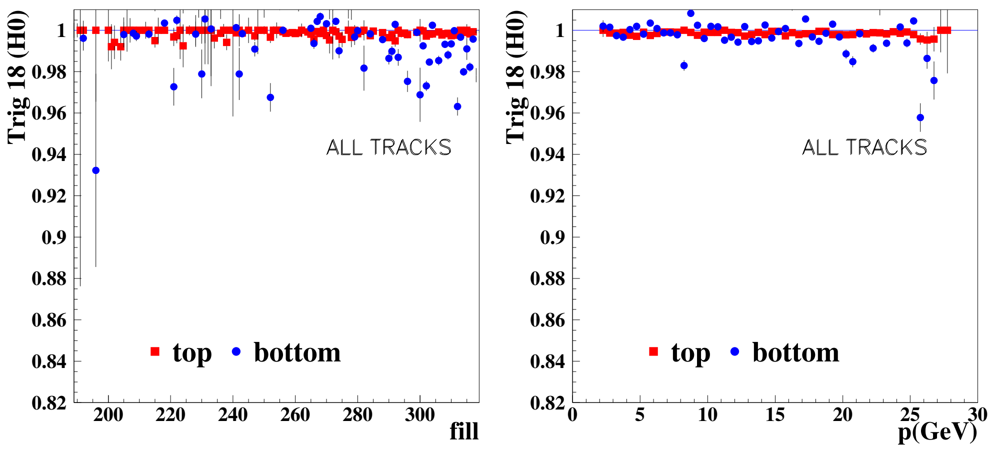

Figure 2.16: Final corrected Trigger 18 efficiencies as a function of time (left) and momentum (right), for 1998 data. The plots are done for the total efficiencies, i.e. for any number of tracks. Only the bottom efficiencies have been corrected.

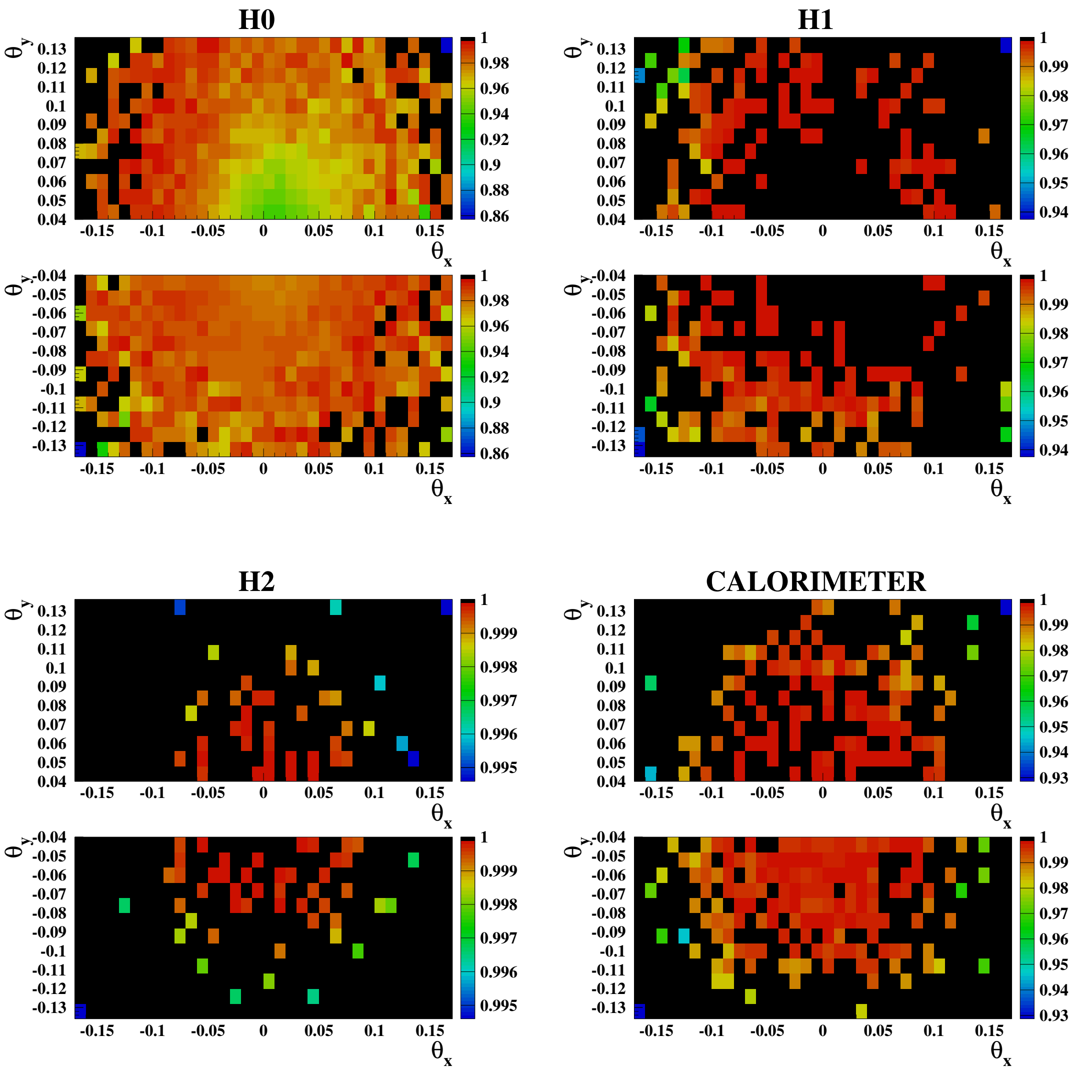

Figure 2.17: Color-coded plots of the efficiency of Trigger 18 (H0,top left), Trigger 19 (H1, top right) Trigger 20 (H2, bottom left) for 1-track event and Trigger 28 (Calorimeter, bottom right) for 2-track events, as a function of θ_x and θ_y, for 2000 data. They show radiation damage, clear from the circular shape of the efficiencies.

efficiencies above 99% everywhere such that further studies are not considered necessary. Some small values are shown at the borders of the detectors, but they are due to small statistics: in those regions the efficiencies have very large error bars (not shown on the plots). In the following we will then concentrate only on the H0 detector, since it was the major source of bad efficiency in Trigger 21.

The time dependence of the H0 efficiency is shown in Fig. 2.18 for 1-track events in the left plot and for any number of tracks in the right plot. As explained before the total efficiency is larger than the efficiency for 1 track only, since the probability of detection increases with the number of tracks. Fig. 2.18 shows that throughout the 2000 data set the efficiency in the bottom detector was higher than the one in the top detector, and two periods can be isolated, separated by fill 97. At that time there was a high voltage change in the H0 detector, that was able to bring the efficiencies up from about 94% to 97% in the top and from 97.5% to 98.5% in the bottom. Also a momentum dependence is visible in the bottom plots of Fig. 2.18, where the efficiencies in the first and last period, and for each period in top and bottom are plotted. The voltage change was not enough to remove the momentum dependence of the efficiency, especially since Fig. 2.17 shows some serious radiation damage. A new H0 detector was built and installed as a consequence of these studies. To get a proper efficiency estimation one then needs to separate the efficiency into bins of all these quantities. Even for the year 2000 and its large statistics this is not feasible. An alternate method was used: for each of the two periods (before and after fill 97), the efficiencies were calculated in bins of 1, 2, and 3-or-more track events and in θ_x, θ_y bins. In a second step, each event was re-weighted by the efficiencies as shown in Eq. (2.27), so that the only dependence left was on momentum, shown in Fig. 2.19. The efficiency in terms of track's momentum seems to be independent of the geometry, since the major effect of the correction was to push the data points up, so that they average 1, but the functional shape is almost unchanged. In a third step, the events were re-weighted by the momentum efficiency, for 1,2 and 3-or-more tracks, for each of the two periods. Fig. 2.20 shows the time dependence of the fully corrected efficiencies. The correction is good to within $\pm 1\%$. Due to the complexity of the correction, it is not reported here, but it is available for use on a DESY account in the form of a subroutine.

2.7.7 Conclusion

The trigger efficiencies have been studied for the two data productions 1998 and 2000, that will be used in the analysis of g_1^d.

In both years the main source of inefficiency was the H0 detector. In 1998 the reason

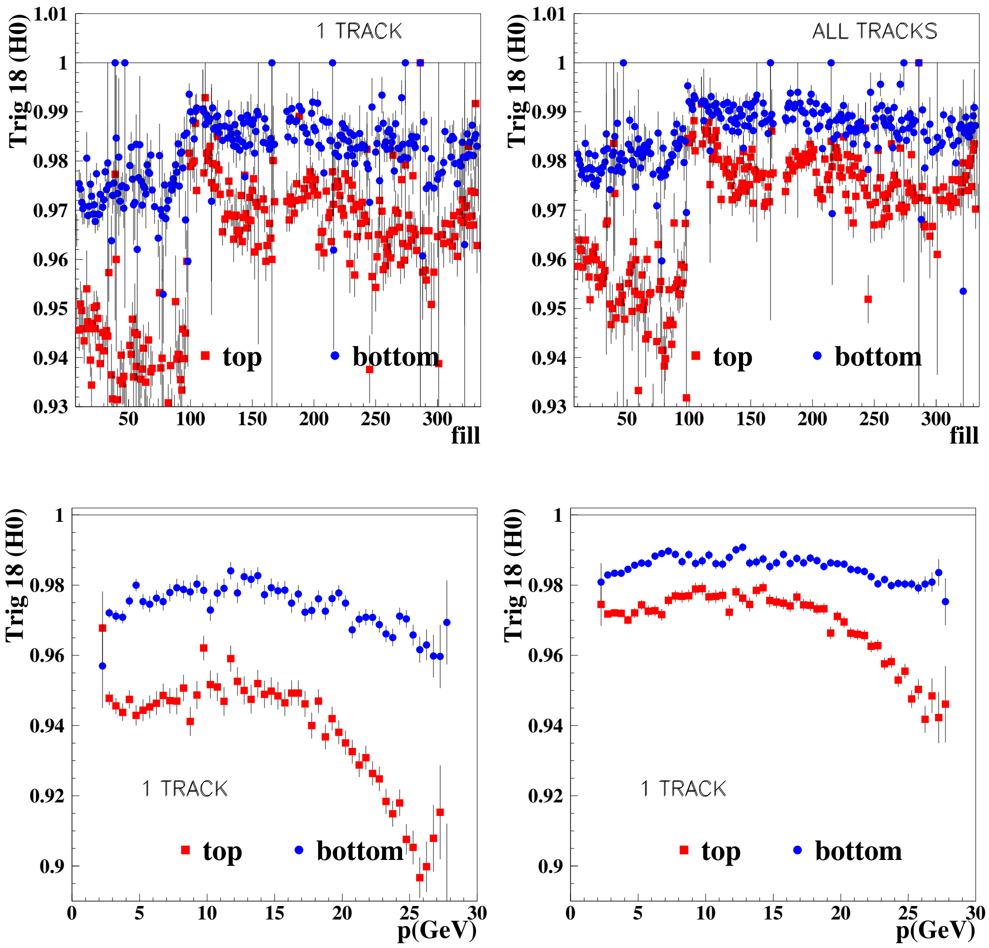

Figure 2.18: Trigger 18 efficiency (H0 detector) versus beam fill number for 1 track events (top-left) and total efficiency (top-right). The bottom plots show the momentum dependency for the two periods separated by fill 97.

for the inefficiency was likely an incorrect voltage setting, while in 2000 it was radiation damage. The H0 detector was replaced by a new one after 2000.

Corrections were obtained that should be applied to any cross section measurement to take into account the trigger efficiencies.

The effect on the g_1^d extraction will be considered in chapter 3.

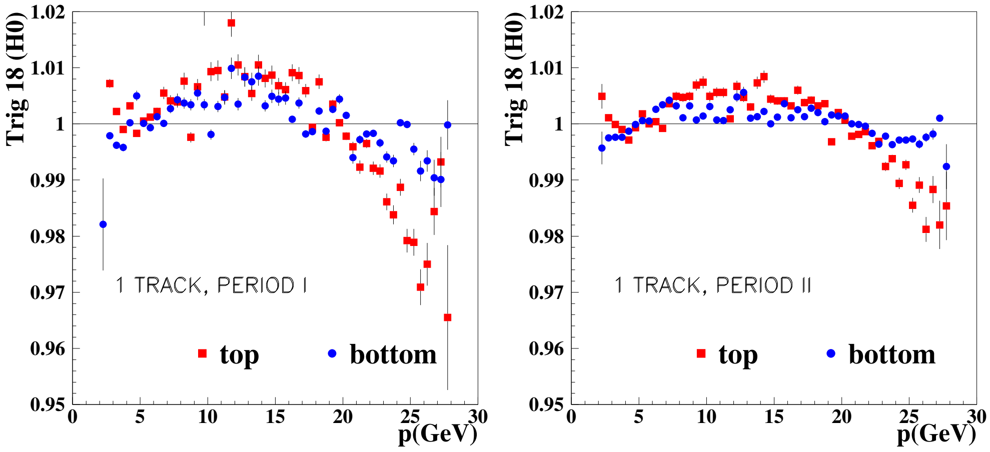

Figure 2.19: After being corrected for the geometric θ_x, θ_y dependence, the efficiency still shows a momentum dependence that has to be corrected in a second step, for the first period (left plot) and the second (right plot).

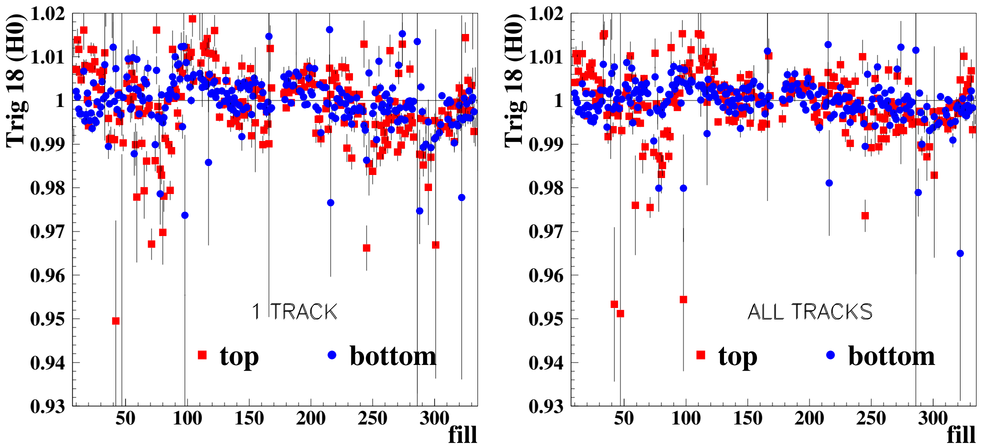

Figure 2.20: Time dependence of trigger 18 after the application of full correction. The correction brings the efficiencies to 1 within 1% for both top and bottom.

Chapter 3

The structure function $\mathbf{g}_1^d$

3.1 Definition of structure functions

The cross section for the *deep inelastic scattering* (DIS) process can be written as the tensor product of a leptonic tensor $L_{\mu\nu}$ (describing the leptonic vertex in the Feynman diagram) with a hadronic tensor $W_{\mu\nu}$ (describing the hadronic vertex), as shown in Fig. 3.1. In the following, the initial and final leptonic four-momentum will be indicated by k and k', the initial nucleon's four-momentum by P, the virtual photon's four-momentum squared will be indicated by q^2, with $Q^2 = -q^2$. Since the leptons are point-like particles, $L_{\mu\nu}$ can be expressed precisely in QED ([1]):

$$L_{\mu\nu} = \text{ Tr }\left[(1+\gamma_5 \not{s})(\not{k}+m_l)\gamma_\mu(\not{k}'+m_l)\gamma_\nu\right] . \qquad (3.1)$$

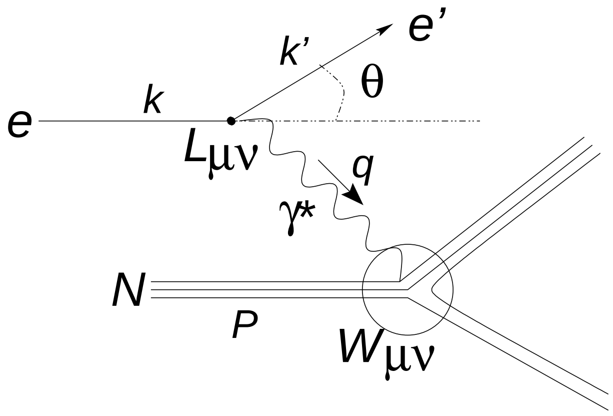

Figure 3.1: Schematic picture of Deep Inelastic Scattering for one photon exchange.

In the last expression m_l indicates the leptonic mass, and s the leptonic polarization. The notation $\not{x}$ stands for $\gamma_\mu x^\mu$, γ_μ (μ=1,...,4) being the Dirac matrices. The matrix γ_5 is given by $\gamma_5 = i\gamma_1\gamma_2\gamma_3\gamma_4$. $L_{\mu\nu}$ consists of a part independent of the lepton polarization s^β (symmetric, labeled with S) and a part that depends on it, (anti-symmetric, labeled with A):

$$L_{\mu\nu} = L_{\mu\nu}^{(S)} + L_{\mu\nu}^{(A)} \ , \tag{3.2}$$

where

$$\begin{aligned} L_{\mu\nu}^{(S)} &= 2(k_\mu k'_\nu + k_\nu k'_\mu - g_{\mu\nu}(k \cdot k' - m_l^2)) \\ L_{\mu\nu}^{(A)} &= -2i\, m_l\, \varepsilon_{\mu\nu\alpha\beta}\, (k - k')^\alpha s^\beta \ , \end{aligned} \tag{3.3}$$

where $\varepsilon_{\mu\nu\alpha\beta}$ is the completely anti-symmetric four dimensional tensor. From the last equation it appears that all polarization effects are suppressed at high energy by a factor m_l (which is small). This is true in the case of transverse polarization, while in the case of longitudinal polarization one has $m_l s^\beta \to k^\beta$, and thus there is no suppression. This shows why it is important to have a longitudinal polarization in order to measure effects coming from the polarization.

Because of the lack of knowledge of the nucleon's internal structure, the hadronic tensor, instead, has to be parameterized through the introduction of (at least) four* *structure functions*, two of which appear when the nucleon is unpolarized, and two more when it is polarized ([20]):

$$W_{\mu\nu} = W_{\mu\nu}^{(S)} + W_{\mu\nu}^{(A)}, \tag{3.4}$$

where:

$$W_{\mu\nu}^{(S)} = 2\left(-g_{\mu\nu} + \frac{q_\mu q_\nu}{q^2}\right)\mathrm{F}_1(x,Q^2) + 2\left(P_\mu - \frac{P\cdot q}{q^2}q_\mu\right)\left(P_\nu - \frac{P\cdot q}{q^2}q_\nu\right)\frac{\mathrm{F}_2(x,Q^2)}{\nu M} \tag{3.5}$$

and

$$W_{\mu\nu}^{(A)} = i\frac{2M}{P\cdot q}\varepsilon_{\mu\nu\alpha\beta}q^\alpha\left[S^\beta \mathrm{g}_1(x,Q^2) + \left(S^\beta - \frac{S\cdot q}{P\cdot q}P^\beta\right)\mathrm{g}_2(x,Q^2)\right] \ , \tag{3.6}$$

where M is the nucleon's mass, and S its polarization.

The structure functions depend on two independent variables, taken as x and Q^2. The dependence on Q^2 can be understood by considering that the structure that the photon

*This is true under the assumption that $Q^2 << M_Z^2$, so that weak interactions may be neglected. For higher energies three more polarized structure functions g_3, g_4, g_5 appear in the expression for $W_{\mu\nu}$.

probes inside the nucleon depends on its energy. The other variable, the Bjorken variable x is defined as $x = Q^2/2P\cdot q$, and is a measure of the inelasticity of the process. For elastic scattering the invariant mass W of the $\gamma^* p$ system must be equal to M, so

$$W^2 = (P+q)^2 = M^2 - Q^2 + 2P\cdot q = M^2 \rightarrow \quad x = 1 \quad \text{elastic scattering} \,. \tag{3.7}$$

For inelastic scattering instead it must be $W > M$, which implies $0 < x < 1$. The quantity x is identified with the fraction of nucleon's momentum carried by the parton that interacts with the virtual photon.

3.1.1 QPM interpretation of the structure functions

It is very convenient to have a technique that allows one to extract the structure functions from the hadronic tensor. This can be easily done by defining four projectors $P_i^{\mu\nu}$ that, when applied to $W_{\mu\nu}$, give the four structure functions.

The projectors for the unpolarized case are ([21]):

$$\begin{aligned} P_1^{\mu\nu} &= \frac{1}{4}\left[\frac{1}{a}P^\mu P^\nu - g^{\mu\nu}\right] \qquad &\rightarrow \qquad \mathrm{F}_1 = P_1^{\mu\nu}W_{\mu\nu} \\ P_2^{\mu\nu} &= \frac{3P\cdot q}{4a}\left[\frac{1}{a}P^\mu P^\nu - \frac{1}{3}g^{\mu\nu}\right] \qquad &\rightarrow \qquad \mathrm{F}_2 = P_2^{\mu\nu}W_{\mu\nu} \,, \end{aligned} \tag{3.8}$$

where $a = M^2 + (P\cdot q)/2x$.

In the same way, we can define, for the polarized case ([21]):

$$P_3^{\mu\nu} = \frac{1}{b}\left\{\left[(q\cdot S) - \frac{(P\cdot q)^2}{M^2(q\cdot S)}\right]q_\lambda + 2(P\cdot q)xS_\lambda\right\}P_\eta \varepsilon^{\mu\nu\lambda\eta} \quad \rightarrow \quad \mathrm{g}_1 = P_3^{\mu\nu}W_{\mu\nu} \tag{3.9}$$

$$P_4^{\mu\nu} = \frac{(P\cdot q)^2}{bM^2(q\cdot S)}[(q\cdot S)S_\lambda + q_\lambda]P_\eta\varepsilon^{\mu\nu\lambda\eta} \quad \rightarrow \quad \mathrm{g}_2 = P_4^{\mu\nu}W_{\mu\nu} \,, \tag{3.10}$$

with $b = -4M\left[\frac{(P\cdot q)}{M^2} + 2(P\cdot q)x - (q\cdot S)^2\right]$.

In the simplest version of the Quark Parton Model (QPM) the nucleon is considered to be made of collinear, free constituents, each carrying a fraction x' of the nucleon four-momentum. Lepton-nucleon DIS is then described as the incoherent sum of all lepton-constituent quark interactions and the hadronic tensor $W_{\mu\nu}$ is given in terms of the elementary quark tensor $w_{\mu\nu}$:

$$W_{\mu\nu} = \sum_{q,s} e_q^2 \frac{1}{2P\cdot q}\int_0^1 \frac{dx'}{x'}\delta(x'-x)n_q(x',s;S)w_{\mu\nu}(x',q;s) \,, \tag{3.11}$$

where the sum runs over quarks and antiquarks, $n_q(x', s; S)$ is the number density of quarks q with charge e_q, momentum fraction x' and spin s, inside the nucleon with spin S and momentum P. The hadronic tensor $w_{\mu\nu}$ is the same as the leptonic tensor $L_{\mu\nu}$ in Eq. (3.3) (since quarks are also charged, spin 1/2 particles), with the replacements $k^\mu \to xP^\mu$, $k'^\mu \to xP^\mu + q^\mu$, and a sum over the final spin s is performed. With these substitutions one gets the symmetric and anti-symmetric quark tensors:

$$\begin{aligned} w^S_{\mu\nu} &= 2[2x^2 P_\mu P_\nu + xP_\mu q_\nu + xq_\mu P_\nu - x(P\cdot q)g_{\mu\nu}] \\ w^A_{\mu\nu} &= 2im_q \varepsilon_{\mu\nu\alpha\beta} s^\alpha q^\beta \ , \end{aligned} \tag{3.12}$$

and the quark mass, for consistency, must be taken as $m_q = xM$, before and after the interaction with the virtual photon. We can now introduce the unpolarized quark number density $q(x)$ and the polarized one $\Delta q(x, S)$ as

$$\begin{aligned} q(x) &= \sum_s n_q(x, s; S) \\ \Delta q(x) &= \sum_s n_q(x, s; S) - \sum_s n_q(x, -s; S) \ . \end{aligned} \tag{3.13}$$

By applying the projection operators $P_i^{\mu\nu}$ to $W_{\mu\nu}$ one obtains the well known Naive Parton Model predictions for the structure functions

$$\begin{aligned} \mathrm{F}_1(x) &= \frac{1}{2}\sum_q e_q^2 q(x) \\ \mathrm{F}_2(x) &= x\sum_q e_q^2 q(x) \\ \mathrm{g}_1(x) &= \frac{1}{2}\sum_q e_q^2 \Delta q(x, S) \\ \mathrm{g}_2(x) &= 0 \ . \end{aligned} \tag{3.14}$$

3.1.2 Asymmetries

In the cross section $\sigma \simeq L_{\mu\nu}W^{\mu\nu}$ the cross terms $L^{(S)}_{\mu\nu}W^{\mu\nu(A)}$ and $L^{(A)}_{\mu\nu}W^{\mu\nu(S)}$ give no contribution. The cross section will then be of the form:

$$L_{\mu\nu}W^{\mu\nu} = L^{(S)}_{\mu\nu}W^{\mu\nu(S)} + L^{(A)}_{\mu\nu}W^{\mu\nu(A)} \ . \tag{3.15}$$

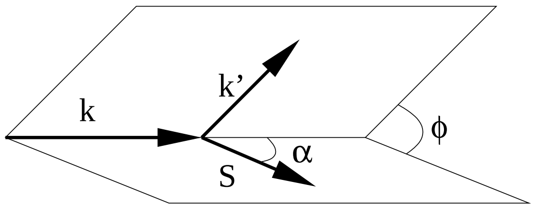

Figure 3.2: Kinematic plane.

The last equation shows why it is natural to create differences in cross sections with nucleons of opposite polarizations in order to extract the polarized structure functions g_1 and g_2: in this way, the contribution of the unpolarized structure functions cancels out.

The most general cross section difference relevant for polarized deep inelastic fixed target lN scattering is ([20]):

$$\begin{aligned}\frac{\partial^3[\sigma(\alpha)-\sigma(\alpha+\pi)]}{\partial x \partial y \partial \phi} &= \frac{8\alpha^2}{Q^2}\left[\cos\alpha\left[\left(1-\frac{y}{2}-\frac{y^2\gamma^2}{4}\right)g_1(x,Q^2)-\frac{y\gamma^2}{2}g_2(x,Q^2)\right]+\right.\\ &- \left.\sin\alpha\cos\phi\,\gamma\sqrt{1-y-\frac{y^2\gamma^2}{4}}\left[\frac{y}{2}g_1(x,Q^2)+g_2(x,Q^2)\right]\right] . \end{aligned} \tag{3.16}$$

This formula contains only information from the anti-symmetric part of the tensor $W_{\mu\nu}$. The angle α, as shown in Fig. 3.2, is the angle between the lepton beam momentum vector k and the nucleon-target polarization vector S; ϕ is the angle between the k-S plane and the k-k' lepton scattering plane, $\gamma = 2Mx/\sqrt{Q^2}$ and $y = (P \cdot q)/(P \cdot k)$ is the fraction of energy transferred in the reaction. The quantities x, y and Q^2 are related to each other by the expression $Q^2 = sxy$, where s is the centre of mass energy in the lepton-nucleon reaction. Effects associated with g_2 are suppressed by a factor $2M/\sqrt{Q^2}$ with respect to the leading terms.

More convenient than the difference of cross sections are asymmetries (with an asymmetric integration over ϕ) like:

$$A(\alpha) = \frac{\sigma(\alpha)-\sigma(\alpha+\pi)}{\sigma(\alpha)+\sigma(\alpha+\pi)} , \tag{3.17}$$

as for example the longitudinal asymmetry

$$A_{\parallel} = \frac{\sigma^{\stackrel{\Leftarrow}{\rightarrow}} - \sigma^{\stackrel{\Rightarrow}{\rightarrow}}}{\sigma^{\stackrel{\Leftarrow}{\rightarrow}} + \sigma^{\stackrel{\Rightarrow}{\rightarrow}}} , \tag{3.18}$$

obtained for $\alpha = 0$ from the cross sections when the polarization of target ($\Leftarrow$, $\Rightarrow$) and beam ($\rightarrow$) are parallel ($\overset{\Rightarrow}{\rightarrow}$) or anti-parallel ($\overset{\Leftarrow}{\rightarrow}$), or the transverse asymmetry $A_\perp$ obtained for $\alpha = \pi/2$. Asymmetries are convenient since, as already discussed in the last chapter on the trigger efficiencies, many detector effects simply cancel in the cross section ratio.

The physically interesting quantities are the virtual photon nucleon asymmetries:

$$\begin{aligned} A_1 &= \frac{\sigma_{1/2} - \sigma_{3/2}}{\sigma_{1/2} + \sigma_{3/2}} \\ A_2 &= \frac{2\sigma_{TL}}{\sigma_{1/2} + \sigma_{3/2}} , \end{aligned} \tag{3.19}$$

where $\sigma_{1/2}$ and $\sigma_{3/2}$ are the virtual photo-absorption cross sections when the projection of the total angular momentum of the photon-nucleon system along the incident lepton direction is 1/2 and 3/2. The term σ_{TL} arises from the interference between transverse and longitudinal scattering amplitudes. A_1 and A_2 can be related via the optical theorem to $A_{||}$ and $A_\perp$, or, equivalently, to the structure functions, by means of the following relations:

$$\begin{aligned} A_{||} &= D(A_1 + \eta A_2) \\ A_\perp &= d(A_2 - \zeta A_1) , \end{aligned} \tag{3.20}$$

with

$$\begin{aligned} A_1 &= \frac{g_1 - \gamma^2 g_2}{F_1} \\ A_2 &= \frac{\gamma(g_1 + g_2)}{F_1} . \end{aligned} \tag{3.21}$$

The kinematic factors D, d, η, ζ are defined as:

$$\begin{aligned} D &= \frac{y(y-2)}{y^2 + 2(1-y)(1+R)} \\ \eta &= \frac{2\gamma(1-y)}{2-y} \\ d &= D\sqrt{\frac{2\varepsilon}{1+\varepsilon}} \\ \zeta &= \frac{\eta(1+\varepsilon)}{2\varepsilon} , \end{aligned} \tag{3.22}$$

with R being the ratio of longitudinal to transverse virtual photon-quark cross sections, and ε being the degree of transverse polarization of the virtual photon:

$$\varepsilon = \frac{1-y}{1-y+\frac{y^2}{2}}. \tag{3.23}$$

From the measured asymmetry $A_{||}$ one can get the structure function g_1 by means of the relation:

$$\frac{\mathrm{g}_1}{\mathrm{F}_1} = \frac{1}{1+\gamma^2}\left(\frac{A_{||}}{D} + (\gamma-\eta)A_2\right) . \tag{3.24}$$

3.1.3 Evaluation of g_1 on nuclear targets

Let us consider DIS on nuclear targets. The assumption of incoherent scattering from the constituent nucleons will be used, which consists in neglecting nuclear effects such as shadowing and Fermi motion ([22]), an approximation only valid at high Q^2. In this hypothesis the unpolarized scattering cross section on the nuclear target is equivalent to the sum of cross sections on the neutron and on the proton.

In the following the assumption of 100% beam polarization will be used for simplicity. The differential cross section asymmetry on a nuclear target A is defined as:

$$A_{||}^{A} = \frac{d\sigma_A^{\leftrightarrows} - d\sigma_A^{\rightrightarrows}}{d\sigma_A^{\leftrightarrows} + d\sigma_A^{\rightrightarrows}} . \tag{3.25}$$

Under the hypothesis of incoherent scattering on a nucleus with Z protons and N neutrons, the differential cross sections $d\sigma_A^{\leftrightarrows(\rightrightarrows)}$ are related to the unpolarized ones on the proton and the neutron by the relation:

$$d\sigma_A^{\leftrightarrows(\rightrightarrows)} = Z d\sigma_p(1 \pm P_p A_{||}^{p}) + N d\sigma_n(1 \pm P_n A_{||}^{n}) \tag{3.26}$$

where $A_{||}^{p,n}$ are the nucleon longitudinal asymmetries, and $P_{p,n}$ are the longitudinal polarizations of the nucleons. The last expression recovers the formula for unpolarized scattering for $P_p = P_n = 0$. It follows that the longitudinal asymmetry originating from the nucleus A is:

$$\begin{aligned} A_{||}^{A} &= \frac{Z d\sigma_p P_p A_{||}^{p} + N d\sigma_n P_n A_{||}^{n}}{Z d\sigma_p + N d\sigma_n} \\ &= f_p P_p A_{||}^{p} + f_n P_n A_{||}^{n} , \end{aligned} \tag{3.27}$$

with

$$f_p = \frac{Z d\sigma_p}{Z d\sigma_p + N d\sigma_n} , \qquad f_n = \frac{N d\sigma_n}{Z d\sigma_p + N d\sigma_n} \tag{3.28}$$

being the fractions of events originating from protons and neutrons respectively.

In the case of a deuterium target, i.e. with $N = Z = 1$, f_p and f_n can be written as:

$$f_p = \frac{\mathrm{F}_1^p}{2\mathrm{F}_1^d} , \qquad f_n = \frac{\mathrm{F}_1^n}{2\mathrm{F}_1^d} \tag{3.29}$$

where we have introduced F_1^d as the deuterium structure function F_1 per nucleon. The appearance of F_1 in Eq. (3.29) is due to the fact that (3.28) contains unpolarized cross sections.

Because of the D-state admixture, one has:

$$P_p^d = P_n^d = \left(1 - \frac{3}{2}\omega_D\right) , \tag{3.30}$$

where ω_D=0.058 ([23]) is the D-state wave probability.

By inserting Eq. (3.30) and (3.29) into Eq. (3.27) one gets:

$$A_{||}^d \mathrm{F}_1^d = \frac{1}{2}\left(1 - \frac{3}{2}\omega_D\right)\left(A_{||}^p \mathrm{F}_1^p + A_{||}^n \mathrm{F}_1^n\right) \tag{3.31}$$

and consequently:

$$\mathrm{g}_1^d = \frac{1}{2}\left(1 - \frac{3}{2}\omega_D\right)\left(\mathrm{g}_1^p + \mathrm{g}_1^n\right) . \tag{3.32}$$

3.1.4 Extraction of g_1^d from the measured asymmetry

The HERMES experiment is able to make measurements of the asymmetry $A_{||}^d$. For the final extraction of the structure function g_1^d information is needed on F_1^d and A_2^d (see Eq. (3.24)). Fits to available data are necessary to evaluate these functions at the values of x and Q^2 of the measured asymmetry.

F_1 parameterization. The unpolarized structure function F_1 can be written in terms of the unpolarized structure function F_2 and R, the ratio of longitudinal to transverse polarized virtual photon cross sections on an unpolarized target, by means of the *Callan-Gross relation* ([1]):

$$\mathrm{F}_1(x, Q^2) = \frac{\mathrm{F}_2(x, Q^2)}{2x[1 + R(x, Q^2)]} . \tag{3.33}$$

Commonly used parameterizations for F_2^d are the 8 ([24]) and 15 ([25]) parameter fits from NMC.

R parameterization. The R parameterization from Whitlow ([26] and [27]) is the average of R_a, R_b and R_c:

$$\begin{aligned} R_a &= 0.06723\ \Theta(x,Q^2) + \frac{0.46714}{(Q^8+12.9757)^{1/4}} \\ R_b &= 0.0635\ \Theta(x,Q^2) + \frac{0.5747}{Q^2} - \frac{0.3534}{Q^4+0.3^2} \\ R_c &= 0.05992\ \Theta(x,Q^2) + \frac{0.50885}{\left((Q^2-Q^2_{thr})^2+4.44396\right)^{1/2}}\ , \end{aligned} \tag{3.34}$$

with

$$\Theta = \frac{1}{\ln\left(\frac{Q^2}{\Lambda^2}\right)} \left[1 + 12\frac{Q^2}{Q^2+1}\ \frac{0.125^2}{x^2+0.125^2}\right]\ , \tag{3.35}$$

$Q^2_{thr} = 5(1-x)^5$, and $\Lambda = 0.2$ GeV. This fit holds for all Q^2 ranges of DIS experiments, but should not be used for $Q^2 < 0.3$ GeV^2. So for Q^2 values lower than 0.3 GeV^2 the value of R is kept fixed at its value for $Q^2 = 0.3$ GeV^2.

The structure function g_2. The structure function g_2 is null at zero-th order QCD, so it does not have a direct QPM interpretation, since it cannot be written as a sum over quark or gluon polarizations. It can be measured through the scattering of a transversely polarized beam off longitudinally polarized targets, and it is in fact linked to the transversely polarized quark distributions inside the nucleon. From Eq. (3.16) it follows that $A_\perp$ (obtained for $\alpha = \pi/2$) depends on the combination of structure functions $g_2 + \frac{y}{2}g_1$, where g_1 is not negligible, so that g_2 cannot be easily isolated. Since $y = (E'-E)/E$, where E is the beam energy and E' the final lepton energy, this also shows that at fixed x and Q^2, g_2 can be isolated by varying the beam energy.

g_2 can be written as:

$$\begin{aligned} g_2(x,Q^2) &= g_2^{WW}(x,Q^2) + \tilde{g}_2(x,Q^2) \\ g_2^{WW}(x,Q^2) &= -g_1(x,Q^2) + \int_x^1 \frac{g_1(y,Q^2)}{y}dy \\ \tilde{g}_2(x,Q^2) &= -\int_x^1 \frac{\partial}{\partial y}\left(\frac{m}{M}h_T(y,Q^2) + \zeta(y,Q^2)\right)\frac{dy}{y}\ . \end{aligned} \tag{3.36}$$

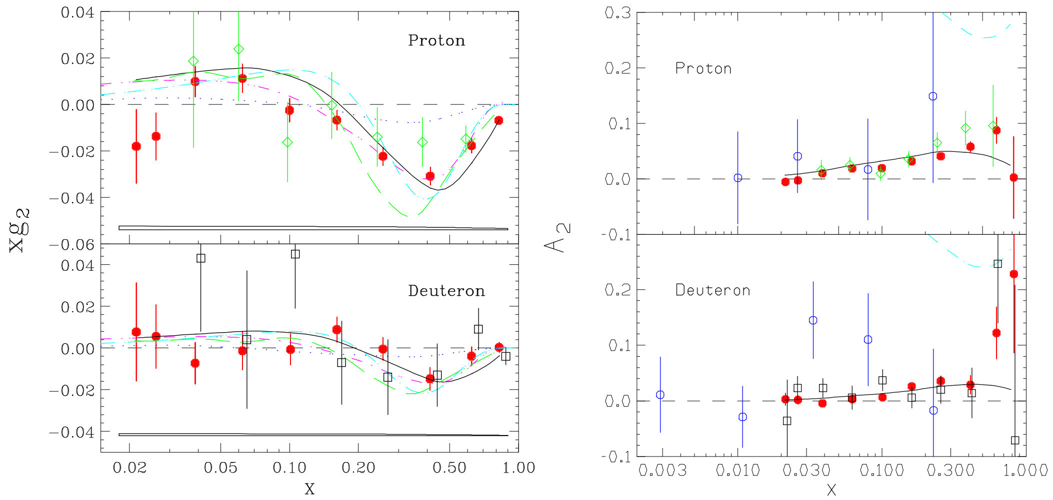

Figure 3.3: New results on $x\mathrm{g}_2$ (left) and the asymmetry A_2 (right) from E155 ([28]) in solid circles, for the proton and the deuteron, compared to pure Wandzura-Wilczek contribution (solid line) and data from SMC ([29] in open circles, E143 ([30]) in open diamonds and older data from E155 ([31]) in open squares. Data on $x\mathrm{g}_2$ is compared to fits from Stratmann ([32]) (dash-dot), Song ([33]) (dotted), Weigel and Gamberg ([34]) (short dashes), and Wakamatsu ([35]) (long dashes).

The Wandzura-Wilczek term g_2^{WW} is pure twist-2 (see section 4.1) and only depends on g_1, so it can be obtained from a measurement of g_1 alone, while $\tilde{\mathrm{g}}_2$ depends on the twist-2 term coming from the transverse quark polarization h_T, and on the twist-3 term coming from quark-gluon interactions, ζ. The h_T term is small for up and down quarks, being dependent on the ratio m/M, thus the term ζ, even though being twist-3, is not negligible compared to it.

Fig. 3.3 shows the results of a recent measurement of g_2 by the E155 ([28]) experiment in the range $0.02 \leq x \leq 0.8$ and $Q^2 \leq 30$ GeV^2, for proton and deuteron.

A common assumption used in the extraction of g_1 from the measured asymmetry is to consider that both quantities η and A_2 are small in the large energy limit: A_2 is bounded by the relation $|A_2| \leq \sqrt{R}$ (shown in the blue dashed lines in the plots), and R is a small quantity. So it is quite accurate to write:

$$A_{\|} \simeq DA_1 \ . \tag{3.37}$$

By neglecting the g_2 term in A_1 (justified by measurements until recently), one obtains from Eq. (3.21):

$$g_1(x, Q^2) \simeq \frac{A_{\|}(x, Q^2)}{D(x, Q^2)} F_1(x, Q^2), \tag{3.38}$$

which expresses g_1 in terms of the measured asymmetry $A_{\|}$, the measured unpolarized structure function $F_1(x)$, and the known coefficient D. This is the approach taken by many experiments in the past.

Because of the improved precision, it is now possible to include an A_2 contribution in the extraction of g_1 from Eq. (3.24). After substituting the expression in Eq. (3.21) for A_2 into Eq. (3.24), one gets an expression in terms of g_1/F_1, A_2 and g_2. Fig. 3.3 shows that the data seem to be consistent with the inclusion of only the Wandzura-Wilczek term into g_2:

$$\begin{aligned} A_2^{WW} &= \frac{\gamma(g_1 + g_2^{WW})}{F_1} = \frac{\gamma}{F_1} \int_x^1 \frac{g_1(y)}{y} dy \\ &= \frac{\gamma}{F_1} \int_x^1 \frac{g_1(y)}{F_1(y)} \frac{F_2(y)}{2y^2(1 + R(y))} dy \ , \end{aligned} \tag{3.39}$$

such that

$$g_1^d = \frac{1}{1+\gamma^2} \frac{F_2^d}{2x(1+R)} \frac{A_{\|}^d}{D} + \frac{\gamma(\gamma - \eta)}{1+\gamma^2} \int_x^1 \frac{g_1(y)}{F_1(y)} \frac{F_2(y)}{2y^2(1+R(y))} dy \ , \tag{3.40}$$

where the obvious x and Q^2 dependencies have been omitted. The Wandzura-Wilczek term can be calculated by using a parameterization for g_1^d/F_1^d from world data, and the fits for F_2^d and R discussed earlier.

3.2 The measured asymmetry

The measurement of the deuterium structure function g_1^d will be presented in the rest of this chapter. As explained in the previous sections, the extraction of g_1^d is the result of the measurement of an asymmetry. It will be shown how the asymmetry is obtained in terms of measured quantities for data taken in 1998 and 2000. Tests of the stability of the results will follow, to conclude with the final results.

The unpolarized cross section σ_0 is related to the scattered lepton count rate N, to the detector acceptance $a(t, x, Q^2)$, the total detection efficiency (tracking + trigger) $\varepsilon(t, x, Q^2)$ and the luminosity $L(t)$ by the relation:

$$N(x, Q^2) = \sigma_0 \int dt \ a(t, x, Q^2) \ \varepsilon(t, x, Q^2) \ L(t) \ , \tag{3.41}$$

where t is time. When one considers instead a polarized cross section, the unpolarized cross section may be expressed as $\sigma_0 = (\sigma^{\stackrel{\Rightarrow}{\rightarrow}} + \sigma^{\stackrel{\Leftarrow}{\rightarrow}})/2$. The polarization will introduce an additional term in the cross section which depends on the polarization of the beam P_B and the target P_T:

$$\begin{aligned} N^{\stackrel{\Rightarrow}{\rightarrow}}(x,Q^2) &= \sigma_0 \int dt\, a(t,x,Q^2)\, \varepsilon(t,x,Q^2)\, L^{\stackrel{\Rightarrow}{\rightarrow}}(t)\, [1 + P_B(t)P_T(t)A_{||}(x,Q^2)] \\ N^{\stackrel{\Leftarrow}{\rightarrow}}(x,Q^2) &= \sigma_0 \int dt\, a(t,x,Q^2)\, \varepsilon(t,x,Q^2)\, L^{\stackrel{\Leftarrow}{\rightarrow}}(t)\, [1 - P_B(t)P_T(t)A_{||}(x,Q^2)] \,. \end{aligned} \tag{3.42}$$

In section 3.1 it was shown that to obtain the asymmetry $A_{||}$ both target and beam need to be polarized. Trivially the asymmetry is zero in the case that the cross section does not depend on the polarization.

The asymmetry can be isolated to get:

$$A_{||} = \frac{N^{\stackrel{\Rightarrow}{\rightarrow}} \int dt\; a\; \varepsilon\; L^{\stackrel{\Leftarrow}{\rightarrow}} - N^{\stackrel{\Leftarrow}{\rightarrow}} \int dt\; a\; \varepsilon\; L^{\stackrel{\Rightarrow}{\rightarrow}}}{N^{\stackrel{\Rightarrow}{\rightarrow}} \int dt\; a\; \varepsilon\; L^{\stackrel{\Leftarrow}{\rightarrow}}\; P_B P_T + N^{\stackrel{\Leftarrow}{\rightarrow}} \int dt\; a\; \varepsilon\; L^{\stackrel{\Rightarrow}{\rightarrow}}\; P_B P_T} \,, \tag{3.43}$$

where the dependencies on x,Q^2 and t have been dropped for simplicity. Under the assumption that the efficiencies and the acceptance do not depend on time, they can be taken outside the integral, so that they cancel out. Finally one gets:

$$A_{||} = \frac{N^{\stackrel{\Rightarrow}{\rightarrow}}\, \mathcal{L}^{\stackrel{\Leftarrow}{\rightarrow}} - N^{\stackrel{\Leftarrow}{\rightarrow}}\, \mathcal{L}^{\stackrel{\Rightarrow}{\rightarrow}}}{N^{\stackrel{\Rightarrow}{\rightarrow}}\, \mathcal{L}_p^{\stackrel{\Leftarrow}{\rightarrow}} + N^{\stackrel{\Leftarrow}{\rightarrow}}\, \mathcal{L}_p^{\stackrel{\Rightarrow}{\rightarrow}}} \,, \tag{3.44}$$

where $\mathcal{L}^{\stackrel{\Rightarrow}{\rightarrow}}$ and $\mathcal{L}^{\stackrel{\Leftarrow}{\rightarrow}}$ are the integrated luminosities, while $\mathcal{L}_p^{\stackrel{\Rightarrow}{\rightarrow}}$ and $\mathcal{L}_p^{\stackrel{\Leftarrow}{\rightarrow}}$ are the integrated luminosities weighted by the product of target and beam polarization:

$$\begin{aligned} \mathcal{L}^{\stackrel{\Rightarrow}{\rightarrow}} &= \int dt\; L^{\stackrel{\Rightarrow}{\rightarrow}}(t) & \mathcal{L}^{\stackrel{\Leftarrow}{\rightarrow}} &= \int dt\; L^{\stackrel{\Leftarrow}{\rightarrow}}(t) \\ \mathcal{L}_p^{\stackrel{\Rightarrow}{\rightarrow}} &= \int dt\; L^{\stackrel{\Rightarrow}{\rightarrow}}(t)\; P_B(t)P_T(t) & \mathcal{L}_p^{\stackrel{\Leftarrow}{\rightarrow}} &= \int dt\; L^{\stackrel{\Leftarrow}{\rightarrow}}(t)\; P_B(t)P_T(t) \,. \end{aligned} \tag{3.45}$$

The asymmetry is obtained from the measured number of DIS events when the deuterium-lepton relative spin is parallel ($\stackrel{\Rightarrow}{\rightarrow}$) or anti-parallel ($\stackrel{\Leftarrow}{\rightarrow}$):

$$A_{||}^d(x,Q^2) = \frac{N_{\mathrm{dis}}^{\stackrel{\Leftarrow}{\rightarrow}}(x,Q^2)\; \mathcal{L}^{\stackrel{\Rightarrow}{\rightarrow}} - N_{\mathrm{dis}}^{\stackrel{\Rightarrow}{\rightarrow}}(x,Q^2)\; \mathcal{L}^{\stackrel{\Leftarrow}{\rightarrow}}}{N_{\mathrm{dis}}^{\stackrel{\Leftarrow}{\rightarrow}}(x,Q^2)\; \mathcal{L}_p^{\stackrel{\Rightarrow}{\rightarrow}} + N_{\mathrm{dis}}^{\stackrel{\Rightarrow}{\rightarrow}}(x,Q^2)\; \mathcal{L}_p^{\stackrel{\Leftarrow}{\rightarrow}}} \,. \tag{3.46}$$

In the last equation the superscript d was introduced on the asymmetry to indicate that we are referring to deuterium.

The measured number of DIS events is likely to contain some contamination either from non-DIS leptons or from hadrons with the same charge as the beam (negative in 1998 and positive in 2000). The non-DIS leptons mostly come from charge symmetric processes (*cs*), such as the decay of photo-produced π^0's into 2γ's of which one or both convert into e^+e^- pairs, or from high energy bremsstrahlung photons that create e^+e^- pairs. Since they come from secondary processes, they are likely to have a lower momentum, and thus be concentrated at high y. This kind of background is treated by supposing that in each kinematic bin the amount of positive and negative leptons coming from such processes is the same, so that the total number of DIS is obtained by subtracting the number of leptons with opposite charge from the number of DIS candidates:

$$A_{||}^{d} = \frac{(N_{\text{cand}}^{\leftrightarrows} - N_{\text{cs}}^{\leftrightarrows})\,\mathcal{L}^{\rightrightarrows} - (N_{\text{cand}}^{\rightrightarrows} - N_{\text{cs}}^{\rightrightarrows})\,\mathcal{L}^{\leftrightarrows}}{(N_{\text{cand}}^{\leftrightarrows} - N_{\text{cs}}^{\leftrightarrows})\,\mathcal{L}_p^{\rightrightarrows} + (N_{\text{cand}}^{\rightrightarrows} - N_{\text{cs}}^{\rightrightarrows})\,\mathcal{L}_p^{\leftrightarrows}}\,. \tag{3.47}$$

The contamination coming from hadrons will be discussed in another section, as the method to handle this contamination is not so straightforward. A systematic error for the hadronic background is estimated.

The statistical error on the measured asymmetry comes from the error propagation on the measured numbers of events:

$$\begin{aligned}\delta A_{||}^{d} =& \sqrt{\left(\frac{\partial A_{||}^{d}}{\partial N_{\text{cand}}^{\leftrightarrows}}\right)^2 N_{\text{cand}}^{\leftrightarrows} + \left(\frac{\partial A_{||}^{d}}{\partial N_{\text{cs}}^{\leftrightarrows}}\right)^2 N_{\text{cs}}^{\leftrightarrows} + \left(\frac{\partial A_{||}^{d}}{\partial N_{\text{cand}}^{\rightrightarrows}}\right)^2 N_{\text{cand}}^{\rightrightarrows} + \left(\frac{\partial A_{||}^{d}}{\partial N_{\text{cs}}^{\rightrightarrows}}\right)^2 N_{\text{cs}}^{\rightrightarrows}} \\ =& \frac{\mathcal{L}^{\leftrightarrows}\mathcal{L}_p^{\rightrightarrows} + \mathcal{L}^{\rightrightarrows}\mathcal{L}_p^{\leftrightarrows}}{\left[(N_{\text{cand}}^{\leftrightarrows} - N_{\text{cs}}^{\leftrightarrows})\,\mathcal{L}_p^{\leftrightarrows} + (N_{\text{cand}}^{\rightrightarrows} - N_{\text{cs}}^{\rightrightarrows})\,\mathcal{L}_p^{\rightrightarrows}\right]^2} \\ &\times\sqrt{(N_{\text{cand}}^{\leftrightarrows} - N_{\text{cs}}^{\leftrightarrows})^2(N_{\text{cand}}^{\rightrightarrows} + N_{\text{cs}}^{\rightrightarrows}) + (N_{\text{cand}}^{\leftrightarrows} + N_{\text{cs}}^{\leftrightarrows})(N_{\text{cand}}^{\rightrightarrows} - N_{\text{cs}}^{\rightrightarrows})^2}\,.\end{aligned} \tag{3.48}$$

3.2.1 Event selection

The data are organized in *slow control* and *fast control*. Slow control quantities do not need to be evaluated on an event-by event basis, since by their nature they vary slowly. These quantities are then measured every ten seconds (every *burst*). Examples of slow-control quantities are target and beam polarization and luminosities. Fast control are instead quantities that need to be measured for every track, such as the momentum, the energy released in the calorimeter, the angles, and so on. The data is then stored in a *run* file containing approximately 7 minutes worth of data.

An analysis code was built to generate the event selection. It first accesses the data file and reads the slow control tables, reading in the luminosities and the polarizations. Later it accesses the tables related to the events in that burst. For each burst it looks for the track with highest momentum in each event, which is the one with the highest probability of being the scattered lepton. Such a track has to have a higher probability of being a lepton (*PID* cut, see next section) than a hadron. Geometrical cuts are applied, ensuring that the entire track is contained in the angular acceptance of the detector and that the reconstructed scattering vertex z_v along the z axis of Fig. 2.1 and the transverse vertex t_v in the direction transverse to the z axis are contained within the target cell:

$$\theta_y \geq 0.04\mathrm{rad} \tag{3.49}$$

$$t_v \leq 0.75\mathrm{cm} \tag{3.50}$$

$$-18\mathrm{cm} \leq z_v \leq 18\mathrm{cm}\ . \tag{3.51}$$

A last geometric requirement is that the track be completely inside the fiducial volume of the calorimeter. Finally, kinematic cuts ensure that the track is consistent with being a DIS event. These requirements are summarized in Table 3.1.

Quantity	Description	Cut
$x = -\dfrac{q^2}{2p\cdot q} = \dfrac{Q^2}{2M(E-E')}$	Momentum fraction carried by the struck parton	$0.0021 < x < 0.85$
$y = \dfrac{p\cdot q}{p\cdot k} = \dfrac{E-E'}{E}$	Energy fraction transferred to the γ^*	$0.1 < y < 0.91$
$Q^2 = -(k-k')^2 = 4EE'\sin^2\left(\dfrac{\theta}{2}\right)$	Four-momentum transfer	$Q^2 > 0.1$ GeV^2
$W^2 = M_p^2 + 2M(E-E') - Q^2$	Invariant mass of the $\gamma^* p$ system	$W^2 > 3.24$ GeV^2

Table 3.1: Definition of kinematic variables and the cuts used to define the DIS region.

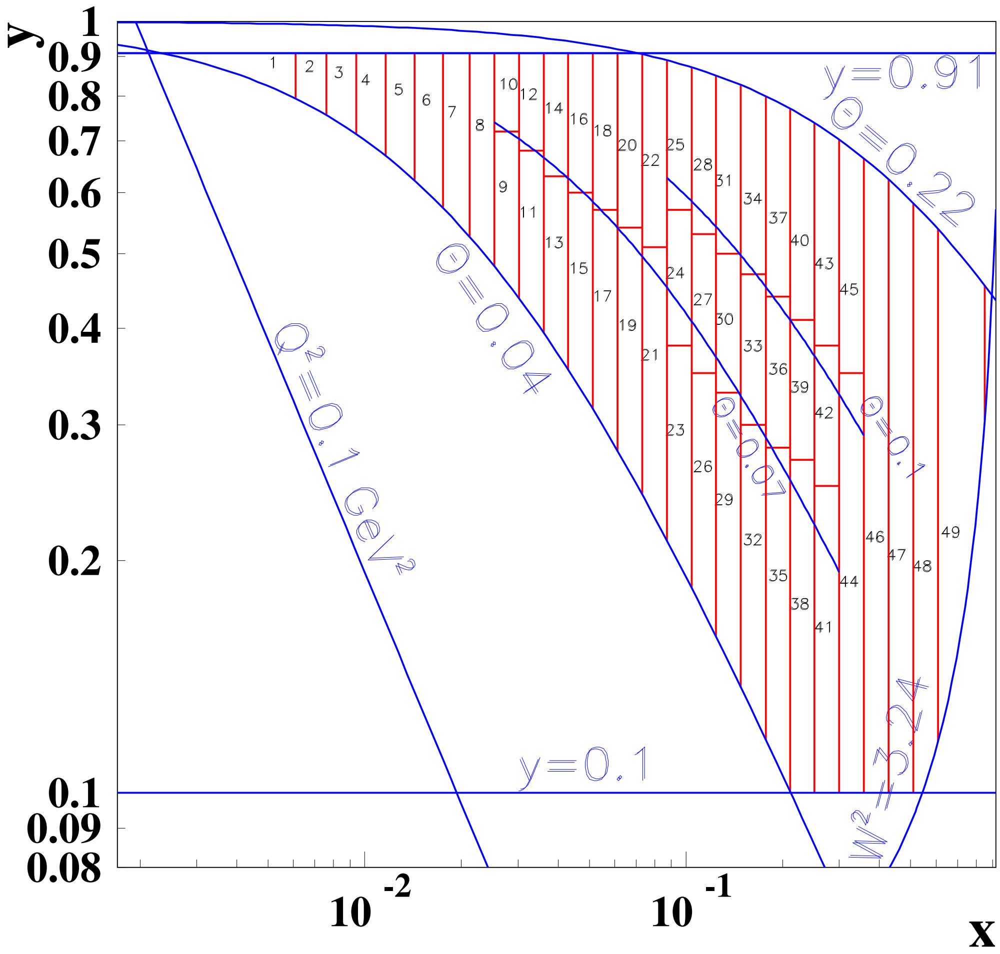

Figure 3.4: Kinematic $x - y$ plane. The 49 bins are identified by numbers on the plot. Each DIS event has its unique position on this plane, which is limited by kinematic cuts ($W^2 > 3.24$ GeV^2, $Q^2 > 0.1$ GeV^2 and $0.1 < y < 0.81$) and by geometrical constraints ($0.04 < \theta < 0.22$ rad).

As shown in a previous section, deep inelastic scattering has two independent quantities, that may be taken as x and Q^2. A common choice is also x and y, and a 2-dimensional plot of y versus x is shown in Fig. 3.4. Fig. 3.5 shows instead the kinematic x, Q^2 plane, and the average Q^2 values in each bin, ranging from 0.2 to 7.5 GeV^2.

All events satisfying the selected cuts will lie in an area within $0.0021 < x < 0.85$ and $0.1 < y < 0.91$. The angular acceptance in $\theta = 0.22$ rad cuts the plane at the top, while

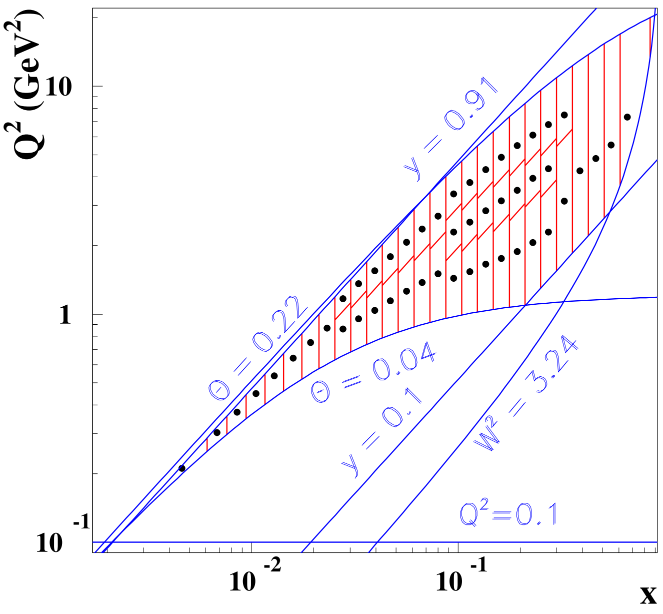

Figure 3.5: The $x - Q^2$ plane. The thick black dots represent the average Q^2 values in each bin.

$\theta = 0.04$ rad cuts it at the bottom left. The cut $W^2 > 3.24$ GeV^2 closes the kinematic region on the bottom right. Fig. 3.4 also shows that some kinematic cuts are redundant. The only necessary ones are the cut on the y variable, and the one on W^2.

The cut of $y = 0.91$ excludes the low momentum region ($p < 2.5$ GeV). The trigger efficiencies have a dependence on momentum, and they reach a plateau only at momenta of the order of 2.5 GeV ([18]). The low y cut is used to exclude a region where the momentum resolution is poor ([6]). The cut on W^2 is used to exclude the region of nucleon resonances.

Due to a dependence of the measured asymmetry on y, where possible, more bins in y were introduced. A total of 49 bins were used in this analysis. In the plots presented in this chapter lower, medium and higher y bins will be indicated respectively with *y-bin=1*, *y-bin=2* and *y-bin=3*. Because many tests have been made on the behavior of $A_{||}^d$ in each bin, each bin number is clearly indicated in Fig. 3.4. The angles $\theta = 0.04$ rad, $\theta = 0.07$ rad, $\theta = 0.1$ rad and $\theta = 0.22$ rad roughly delimit the different y bins.

3.2.2 PID scheme

The track must be efficiently identified as a lepton. Information from the preshower and the calorimeter enter into PID3, while the TRD identification is contained in PID5. These quantities have already been introduced in section 2.6.5 and provide the means for the hadron-lepton separation. As was already pointed out, flux terms must be used. They are often neglected in analyses, which implies an incorrect assumption of equal fluxes of hadrons and leptons in the detector over the entire kinematic range. The requirement used to identify a lepton is then:

$$\mathrm{PID} = \mathrm{PID3} + \mathrm{PID5} - \log_{10}\phi > \mathrm{PID}_{\mathrm{cut}}\ . \tag{3.52}$$

Fig. 3.6 schematically shows the PID distributions for hadrons and leptons. A PID cut cannot be placed at too high a PID value since in this way too many leptons would be excluded thus lowering the lepton efficiency, defined as the number of identified leptons over the total number of leptons (horizontal shaded area in the figure). On the other hand a low cut would increase the hadron contamination (vertically shaded area), which is the number of hadrons above the cut over the total number of hadrons. Fig. 3.7 shows the hadron contaminations and lepton efficiencies for the PID cut of 1, chosen as a good compromise between the two.

The flux factors. The flux factors are calculated with an iterative procedure ([40]). It has been shown in Eq. (2.13) that

$$PID = PID' - \log_{10}\phi = 0 \tag{3.53}$$

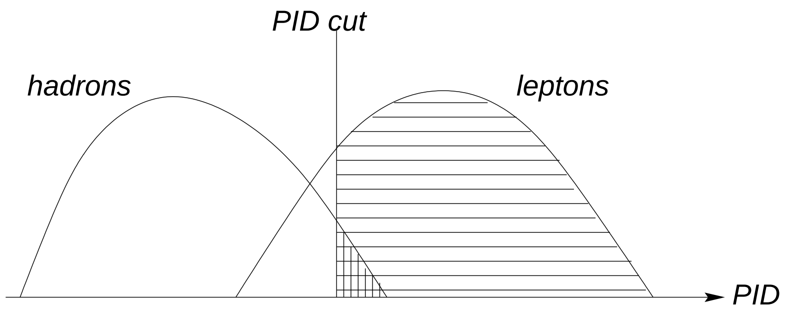

Figure 3.6: Scheme of the PID distributions for leptons and hadrons. The PID cut must be a compromise between high PID lepton efficiency and low hadron contamination.

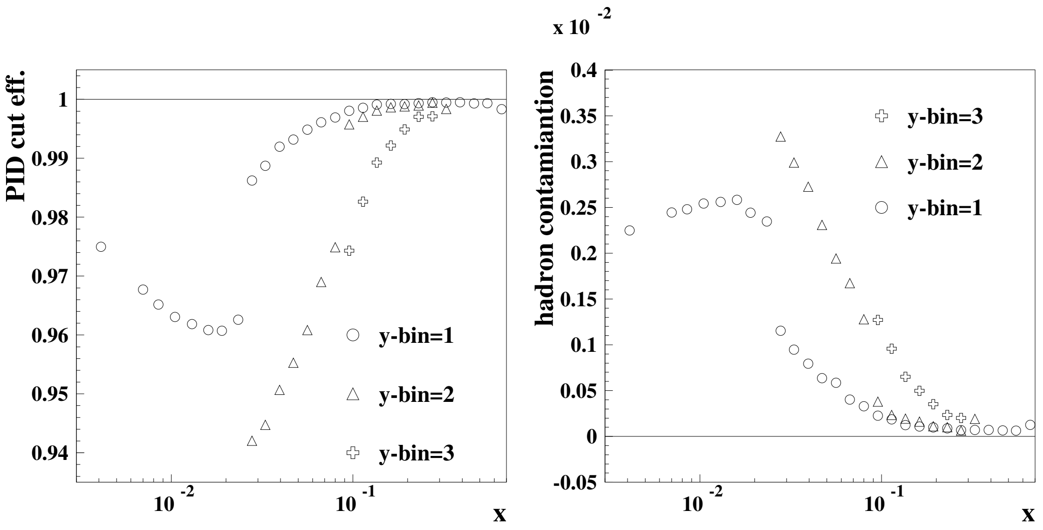

Figure 3.7: Left: efficiency of the PID cut equal to 1. Right: hadron contamination for the same PID cut. For each x value, the lepton efficiencies are higher for the higher momenta (lower y) bins and the hadron contamination is lower ([40]).

is the point where the probability of being a lepton is equal to the one of being a hadron. The fluxes of hadrons and leptons are proportional to the number of particles of each type, which in turn can be obtained from the PID distributions $n(\mathrm{PID})$:

$$
\begin{aligned}
\phi_e \propto n_e &= \int_{\mathrm{PID}_{\mathrm{cut}}}^{\infty} n(\mathrm{PID}')d(\mathrm{PID}') \\
\phi_h \propto n_h &= \int_{-\infty}^{\mathrm{PID}_{\mathrm{cut}}} n(\mathrm{PID}')d(\mathrm{PID}') \ .
\end{aligned}
\tag{3.54}
$$

Since the flux itself is written in terms of the PID, one obtains an equation that can be solved iteratively. Eqs. (3.54) show that the flux terms depend also on the PID cut, so that they can only be used in conjunction with the PID cut used to obtain them. Also, they are specific to the trigger requirement used since the relative flux of hadrons and leptons depend on the physical process involved. As with the DIS cross section, the fluxes depend on two kinematic quantities, usually taken to be the momentum p and the polar angle θ of the track, so they have been calculated in 27 bins of momentum and 7 bins of θ. After the calculation they have been smoothed out to avoid fluctuations, which may be significant in the region of high momentum and angle, because of the low quantity of data. The $\log_{10}\phi$ term can assume values in general between -2 and +2, showing that the assumption of $\log_{10}\phi = 0$ is absolutely wrong, since it neglects a range of four orders of magnitude in the flux ratio.

3.3 Data

From the 1998 and 2000 data production 4413 and 22944 runs were selected with a *good data quality*. Good data quality requirements include the absence of high voltage trips, a well defined polarization, a measurement of beam polarization updated at most 5 minutes prior to the burst and no dead blocks in the calorimeter.

A study quantified the loss of luminosity due to performance deficiencies of the detector in 1998 and 2000, a necessity to identify the major reasons why data was rejected, and thus indicate needed improvements for future productions (see Table 3.2).

By requiring that the target gas be polarized deuterium, 26094 runs were selected for 2000. Only a small fraction of the total data available from 1998 (runs between 5398 to 10548) was analyzed, a total of 4611 deuterium runs. Runs prior to 5398 had bad data quality, which prevented them from being used for any analysis.

The luminosity for each burst is calculated as the product of the luminosity rate times the burst's time length. As will be explained in the next section, there is more than one quantity representing the luminosity, available in HERMES . The raw `LumiRate` is the measurement of luminosity made by the luminosity detector, and its value smoothed in time is the `LumiFit`. In any analysis the `LumiFit` has to be used. Some problems arise from bursts that have been rejected because of an ill-defined luminosity measurement. This problem is present for both luminosity quantities, being extreme in the `LumiRate`, where spikes are present. The `LumiFit` shows instead very often negative unphysical values when the measurement was meaningless. For such bursts the luminosity value from the previous burst was used.

The final results on the total luminosity loss are listed in Table 3.2. The results are separated for top and bottom detectors. The total and incremental values are shown for both years.

The first four entries are related to target data quality. When the target was flipping between polarization states and so had an ill-defined state, only 0.63% of the total

	2000				1998			
	TOTAL %		INCR. %		TOTAL %		INCR. %	
EXPLANATION	TOP	BOT.	TOP	BOT.	TOP	BOT.	TOP	BOT.
flipping	0.63	0.63	0.63	0.63	0.69	0.69	0.69	0.69
P_T unreasonable	2.25	2.25	2.25	2.25	1.08	1.08	1.08	1.08
α_R bad or unavailable	2.12	2.12	2.33	2.33	1.07	1.07	1.08	1.08
bad target data quality	3.83	3.83	4.40	4.40	1.69	1.69	1.73	1.73
P_B <30% or P_B >80%	1.77	1.77	6.05	6.05	0.33	0.33	1.98	1.98
P_B meas>5 min ago	1.62	1.62	7.16	7.16	3.01	3.01	4.78	4.78
I_B <5 mA or $I_B > 50$ mA	0.02	0.02	7.16	7.16	0.01	0.01	4.78	4.78
$\mathcal{L}$ <5 Hz or $\mathcal{L}$ >60 Hz	1.90	1.90	8.74	8.74	0.01	0.01	4.78	4.78
bad CALO	2.22	4.24	10.40	12.33	0.35	0.46	5.09	5.20
bad PRE or LUMI	1.52	1.52	11.65	13.56	0.35	0.36	5.09	5.20
bad TRD	0.32	0.10	11.87	13.62	0.56	0.64	5.62	5.83
HV trip	0.17	0.11	11.95	13.68	0.60	0.79	6.12	6.52
bad RICH	0.93	0.84	12.77	14.41	0.62	0.61	6.67	7.06
logbook info	0.48	0.48	12.88	14.53	0.00	0.00	6.67	7.06
deadtime	0.19	0.19	12.98	14.63	0.60	0.60	7.05	7.44
burstlength	0.10	0.10	12.98	14.63	0.01	0.01	7.05	7.45
first burst of run	3.62	3.62	16.01	17.63	1.86	1.86	8.42	8.81
udst bad	0.58	0.58	16.30	17.92	0.63	0.63	8.85	9.23

Table 3.2: Luminosity loss in the years 1998 and 2000. A direct comparison between the two years is not possible from the data in this table, since only part of the data is used from the 1998 data production.

luminosity was lost. This means that with the high flipping rate, which is roughly 1 minute, only a small amount of data was lost. Unrealistic values of measured P_T or α_r (see Eq. (2.6)) are in the second and third row. The target group also studies the target performance and provides its own data quality information. The bad target data quality amounts to a total of $\simeq$4% in 2000 and $\simeq$2% in 1998.

The second set of four entries in the table is related to beam information. Beam polarization values below 30% are discarded because they are too low, while values above 80% are unrealistically high. If the beam polarimeters did not update the polarization measurement, the values are not reliable and discarded. Unrealistic values of current and luminosity are also discarded, thus bringing the total of luminosity lost because of bad beam quality to 3%.

Bad detector performance is in the third set of entries, which include bad calorimeter blocks (mostly in the first period of 2000), a non-functioning luminosity monitor, preshower and RICH, high voltage trips in tracking detectors or the TRD, for a total of about 6% in 2000 and 2% in 1998. The functionality of these detectors is necessary for the DIS analysis. The RICH is not essential in the g_1 analysis, but since the luminosity lost for bad RICH performance is less than 1%, it was deemed preferable to take data with overall detector conditions as good as possible.

Other information coming from the shift crew during data taking is included under *logbook info*, and allows 0.5% to be discarded in 2000. Unphysical values of the trigger dead-time and burst length are also discarded.

Bursts for which the burst number is not continuous, which is usually at the beginning of each run and fill, are also rejected, for data acquisition problems that have to do with the synchronization. They are taken into account in the last two entries of the table. Finally, 16% (top detector) and 18% (bottom detector) of the total delivered luminosity were rejected in the 2000 data production because of bad data quality, while for the second half of 1998 data production this is true for about 9% of the total luminosity.

The total number of events selected for 1998 and 2000 are plotted in Fig. 3.8, while the actual numbers are in Table F.1 for 1998 and F.2 for 2000.

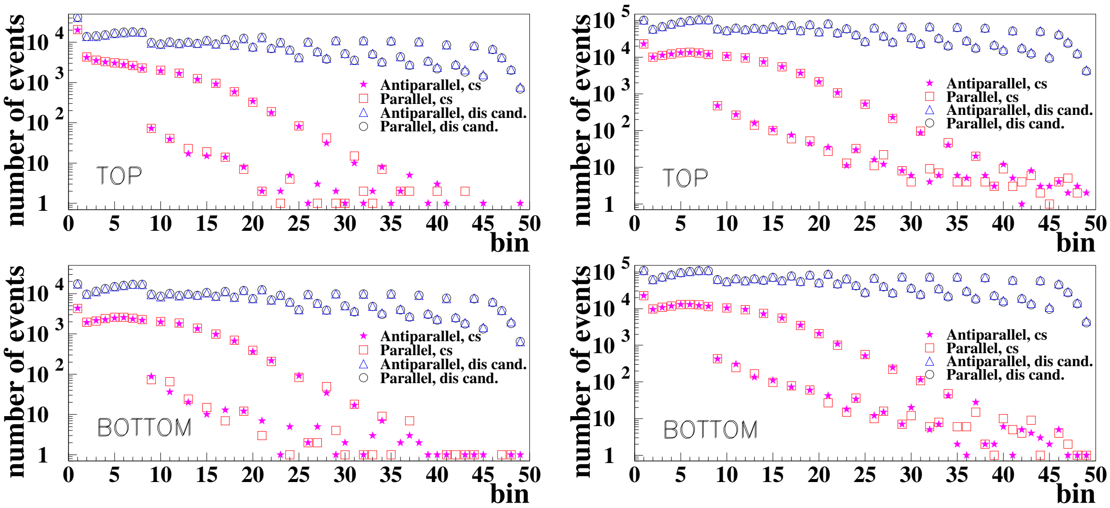

Figure 3.8: Number of DIS events compared to number of charge symmetric events for 1998 (left) and 2000 (right).

3.4 Møller and Bhabha asymmetries

A residual electron polarization in the target gas can contribute to a polarization dependence in the luminosity measurement. For this reason the raw luminosity rate is usually fitted on a fill-by-fill basis, so that the effect for the two spin states cancels out in the fitting procedure. The fitted values are provided by the luminosity experts. Until the 1999 production the fit was done to the luminosity rate itself, providing the `LumiFit` values.

Afterwards, since the current I is related to the luminosity L, the electron charge e and the target density ρ by the relation

$$I = \frac{Le}{\rho} \,, \tag{3.55}$$

a fit was made to the ratio of luminosity to current, since the target density is a stable quantity throughout a fill. A new fitted value for the luminosity was introduced, denoted as `LumiFitBstGai`. This quantity has the advantage of being also gain-corrected.

The luminosity asymmetry, called Møller or Bhabha depending on the beam charge, can be calculated as a function of time using the current as a normalization factor

$$A_{\text{Møller}} = \frac{\mathcal{L}^{\leftrightarrows} I^{\rightrightarrows} - \mathcal{L}^{\rightrightarrows} I^{\leftrightarrows}}{\mathcal{L}^{\leftrightarrows} I_P^{\rightrightarrows} + \mathcal{L}^{\rightrightarrows} I_P^{\leftrightarrows}} \,. \tag{3.56}$$

Such an asymmetry was calculated for `LumiRate` and `LumiFitBstGai` as a function of time. The results are shown in Fig. 3.9 for top (left) and bottom (right) detectors, for 1998 and 2000 data. It appears clear from the plots that the asymmetry calculated with `LumiRate` is not compatible with zero, and has values of order 0.00125±0.0002 for 2000 and -0.0012±0.0003 for 1998. The signs are opposite because the beam charge was opposite in the two years (positrons in 2000 and electrons in 1998).

It is worth noting that the asymmetries for top and bottom detectors are different not because they have different measured luminosities but because some data may have been rejected in top or bottom, because of bad data quality, giving different total luminosity values. In conclusion the fitted luminosity has been used in 1998 and 2000 for the extraction of the DIS asymmetry, and it was verified to have a negligible contamination from Møller and Bhabha rates.

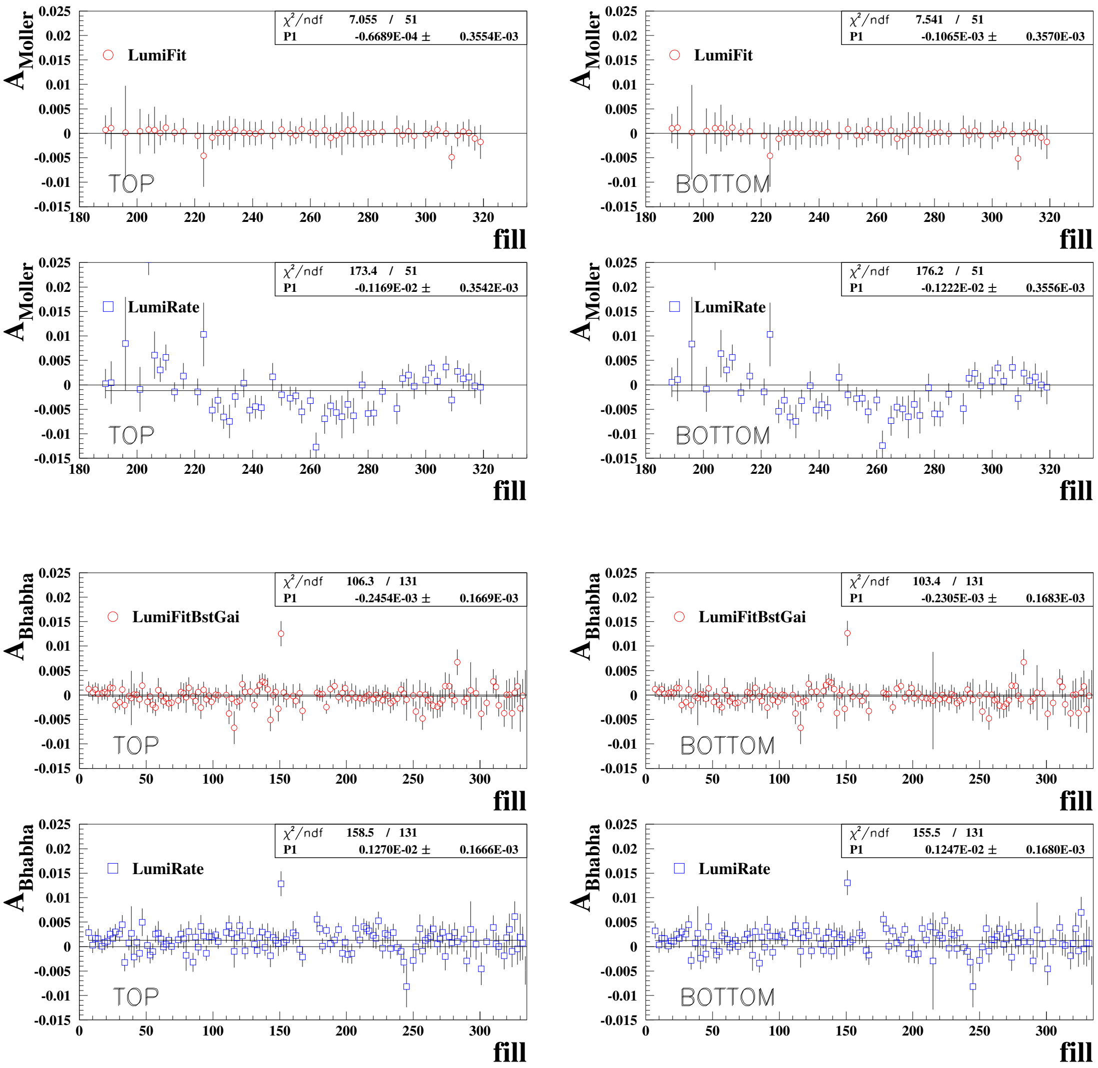

Figure 3.9: Møller Asymmetry for top (left) and bottom (right) detectors, calculated with the different luminosity quantities available at HERMES. The top four plots are obtained from 1998 data, while the bottom four plots are from 2000 data. A straight line fit is made to each set of data points, with the results given by P1.

3.5 Alignment correction

The top and bottom detectors are slightly misaligned with respect to the target cell, a problem studied for the 1997 data production in Ref.[36], where also an alignment correction was obtained. This is most visible in histograms of z_v, which should be symmetric

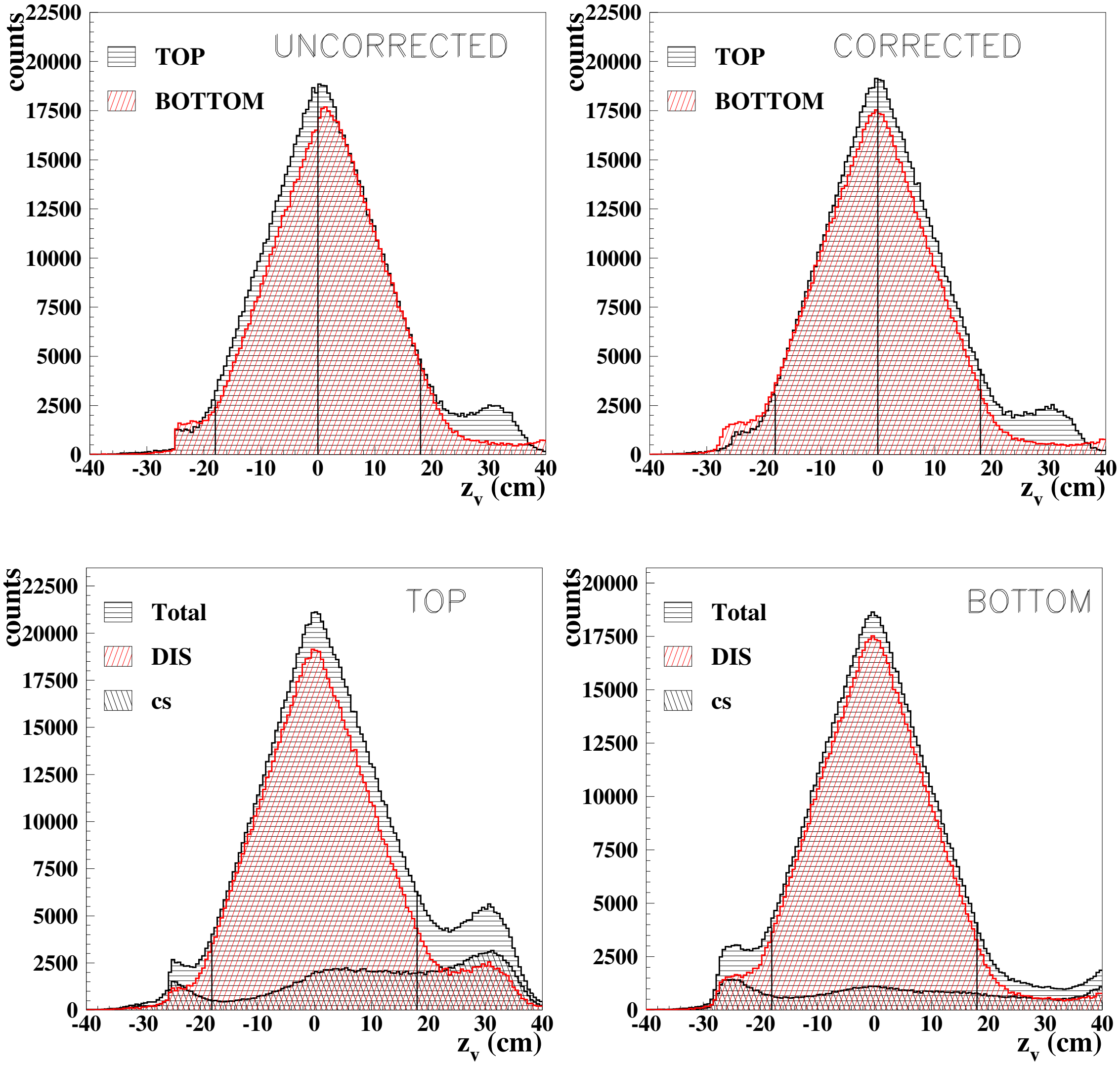

Figure 3.10: Top plots: comparison of z_v distributions without (left) and with (right) the application of the alignment correction. Bottom plots: z_v distributions of total, DIS and charge symmetric events, for top (left) and bottom (right) events. The vertical lines show the usual cuts at $z_v = \pm 18$ cm.

around $z_v = 0$, for both top and bottom detectors. The top-left plot of Fig. 3.10 shows a top-bottom comparison of z_v distributions of DIS events, for 1998 data. The two distributions are not symmetric around $z_v = 0$ as they should be, and their peak positions are shifted by about 2 cm. This problem results in wrong measurements of the scattering an-

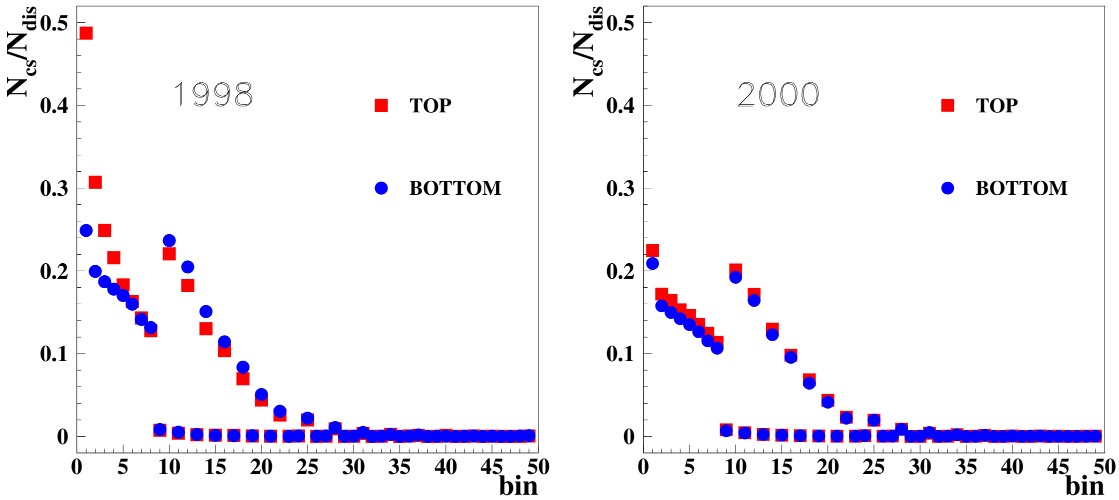

Figure 3.11: Ratio of charge symmetric events over DIS candidates for 1998 data (left) and 2000 (right) data. In 1998 data the number of cs in the top detector has a steep rise that has been explained with a spring finger left hanging inside the detector acceptance.

gles and z_v, so must be corrected. The 1997 correction factor has been applied to the data and the effect is shown on the top-right plot of the same figure. The correction highly improves the data/Monte Carlo comparison ([37]), and all plots shown in this thesis for the 1998 data have the correction applied.

The z_v distribution for top DIS events even after being corrected, still shows an excess of events in the positive z_v region, coming from a peak located at about 32 cm.

In 1998 a spring finger, 3-4 mm long and 0.5 mm thick, used to connect the beam pipe to the target cell, was forgotten inside the target region, hanging from the top of the cell. Beam scattering off of this object thus created this peak. The target spring finger (TSF) was removed only in May 1999, and it was thus present throughout the 1998 production, but did not affect later productions. As a comparison, Fig. 3.11 shows the ratio of charge symmetric (*cs*) to DIS events for 1998 (left) and 2000 (right), where it shows that the 2000 distribution is back to the levels of 1997. The TSF contribution is highest in the low x region.

The bottom plots of Fig. 3.10 show the distribution of total (DIS+*cs*), DIS and *cs* events for top and bottom detectors. Common to both detector halves is a peak located at -25 cm, coming from scattering off the HERA collimator C2, while the top detector alone is affected by the large background coming from the TSF. The usual *cs* subtraction reduces the size of the background but does not eliminate it completely, meaning that there is an actual excess of events with the same charge as the beam originating from C2 and from the TSF, which, being unpolarized material, has no spin dependence. The collimator peak has hardly any tail in the accepted region of z_v between -18 and +18 cm, while the tail from the TSF is instead considerable in size, and the major source of background. This will be discussed further in section 3.11.3.

3.6 Asymmetries for 1998 and 2000

The asymmetry $A_{||}^d$ has been measured in the 49 kinematic bins, and the results are shown in Fig. 3.12, where for clarity the data have been separated into the 3 y bins.

As explained before, the detector is divided into two symmetric halves, which can effectively be treated as two different detectors. This fact proves helpful to check the agreement of the two results and thus keep systematic effects under control.

The statistics of 2000 is overwhelming, and will have the highest weight on the final results. The asymmetries agree very well in the whole kinematic range, but nevertheless

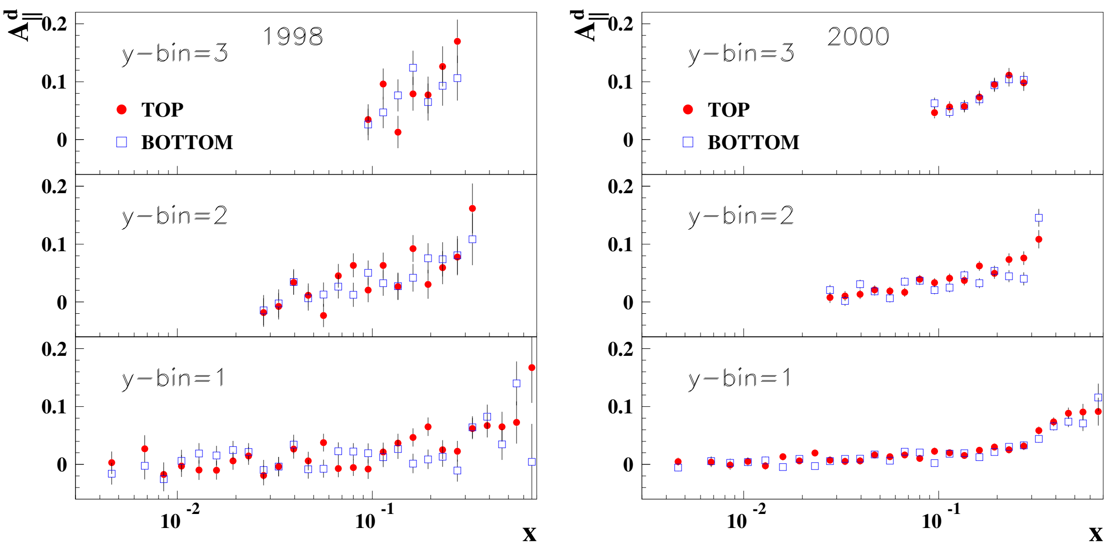

Figure 3.12: The measured asymmetries for 1998 data (left) and 2000 (right).

many studies have been performed on its stability, that will be shown in the next sections.

The final result for g_1^d will involve the weighted average of top and bottom asymmetries, which, in each kinematic bin, reads:

$$\begin{aligned} A_{||}^d &= \frac{A_{||}^d(TOP)w(TOP) + A_{||}^d(BOT)w(BOT)}{w(TOP) + w(BOT)} \\ \sigma^2 &= \frac{1}{w(TOP) + w(BOT)}\,, \end{aligned} \tag{3.57}$$

where w stands for the weight $1/\sigma^2$.

3.7 2000 Beam helicity flips

In the 2000 running period the beam helicity was switched between +1 and -1 for a total of 7 periods. The resulting asymmetries for these periods have to be checked for consistency throughout the seven periods. Table 3.3 gives a summary of the beam helicity information through 2000. Statistical tests (which will be described later) were made, and they didn't show any unexpected behavior. Here it will only be shown that the asymmetry for the positive helicity, spanning four periods, agrees with the one resulting from the three periods with negative helicity. Fig. 3.13 (left) shows the agreement for top and bottom detectors.

First run	Last run	Helicity	# of runs	# of fills
1	6109	+1	5075	57
6110	9404	-1	2430	31
9405	13204	+1	3112	39
13205	18168	-1	3669	33
18169	22579	+1	3467	33
22580	26713	-1	3123	37
26714	30354	+1	2068	33

Table 3.3: Summary of 2000 beam helicity conditions.

3.8 Effect of trigger efficiencies on the asymmetry

As discussed in section 2.7 the trigger efficiencies in 1998 and 2000 reached values as low as 90%. Fortunately they have no effect on the measured asymmetry since every effect coming from detector efficiencies cancels in the asymmetry ratio, provided that the efficiencies are spin independent, which has been tested. As a confirmation, the correction has been applied to 2000 data. Each event in each kinematic bin has been weighted by the trigger efficiency as a function of momentum, the time period, the geometry and the number of tracks. In this way the total number N of events in each bin has been substituted by:

$$N \to \sum_{i=1}^{N} \frac{1}{\varepsilon(\text{time}, \#\text{ of tracks}, \text{momentum}, \theta_x, \theta_y)} \ . \tag{3.58}$$

The results are shown in Fig. 3.13, where the difference of uncorrected to corrected, over uncorrected asymmetries is plotted. The error bars take into account the fact that the two data sets are completely correlated (see App.E). Large values of error bars are due to very small values of the asymmetries, which enlarge the errors. In conclusion, the trigger inefficiencies have been verified to have no effect on the results.

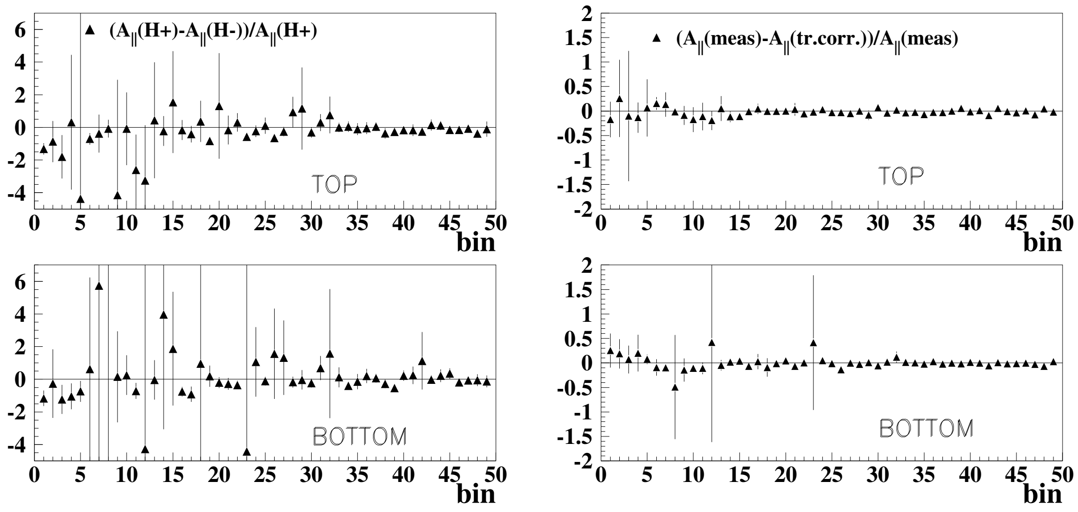

Figure 3.13: Left: comparison between the asymmetries calculated for the two possible beam helicities (2000 data). $A_{||}(H+)$ indicates the asymmetry calculated for positive beam helicity, while $A_{||}(H-)$ is the asymmetry for negative beam helicity. Right: effect of the trigger efficiencies on the asymmetry obtained from the 2000 data set. The two asymmetries are in very good agreement, which shows the independence of the asymmetry on the efficiencies.

3.9 Dependence on φ

The asymmetry should not have any dependence on the azimuthal angle φ (see Fig. 2.2). To test it the detector has been ideally sliced into 50 top ($0 < \varphi < \pi$) and bottom ($\pi < \varphi < 2\pi$) bins. In each kinematic bin the asymmetry in each φ bin, denoted with i, and its deviation with the final asymmetry (that includes all φ bins) have been calculated, where the deviation is defined as (see App. E)

$$\text{deviation} = \frac{A_{||}^d(\varphi_i \leq \varphi < \varphi_{i+1}) - A_{||}^d(0 \leq \varphi \leq 2\pi)}{\sqrt{\sigma_i^2 - \sigma^2}} \, , \tag{3.59}$$

and σ_i is the error of the asymmetry in the ith φ bin and σ is the total error. The deviations for each kinematic and φ bin are shown in the top plots of Fig. 3.14 for 1998 and 2000, while the bottom plots represent the average deviations over all kinematic bins, for each φ bin. The data from 1998 has larger fluctuations but they are mostly due to the smaller statistics. No effect has been detected.

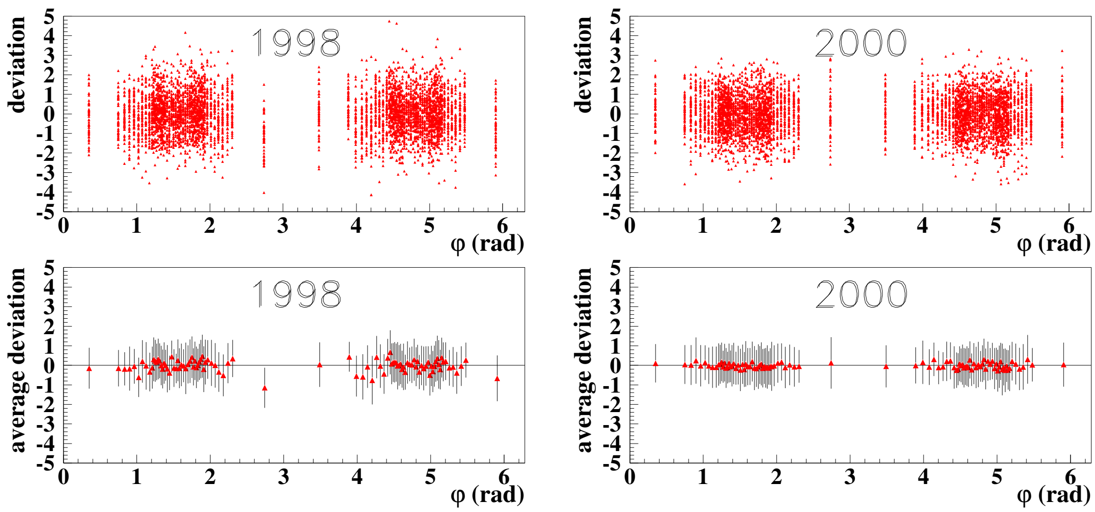

Figure 3.14: Top plots: deviations of the asymmetry over all kinematic bins, for each φ bin. Bottom plots: average deviations in each φ bin. The errors are the standard deviations of the distributions in the top panels. Left plots are for 1998 data while right plots are for 2000.

3.10 Statistical tests

As a general consistency check one can apply various statistical tests to the data, to verify that the results do not depend on variables for which there should be no dependence. This section deals with these tests.

3.10.1 z^2 test

The asymmetry is tested against non-statistical dependencies on physical quantities.

A simple test is the z^2 test ([38]), effectively a χ^2 test, treated in detail in App.D. The asymmetry is divided into N bins of one variable (which can be referred to as t) it should not depend on, for example time. The physical quantity of interest (in this case $A^d_{||}$) is divided into bins of such a variable. The z^2 value gives an estimate of the spread of this quantity in the bins. Given $A^d_{||i}$ (the value of $A^d_{||}$ in a definite bin of x and y and bin i in t), σ_i (the statistical uncertainty in that bin), and $< A^d_{||} >$ (the final value with statistical uncertainty σ), then z^2 is defined as:

$$z^2 = \frac{1}{N-1} \sum_i^N \frac{1}{\sigma_i^2} \left(A^d_{||i} - < A^d_{||} > \right)^2 . \tag{3.60}$$

The ideal case should give $z = 1$. The allowed spread (68% confidence interval) is ([38]):

$$\sigma_z = \frac{1}{\sqrt{2(N-1)}} . \tag{3.61}$$

The z^2 test can be used to test the validity of the assumptions on the errors. If there is some unknown systematic error, then the value of z will significantly differ from 1. On one hand, the z^2 test is a way to alert of the presence of systematic effects that should be corrected for. On the other hand when it is not possible to cure the bias, it's quite common practice to normalize the error bars by multiplying them by the quantity z so that the new z will be equal to 1. This procedure has to be used with care, since it's a way to hide systematic effects with enlarged error bars.

The z^2 test has been used to check that the asymmetry had no large fluctuations in time, z_v position, φ and current. The results are shown in Fig. 3.15 and Fig. 3.16. No dependence has been detected. Each test has been done for top and bottom detectors separately.

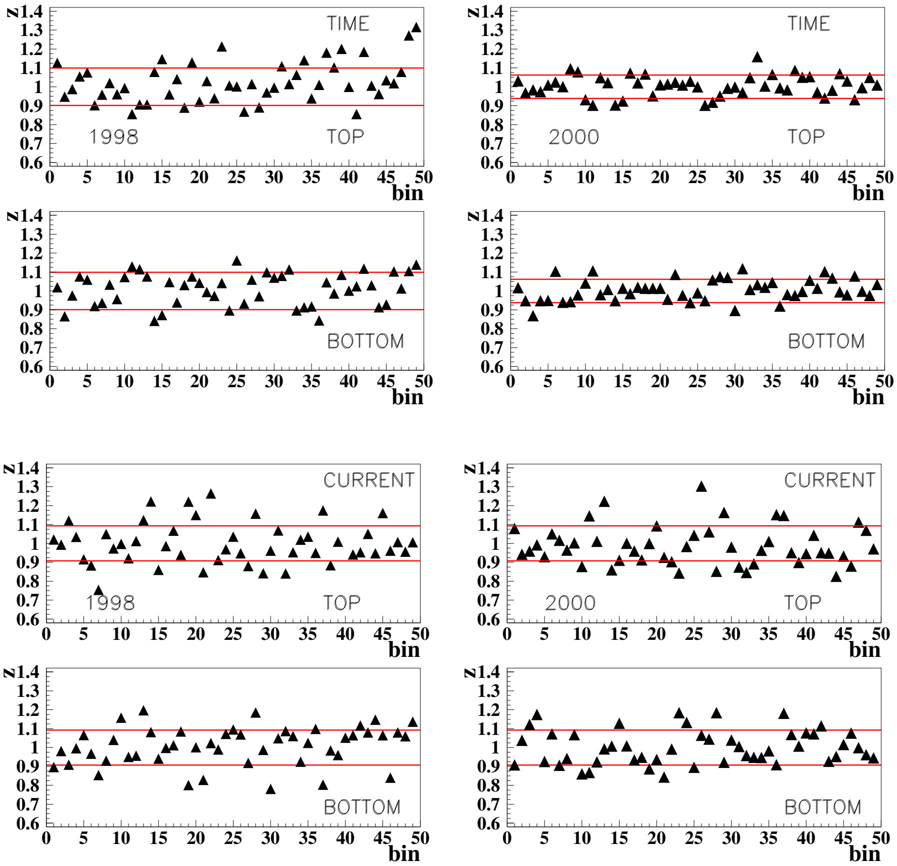

Figure 3.15: The z^2 test applied to the time (top four plots) and current (bottom four plots) dependence of $A_{||}^d$. The dotted lines represent the 1σ level. The left plots refer to 1998 and the right ones to 2000. The 1 σ levels for time in 2000 are smaller since there are more bins in time, given the much increased statistics with respect to 1998.

3.10.2 Mann-Whitney test

This test ([39]) is used to check whether or not there are any trends in the data. It is applied to *two* sets of samples. As an hypothesis for the test the two samples have to be independent, the dependent variable has to be intrinsically continuous, and it has to be possible to *order* the elements of the set according to an ordering criterion. The purpose is to understand if there is a trend in the data, i.e. if one set tends more than the other towards lower or higher values. The *null hypothesis* of no trend is the hypothesis for which the data are uniformly distributed.

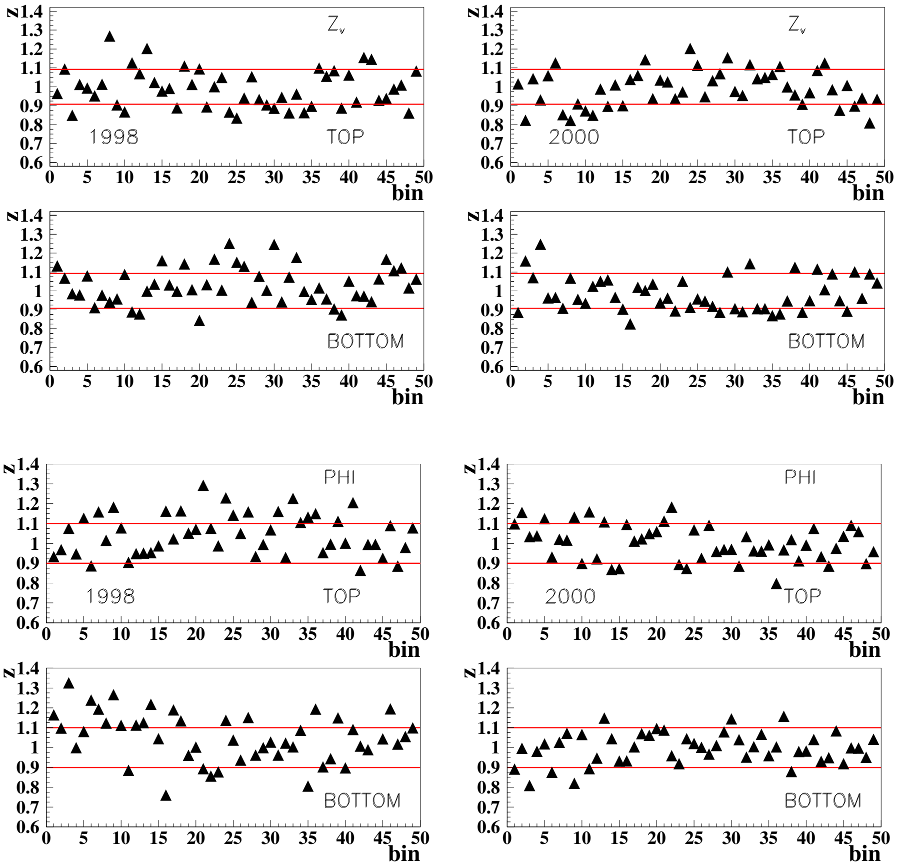

Figure 3.16: The z^2 test applied to the z_v (top four plots) and φ (bottom four plots) dependence of $A_{||}^d$. The dotted lines represent the 1σ level. The left plots refer to 1998 and the right ones to 2000.

Let us suppose we have two sets of data, the first set A containing N_A elements and the second set B containing N_B elements, so that the total number of elements is $N = N_A + N_B$.

The elements of the two sets together are sorted in increasing order, and to each of them a *rank* number is assigned. In the case of ties, i.e. if more than one data point has the same rank, the assigned rank is the average rank they would get in case they were not ties. The goal is to assess if the distribution of A's and B's is random or not, i.e. if A's tend to have lower rank or higher rank. Let us now introduce the numbers T_A^{obs} as the sum of the ranks of the elements belonging to group A, T_B^{obs} as the sum of rank of elements in B, T_{AB} as the total sum of ranks, and M_{AB} as the mean rank. These are:

$$T_{AB} = \frac{N(N+1)}{2} = \frac{(N_A + N_B)(N_A + N_B + 1)}{2} \qquad M_{AB} = \frac{T_{AB}}{N} = \frac{(N_A + N_B + 1)}{2}. \tag{3.62}$$

If the *null hypothesis* were true the ranks in the two groups would be distributed uniformly around the average, so that

$$T_A^{\text{exp}} = M_{AB} N_A \quad , \quad T_B^{\text{exp}} = M_{AB} N_B \; . \tag{3.63}$$

It can be shown ([39]) that the sampling distributions for T_A^{obs} and T_B^{obs} tend to approximate the normal distribution for $N_A, N_B > 5$, with the same variance and standard deviation, equal to:

$$\sigma_T = \sqrt{\frac{N_A N_B (N_A + N_B + 1)}{12} \left(1 - \frac{\sum t_i (t_i^2 - 1)}{N(N^2 - 1)} \right)} \; , \tag{3.64}$$

where t_i is the number of ties for each rank value. The correction for ties is small and can be safely neglected if there are few ties and N is large.

Given the mean M and standard deviation σ_T of a distribution, one can create a z-ratio, i.e. a quantity that refers to the unit normal distribution:

$$z = \frac{(T^{\text{obs}} - M) \pm 0.5}{\sigma_T} \; , \tag{3.65}$$

where the term ± 0.5 is a *correction for continuity* equal to -0.5 when $T > M$, and equal to +0.5 for $T < M$. It is easy to prove that $z_A = -z_B$ so that only one of the two is needed for the Mann-Whitney test.

The Mann-Whitney test can be easily applied to the study of the time dependence of the asymmetry $A_{||}^d$. There are a number of ways to obtain two sets of data, each sensitive to a different kind of trend.

In a given kinematic bin, the values in time of the top (bottom) detector asymmetry can be assigned to set A (B): this is a way to check whether the top asymmetry was consistently above or below the bottom one and vice-versa. Results of this test are shown in Fig. 3.17 for 1998 and 2000.

Another test can be performed by associating a data point to group A (B) if its difference with the total $A_{||}^d$ is positive (negative). The values for $A_{||i}^d - A_{||}$ were ordered in

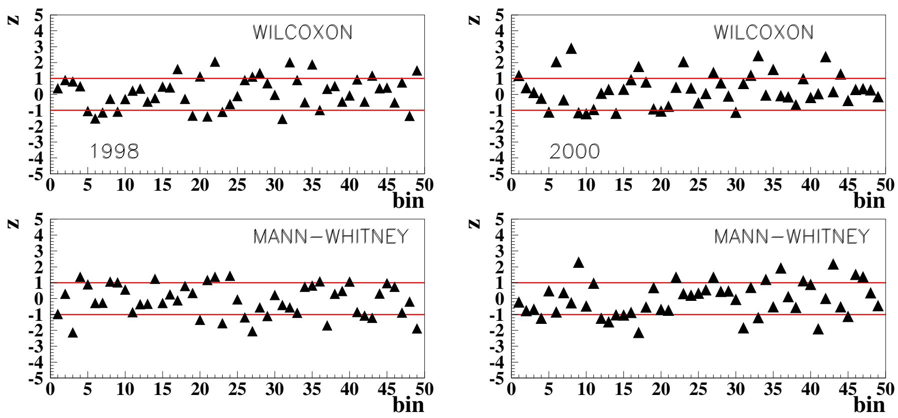

Figure 3.17: The Wilcoxon and Mann-Whitney tests applied to the comparison of top and bottom detectors time dependence of $A_{||}^d$ for 1998 data (left) and 2000 data (right plots). The dotted lines represent the 1σ level.

increasing (or decreasing) order of their absolute value, so that a succession of A's and B's was obtained. At this point the procedure outlined in this section was employed. The results are shown in Fig. 3.18 for 1998 and 2000. This test assesses if the final top or bottom detector asymmetry is the result of averaging values that were consistently above or below the average in one period. This effect would not be detected by the z^2 test, which, being a χ^2 test, is only sensitive to the deviations of each point from the average.

The Mann-Whitney test can be a powerful tool to see whether data is clustered around low or high values, but it has also some shortcomings, in the case that the elements of one group tend to assume both low and high values, while the elements of the other group tend to the middle values. The Mann-Whitney test would fail to recognize the trend of the data and would give the false answer of no trend.

3.10.3 Wilcoxon test

The Wilcoxon test ([39]) is another test intended to verify if there are trends in 2 sets of data. The hypothesis that the two sets have to satisfy are that the scales for the measurements of the data in the two sets A and B have to be the same. The data are supposed to have an underlying normal distribution. The two paired values from the two sets have been randomly taken from the source populations. Since each element of each set will

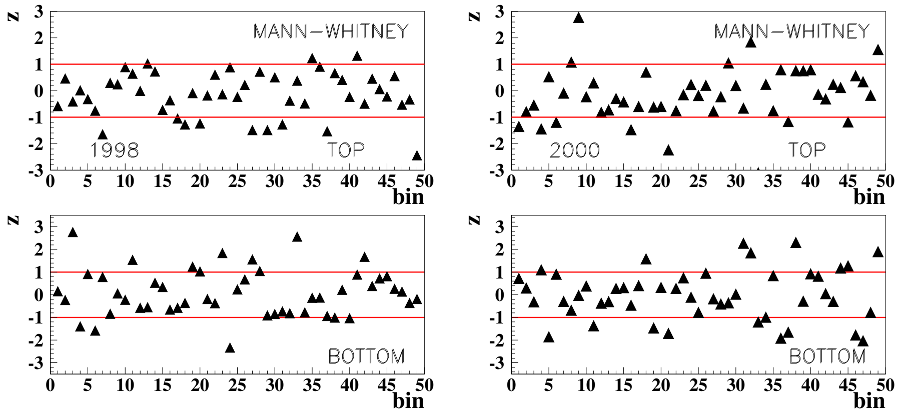

Figure 3.18: The Mann-Whitney test applied to the time dependence of $A_{||}^d$ for top and bottom detectors for 1998 data (left) and 2000 (right). The dotted lines represent the 1σ level.

be paired to an element of the other set, the two sets need to have the same number of elements.

The difference between each couple of elements is computed and ordered in increasing absolute values and then ranked as in the case of the Mann Whitney test. Positive differences will be assigned to the set A and negative differences to set B. Differences equal to zero have to be treated in a slightly different way: if they are an even number then half of it will be assigned to each set, while if they are in an odd number then one will be discarded.

It can be shown that for large N the distribution of ranks tend to approximate a gaussian distribution with standard deviation

$$\sigma_T = \sqrt{\frac{N(N+1)(2N+1)}{24} - \frac{1}{48}\sum t_i(t_i^2 - 1)}\ , \tag{3.66}$$

so that one can create a unit normal distribution in the same way as Eq. (3.65). This test has been performed for the difference of asymmetries in top and bottom detectors, and the results are shown in Fig. 3.17 for 1998 data in the left and 2000 data in the right, and again no trend has been detected. The test can be applied also to top or bottom detectors separately by assigning the asymmetry in a time bin to the set A or B if its difference with respect to its average is positive or negative, and then ordering the differences in increasing absolute values. This has been done and the results are shown in Fig. 3.19.

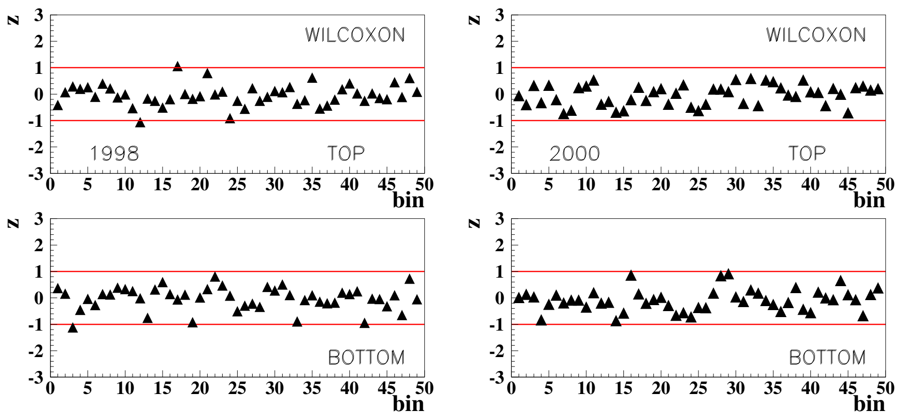

Figure 3.19: The Wilcoxon test applied to the time dependence of $A_{||}^{d}$ for top and bottom detectors for 1998 data (left) and 2000 (right).

3.11 Systematic uncertainties

3.11.1 Study of z_v cut dependence of the asymmetry

The z_v is the position of the interaction point along the z axis. The target cell is only 40 cm long, and the zero of the z axis is at the center of the target cell. This means that a reconstructed target vertex cannot be accepted if it has $|z_v| >$20 cm.

A standard cut of 18 cm is generally used, as a compromise to exclude the more external regions of z_v with their high background and keep the scattering vertex well contained in the target. On the other hand the cut cannot be so tight as to significantly lower the statistics.

Many studies have been made to test the stability of the asymmetry with respect to the z_v. The z_v cut has been varied around its standard value and the asymmetry calculated. The deviations of the asymmetry from the nominal value as the z_v cut is varied from 14 cm to 22 cm, defined as

$$\text{deviation} = \frac{A_{||}^{d}(z_v \le |z_v^i|) - A_{||}^{d}(-18\text{cm} < z_v \le 18\text{cm})}{\sqrt{|\sigma_i^2 - \sigma^2|}} \tag{3.67}$$

have been calculated for each kinematic bin, for top and bottom separately. In the last expression z_v^i indicates the z_v cut and σ_i the statistical error on the asymmetry for that cut. The top Fig. 3.20 shows the deviations for 1998 and 2000, while the average deviations

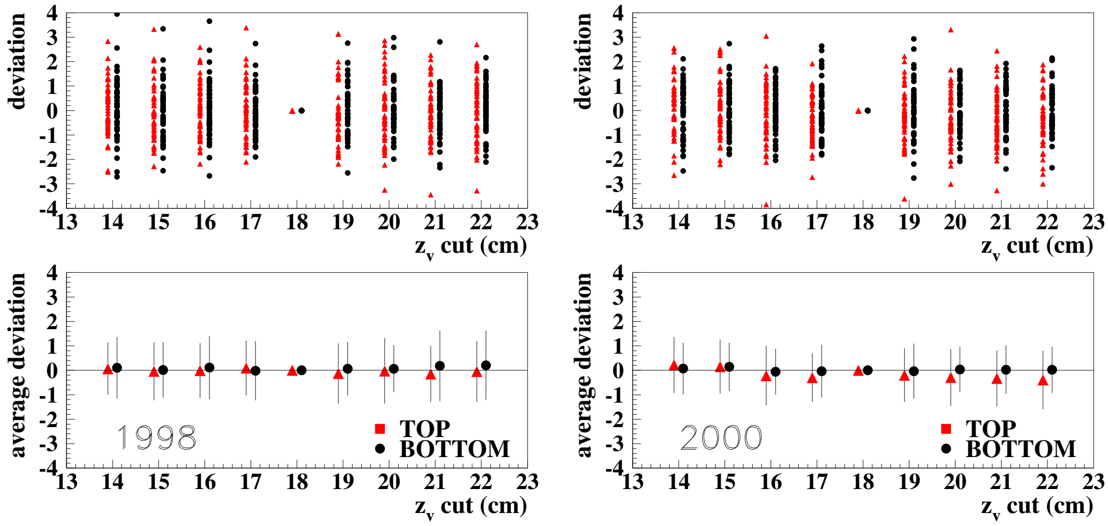

Figure 3.20: Top plots: deviations of the asymmetry with respect to the standard cut $z_v = 18$ cm, over all kinematic bins, for top and bottom separately. The left plots are for 1998 data while the right ones are for 2000. Bottom: deviations averaged over all kinematic bins.

per cut and their standard deviations are shown in the bottom plots, and they are nicely consistent with zero everywhere.

Fig. 3.21 shows the results of a z^2-*like* test performed. The deviations of the asymme-

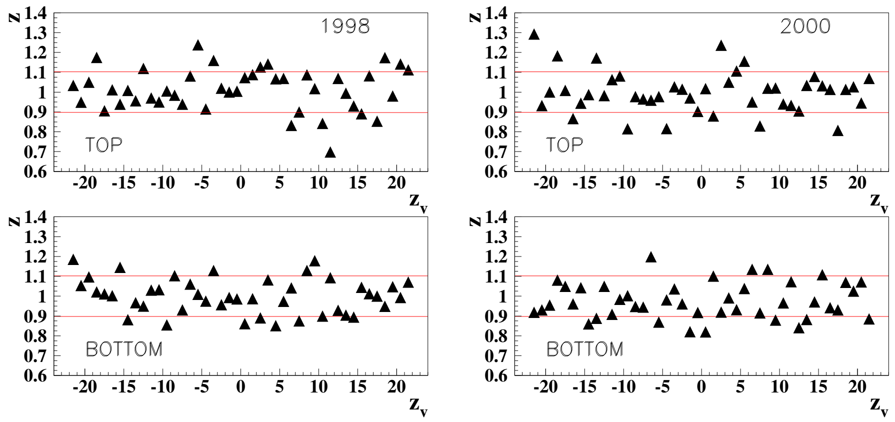

Figure 3.21: A test similar to the z^2 doesn't show any dependence of the asymmetry on z_v. The left plots are for 1998 data while the right ones are for 2000.

try with respect to the asymmetry calculated for a z_v cut of 18 cm have been computed in different z_v bins:

$$z_i^2 = \frac{1}{49-1}\sum_i^{49}\frac{1}{\sigma_i^2}\left(A_{||}^d(z_v^i < z_v \leq z_v^{i+1}) - A_{||}^d(-18\text{cm} < z_v \leq 18\text{cm})\right)^2 , \tag{3.68}$$

where z_v^i are the values of z_v used to define the binnings. No large deviation is detected.

3.11.2 Dependence of the asymmetry on the θ_y cut

As for the z_v cut, the θ_y cut has also been studied to verify the stability of the asymmetry. The angle θ_y defines the angular acceptance in the vertical direction, and it is sensitive to misalignments. The θ_y cut of 0.04 rad has been varied from 0.038 to 0.044 around the standard cut of 0.040 rad, and the deviations of the asymmetry in each kinematic bin are studied. The top Fig. 3.22 shows the deviations of the asymmetry with respect to the standard asymmetry for each cut, while the bottom plots are the average deviations with their standard deviations, for each cut. No effect is detected.

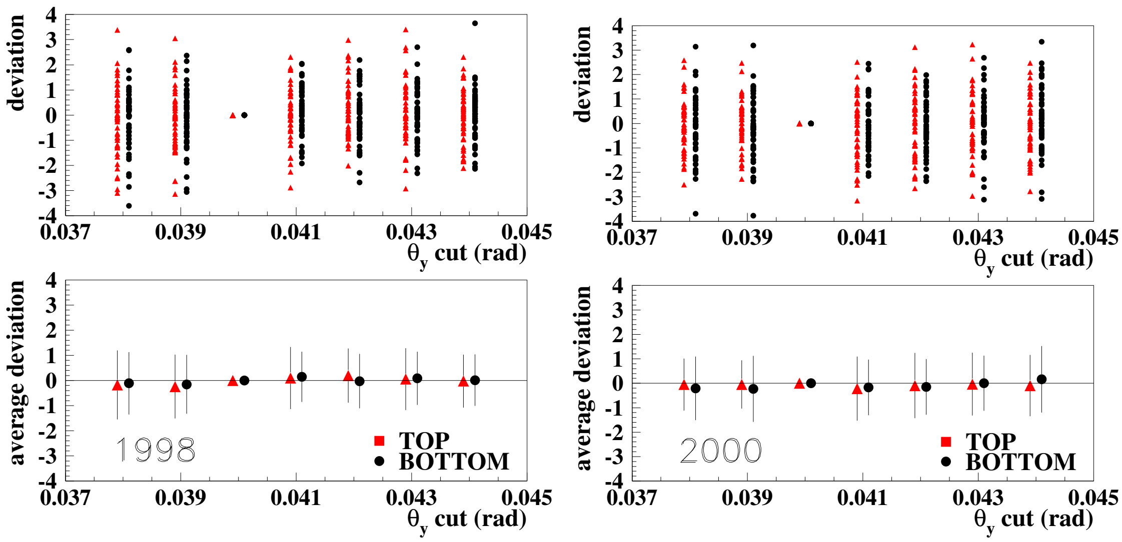

Figure 3.22: Top: deviations of the asymmetry calculated by varying the θ_y cut, with respect to the standard cut. Bottom: average deviations for each cut. The errors are the standard deviations of the plots in the top panels. The left plots are for 1998 data while the right ones are for 2000.

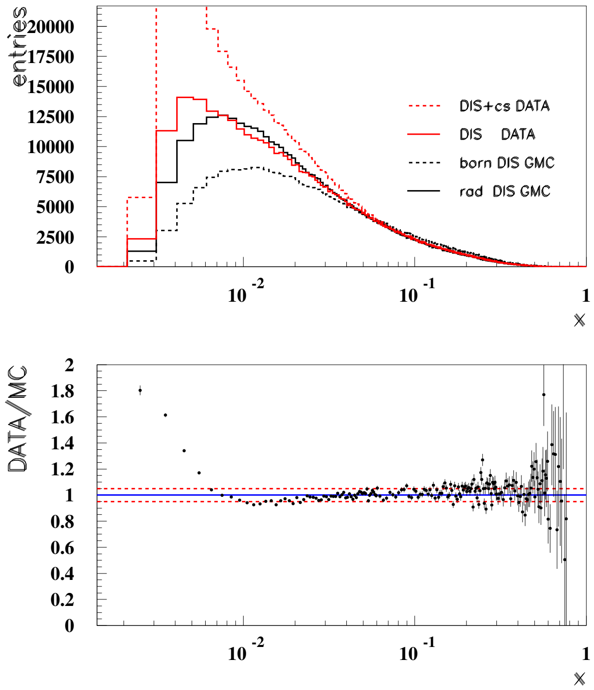

Figure 3.23: Data-Monte Carlo comparison for top detector events ([37]). There is a clear excess in the data at low-x, explained as coming from the TSF. This is not seen for a bottom detector-Monte Carlo comparison.

3.11.3 1998 data: Target Spring Finger Problem

A serious problem exists in the 1998 data in the study of low x bins. The z_v distribution of DIS top events shows a peak at around 32 cm coming from the TSF, as was shown in Fig. 3.10. The bottom distribution seems much more consistent with the values from the 1997 production.

As Fig. 3.10 shows, a common charge-symmetric subtraction doesn't help to solve the problem: the peak is still visible. This means that the events building up in that peak could come from a different process that is not removed by the usual subtraction. These events could come from DIS scattering off the aluminum of the TSF.

The way the asymmetry is corrected due to this additional rate is by trying to disentangle the *true* rate from the TSF rate.

From data-MC comparison shown in Fig. 3.23 it is justified to assume that the TSF only affects the top events. In this case we can write the top and bottom total number of

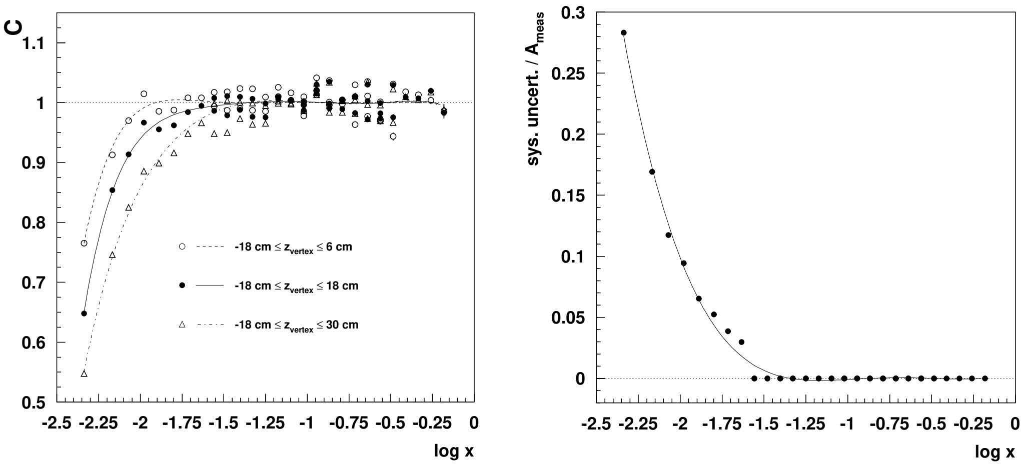

Figure 3.24: Left: correction factor C to be applied to the asymmetry to correct it due to TSF events, as a function of z_v and x. The correction is relevant only in low x bins. Right: the systematic uncertainty on the asymmetry, estimated as the difference between the corrected asymmetry at 18 cm and 30 cm (where the TSF contribution is a maximum).

events as:

$$\begin{aligned} N^{-(\mathrm{TOP})}_{\mathrm{meas}} &= N^{(\mathrm{TOP})}_{\mathrm{dis}} + N^{-(\mathrm{TOP})}_{\mathrm{cs}} + N^{(\mathrm{TOP})}_{\mathrm{TSF}} \\ N^{-(\mathrm{BOT})}_{\mathrm{meas}} &= N^{(\mathrm{BOT})}_{\mathrm{dis}} + N^{-(\mathrm{BOT})}_{\mathrm{cs}}\,, \end{aligned} \tag{3.69}$$

where we dropped the negative sign on N_{dis} since in 1998 there was an electron beam, and $N^{(\mathrm{TOP})}_{\mathrm{TSF}}$ is the *cs*-corrected TSF rate. From a high x fit ([37]) not including the 7 low-x points, it was determined that the ratio of top to bottom DIS events, normalized to the luminosities, is a stable quantity:

$$\frac{N^{(\mathrm{TOP})}_{\mathrm{dis}}/\mathcal{L}^{\mathrm{TOP}}}{N^{(\mathrm{BOT})}_{\mathrm{dis}}/\mathcal{L}^{\mathrm{BOT}}} \simeq 0.96 \tag{3.70}$$

so that by inserting Eq. (3.70) into Eq. (3.69) we get:

$$N^{(\mathrm{TOP})}_{\mathrm{TSF}} = N^{-(\mathrm{TOP})}_{\mathrm{meas}} - N^{-(\mathrm{TOP})}_{\mathrm{cs}} + 0.96(N^{-(\mathrm{BOT})}_{\mathrm{meas}} - N^{-(\mathrm{BOT})}_{\mathrm{cs}}) \tag{3.71}$$

where the luminosities cancel in the ratio. The TSF rate was checked to be independent of the spin state so that it acts as a dilution factor on the asymmetry:

$$A_{||}^{\text{TOP}} = \frac{A_{||\text{meas}}^{\text{TOP}}}{1 - N_{\text{TSF}}^{(\text{TOP})}/N_{\text{dis}}^{(\text{TOP})}} = \frac{1}{C}\, A_{||\text{meas}}^{\text{TOP}} \,. \tag{3.72}$$

The systematic error due to the TSF was assessed from the z_v cut variation, as shown in Fig. 3.24, which shows in the left plot the TSF contribution for different z_v cuts. As expected, for cuts that include higher values of z_v the correction gets stronger, since the TSF contributes more. The systematic uncertainty was then defined as the difference between the asymmetry with a z_v cut at 30 cm and at 18 cm, as shown in the right panel in Fig. 3.24:

$$\Delta A_{||}^{\text{TSF}} = |A_{||}^{30} - A_{||}^{18}| \,. \tag{3.73}$$

The TSF affects also the luminosity, since it affects the count rate, and this contribution affects all 49 bins.

3.11.4 Hadronic background

In the extraction of the asymmetry one has to take into account that there is a fraction of hadrons misidentified as DIS leptons. The number of hadrons turns out to be spin-dependent and to have a non-trivial spin asymmetry:

$$A_{h^\pm} = \frac{N^{\overset{\Leftarrow}{\rightarrow}}\mathcal{L}^{\overset{\Rightarrow}{\rightarrow}} - N^{\overset{\Rightarrow}{\rightarrow}}\mathcal{L}^{\overset{\Leftarrow}{\rightarrow}}}{N^{\overset{\Leftarrow}{\rightarrow}}\mathcal{L}_p^{\overset{\Rightarrow}{\rightarrow}} + N^{\overset{\Rightarrow}{\rightarrow}}\mathcal{L}_p^{\overset{\Leftarrow}{\rightarrow}}} \,. \tag{3.74}$$

The hadron asymmetry has been extracted by requiring PID<-2, which is a tight requirement for the hadron identification. The extracted asymmetries are small compared to the DIS asymmetry everywhere except in the small x region, where the two are comparable.

A correction for the hadronic background must be obtained. Let us introduce h_{cand} and h_{cs} as the fraction of DIS candidates and charge-symmetric background which comes from hadrons, and $\varepsilon_{\text{cand}}$ and ε_{cs} as the PID efficiencies in the identification of a particle as a lepton or a hadron in the case of DIS candidates and *cs* background.

The *true* number of DIS events is obtained by subtracting the contribution of misidentified hadrons and charge symmetric particles:

$$\begin{aligned} N_{\text{dis}} &= \frac{N_{\text{cand}}}{\varepsilon_{\text{cand}}}(1 - h_{\text{cand}}) - \frac{N_{\text{cs}}}{\varepsilon_{\text{cs}}}(1 - h_{\text{cs}}) \\ &= N_{\text{cand}}^{\text{true}}(1 - h_{\text{cand}}) - N_{\text{cs}}^{\text{true}}(1 - h_{\text{cs}}) \,, \end{aligned} \tag{3.75}$$

where $N^{\text{true}}_{\text{cand}} = N_{\text{cand}}/\varepsilon_{\text{cand}}$ and $N^{\text{true}}_{\text{cs}} = N_{\text{cs}}/\varepsilon_{\text{cand}}$ are the true candidates and *cs*, corrected for efficiencies.

The real asymmetry has then to be disentangled from these contributions. The *cs* contribution is taken into account just by subtracting the number of *cs* events from the number of DIS candidates. The true asymmetry is:

$$
\begin{aligned}
A_{||}^{\text{true}} &= \frac{N_{\text{dis}}^{\leftrightarrows}\mathcal{L}^{\rightrightarrows} - N_{\text{dis}}^{\rightrightarrows}\mathcal{L}^{\leftrightarrows}}{N_{\text{dis}}^{\leftrightarrows}\mathcal{L}_p^{\rightrightarrows} + N_{\text{dis}}^{\rightrightarrows}\mathcal{L}_p^{\leftrightarrows}} \\
&= \frac{\left[N_{\text{cand}}^{\text{true}\leftrightarrows}(1-h_{\text{cand}}^{\leftrightarrows}) - N_{\text{cs}}^{\text{true}\leftrightarrows}(1-h_{\text{cs}}^{\leftrightarrows})\right]\mathcal{L}^{\rightrightarrows} - \left[N_{\text{cand}}^{\text{true}\rightrightarrows}(1-h_{\text{cand}}^{\rightrightarrows}) - N_{\text{cs}}^{\text{true}\rightrightarrows}(1-h_{\text{cs}}^{\rightrightarrows})\right]\mathcal{L}^{\leftrightarrows}}{\left[N_{\text{cand}}^{\text{true}\leftrightarrows}(1-h_{\text{cand}}^{\leftrightarrows}) - N_{\text{cs}}^{\text{true}\leftrightarrows}(1-h_{\text{cs}}^{\leftrightarrows})\right]\mathcal{L}^{\rightrightarrows} + \left[N_{\text{cand}}^{\text{true}\rightrightarrows}(1-h_{\text{cand}}^{\rightrightarrows}) - N_{\text{cs}}^{\text{true}\rightrightarrows}(1-h_{\text{cs}}^{\rightrightarrows})\right]\mathcal{L}^{\leftrightarrows}} \\
&= \frac{A_{||}^{\text{meas}} - A_{||}^{h_{\text{cand}}}\,\tilde{h}_{\text{cand}} + A_{||}^{h_{\text{cs}}}\,\tilde{h}_{\text{cs}}}{1 - \tilde{h}_{\text{cand}} + \tilde{h}_{\text{cs}}}\,,
\end{aligned}
\tag{3.76}
$$

where

$$
\tilde{h}_{\text{cand}} = \frac{N_{\text{cand}}^{\leftrightarrows}h_{\text{cand}}^{\leftrightarrows}\mathcal{L}^{\rightrightarrows} + N_{\text{cand}}^{\rightrightarrows}h_{\text{cand}}^{\rightrightarrows}\mathcal{L}^{\leftrightarrows}}{\left(N_{\text{cand}}^{\leftrightarrows}\mathcal{L}^{\rightrightarrows} + N_{\text{cand}}^{\rightrightarrows}\mathcal{L}^{\leftrightarrows}\right) - \left(N_{\text{cs}}^{\leftrightarrows}\mathcal{L}^{\rightrightarrows} + N_{\text{cs}}^{\rightrightarrows}\mathcal{L}^{\leftrightarrows}\right)} \tag{3.77}
$$

$$
\tilde{h}_{\text{cs}} = \frac{N_{\text{cs}}^{\leftrightarrows}h_{\text{cs}}^{\leftrightarrows}\mathcal{L}^{\rightrightarrows} + N_{\text{cs}}^{\rightrightarrows}h_{\text{cs}}^{\rightrightarrows}\mathcal{L}^{\leftrightarrows}}{\left(N_{\text{cand}}^{\leftrightarrows}\mathcal{L}^{\rightrightarrows} + N_{\text{cand}}^{\rightrightarrows}\mathcal{L}^{\leftrightarrows}\right) - \left(N_{\text{cs}}^{\leftrightarrows}\mathcal{L}^{\rightrightarrows} + N_{\text{cs}}^{\rightrightarrows}\mathcal{L}^{\leftrightarrows}\right)}\,. \tag{3.78}
$$

The effect of the hadronic contamination has been estimated ([40]) from the ratio of background-corrected to uncorrected values of $A_{||}^{d}/D$. The correction is very small, reaching a maximum value of 0.04% around x=0.01, and it is negligible for x >0.12.

3.11.5 Radiative corrections

In the extraction of g_1^d from the measured asymmetry, g_1^d has to be corrected for radiative processes. To extract the Born asymmetry from the measured results different sources of radiative effects must be taken into account.

Elastic and quasi-elastic background. The electron can exchange a photon with the nucleus or the nucleon, without breaking them, and these processes are referred to as elastic and quasi-elastic. These processes constitute a pure background to the DIS events and their cross sections simply have to be subtracted from the measured values. By definition

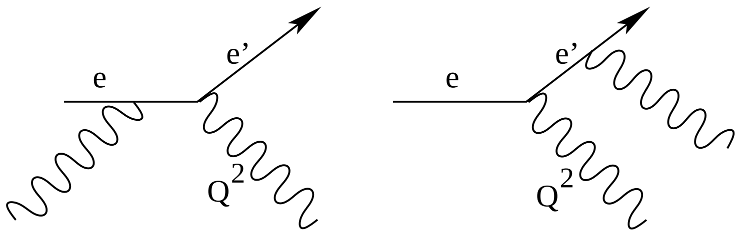

Figure 3.25: Initial state radiation (left), and final state radiation (right).Even if these events are DIS, their measured Q^2 and x are not the true ones, so an unfolding method is needed to bring back each event into the kinematic bin it belongs to.

the elastic peak is at $x = 1$, but also low Q^2 means elastic, since for low momentum transfer the nucleon does not break. Since in our experiment low Q^2 is also low x, then we have a high elastic and quasi-elastic contribution at low x, mostly in the first 10 kinematic bins. A way to get rid of the elastic tails in an almost clean way is to do *hadron tagging*, that is to require a hadron in the final state, associated to the event, to make sure that the event was pure DIS, thus not elastic. Problems arise in this procedure, since very often hadrons are not detected, due to the small acceptance of the detector: there is a loss up to 15-20% due to hadron tagging.

Radiation A DIS electron can radiate a photon before or after the DIS interaction (see Fig. 3.25), thus changing the measured kinematic quantities, such as Q^2 and x. Because $Q^2 = 4EE' \sin^2(\theta/2)$, regardless whether the initial E or the final E' energies are lower than measured, Q^2_{meas} will always be lower than Q^2_{true}. For x the situation is different: $x = 2EE' \sin^2(\theta/2)/(M(E - E'))$, so that the true value of x will be higher (lower) than the measured one if the photon is radiated after (before) the DIS interaction. The event is then placed into the wrong kinematic bin.

The Born asymmetry is usually extracted with a Monte Carlo simulation. A model asymmetry $A^{\text{model}}_{\text{Born}}$ obtained from a fit to world data is used as an input to the POLRAD ([41]) program, which computes the asymmetry corrected for radiative processes $A^{\text{model}}_{\text{corr}}$. Given $A^{\text{model}}_{\text{Born}}$, $A^{\text{model}}_{\text{corr}}$ and the measured asymmetry which in this context we can denote with $A^{\text{exp}}_{\text{corr}}$, the Born asymmetry is extracted with an ansatz, requiring that the difference between Born and corrected asymmetry is the same for model and experiment:

$$A^{\rm exp}_{\rm Born} = (A^{\rm model}_{\rm Born} - A^{\rm model}_{\rm corr}) + A^{\rm exp}_{\rm corr} \, . \tag{3.79}$$

As a consequence of this method the central values of the measured asymmetry are shifted, while the statistical errors are unchanged. It has been used before in HERMES publications such as Ref.[42].

A second commonly used ansatz ([43]) is that the ratio is constant:

$$A^{\rm exp}_{\rm Born} = \left(\frac{A^{\rm model}_{\rm Born}}{A^{\rm model}_{\rm corr}} \right) \cdot A^{\rm exp}_{\rm corr} \, , \tag{3.80}$$

which changes both central values and statistical errors. Usually an error is assessed to the extraction of the Born asymmetry by comparing the results of two methods. In the case of deuterium data the asymmetry is very small and consistent with zero in the small x region, where the corrections are higher, so that the multiplicative ansatz of Eq. (3.80) cannot be reliably used.

The Born asymmetry was actually obtained with a method already applied by SMC ([44]), by using the relation ([45]):

$$A^{\rm exp}_{\rm Born} = \frac{1}{\lambda} \left(A^{\rm exp}_{\rm corr} \left(\lambda + \frac{\sigma^{\rm unpol}_{\rm bg}}{\sigma^{\rm unpol}_{\rm DIS}} \right) - \frac{\sigma^{\rm pol}_{\rm bg}}{\sigma^{\rm unpol}_{\rm DIS}} \right) \, , \tag{3.81}$$

where $0.9 < \lambda < 1.2$ is a spin dependent term which contains the virtual photon corrections and soft real bremsstrahlung corrections, $\sigma^{\rm (un)pol}_{\rm bg}$ are the background (un)polarized tails and $\sigma^{\rm unpol}_{\rm DIS}$ the unpolarized DIS cross-sections. Corrections are large ($A_{\rm Born}/A_{\rm meas} \simeq 0.3$) in the low x region, decreasing rapidly, with a ratio of 0.9 around the 15th bin, and 1.0 around the 30th.

As a consistency check, the asymmetry using the hadron tagging method has also been calculated from data. The radiative corrections to the latter do not require the subtraction of elastic contributions so that they only need to be corrected for the DIS part. The agreement between the Born asymmetries obtained from full data and hadron-tagged was quite good and gave good confidence in the method. The final systematic error is obtained from the difference of the *additive* method of Eq. (3.79) and the *SMC-like* method. The error in g_1^d/F_1^d coming from the extraction method is as high as 0.013 in the lowest x bin, decreasing rapidly to 0.002 in the 8th bin, from which point it is negligible compared to the error coming from the target and beam polarizations.

3.11.6 Other sources of systematic uncertainties

In this section the other sources of systematic uncertainties will be discussed. The main detector uncertainties come from the target and beam polarizations, and from the normalization. The total systematic errors have been obtained from a sum in quadrature of the individual errors. They are dominated by radiative corrections at low x and by beam and target polarization in the high x region.

Polarizations. The target group estimated a target polarization error of 4% on 2000 data, and 8% on 1998 data, as a preliminary upper limit. The beam polarization uncertainty was estimated to be 3.4% in 1998 and 2% in 2000. The systematic uncertainties coming from beam and target polarization in 1998 were smoothed out with a simple polynomial fit to g_1/F_1 ($\sigma_{target}(g_1/F_1) = -0.03 + 1.01x - 0.49x^2$, with a $\chi^2 = 1.015$), since the data points had large fluctuations. This was not necessary for 2000 data.

Normalization. A wrong estimation of the luminosity brings a normalization problem in the asymmetry, and a way to estimate the error is by calculating the asymmetry with two different normalization methods. Beam current and fitted luminosity are two independently measured quantities, and the results using the two quantities in the asymmetry should agree since the two differ only by a multiplicative factor coming from the target density, a stable quantity.

Fig. 3.26 shows the difference between the asymmetry calculated with current and fitted luminosity, for top and bottom detectors: a very constant value, 0.0009, was found for 2000, but not for 1998. The difference can be explained with the different fitting procedure for the two years, and the different beam charge. It is interesting to see that the difference between the asymmetry calculated for the raw luminosity rate and the one obtained with the fitted luminosity is of the same order of magnitude as the Møller asymmetry.

The systematic error on g_1^d/F_1^d due to the normalization uncertainty was estimated as $\sigma_{norm} = (A_{||}(\texttt{LumiFitBstGai}) - A_{||}(\texttt{current}))/D(1+\gamma^2)$ which, for the case of 2000,

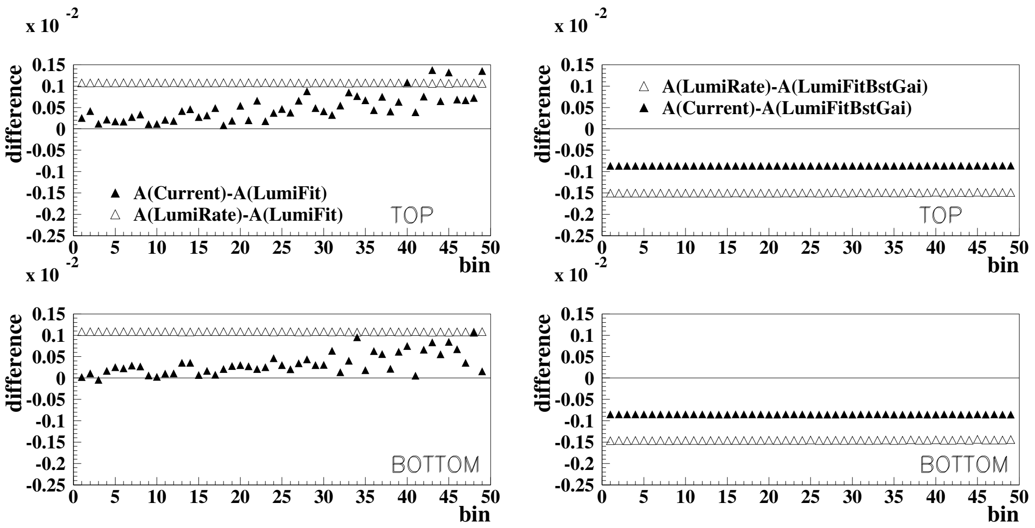

Figure 3.26: Comparison of different normalization methods for 1998 (left) and 2000 (right), for top and bottom detectors.

is $\sigma_{norm} = 0.0009/D(1+\gamma^2)$ (see Eq. (3.24)).

This error is believed to also take into account the TSF contribution to the luminosity in 1998 data. Since the current is not affected by the TSF, there is no need to consider another systematic contribution coming from the wrong evaluation of luminosity because of the TSF.

A proper evaluation of normalization and polarization uncertainties is very important because these quantities cause g_1 to be measured only up to a normalization factor. This issue will be addressed in next chapter, where how to correct for this problem when making fits to world data will be discussed.

Background. The contribution coming from the hadronic background was obtained through a fit of the ratio of g_1^d/F_1^d as a function of x with and without the hadronic contaminations. The fit slightly overestimated the error in order to include all the points. Details are in Ref.[40].

Parameterization of A_2. The common assumption that $g_2 = 0$ has been ruled out by the E155 experiment ([31]), as was shown in Fig. 3.3. The uncertainty coming from the knowledge of A_2 was estimated through the difference of a fit to A_2 data from E155 and

$A_2(\mathrm{g}_2 = \mathrm{g}_2^{WW})$, versus x. The E155 results were fitted to $A_2 = 0.22x/\sqrt{Q^2}$ in Ref.[40].

The $\mathrm{g}_1^d/\mathrm{F}_1^d$ parameterization used for the calculation of A_2^{WW} in Eq. (3.39) was ([46]):

$$\frac{\mathrm{g}_1^d}{\mathrm{F}_1^d} = (e^{-8.29x} - 1)(0.0324^{0.143} - x^{0.143}) \ . \tag{3.82}$$

Parameterization of $\mathbf{F}_2^d$. Available parameterizations for F_2^d are the eight ([24]) and the fifteen ([25]) parameter fits from NMC, which do not include more recent data from NMC ([47]) and E665 ([48]). F_2^d can also be obtained from the relation

$$\mathrm{F}_2^d = \frac{1}{2}\left(\frac{\mathrm{F}_2^n}{\mathrm{F}_2^p} + 1\right) \cdot \mathrm{F}_2^p \tag{3.83}$$

by using the available parameterizations of $\mathrm{F}_2^n/\mathrm{F}_2^p$ from NMC ([24]) and the ALLM F_2^p described in Refs. [49] and [50].

The agreement of these three possible parameterizations with the newer data from NMC and E665 was tested. Special care was taken for the agreement within the HERMES kinematic range. The P8 fit from NMC had large deviations from the data, so it was discarded ([51]). The other two fits agreed well with data. The fifteen parameter fit was used in this thesis for the extraction of g_1^d. The systematic error was estimated as 2.5% over the whole kinematic range, except the lowest x point, with 3%. This value comes from the quadratic combination of the normalization uncertainties of NMC and E665.

Fig. 3.27 shows the various contributions to the total systematic uncertainty coming from the different sources, separately for 1998 and 2000. Fig. 3.28 shows the final results for $\mathrm{g}_1^d/\mathrm{F}_1^d$ and $x\mathrm{g}_1^d$. Data from 2000 are clearly dominating the result over the 1998 dataset. The final combined result of the two years was obtained from the weighted average of the two. The systematic errors were also weighted with the statistical error to get the final systematic errors.

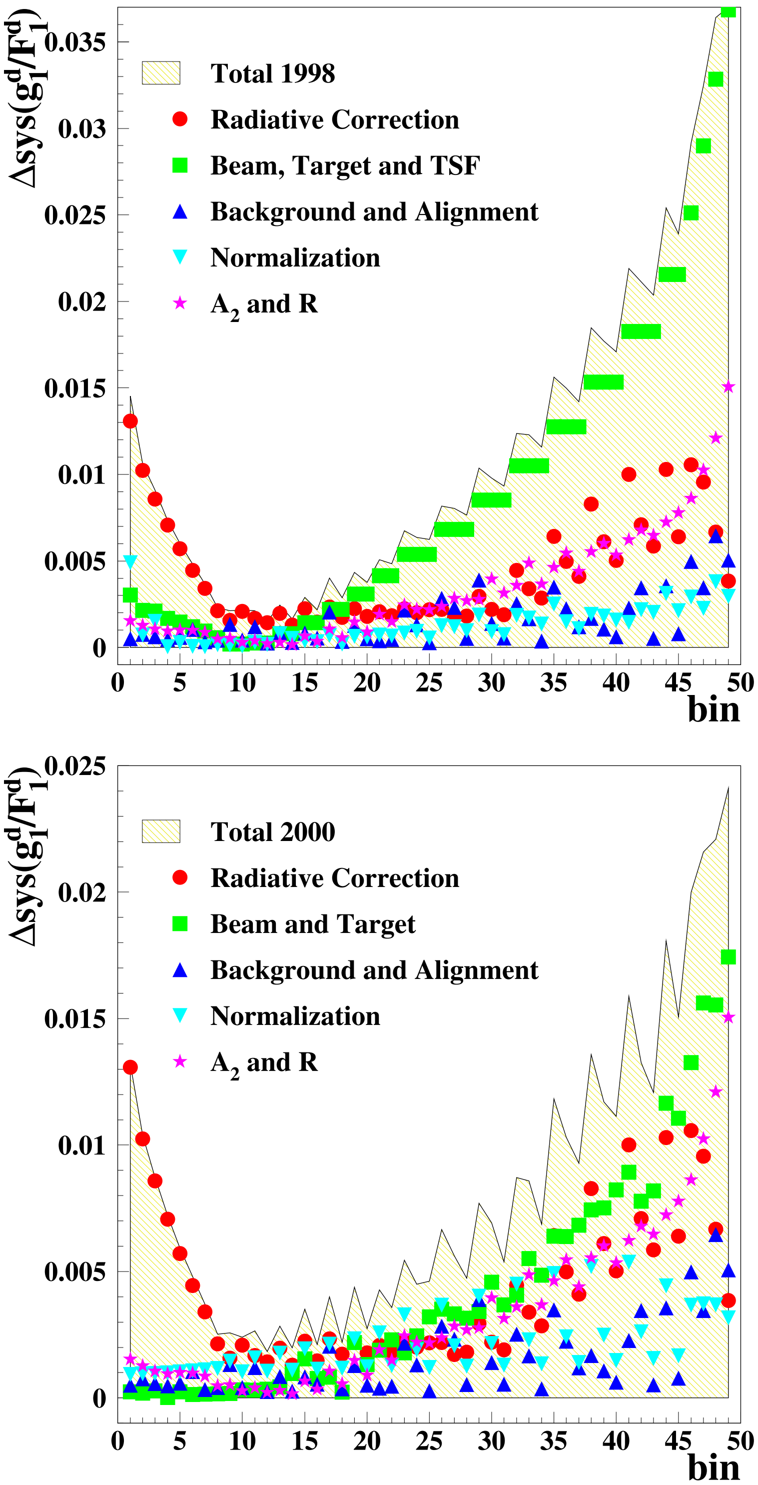

Figure 3.27: Systematic errors on g_1^d/F_1^d for 1998 and 2000, and their source.

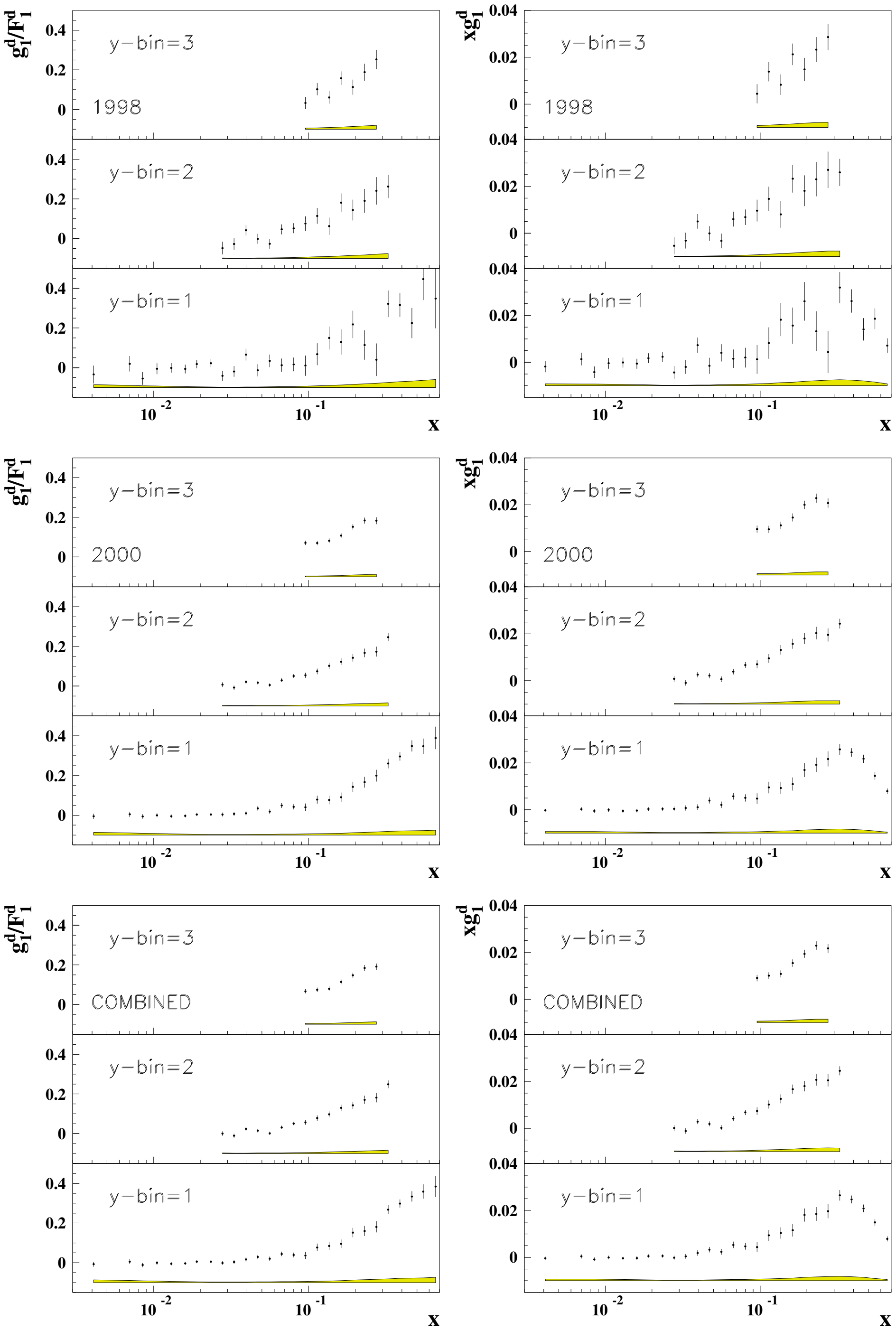

Figure 3.28: The extracted g_1^d/F_1^d (left) and xg_1^d (right) as a function of x for 1998 (top), 2000 (middle) and the combined results of 1998 and 2000 (bottom). The results are shown in bins of the y variable. The statistics of 2000 data dominate the final results. The errors on the data points are statistical, while the bands represent the systematic errors.

Chapter 4

Deep inelastic scattering

4.1 Operator Product Expansion

The Operator Product Expansion (OPE) ([52], [53]) was designed exclusively for the understanding of deep inelastic lepton-nucleon scattering and to describe the Q^2 behavior of the structure functions. It is a powerful tool for deriving sum rules (relations among the first moments of structure functions) in terms of very general quantum field theoretical considerations without the need for a specific hadronic model. Sum rules obtained from the OPE thus provide a direct test of QCD.

$W_{\mu\nu}$ is the Fourier transform of the nucleon matrix element of the commutator of electromagnetic currents $J(x)$:

$$W_{\mu\nu}(q,P,S) = \frac{1}{2\pi}\int d^4x e^{iq\cdot x}\,\langle PS|\,[J_\mu(x),J_\nu(x)]\,|PS\rangle\ , \tag{4.1}$$

where $|PS\rangle$ is the nucleon state with momentum P and spin S. The *forward Compton amplitude* is:

$$\begin{aligned} T_{\mu\nu}(q;P,S) &= i\int d^4x\ e^{iq\cdot x}\,\langle PS|\,\mathrm{T}(J_\mu(x),J_\nu(0))\,|PS\rangle \\ &= \langle PS|\,t_{\mu\nu}\,|PS\rangle\ , \end{aligned} \tag{4.2}$$

with

$$t_{\mu\nu} = i\int d^4x\ e^{iq\cdot x}\ \mathrm{T}(J_\mu(x),J_\nu(0))\ , \tag{4.3}$$

where T stands for the *time ordered product*. $W_{\mu\nu}$ and $T_{\mu\nu}$ can be split into two parts of definite symmetry (S,A), and it can be shown (from the optical theorem) that $W_{\mu\nu}$ can be related to $T_{\mu\nu}$ (see Fig. 4.1):

$$W_{\mu\nu}^{(S,A)} = \frac{1}{\pi}\mathrm{Im}\, T_{\mu\nu}^{(S,A)} \; . \tag{4.4}$$

$W_{\mu\nu}^{(S)}$ is independent of spin, so we can neglect it for our purposes, since we are interested in polarization effects.

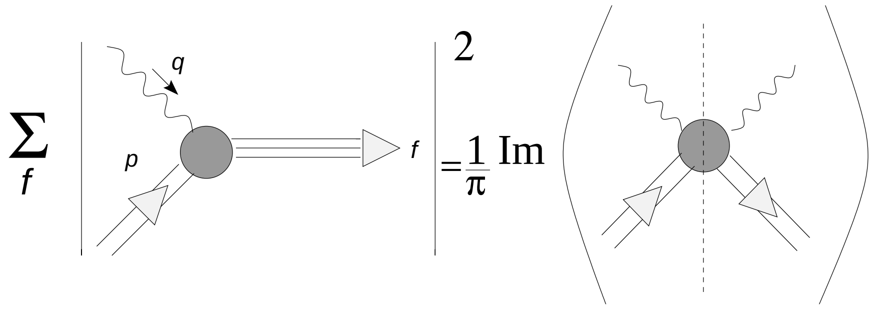

Figure 4.1: The optical theorem relates the Deep Inelastic Scattering process (left) to the Virtual Photon Compton Scattering (right).

Since the forward Compton amplitude is a matrix element of a product of currents (see Eq. (4.2)), an alternative method for calculating $W_{\mu\nu}$ is to expand this product as a series of local (dependent on the position) operators, and this can be achieved by using the optical theorem which relates $W_{\mu\nu}$ to $T_{\mu\nu}$. This method makes use of asymptotic freedom: the computation of the operator product coefficients will take place explicitly at a small distance of order $1/Q$, which allows the calculation of these coefficients in a perturbation theory whose coupling constant is $\alpha_s(Q^2)$.

Let us consider the *antisymmetric* part of the Fourier transform of the operator product appearing in Eq. (4.2). It is the Fourier transform of the product of two local operators in two close-by points x and 0. The main goal of the Operator Product Expansion is to expand $t_{\mu\nu}$ in terms of local operators $\mathcal{O}_i$.

Let us then consider the product of two local operators ([54])

$$\mathcal{O}_a(x)\mathcal{O}_b(0) \; . \tag{4.5}$$

In the limit $x \to 0$ they are evaluated practically in the same point. In this limit the operator product can be written as an expansion of local operators:

$$\lim_{x\to 0} \mathcal{O}_a(x)\mathcal{O}_b(0) = \sum_k c_k(x)\mathcal{O}_k(0) \tag{4.6}$$

where the dependence on x is now in the coefficient functions $c_k(x)$. The two sides in Eq. (4.6) are equivalent as long as one does not probe this relation at distance scales smaller than x. Because of asymptotic freedom, the coupling constant α_s is small at short distances; thus the coefficient functions can be computed as a perturbative expansion, since all non-perturbative effects occur at scales much larger than x, and do not affect the computation of the coefficient functions. The same reasoning is valid when one takes the Fourier transform to go to momentum space: by taking the limit $q \to \infty$, one forces $x \to 0$, so that the product can be expanded in local operators:

$$\lim_{q\to\infty} \int d^4x\; e^{iq\cdot x} \mathcal{O}_a(x)\mathcal{O}_b(0) = \sum_k c_k(q)\mathcal{O}_k(0)\ . \tag{4.7}$$

This expansion is valid for all matrix elements, provided that q is much larger than the characteristic momentum of any external state. In Eq. (4.3) the operators are currents, containing quark operators; at small distances the contribution of gluons will have to be considered, so that a general expansion will contain both quark and gluon operators, with arbitrary dimension d and spin n. Only the coefficient functions will be dependent on q and the operators will not depend on it. The fact that the operators $\mathcal{O}_k(0)$ are of spin n means that they will have n free indices $\mu_1 ... \mu_n$, so that the expansion (4.7) will look like:

$$\sum_k c_k(q)(\mathcal{O}_{d,n})_k^{\mu_1...\mu_n}\ . \tag{4.8}$$

The indices in the operators will come from the components of P alone, in the case of a vector operator, while there will be a helicity vector component, in the case of an axial operator. In the case under study, of $T_{\mu\nu}$, there are 2 free indices μ and ν, so the indices in the coefficient functions (components of q) and those in the operator $\mathcal{O}$ have to be contracted in such a way to leave 2 free indices μ and ν. This leaves the following possibilities for the dependencies on P^μ, q^μ, and S^μ in the case of vector (left column) and axial (right column) operators:

$$\begin{aligned}
&(q_\mu q_\nu\; q_{\mu_1}...q_{\mu_n})(P^{\mu_1}...P^{\mu_n})\ , && (q_\mu q_\nu\; q_{\mu_1}...q_{\mu_n})(S^{\mu_1}P^{\mu_2}...P^{\mu_n})\ ,\\
&(q_\mu\; q_{\mu_1}...q_{\mu_{n-1}})(P_\nu\; P^{\mu_1}...P^{\mu_n-1})\ , && (q_\mu\; q_{\mu_1}...q_{\mu_{n-1}})(P_\nu\; S^{\mu_1}P^{\mu_2}...P^{\mu_n-1})\ ,\\
&(q_{\mu_1}...q_{\mu_n-2})(P_\mu P_\nu\; P^{\mu_1}...P^{\mu_n-2})\ , && (q_{\mu_1}...q_{\mu_n-2})(P_\mu P_\nu\; S^{\mu_1}P^{\mu_2}...P^{\mu_n-2})\ .
\end{aligned}$$

	ψ	$G_{\mu\nu}$	D_μ	$D_\mu D^\mu$
d	3/2	2	1	2
n	1/2	1	1	0
t	1	1	0	2

Table 4.1: Twist t of some operators, given their dimension d and spin n.

For each case, in the left brackets there is the dependence of the coefficient functions on q^μ, while in the right brackets there is the dependence on P^μ and S^μ (the dependency on S^μ is present only in the axial operators).

One has then to evaluate Eq. (4.3) between two hadron states (see Eq. (4.2)). The expression in Eq. (4.3) has dimension 2, each hadron state has dimension -1, so that $T_{\mu\nu}$ has dimension 0. $T_{\mu\nu}$ is the product of the coefficient functions times the matrix elements of the operators $\mathcal{O}$:

$$T_{\mu\nu} \sim c_k \ < \mathcal{O} > \quad \rightarrow \quad \dim[T_{\mu\nu}] = \dim[c_k] + \dim[< \mathcal{O} >] = 0 \ . \tag{4.9}$$

The dimension of $< \mathcal{O} >$ must be $d-2$ (=dim[$\mathcal{O}$]-2dim[$|PS\rangle$]). Since in the DIS limit both $P \cdot q$ and $S \cdot q$ are of order Q^2, on dimensional grounds the Q^2 behavior of $< \mathcal{O} >$ must be

$$< \mathcal{O} > \sim M^{d-2-n} Q^n \ , \tag{4.10}$$

so that the dimension of the coefficient functions must be Q^{2-d}. The overall behavior of $T_{\mu\nu}$ has to be, then:

$$\begin{aligned} T_{\mu\nu} \sim Q^{2-d}\, Q^n M^{d-2-n} &= \left(\frac{Q}{M}\right)^{n+2-d} \\ &\sim Q^{2-t} \ , \end{aligned} \tag{4.11}$$

where we introduced the *twist* t as the difference between the dimension and the spin of an operator:

$$t = d - n = \text{dimension - spin} \ . \tag{4.12}$$

Table 4.1 shows the twist of four common operators (quark field ψ, gluon field $G_{\mu\nu}$, covariant derivative D_μ, and $D_\mu D^\mu$), given their spin and dimension.

The most important operators in the operator product expansion are those with lower twist, since those with higher twist will have a negligible contribution at high Q^2. Twist-2 operators contribute a finite amount in the DIS limit, twist-3 operators are suppressed by M/Q, etc. Any gauge invariant operator must contain at least two quark fields, or two gluon field tensors, together with any number of covariant derivatives, so the lowest possible twist is 2.

4.1.1 The expansion

It is important to note that the Operator Product Expansion approach can be used only because of the fully inclusive nature of DIS under consideration: $W_{\mu\nu}$ reduces to Eq. (4.1) as it is a sum over all possible final states X

$$W_{\mu\nu} \propto \sum_X \langle PS| J_\mu |X\rangle \langle X| J_\nu |PS\rangle . \tag{4.13}$$

The most general form of the expansion of the *antisymmetic* part of the Fourier transform of the operator product appearing in Eq. (4.2) is, in terms of twist 2 and 3 operators ([55]):

$$t_{\mu\nu} = i \int d^4x e^{iq\cdot x} \mathrm{T}(J_\mu(x), J_\nu(0)) = \tag{4.14}$$

$$= -i \sum_{n=1,3,5}^{\infty} \left(\frac{2}{Q^2}\right)^n q_{\mu_1}..q_{\mu_{n-2}} \sum_i \delta_i \left\{ \varepsilon_{\mu\nu\lambda\sigma} q^\lambda q_{\mu_{n-1}} E^n_{1,i}(Q^2,\alpha_s) \mathcal{O}^{\sigma\mu_1..\mu_{n-1}}_{1,i} + \right.$$
$$\left. + \left(\varepsilon_{\mu\rho\lambda\sigma} q_\nu q^\rho - \varepsilon_{\nu\rho\lambda\sigma} q_\mu q^\rho - q^2 \varepsilon_{\mu\nu\lambda\sigma}\right) \frac{n-1}{n} E^n_{2,i}(Q^2,\alpha_s) \mathcal{O}^{\lambda\sigma\mu_1..\mu_{n-2}}_{2,i} \right\}$$

where i identifies the possible operators: $i = 1,..,8,\psi,G$, and $E_{1,i}$, $E_{2,i}$ are the coefficient functions, also called *Wilson coefficients*.

The operators with $i = 1,..,8$ transform as SU(3) flavor octet (see App.A), while those with $i = \psi$ (quark operators) and $i = G$ (gluon operators) are flavor singlets. The operators of twist 2 and 3 are shown in Table 4.2. We will come back to the fact that gluon operators enter in the lower twist expansion.

4.1.2 Determination of the coefficient functions

The generic term in Eq. (4.3) can be written as the sum of quark $\mathcal{O}_Q$ and gluon $\mathcal{O}_G$ operators:

$$JJ \sim c_Q \mathcal{O}_Q + c_G \mathcal{O}_G , \tag{4.15}$$

so that the matrix element on a quark state $|Q\rangle$ is:

$$\langle Q| JJ |Q\rangle \sim c_Q \langle Q| \mathcal{O}_Q |Q\rangle + c_G \langle Q| \mathcal{O}_G |Q\rangle . \tag{4.16}$$

twist	i	operator	
2	1...8	$\mathcal{O}_{1,i}^{\sigma\mu_1..\mu_{n-1}} = (i)^{n-1}\left\{\bar{\psi}\gamma_5\gamma^\sigma D^{\mu_1}..D^{\mu_{n-1}}\left(\frac{\boldsymbol{\lambda}_i}{2}\right)\psi\right\}_{\mathrm{S}}$	$n \geq 1$
2	ψ	$\mathcal{O}_{1,\psi}^{\sigma\mu_1..\mu_{n-1}} = (i)^{n-1}\left\{\bar{\psi}\gamma_5\gamma^\sigma D^{\mu_1}..D^{\mu_{n-1}}\psi\right\}_{\mathrm{S}}$	$n \geq 1$
2	G	$\mathcal{O}_{1,G}^{\sigma\mu_1..\mu_{n-1}} = (i)^{n-1}\mathrm{Tr}\left\{\varepsilon^{\sigma\alpha\beta\gamma}G_{\beta\gamma}D^{\mu_1}..D^{\mu_{n-2}}G_\alpha^{\mu_{n-1}}\right\}_{\mathrm{S}}$	$n \geq 2$
3	1...8	$\mathcal{O}_{2,i}^{\lambda\sigma\mu_1..\mu_{n-2}} = (i)^{n-1}\left\{\bar{\psi}\gamma_5\gamma^\lambda D^\sigma D^{\mu_1}..D^{\mu_{n-2}}\left(\frac{\boldsymbol{\lambda}_i}{2}\right)\psi\right\}_{\mathrm{S}'}$	$n \geq 2$
3	ψ	$\mathcal{O}_{2,\psi}^{\lambda\sigma\mu_1..\mu_{n-2}} = (i)^{n-1}\left\{\bar{\psi}\gamma_5\gamma^\lambda D^\sigma D^{\mu_1}..D^{\mu_{n-2}}\psi\right\}_{\mathrm{S}'}$	$n \geq 2$
3	G	$\mathcal{O}_{2,G}^{\lambda\sigma\mu_1..\mu_{n-2}} = (i)^{n-1}\mathrm{Tr}\left\{\varepsilon^{\sigma\alpha\beta\gamma}G_{\beta\gamma}D^{\mu_1}..D^{\mu_{n-2}}G_\alpha^\lambda\right\}_{\mathrm{S}'}$	$n \geq 2$

Table 4.2: Lower twist operators. $\boldsymbol{\lambda}_i$ are the SU(3) matrices defined in App.A. S stands for symmetry over all indices, while S$'$ means symmetry over $\lambda\sigma$, and over $\mu_1..\mu_{n-2}$.

The electromagnetic current is a quark operator, so that the left hand side is of order α_s^0. The matrix element $\langle Q|\,\mathcal{O}_Q\,|Q\rangle$ is also of order α_s^0, while the term $\langle Q|\,\mathcal{O}_G\,|Q\rangle$ must be of order α_s^1 since there are at least two gluons in $\mathcal{O}_G$. Thus one can determine c_Q to leading order by taking the matrix element of both sides of the OPE, and by neglecting the contribution of gluon operators because it is suppressed by one power of α_s.

Scattering off a free quark ([54]). In the following we will suppose that there is only one quark flavor. The quark matrix element of the left hand side of the OPE in Eq. (4.15) is:

$$M^{\mu\nu} = i\, e_f^2\, \bar{u}_{p,s}\gamma^\mu i\frac{(\not{p}+\not{q})}{(q+p)^2}\gamma^\nu u_{p,s} + \text{crossed diagram } (\mu \leftrightarrow \nu, q \to -q)\,, \tag{4.17}$$

where e_f is the quark charge, p is the quark initial momentum, q is the photon four-momentum, $u_{p,s}$ is the Dirac spinor for the quark field, and $\bar{u}_{p,s} = u_{p,s}^\dagger\gamma^0$, $u_{p,s}^\dagger$ being the hermitian conjugate of $u_{p,s}$. The first term in Eq. (4.17) refers to the first diagram in Fig. 4.2, while the crossed diagram is the one on the right. Since the second diagram can be

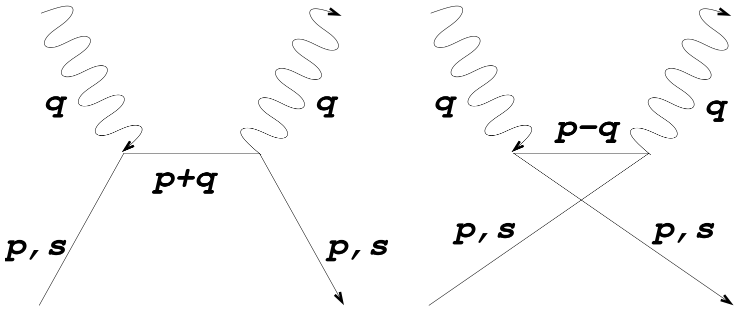

Figure 4.2: The lowest order diagrams contributing to the matrix element $M^{\mu\nu}$.

derived from the first one by replacing $\mu \leftrightarrow \nu$ and $q \to -q$, we will just concentrate on the first diagram. The expansion of the denominator gives (for on-shell massless quarks):

$$(p+q)^2 = 2p\cdot q + q^2 = q^2\left(1+\frac{2p\cdot q}{q^2}\right) = q^2(1-\omega)\ , \tag{4.18}$$

and $\omega = -2(p\cdot q)/q^2$. The numerator contains the product of 3 gamma-matrices, that can be simplified by using the identity:

$$\gamma^\mu\gamma^\alpha\gamma^\nu = g^{\mu\alpha}\gamma^\nu + g^{\nu\alpha}\gamma^\mu - g^{\mu\nu}\gamma^\alpha + i\varepsilon^{\mu\nu\alpha\lambda}\gamma_\lambda\gamma_5\ . \tag{4.19}$$

Also:

$$\not{p}u_{p,s} = 0\ ,\quad \bar{u}_{p,s}\gamma_\lambda u_{p,s} = 2p_\lambda\ ,\quad \bar{u}_{p,s}\gamma_\lambda\gamma^5 u_{p,s} = 2hp_\lambda\ , \tag{4.20}$$

where h is the quark helicity. So, by combining the various terms, and using the identity (valid for $\omega < 1$!) $(1-\omega)^{-1} = \sum \omega^n$, we get for the first diagram in Fig. 4.2:

$$M^{\mu\nu} = -\frac{2}{q^2}\,e_f^2\,\sum_{n=0}^{\infty}\omega^n[(p+q)^\mu p^\nu + (p+q)^\nu q^\mu - g^{\mu\nu}p\cdot q + ih\varepsilon^{\mu\nu\alpha\lambda}q_\alpha p_\lambda]\ . \tag{4.21}$$

Let us now just concentrate on the spin dependent part of Eq. (4.21), and let us add to it the cross diagram term of Eq. (4.17):

$$\begin{aligned}
M^{\mu\nu} &= -\frac{2}{q^2}\,e_f^2\,\sum_{n=0}^{\infty}\omega^n ih\varepsilon^{\mu\nu\alpha\lambda}q_\alpha p_\lambda + \text{crossed diagram } (\mu\leftrightarrow\nu, q\to -q, \omega\to-\omega)\\
&= -\frac{2}{q^2}\,e_f^2\,\sum_{n=0}^{\infty} ih\varepsilon^{\mu\nu\alpha\lambda}q_\alpha p_\lambda\omega^n\,(1+(-1)^n)\\
&= -\frac{4}{q^2}\,e_f^2\,\sum_{n=0,2,4}^{\infty}\left(\frac{2p\cdot q}{q^2}\right)^n ih\varepsilon^{\mu\nu\alpha\lambda}q_\alpha p_\lambda\\
&= \sum_{n=1,3,5}^{\infty} 2\left(\frac{2}{-q^2}\right)^n q^{\mu_2}...q^{\mu_n} ih\varepsilon^{\mu\nu\alpha\lambda}q_\alpha\, p_\lambda p_{\mu_2}...p_{\mu_n}\, e_f^2\ .
\end{aligned} \tag{4.22}$$

As previously stated, the coefficient functions depend only on q, while the matrix elements depend only on p. By equating the first term of Eq. (4.14) and Eq. (4.22) we determine the expression for the coefficient functions $E^n_{1,i}$:

$$\sum_i \delta_i E^n_{1,i} = e_f^2 \ . \tag{4.23}$$

Scattering off a nucleon ([54]). To compute $T^{\mu\nu}$ we need the hadronic matrix element of the OPE. These matrix elements are unfortunately unknown, so we need to parameterize them in terms of a known tensor structure times an unknown normalization coefficient a_n. Let us take the example of a spin 1/2 target. The matrix element of an axial vector on the target will be of the form:

$$\langle PS| \mathcal{O}_A^{\mu_1 \cdots \mu_n} |PS\rangle = a_n [S^{\mu_1} P^{\mu_2} ... P^{\mu_n}]_{\mathrm{S}} = a_n S^{\mu_1} P^{\mu_2} ... P^{\mu_n} + \text{higher twist terms}^* \tag{4.24}$$

where S indicates permutation over all indices. One then finds, following the same reasoning as in the free quark matrix case (see Eq. (4.22)):

$$\begin{aligned} T^{\mu\nu} &= \sum_{n=1,3,5}^{\infty} 2 \sum_i \delta_i \ E^n_{1,i} \ i \ \varepsilon^{\mu\nu\alpha\mu_1} \ q_\alpha \ \frac{2^n q^{\mu_2} ... q^{\mu_n}}{(-q^2)^n} \ a^i_n \ S_{\mu_1} P_{\mu_2} ... P_{\mu_n} \\ &= \sum_{n=1,3,5}^{\infty} 2 \sum_i \ \delta_i \ E^n_{1,i} \ i \ \varepsilon^{\mu\nu\alpha\mu_1} \ q_\alpha \ S_{\mu_1} \ a^i_n \ \omega^{n-1} \\ &= i \ \varepsilon^{\mu\nu\alpha\lambda} \ q_\alpha \ S_\lambda \ \frac{\tilde{\mathrm{g}}_1}{P \cdot q} \end{aligned} \tag{4.25}$$

with

$$\tilde{\mathrm{g}}_1 = \sum_{n=1,3,5}^{\infty} 2 \sum_i \delta_i E^n_{1,i} a^i_n \omega^n \tag{4.26}$$

where we used the definition $\omega = -2(P \cdot q)/q^2$. The quantity $\tilde{\mathrm{g}}_1$ is the Compton scattering analog of g_1 for DIS[†], and the OPE has allowed us to compute it as a power series in

[*] In reality the relation would be $[S^{\mu_1} P^{\mu_2} ... P^{\mu_n}]_{\mathrm{S}} = S^{\mu_1} P^{\mu_2} ... P^{\mu_n} + \mathcal{R}^{\mu_1 \cdots \mu_n}$. The tensor $\mathcal{R}$ has no symmetric part and has spin $n-1$, rather n. Thus its contribution is of higher twist, even though it came from the matrix element of a twist 2 operator.

[†] $T_{\mu\nu}$ has an expansion similar to $W_{\mu\nu}$:

$$\begin{aligned} T_{\mu\nu} &= \left(-g_{\mu\nu} + \frac{q_\mu q_\nu}{q^2}\right) \tilde{\mathrm{F}}_1 + \left(P_\mu - \frac{P \cdot q}{q^2} q_\mu\right) \left(P_\nu - \frac{P \cdot q}{q^2} q_\nu\right) \frac{\tilde{\mathrm{F}}_2}{P \cdot q} + \\ &+ \frac{i\tilde{\mathrm{g}}_1}{P \cdot q} \varepsilon_{\mu\nu\alpha\beta} \ q^\alpha S^\beta + \frac{i\tilde{\mathrm{g}}_2}{(P \cdot q)^2} \varepsilon_{\mu\nu\alpha\beta} \ q^\alpha \left(P \cdot q \ S^\beta - S \cdot q \ P^\beta\right) \ . \end{aligned} \tag{4.27}$$

ω about $\omega = 0$ in QCD. The nth term in the expansion is due to an operator of twist 2 and spin n. It is important to note that this expression was derived using the assumption that $|\omega| < 1$; however, the physical region is just the opposite:

$$\omega = 2\frac{P \cdot q}{Q^2} = \frac{1}{x} > 1 \; . \tag{4.28}$$

From the optical theorem it follows that the relation between $\tilde{g_1}$ and g_1 is:

$$\tilde{g}_1(\omega + i\varepsilon) - \tilde{g}_1(\omega - i\varepsilon) = 4\pi i \; g_1(\omega) \; . \tag{4.29}$$

The coefficient functions can be extracted with an integration on the ω plane, as shown

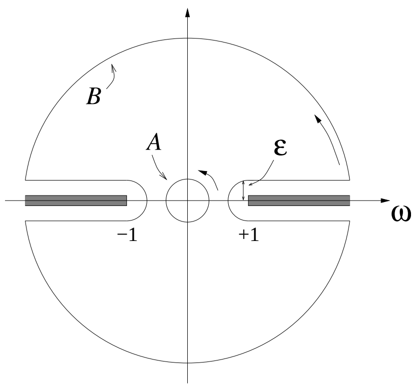

Figure 4.3: The ω plane.

in Fig. 4.3, with a contour of integration A with $|\omega| < 1$:

$$\frac{1}{2\pi i}\int_A \sum_{n=1,3,5}^{\infty} 2\sum_i \delta_i \; E^n_{1,i} \; a^i_n \; \omega^n \; \frac{1}{\omega^{k+1}} \; d\omega = \frac{1}{2\pi i}\int_A \tilde{g}_1 \; \frac{1}{\omega^{k+1}} \; d\omega \; , \tag{4.30}$$

from which it follows that:

$$2\sum_i \delta_i \; E^n_{1,i} \; a^i_n = \frac{1}{2\pi i}\int_{\mathcal{A}} \tilde{g}_1 \; \frac{1}{\omega^{n+1}} d\omega \; . \tag{4.31}$$

The contour A can be modified to a contour B that includes the physical region, by expanding that radius to infinity. Under the hypothesis that there is no contribution from the region at infinity we get the *momentum sum rule* for the odd momenta of g_1:

$$2\sum_i \delta_i E^n_{1,i} a^i_n \quad = \quad \frac{1}{2\pi i}\int_{\mathcal{B}} \tilde{g}_1 \frac{1}{\omega^{n+1}} d\omega$$

$$\begin{aligned}
&= \frac{1}{2\pi i}\left[\int_{-\infty}^{-1}\tilde{\mathrm{g}}_1(\omega+i\varepsilon)\frac{1}{\omega^{n+1}}d\omega - \int_{-\infty}^{-1}\tilde{\mathrm{g}}_1(\omega-i\varepsilon)\frac{1}{\omega^{n+1}}d\omega + \right.\\
&+ \left.\int_{1}^{\infty}\tilde{\mathrm{g}}_1(\omega+i\varepsilon)\frac{1}{\omega^{n+1}}d\omega - \int_{1}^{\infty}\tilde{\mathrm{g}}_1(\omega-i\varepsilon)\frac{1}{\omega^{n+1}}d\omega\right]\\
&= \frac{1}{2\pi i}\left[\int_{-\infty}^{-1}4\pi\, i\mathrm{g}_1(\omega)\frac{1}{\omega^{n+1}}d\omega + \int_{1}^{\infty}4\pi\, i\mathrm{g}_1(\omega)\frac{1}{\omega^{n+1}}d\omega\right]\\
&= 2\left(1-(-1)^{n+1}\right)\int_{1}^{\infty}4\pi i\,\mathrm{g}_1(\omega)\frac{1}{\omega^{n+1}}d\omega\\
&= 4\int_0^1 x^{n-1}\mathrm{g}_1(x)dx \qquad n \text{ odd}
\end{aligned} \tag{4.32}$$

where we used the fact that $\omega = 1/x$ and:

$$\mathrm{g}_1(-\omega) = -\mathrm{g}_1(\omega) \tag{4.33}$$

coming from its definition. The integral appearing in the last line of Eq. (4.32) is called the n-th moment of g_1. The momentum sum rules relate a quantity defined at high energy (such as g_1) to a low energy quantity, the zero momentum transfer matrix element of a local operator. In the same way, one can derive sum rules for the even moments of the unpolarized structure function F_1. For the other moments there are no sum rules, even if there have been many attempts to define some. The only questionable assumption in the derivation of the sum rules is that the contour at infinity (which means $x = 0$) gives no contribution. This contribution can be experimentally checked to be zero, and a confirmation of this hypothesis would come from the measurement of g_1 at small x. The sum rules become more convergent at higher moments, so any problem of convergence is in the lower moments.

4.2 Sum Rules

4.2.1 First moments

As previously discussed, the Operator Product Expansion gives results for the moments of the structure functions in terms of hadronic matrix elements of certain operators multiplied by perturbatively calculable coefficient functions. We are mainly focusing on g_1. The general expression for the moments of g_1 is given by Eq. (4.32):

$$\int_0^1 \mathrm{d}x\, x^{n-1}\mathrm{g}_1(x,Q^2) = \frac{1}{2}\sum_i \delta_i a_n^i E_{1,i}^n(Q^2,\alpha_s) \qquad n = 1,3,5,... \tag{4.34}$$

The presence of $E^n_{1,i}$ implies that only operators of spin n contribute to the n-th moment, which implies that in the case $n = 1$ only operators of spin 1 contribute. These operators, from Table 4.2 are the octet of quark SU(3)$_F$ axial-vector currents $J^j_{5\mu}$ (j=1,...,8) and the flavor singlet axial current $J^0_{5\mu}$:

$$
\begin{aligned}
J^j_{5\mu} &= \bar{\psi}\gamma_\mu\gamma_5\left(\frac{\boldsymbol{\lambda}_j}{2}\right)\psi \quad j = 1, ..., 8 && (4.35)\\
J^0_{5\mu} &= \bar{\psi}\gamma_\mu\gamma_5\psi \;, && (4.36)
\end{aligned}
$$

where the $\boldsymbol{\lambda}_j$ matrices are defined in App.A. The terms a^i_1 (which in the following we will refer to as a_i) are the matrix elements of the currents taken between nucleon states of definite momentum and spin direction[‡].

The forward matrix elements can only be proportional to the covariant spin vector $S_\mu(h)$ (corresponding to the definite helicity h), so that the conventional definition of a_i (see Eq. (4.24)) is:

$$
\begin{aligned}
\langle PS|\, J^j_{5\mu}\, |PS\rangle &= M a_j S_\mu \\
\langle PS|\, J^0_{5\mu}\, |PS\rangle &= 2M a_0 S_\mu \;, && (4.37)
\end{aligned}
$$

M being the nucleon's mass. The relative factor 2 in Eq. (4.37) reflects the fact that the SU(3) currents are defined using the generators of the group, i.e. $\boldsymbol{\lambda}_j/2$ in Eq. (4.35).

It is also possible to show([21]) that the matrix elements of the flavor axial currents on the nucleon are related to the polarized quark distributions:

$$
\langle PS|\, \bar{\psi}_f\gamma_\mu\gamma_5\psi_f\, |PS\rangle = 2MS_\mu \int_0^1 dx\; [\Delta q_f + \Delta\bar{q}_f] \;, \qquad (4.38)
$$

so that the coefficients appearing in the first moment of g_1 are actually sums of polarized distributions, and, in particular:

$$
\begin{aligned}
a_3 &= \int_0^1 dx[(\Delta u(x) + \Delta\bar{u}(x)) - (\Delta d(x) + \Delta\bar{d}(x))] \\
a_8 &= \frac{1}{\sqrt{3}}\int_0^1 dx[(\Delta u(x) + \Delta\bar{u}(x)) + (\Delta d(x) + \Delta\bar{d}(x)) - 2(\Delta s(x) + \Delta\bar{s}(x))] \\
a_0 &= \Delta\Sigma = \int_0^1 dx[(\Delta u(x) + \Delta\bar{u}(x)) + (\Delta d(x) + \Delta\bar{d}(x)) + (\Delta s(x) + \Delta\bar{s}(x))] \;.
\end{aligned}
\qquad (4.39)
$$

‡ $J^0_{5\mu}$ is sometimes defined as in (4.35) with $\boldsymbol{\lambda}_0/2 = (1/\sqrt{6})\hat{I}$, where $\hat{I}$ is the unit matrix.

The natural interpretation of a_0 is that it represents the total spin of the nucleon carried by the quarks, but it will be shown why this assumption cannot hold.

The first moment of g_1 (also known as Γ_1) can be expressed in terms of a_3, a_8 and a_0 as:

$$\Gamma_1^p = \int_0^1 dx\ g_1^p(x) = \frac{1}{12}\left[a_3 + \frac{1}{\sqrt{3}}a_8 + \frac{4}{3}a_0\right] . \tag{4.40}$$

Last relation implies that the coefficients δ_i are:

$$\delta_3 = \frac{1}{6}\ ,\ \ \delta_8 = \frac{1}{6\sqrt{3}}\ ,\ \ \delta_0 \equiv \delta_\psi = \delta_G = \frac{2}{9}\ , \tag{4.41}$$

and the others can be considered as equal to zero.

4.2.2 Information from β-decay

In hyperon β-decays the hadronic transitions can be described by matrix elements of the form $\langle B_i|\, j_+^\mu\, |B_k\rangle$ where j_+^μ is the charged hadronic current that couples to the W boson in the electroweak lagrangian, and B_i are the standard SU(3) labelling for the hyperons ([56]). Generally they are of the form of a Kobayashi-Maskawa matrix element multiplied by a combination of the vector J_μ^i and axial currents $J_{5\mu}^i$.

Under the general assumptions that the vector and axial currents transform as an octet under SU(3)$_F$ and are conserved and that the momentum transfer and the mass differences in the hadronic transitions are negligible, then all the hyperon β decays are described in terms of two constants F and D defined by the matrix elements:

$$\langle B_j; PS|\, J_{5\mu}^i\, |B_k; PS\rangle = 2M_B S_\mu(-if_{ijk}F + d_{ijk}D) \quad i,j,k = 1,...,8 \tag{4.42}$$

where f_{ijk} and d_{ijk} are the usual SU(3)$_F$ group constants, and they are in App.A.

These matrix elements are the same entering the first moment of g_1, so that they can be used as constraints in the extraction of a_0.

By using the standard SU(3) assignments for the baryon octet, one finds, from Eq. (4.42):

$$\begin{aligned} a_3 &= F + D \\ a_8 &= \frac{1}{\sqrt{3}}(3F - D)\ . \end{aligned} \tag{4.43}$$

Decay	Information
$n \to p$	$F + D$
$\Lambda \to p$	$F + \frac{1}{3}D$
$\Sigma^- \to n$	$F - D$
$\Sigma^\pm \to \Lambda$	$-\sqrt{\frac{2}{3}}D$
$\Xi^- \to \Lambda$	$F - \frac{1}{3}D$
$\Xi^- \to \Sigma^0$	$F + D$

Table 4.3: Combinations of constants F and D that enter into some hyperon β decays. They can be used as constraints on the integrals of quark distributions.

As previously discussed, Γ_1 is a linear combination of a_0, a_3 and a_8. The knowledge of a_3 and a_8 can then be used to get information on Γ_1. Table 4.3 shows the combinations of F and D that are obtained in some hyperon β decays.

4.2.3 The Spin Crisis

As we have shown, one can get information about the quantities a_3 and a_8 from the study of hyperon β-decays. By adding this information to the measurement of g_1 and of its first moment, it is then possible to measure a_0:

$$a_0 = \frac{3}{4}\left\{12\Gamma_1^p - a_3 - \frac{1}{\sqrt{3}}a_8\right\} = \Delta\Sigma \ . \tag{4.44}$$

There are inherent problems in this determination. Measuring the first moment of g_1 requires the measurement of g_1 over the entire x range, from 0 to 1. The region $x \to 1$ is quite harmless, as $\mathrm{g}_1 \to 0$ in this limit, but the region $x \to 0$ brings a great uncertainty in the result, since the error bars are very large and it is very difficult to make measurements in that region. This means that one can only rely on an extrapolation to the unmeasured region, and any result will then depend on the form of extrapolation used. The first experiment to measure Γ_1^p was EMC ([5],[57]), which got the quite astonishing result (see Fig. 4.4):

$$\Gamma_1^p = -.126 \pm 0.010 \pm 0.015 \quad \text{(EMC)} \ . \tag{4.45}$$

By using the values in Ref.[58] from hyperon β decay:

$$3F - D = 0.579 \pm 0.025 \ , \qquad F + D = 1.2573 \pm 0.0028 \ , \tag{4.46}$$

it was obtained:

$$a_0 \sim 0.046 \;, \tag{4.47}$$

which was interpreted as the quark spin content of the nucleon $\Delta\Sigma$, being very small and consistent with zero.

Of course to get this result they also had to use some information from unpolarized data experiments, as R from SLAC, and F_2 from NMC, for which there are now more precise measurements. But in any case, it was a striking result, since one would naively expect $a_0 \sim 1$, i.e. that the spin of the nucleon is carried mostly by the quarks, and the result they obtained was surprisingly small. Apart from the experimental accuracy, there are a few issues that should be taken into consideration when trying to understand the EMC results: the extrapolation to $x \to 0$ and higher twist effects.

4.2.4 Extrapolation to $x \to 0$

As already stated, any result on Γ_1^p will be very dependent on the assumptions of the behavior at small x of g_1, since it appears to rise to infinity as x approaches zero (it is to be noted that Fig. 4.4 shows $x g_1^p(x)$). An extrapolation is necessary to obtain the behavior in the unmeasured regions. The problem is that the literature is full of theoretical

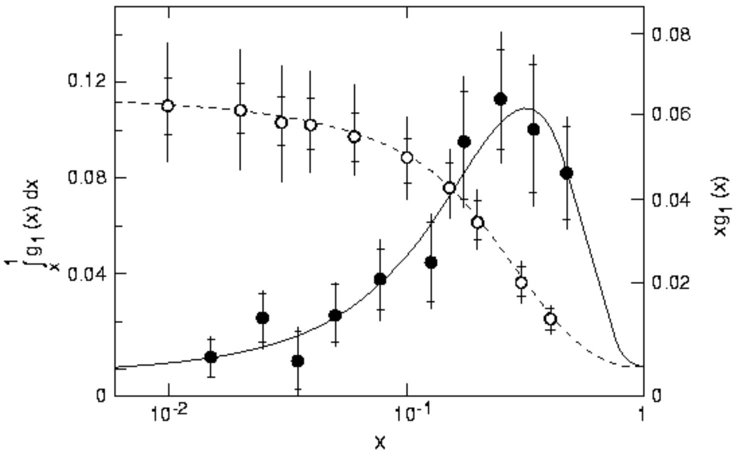

Figure 4.4: The extrapolation to low x done by EMC ([5]). Black points indicate the measured values of xg_1, while the open points are the values of the integral of g_1 from x=1 to the point.

predictions, that can be very different from each other and yield very different results.

Many experimental analyses ([59],[60]) assumed a nearly constant behavior and extrapolated to the unmeasured region from $x \simeq 10^{-2}$ to x=0.

A usual assumption is that of Regge behavior ([61],[62]):

$$g_1(x, Q_0^2) \to x^{-\alpha_{a_1}} \qquad -0.5 \lesssim \alpha_{a_1} \lesssim 0 \tag{4.48}$$

where α_{a_1} is the intercept of the degenerate $a_1(1260)$, $f_1(1285)$, $f_1(1420)$ trajectory. The scale Q_0^2 where the Regge behavior is supposed to start is left completely unrestricted by Regge arguments.

It has been shown ([63]) that a logarithmic rise at small x could be induced by a pomeron coupling via vector γ_μ:

$$g_1(x) \to \ln \frac{1}{x} \; . \tag{4.49}$$

In Ref. [64] a two-gluon pomeron model is analyzed, leading to a slightly more negative behavior:

$$g_1(x) \to 1 + 2 \ln x \; . \tag{4.50}$$

By applying negative parity pomeron cuts([65],[66],[67]), another divergent behavior is obtained:

$$g_1(x, Q_0^2) \to \frac{1}{x} \ln^2 x \; . \tag{4.51}$$

Different assumptions in the low x region can lead to very different results, and that is why more data are needed at lower x.

Also, for many fixed target experiments (including HERMES) the low x region also coincides with the low Q^2, which makes the interpretation of the results more difficult, because the contributions of higher twist effects are not negligible anymore, and have to be included in the analysis. The problem of higher twist was not present in the EMC data, because of the average Q^2 of 17.2 GeV^2, but it is certainly not negligible for $Q^2 \leq 1$ GeV^2 region, which includes the low x HERMES region.

4.2.5 The axial anomaly

Even if the extrapolation method may have brought some difference in the results obtained by EMC, thereby changing the total amount of spin carried by the quarks, another more profound effect was discovered later, casting a new light on the interpretation of the moments of g_1.

It was shown that it is natural to assume that a_0 is the quark content of the nucleon. As it turns out, the axial current $J^0_{5\mu}$ (of which a_0 is the matrix element on the nucleon state) is not conserved, and as such it has an intrinsic dependence on Q^2.

Returning to the first moment of g_1, it does not receive any direct gluonic contribution, since there is no gluonic operator of twist 2 and spin $n = 1$ (see Table 4.2). The gluon nevertheless gives a contribution to the integral, through the *axial anomaly* ([68],[69]) .

Let us consider the axial current

$$J^{0f}_{5\mu} = \bar{\psi}_f \gamma_\mu \gamma_5 \psi_f \tag{4.52}$$

for quarks of definite flavor f. From the Dirac equation of motion, its covariant derivative is:

$$D^\mu J^f_{5\mu} = 2im_q \bar{\psi}_f \gamma_5 \psi_f \ , \tag{4.53}$$

where m_q is the quark mass. In the chiral limit $m_q \to 0$ this current seems conserved. This cannot be the case, since this fact would lead to a symmetry between left and right-handed quarks, and so to a degeneracy in terms of the parity of the hadron spectrum: there would be for example, two protons, two neutrons... with two different parities. There is in fact an anomalous contribution to the covariant derivative, coming from the triangle diagram in Fig. 4.5:

$$D^\mu J^f_{5\mu} = \frac{\alpha_s}{2\pi} \mathrm{Tr}\left[G_{\mu\nu}\tilde{G}^{\mu\nu}\right] \ T\left(\frac{m_q^2}{k^2}\right) \ , \tag{4.54}$$

where the function $T(m_q^2/k^2)$ comes from the calculation of the triangle diagram, k being the gluon virtuality. The anomaly T is a quite complicated function, with the properties:

$$\begin{aligned} T\left(\frac{m_q^2}{k^2}\right) &\to 1 \qquad \text{for} \quad \left(\frac{m_q^2}{k^2}\right) \to 0 \\ T\left(\frac{m_q^2}{k^2}\right) &\to 0 \qquad \text{for} \quad \left(\frac{m_q^2}{k^2}\right) \to \infty \ . \end{aligned} \tag{4.55}$$

The anomaly introduces an interaction between quarks and gluons in the nucleon through the triangle diagram. As a consequence the matrix element of the axial current $J^0_{5\mu}$ will

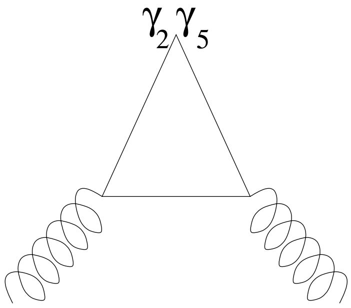

Figure 4.5: The anomalous contribution.

get contributions not only from the quarks but also from the gluons. Because the function T only contributes for massless quarks, the contribution that a_0 receives from the additional term is:

$$\begin{aligned} a_0^{gluons} &= -n_f \frac{\alpha_s}{2\pi} \int_0^1 dx \Delta G(x, Q^2) \\ &= -n_f \frac{\alpha_s}{2\pi} \Delta G(Q^2) \,, \end{aligned} \tag{4.56}$$

and the gluons contribute to the first moment of g_1 with the additional term:

$$\Gamma_{1,p}^{gluons} = -\frac{n_f}{9} \frac{\alpha_s}{2\pi} \Delta G(Q^2) \,, \tag{4.57}$$

where n_f is the number of active massless flavors.

Although the result in Eq. (4.57) was derived perturbatively, it is believed to be exact in QCD. The Naive Parton Model result for $a_0 = \Delta\Sigma$ is then incorrect, and it is, instead:

$$a_0 = \Delta\Sigma - n_f \frac{\alpha_s}{2\pi} \Delta G \,. \tag{4.58}$$

The last result is of fundamental importance, since it implies that the measurement of a small value for a_0 does not necessarily mean that $\Delta\Sigma$, the nucleon's spin contribution from the quark helicities, is small. Even if the gluon distribution is multiplied by α_s, it is not negligible in the high Q^2 limit, since it will be shown in Eq. (4.73) that it is a finite quantity over the whole Q^2 range.

Also, the result implies that the difference between $J_{5\mu}^0$ and the gluonic current K^μ that brings the axial anomaly is a conserved current. Its matrix element on a nucleon state is then a conserved quantity, which is:

$$\langle PS | \, J_{5\mu}^0 - K^\mu \, | PS \rangle = 2M \left(\Delta\Sigma - n_f \frac{\alpha_s}{2\pi} \Delta G + n_f \frac{\alpha_s}{2\pi} \Delta G \right) = 2M \; \Delta\Sigma \,, \tag{4.59}$$

which is the quark contribution to the spin of the nucleon.

4.2.6 Bjorken Sum Rule

The Bjorken sum rule gives predictions on the difference of the first moments of the structure functions g_1 on the proton and the neutron.

Let us recall Eq. (4.40) for the first moments. The perturbative expansion for $E_{1,i}$ is ([70]):

$$\begin{aligned} E^1_{1,3} = E^1_{1,8} = E_{NS} &= 1 - \frac{\alpha_s}{\pi} - 3.58\left(\frac{\alpha_s}{\pi}\right)^2 - 20.22\left(\frac{\alpha_s}{\pi}\right)^3 + ... \\ E^1_{1,0} = E_S &= 1 - 0.333\frac{\alpha_s}{\pi} - 1.10\left(\frac{\alpha_s}{\pi}\right)^2 + ... \,. \end{aligned} \tag{4.60}$$

where the non-singlet and singlet Wilson coefficients E_{NS} and E_S (that are equal to 1 to lowest order in α_s) were introduced. In the next section the reason for this nomenclature will become clear.

The first moment of the neutron structure function g_1^n can be obtained by isospin symmetry, by exchanging $u \leftrightarrow d$ in Γ_1^p:

$$\begin{aligned} \Gamma_1^p &= \int_0^1 dx\, g_1^p(x) = \frac{1}{12}\left[\left(a_3 + \frac{1}{\sqrt{3}}a_8\right)E_{NS}(Q^2) + \frac{4}{3}a_0 E_S(Q^2)\right] \\ \Gamma_1^n &= \int_0^1 dx\, g_1^n(x) = \frac{1}{12}\left[\left(-a_3 + \frac{1}{\sqrt{3}}a_8\right)E_{NS}(Q^2) + \frac{4}{3}a_0 E_S(Q^2)\right] \,. \end{aligned} \tag{4.61}$$

The terms a_0 and a_8 come from matrix elements of the operators $J^0_{5\mu}$ and $J^8_{5\mu}$, and are invariant under isotopic spin rotations (see App.A). The current $J^3_{5\mu}$, instead, changes sign when going from a proton to a neutron matrix element (that is interchanging u with d quarks). The Bjorken sum rule ([71]) follows:

$$\int_0^1 dx\left(g_1^p(x,Q^2) - g_1^n(x,Q^2)\right) = \frac{a_3}{6}E_{NS}(Q^2)\,. \tag{4.62}$$

This sum rule, derived using only current algebra and isospin symmetry ($\Delta u^p = \Delta d^n$), has very little model dependence, and is fundamental to QCD.

Another sum rule is the *Ellis-Jaffe* ([72]) sum rule, which involves the integral of g_1^p and g_1^n separately, and is derived under SU(3) assumptions and the hypothesis that the strange quark and sea polarizations are vanishing: $\Delta s = \Delta\bar{s} = \Delta\bar{q} = 0$. In Fig. 4.6 the current situation is shown. It is a plot of the neutron first moment Γ_1^n versus the first moment of the proton Γ_1^p. The predictions of the Bjorken and Ellis-Jaffe sum rules are shown in the diagonal band from lower left to upper right in the figure. The data and the Bjorken sum rule overlap within one sigma, while the Ellis-Jaffe sum rule predictions are roughly two sigma away from data, showing that the hypothesis of SU(3) and a vanishing sea polarization can be significantly violated.

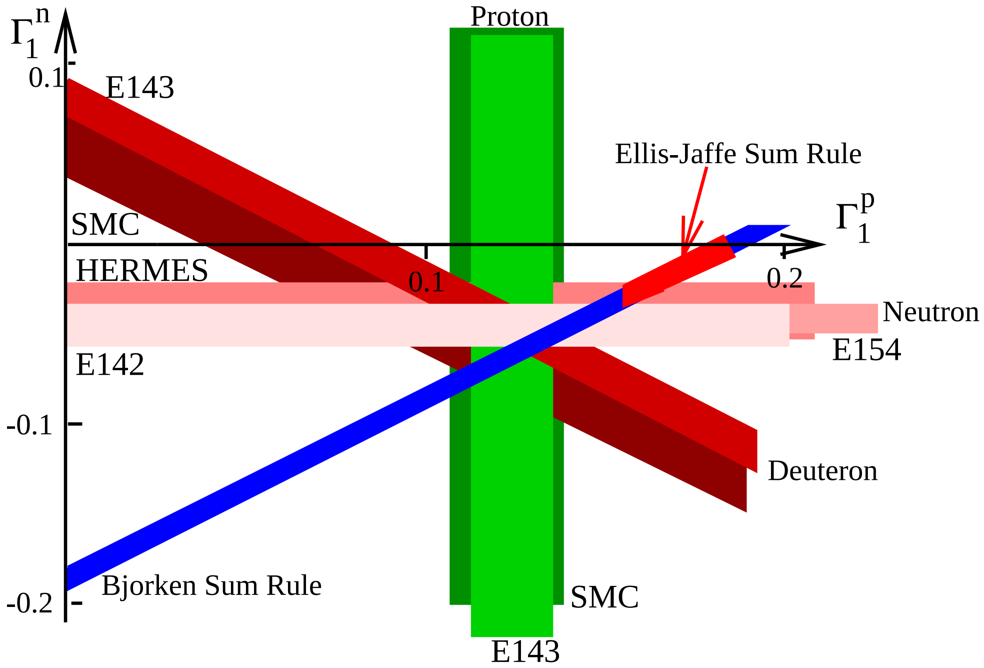

Figure 4.6: World data on the first moment of the neutron versus the first moment of the proton.

4.3 Q^2 evolution of parton distributions

Because g_1 depends on Δq_f, the idea of inverting it to obtain insight into the polarized distributions is very tempting. This can be done by considering the fact that QCD corrections bring a Q^2 dependence into the structure functions, not existing in the Naive Parton Model. Such a dependence is the result of the interaction among quarks and gluons, and by studying it, it is possible to extract not only the quark's contribution to the spin of the nucleon, but also the gluon's . In the remaining part of this chapter the framework for the derivation of the polarized distributions will be presented. This will prove useful when in the next chapter the distributions will be obtained using world data on g_1, including the precise new HERMES deuterium data.

4.3.1 Leading order corrections

The parton distributions and the structure functions are independent of Q^2 in the Naive Parton Model where only the $qq\gamma^*$ vertex of Fig. 4.7 enters into the theory.

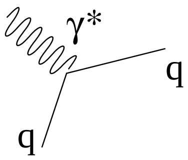

Figure 4.7: Zero order diagram in α_s:$\gamma^* q \to q$.

Beyond the 0th order in α_s the dynamical contribution given by the gluons has to be considered, and the parton distributions acquire a dependence on Q^2 §. As shown in Fig. 4.8, the processes that bring this dependence are *photon-gluon fusion* ($\gamma^* g \to q\bar{q}$) and *gluon radiation* ($\gamma^* q \to gq$).

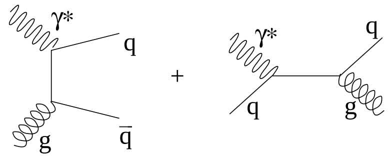

Figure 4.8: LO diagrams in α_s:$\gamma^* g \to q\bar{q}$ and $\gamma^* q \to gq$.

The Q^2 dependence of the parton distributions is described by the LO Q^2-evolution (or *renormalization group*) equations ([73]):

$$\begin{aligned} \frac{d}{dt}\Delta q_{NS}(x,Q^2) &= \frac{\alpha_s(Q^2)}{2\pi} P_{NS}^{(0)} \otimes \Delta q_{NS} \\ \frac{d}{dt}\begin{pmatrix} \Delta\Sigma(x,Q^2) \\ \Delta G(x,Q^2) \end{pmatrix} &= \frac{\alpha_s(Q^2)}{2\pi} \begin{pmatrix} P_{qq}^{(0)} & 2n_f P_{qG}^{(0)} \\ P_{Gq}^{(0)} & P_{GG}^{(0)} \end{pmatrix} \otimes \begin{pmatrix} \Delta\Sigma \\ \Delta G \end{pmatrix} \end{aligned} \tag{4.63}$$

where n_f is the number of active flavors, and

$$\alpha_s(Q^2) \sim \frac{4\pi}{\beta_0 \ln \frac{Q^2}{\Lambda^2}} \tag{4.64}$$

§In the following all processes that involve *one* gluon vertex will be referred to as *leading order* (LO) processes, while *next-to-leading order* (NLO) will refer to those involving *two* gluon vertices.

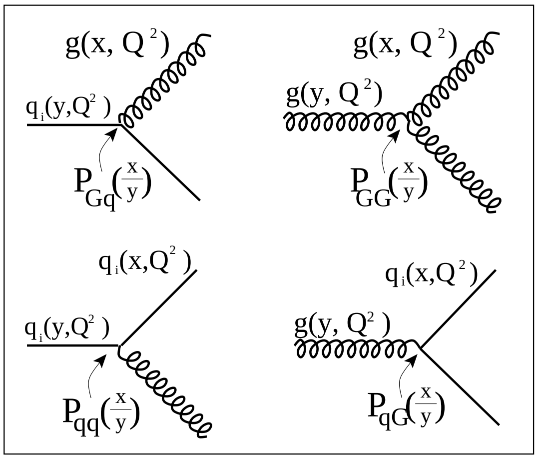

Figure 4.9: Splitting functions.

with $\beta_0 = 11 - 2n_f/3$, and $\Lambda \sim 0.2$ GeV is the energy scale above which the perturbative approach can be used to describe QCD effects (see App.B).

The *splitting functions* $P_{ab}(x/y)$ can be interpreted as the probability for a parton (quark or gluon) a of momentum y to radiate a parton b of momentum x, so that the initial parton's momentum is reduced by a fraction x/y (see Fig. 4.9). These functions can be expanded in α_s, so that only their LO expansion $P_{ab}^{(0)}$ enters into the LO evolution equations. Splitting functions at LO can be found in Ref.[20]. The convolution $\otimes$ is defined as:

$$(P \otimes q)(x, Q^2) = \int_x^1 \frac{dy}{y} P\left(\frac{x}{y}\right) q(y, Q^2)\ . \tag{4.65}$$

The *non-singlet* (NS) quark distributions are those particular combinations of quark distributions where the gluons and the quark sea cancel, and for this reason the evolution equations will not depend on the gluons:

$$\Delta q_{NS} = \Delta u - \Delta\bar{u}, \quad \Delta d - \Delta\bar{d}, \quad (\Delta u + \Delta\bar{u}) - (\Delta d + \Delta\bar{d}),$$
$$(\Delta u + \Delta\bar{u}) + (\Delta d + \Delta\bar{d}) - 2(\Delta s + \Delta\bar{s}), \quad \text{etc.} \tag{4.66}$$

The *singlet quark distribution* Σ is instead just

$$\Delta\Sigma = (\Delta u + \Delta\bar{u}) + (\Delta d + \Delta\bar{d}) + (\Delta s + \Delta\bar{s}), \tag{4.67}$$

which can be interpreted as the spin content of the nucleon coming from the quarks. It has to be noted that $\Delta\Sigma$ refers to the sum of all quark and antiquark flavors, and therefore there is a factor $2n_f$ in front of $P_{qG}^{(0)}$ in Eq. (4.63). By comparing Eqs.(4.66) and (4.67) with (4.39) we see that a_3 and a_8 are *non singlet* and a_0 is a *singlet* quark distribution.

The inclusion of these diagrams changes also the form of the quark (Δq_0) and gluon (ΔG_0) distributions:

$$\Delta q(x,Q^2) = \Delta q_0(x) + \frac{\alpha_s}{2\pi} t \left(\Delta q_0 \otimes P_{qq}^{(0)} + \Delta G_0 \otimes P_{qG}^{(0)} \right) \quad , \quad t = \ln\left(\frac{Q^2}{Q_0^2}\right) \tag{4.68}$$

where Δq_0 and ΔG_0 denote the unphysical (and unrenormalized) bare parton distributions, while Q_0 is a reference scale at which the distributions are known (from experiment or from theory).

$\mathcal{O}(\alpha_s)$ **corrections to g_1.** The leading order discussed so far originated from calculating the logarithmic $\mathcal{O}(\alpha_s)$ contributions of the processes $\gamma^* q \to gq$ and $\gamma^* g \to q\bar{q}$ (Fig. 4.8) to the zero-th order bare term $\gamma^* q \to q$ of Fig. 4.7 of g_1:

$$\begin{aligned} \mathrm{g}_1(x,Q^2) &= \frac{1}{2}\sum_{q,\bar{q}} e_q^2 \left\{ \Delta q_0(x) + \frac{\alpha_s}{2\pi}\, t\, \left[\Delta q_0 \otimes P_{qq}^{(0)} + \Delta G_0 \otimes P_{qG}^{(0)} \right] \right\} \\ &= \frac{1}{2}\sum_{q,\bar{q}} e_q^2 \Delta q(x,Q^2) \; . \end{aligned} \tag{4.69}$$

As before, $t = \ln(Q^2/Q_0^2)$. The LO approximation just results in the redefinition of the quark distributions, without changing the form of g_1: in leading order the gluon distribution does not contribute directly to the structure function $\mathrm{g}_1(x,Q^2)$, but only indirectly via the evolution equations.

LO Q^2 behavior of distributions. App.C shows that the formalism of the evolution equations applies also to the moments of the parton distributions, in what is called the *Mellin space* ([74]).

Quantities of great importance are the first moments ($n = 1$) of the polarized quark distributions, since they are used to derive sum rules that can be experimentally tested. The first moments of the splitting functions ([20]) are:

$$\begin{aligned} P_{NS}^{(0)1} = P_{qq}^{(0)1} &= 0 \\ P_{qG}^{(0)1} &= 0 \end{aligned}$$

$$\begin{aligned} P_{Gq}^{(0)1} &= 2 \\ P_{GG}^{(0)1} &= \frac{11}{2} - \frac{n_f}{3} = \frac{\beta_0}{2} \,. \end{aligned} \tag{4.70}$$

By using Eq. (C.3) in App.C we see that the non-singlet sector has no Q^2 dependence, since $P_{NS}^{(0)n} = 0$. In the singlet sector, instead, we have:

$$\frac{d}{dt}\begin{pmatrix} \Delta\Sigma(Q^2) \\ \Delta G(Q^2) \end{pmatrix} = \frac{\alpha_s(Q^2)}{2\pi}\begin{pmatrix} 0 & 0 \\ 2 & \frac{\beta_0}{2} \end{pmatrix}\begin{pmatrix} \Delta\Sigma(Q_0^2) \\ \Delta G(Q_0^2) \end{pmatrix} \,. \tag{4.71}$$

These equations imply trivially that also $\Delta\Sigma$ is Q^2 independent:

$$\frac{d}{dt}\Delta\Sigma(Q^2) = 0 + \mathcal{O}(\alpha_s^2) \,, \tag{4.72}$$

while they bring the interesting result (obtained by relating α_s to β_0 through Eq. (4.64)):

$$\frac{d}{dt}\left[\alpha_s(Q^2)\Delta G(Q^2)\right] = 0 + \mathcal{O}(\alpha_s^2) \,. \tag{4.73}$$

Therefore the product $\alpha_s(Q^2)\Delta G$ behaves more like an object of order α_s, although strictly speaking it refers to a combination that enters only in NLO, and any combination could be in principle potentially large, irrespective of the value of Q^2. From a theoretical point of view it's important to stress that the combination $\alpha_s(Q^2)\Delta G$ becomes Q^2 dependent at NLO, however for practical purposes the Q^2 dependence is too small to be able to distinguish $\Delta\Sigma$ and $\alpha_s(Q^2)\Delta G$ just by examining their Q^2 dependence.

4.3.2 Next to Leading Order corrections

In NLO, i.e. beyond the leading logarithmic order, more terms have to be included in the expression for g_1, in part coming from the contribution of the splitting functions $P_{ij}^{(1)}$, and in part from the $\ln Q^2$-independent terms and from the Wilson coefficients (the coefficient functions) that are usually introduced in the framework of the OPE. These quantities have the unpleasant feature that they depend on the regularization scheme adopted.

The NLO evolution equations are a generalization of the LO ones. The reason is that the splitting functions $P_{ij}^{(1)}$ have to allow transitions between quarks and antiquarks and among the different quark flavors, as illustrated in Fig. 4.11¶.

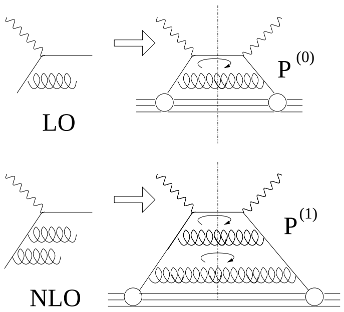

Figure 4.10: 1-loop and 2-loop splitting functions.

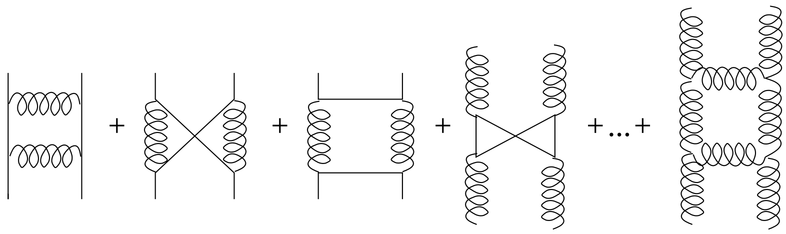

Figure 4.11: Diagrams relevant for the calculation of $P_{ij}^{(1)}$

The NLO evolution equations are ([75], [76]):

$$\begin{aligned}
\frac{d}{dt}\Delta q_{NS\pm}(x,Q^2) &= P_{NS\pm}\Delta q_{NS} \\
\frac{d}{dt}\begin{pmatrix} \Delta\Sigma(x,Q^2) \\ \Delta G(x,Q^2) \end{pmatrix} &= \begin{pmatrix} P_{qq} & 2n_f P_{qG} \\ P_{Gq} & P_{GG} \end{pmatrix} \otimes \begin{pmatrix} \Delta\Sigma(x,Q_0^2) \\ \Delta G(x,Q_0^2) \end{pmatrix} ,
\end{aligned} \tag{4.74}$$

where

$$\alpha_s(Q^2) \sim \frac{4\pi}{\beta_0 \ln\frac{Q^2}{\Lambda^2}}\left[1-\frac{\beta_1}{\beta_0^2}\frac{\ln\ln\frac{Q^2}{\Lambda^2}}{\ln\frac{Q^2}{\Lambda^2}}\right] , \qquad \beta_1 = 102-\frac{38n_f}{3} = 9 \text{ for } n_f = 3 , \tag{4.75}$$

and

$$P_{ij,NS\pm} = \frac{\alpha_s(Q^2)}{2\pi}P_{ij,NS}^{(0)} + \left(\frac{\alpha_s(Q^2)}{2\pi}\right)^2 P_{ij,NS\pm}^{(1)} . \tag{4.76}$$

In NLO, in contrast to LO, there are two independent NS evolution equations because of the additional transitions between different, non diagonal flavors ($u \to d$, $u \to s$,...) and $q\bar{q}$ mixings ($u \to \bar{u}$). Thus we have in $NS+$ the combinations $\Delta q - \Delta\bar{q}$ and in $NS-$

¶The splitting functions $P^{(0)}$ and $P^{(1)}$ are often referred to as 1-loop and 2-loop splitting functions. This comes from borrowing Wilson's and the OPE language, as can be seen in Fig. 4.10, where it appears clear how the Compton formalism helps in the calculation of these functions.

the combinations $\Delta q + \Delta\bar{q}$:

$$\Delta q_{NS+} = \Delta u - \Delta\bar{u},\;\; \Delta d - \Delta\bar{d}$$

$$\Delta q_{NS-} = (\Delta u + \Delta\bar{u}) - (\Delta d + \Delta\bar{d}),\;\; (\Delta u + \Delta\bar{u}) + (\Delta d + \Delta\bar{d}) - 2(\Delta s + \Delta\bar{s})\ .$$

NLO corrections to g_1. At NLO the splitting functions $P^{(1)}$ have to be included in the equations for the evolution of the regularized quark distributions. The same applies for the coefficient functions coming from the OPE, in the expression for g_1. These quantities depend on the regularization scheme adopted. Common choices are the dimensional regularization and the 't Hooft-Veltman prescription ([77]) for γ_5. In $D = 4 - 2\varepsilon$ dimensions (ε being a *small* parameter) one obtains ([78]):

$$\begin{aligned} &\mathrm{g}_1(x,Q^2) = \\ &\frac{1}{2}\sum_{q,\bar{q}} e_q^2 \left[\Delta q_0(x) + \frac{\alpha_s(Q^2)}{2\pi}\left(\ln\left(\frac{Q^2}{\mu^2}\right) - \frac{1}{\varepsilon} + \gamma_E - \ln 4\pi\right) \times \right. \\ &\left.\left(\Delta q_0 \otimes (P_{qq}^{(0)} + C_q) + \Delta G_0 \otimes (P_{qG}^{(0)} + C_G)\right)\right]\ , \end{aligned} \tag{4.77}$$

where γ_E is the Euler-Mascheroni constant ($\gamma_E \simeq 0.57721566...$) and the coefficient functions C_q and C_G are defined at the end of App.C. In order to get rid of the singularities one redefines the quark distributions:

$$\begin{aligned} \Delta q(x,Q^2) &= \Delta q_0(x) \\ &+ \frac{\alpha_s(Q^2)}{2\pi}\left(\ln\left(\frac{Q^2}{\mu^2}\right) - \frac{1}{\varepsilon} + \gamma_E - \ln 4\pi\right)\left(\Delta q_0 \otimes P_{qq}^{(0)} + \Delta G_0 \otimes P_{qG}^{(0)}\right)\ , \end{aligned} \tag{4.78}$$

and a similar expression holds for the redefined gluon distribution. The NLO contribution to g_1 is then:

$$\mathrm{g}_1(x,Q^2) = \frac{1}{2}\sum_{q,\bar{q}} e_q^2 \left[\Delta q + \frac{\alpha_s(Q^2)}{2\pi} C_q \otimes \Delta q(x,Q^2) + \frac{\alpha_s(Q^2)}{2\pi} 2C_G \otimes \Delta G(x,Q^2)\right]\ . \tag{4.79}$$

As we see, the splitting functions $P^{(1)}$ do not enter directly in the expression of g_1 at NLO, but they are implicit in the expression for ΔG and Δq since they evolve according to the NLO evolution equations.

In Fig. 4.12 is shown world data on the polarized structure function g_1^p. In this plot the Q^2 dependence appears quite clear, especially at low x. This can be understood by considering that the Q^2 dependence is an effect of gluons, and gluon emission from a quark reduces their initial momentum resulting in a lower x.

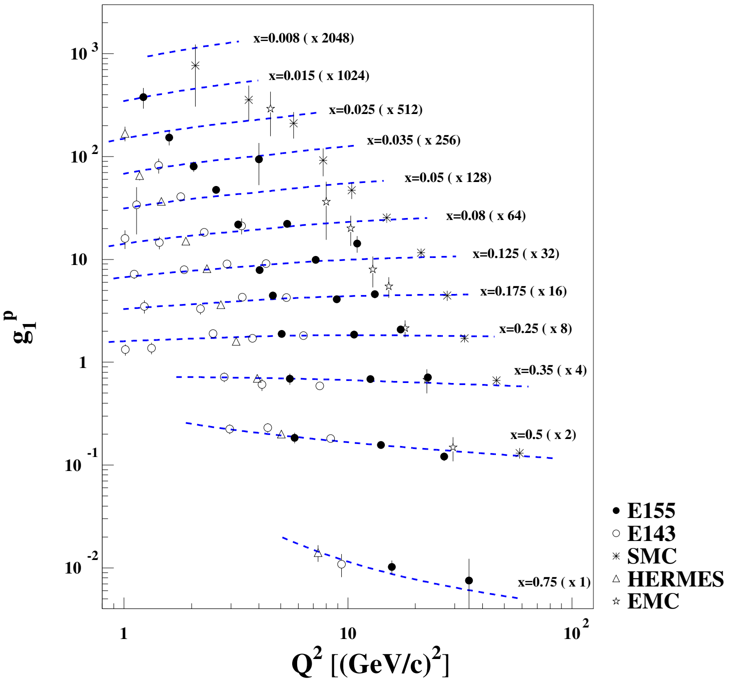

Figure 4.12: World data on g_1^p from the experiments E155 ([79]), E143 ([80]), SMC ([44]), HERMES ([43]) and EMC ([57]).

Scheme Convention. In any realistic analysis beyond LO, the Wilson coefficients $C_{q,G}$ and splitting functions are not uniquely determined so that it is a matter of convention how much of the NLO corrections to attribute to C_i and how much to $P_i^{(1)}$. This is usually referred to as *renormalization/factorization scheme convention* ([20]). The important concept is that, to a given perturbative order in α_s, *any physically directly measurable quantity (such as g_1) must be independent of the convention chosen* (scheme independence), and that the convention dependent terms appear only beyond this order, and are perturbatively small. App.C shows how Wilson coefficients and splitting functions can be simultaneously redefined and thus leave the measurable quantity g_1 unchanged.

So, although the parton distributions have no scheme dependence in LO, they do depend on the renormalization scheme in NLO and beyond. In the unpolarized case the most commonly used is the *modified minimal subtraction* $\overline{MS}$. Schemes and parton densities differ from each other by terms of order $\alpha_s(Q^2)$, going to zero as Q^2 increases. In the polarized case there are two significant differences.

First, the singlet densities $\Delta\Sigma(x, Q^2)$ in two different schemes will differ by terms of the order

$$\alpha_s(Q^2)\Delta G(x, Q^2) \ , \tag{4.80}$$

which appears to be of order α_s. But we saw that the first moment $\Delta G(Q^2)$ grows as $1/\alpha_s(Q^2)$, so that the difference of $\Delta\Sigma$ in two different schemes could be potentially large.

Second, there are ambiguities in handling the renormalization of operators involving γ_5 in n dimensions, so that the specification $\overline{MS}$ does not define a unique scheme. There is actually a whole family of $\overline{MS}$ schemes, and strictly speaking each should carry a label indicating how γ_5 is treated. The scheme conventionally known as $\overline{MS}$ ([75], [81]) has the feature that the nonsinglet densities are conserved, i.e. they are independent of Q^2, corresponding to the conservation of the axial current. The first moment of $\Delta\Sigma$ instead, is not conserved, so that it is difficult to know how to compare the DIS experimental results on $\Delta\Sigma$, with results from constituent quark models, at low Q^2. To avoid these problems the AB scheme ([82], [83]) was introduced. It involves a modification of the $\overline{MS}$ scheme:

$$\begin{aligned} \Delta\Sigma(x, Q^2)_{AB} &= \Delta\Sigma(x, Q^2)_{\overline{MS}} + n_f \frac{\alpha_s(Q^2)}{2\pi} \int_x^1 \frac{dy}{y} \Delta G(y, Q^2)_{\overline{MS}} \\ \Delta G(x, Q^2)_{AB} &= \Delta G(x, Q^2)_{\overline{MS}} \ , \end{aligned} \tag{4.81}$$

or, in the Mellin momentum space:

$$\Delta\Sigma(Q^2)_{AB} = \Delta\Sigma(Q^2)_{\overline{MS}} + n_f \frac{\alpha_s(Q^2)}{2\pi} \Delta G(Q^2)_{\overline{MS}} \ . \tag{4.82}$$

In the AB scheme $\Delta\Sigma$ is independent of Q^2 at all orders. The singlet part of the first moment of g_1 then depends on $\Delta\Sigma$ and ΔG only in the combination

$$a_0(Q^2) = \Delta\Sigma(Q^2)_{\overline{MS}} = \Delta\Sigma(Q^2)_{AB} - n_f \frac{\alpha_s(Q^2)}{2\pi} \Delta G(Q^2) \ , \tag{4.83}$$

and the unexpected small value found by the EMC experiment can be nicely explained by a cancellation between $\Delta\Sigma$ and the contribution of gluons. For this explanation to be correct it is important to have both a positive sign and a large value for the first moment of the polarized gluon distribution at small $Q^2 \sim 1 - 10\mathrm{GeV}^2$.

Chapter 5

Extraction of polarized parton distributions

5.1 Introduction

In 1998 the SMC collaboration performed a next-to-leading order analysis ([84]) of the spin structure function g_1, including data from CERN, SLAC, DESY and the SMC final set of data of g_1 at low x. The SMC collaboration used two analysis codes, one of which was calculating the distribution functions in Mellin space and the other was instead using finite differences to solve the Q^2 evolution differential equations.

This chapter shows results for a similar analysis carried out with the finite differences program used by the SMC collaboration. Some improvements have been made to the original SMC analysis code, from minor changes such as updates of constants and the correction of a missing term in the α_s routine, to major changes that allow to calculate in an automatic way the statistical error bands to the obtained fits to distribution functions and structure functions.

The structure of the code has been described at length in Refs. [85] and [86].

5.2 Experimental Data

Table 5.1 shows the experiments that performed measurements on polarized structure functions. Also shown are the x and Q^2 region they access. The fourth column is the normalization uncertainty quoted by each experiment, which gives the uncertainty related to luminosity as well as target and beam polarization measurements. For each target type

Experiment	x range	Q^2 (GeV^2)	Norm.(%)	type	# p	# d	# n
E142[59]	0.035 - 0.466	1.10 - 5.50	3.0	g_1	-	-	8
				g_1/F_1	-	-	-
				A_1	-	-	28
E143 [93]	0.031 - 0.749	1.27 - 9.52	3.7	g_1	28	28	-
				g_1/F_1	82	82	-
				A_1	-	-	-
E154	0.017 - 0.564	1.20 - 15.0	3.0	g_1	-	-	17[94]
				g_1/F_1	-	-	-
				A_1	-	-	11[95]
E155	0.015 - 0.750	1.22 - 34.73	7.6	g_1	-	24[96]	-
				g_1/F_1	24[79]	24[96]	-
				A_1	-	-	-
HERMES	0.028 - 0.660	1.13 - 7.46	3.0	g_1	39[43]	39	9[42]
				g_1/F_1	39[43]	39	-
				A_1	-	-	9
SMC [44]	0.005 - 0.480	1.30 - 58.0	4.0	g_1	12	12	-
				g_1/F_1	-	-	-
				A_1	10	65	-
EMC [57]	0.015 - 0.466	3.5 - 29.5	9.6	g_1	10	-	-
				g_1/F_1	-	-	-
				A_1	10	-	-
Total				g_1	89	103	34
				g_1/F_1	145	145	-
				A_1	20	65	48

Table 5.1: World data on g_1, g_1/F_1, A_1. For each experiment the x and Q^2 ranges are reported, together with the normalization uncertainty, the type of quantity measured, and the number of data points for each given target. The HERMES deuterium data points are only 39 because the 1 GeV^2 Q^2 cut removed the first 10 low x points. Square brackets indicate the published article. The table only includes data obtained directly on the given target (if for example, g_1^n was obtained from g_1^p and g_1^d then it is not included in this table). Also, data published exclusively at a lower x and Q^2, like in Ref. [97], are not included in the table, since none of those points is included in the fits.

the quantity reported in the paper is shown (g_1, g_1/F_1 or A_1), together with a reference to the publication and the number of data points.

The quantity most closely related to the measured asymmetry was considered in the evolution. This means that if an experiment quoted values for g_1/F_1 and g_1, g_1/F_1 was preferred to the values on g_1. The reason is that each experiment could have different assumptions on R or F_1 or A_2, so where possible an attempt was made to use the same assumptions on the unpolarized quantities R and F_1, and on A_2. In this way a total of 473 data points was obtained.

It is generally believed that higher twist effects are certainly non negligible anymore below $Q^2 = 1$ GeV^2, so a cut is placed and data are not accepted below 1 GeV^2. In unpolarized analyses, where the amount of data is much larger, cuts are usually placed at around 4 GeV^2, but polarized experiments have much lower Q^2 values, so such a cut would decrease the number of data points significantly.

5.3 Description of the code

The main theory ideas treated in ch.4 will be briefly summarized, and the main features of the code explained.

The structure function g_1 has a dependence on x and Q^2, the latter acquired by diagrams involving gluons. It can be expressed as a convolution of the distributions with coefficient functions $C(x, Q^2)$ ([78]):

$$\begin{aligned} g_1^{p,n}(x,Q^2) &= \frac{1}{2} < e^2 > \int_x^1 \frac{dy}{y} \left[C_\Sigma \left(\frac{x}{y}, \alpha_S(Q^2) \right) \Delta\Sigma(y,Q^2) \right. \\ &+ \left. 2n_f C_G \left(\frac{x}{y}, \alpha_S(Q^2) \right) \Delta G(y,Q^2) + C_{NS}^{p,n} \left(\frac{x}{y}, \alpha_S(Q^2) \right) \Delta q_{NS}^{p,n}(y,Q^2) \right] \\ g_1^d(x,Q^2) &= \frac{1}{2} \left(1 - \frac{3}{2}\omega_D \right) \left(g_1^p(x,Q^2) + g_1^n(x,Q^2) \right) , \end{aligned} \tag{5.1}$$

where $\omega_D = 0.058$ is the D-state wave probability for the deuteron.

The distributions $\Delta\Sigma$ and $\Delta q_{NS}^{p,n}$ are defined as:

$$\begin{aligned} \Delta\Sigma &= (\Delta u + \Delta\bar{u}) + (\Delta d + \Delta\bar{d}) + (\Delta s + \Delta\bar{s}) \\ \Delta q_{NS}^p &= \frac{1}{2} \left(2(\Delta u + \Delta\bar{u}) - (\Delta d + \Delta\bar{d}) - (\Delta s + \Delta\bar{s}) \right) \\ \Delta q_{NS}^n &= \frac{1}{2} \left(2(\Delta d + \Delta\bar{d}) - (\Delta u + \Delta\bar{u}) - (\Delta s + \Delta\bar{s}) \right) . \end{aligned} \tag{5.2}$$

The difference between g_1^p and g_1^n is in the non-singlet distributions, which differ only for the exchange of $u \leftrightarrow d$.

Given measurements of $g_1^{p,n,d}$ at different Q^2 values, the distributions ΔG, $\Delta\Sigma$ and $\Delta q_{NS}^{p,n}$ can be singled out by making use of their different Q^2 evolution:

$$\begin{aligned} \frac{d}{dt}\Delta\Sigma(x,t) &= \frac{\alpha_s}{2\pi} \int_x^1 \frac{dy}{y} \left[P_{\Sigma\Sigma} \left(\frac{x}{y}, \alpha_S(t) \right) \Delta\Sigma(y,t) + 2n_f P_{\Sigma G} \left(\frac{x}{y}, \alpha_S(t) \right) \Delta G(y,t) \right] \\ \frac{d}{dt}\Delta G(x,t) &= \frac{\alpha_s}{2\pi} \int_x^1 \frac{dy}{y} \left[P_{G\Sigma} \left(\frac{x}{y}, \alpha_S(t) \right) \Delta\Sigma(y,t) + P_{GG} \left(\frac{x}{y}, \alpha_S(t) \right) \Delta G(y,t) \right] \end{aligned}$$

$$\frac{d}{dt}\Delta q_{NS}^{p,n}(x,t) = \frac{\alpha_s}{2\pi}\int_x^1 \frac{dy}{y} P_{NS}^{p,n}\left(\frac{x}{y}, \alpha_S(t)\right) \Delta q_{NS}^{p,n}(y,t) \ . \tag{5.3}$$

The non-singlet distributions evolve independently from ΔG since the gluon contributions cancel in the differences of Eq. (5.2).

The polarized splitting functions at NLO have been calculated in Refs. [75] and [76] in the $\overline{MS}$ scheme that is going to be used.

5.3.1 Initial parameterization

The distributions are parameterized at an initial $Q^2 = Q_0^2$. They have to be general enough to describe the data, and they have to contain a low number of parameters, so that the available data may well constrain the parameters. A common choice ([84], [87]) consists in a parameterization borrowed from the unpolarized fits ([88]) of the kind:

$$\Delta f(x, Q_0^2) = N_f(\alpha_f, \beta_f, \gamma_f, \eta_f, \rho_f)\, x^{\alpha_f}\, (1-x)^{\beta_f}\, (1 + \gamma_f x + \rho_f x^{\frac{1}{2}})\ \eta_f \ , \tag{5.4}$$

where Δf denotes $\Delta\Sigma$, Δq_{NS}^p, Δq_{NS}^n or ΔG. The parameter α_f describes the low x behavior of the distribution, while β_f describes the high x behavior. The coefficients γ_f and ρ_f instead describe the intermediate x region.

The coefficients N_f are chosen to satisfy the relation:

$$N_f(\alpha_f, \beta_f, \gamma_f, \eta_f, \rho_f) \int_0^1 dx\, x^{\alpha_f} (1-x)^{\beta_f} (1 + \gamma_f x + \rho_f x^{\frac{1}{2}}) = 1 \ , \tag{5.5}$$

so that η_f is the first moment of the distribution at the starting scale:

$$\eta_f = \int dx\, \Delta f(x, Q_0^2) \ . \tag{5.6}$$

This implies that N_f is the expression:

$$N_f^{-1} = \left(1 + \gamma_f \frac{\alpha_f + 1}{\alpha_f + \beta_f + 2}\right) \frac{\Gamma(\alpha_f+1)\Gamma(\beta_f+1)}{\Gamma(\alpha_f+\beta_f+2)} + \rho_f \frac{\Gamma\left(\alpha_f + \frac{3}{2}\right)\Gamma(\beta_f+1)}{\Gamma\left(\alpha_f + \beta_f + \frac{5}{2}\right)} \ . \tag{5.7}$$

5.3.2 Minimization

These parameterizations are then numerically evolved to the measured Q^2 of the data using the evolution equations. The free parameters are evaluated by minimizing the χ^2, defined as a sum over the N data points:

$$\chi^2 = \sum_{i=1}^{N} \frac{\left[\mathrm{g}_1^{\mathrm{calc}}(x,t) - \mathrm{g}_1^{\mathrm{data}}(x,t)\right]^2}{\left[\sigma_{\mathrm{data}}(x,t)\right]^2} \tag{5.8}$$

and the errors σ_{data} are only statistical. The minimization is performed by the MINUIT program, described in Ref.[89].

5.4 Evaluation of best parameters

The distributions described in Eq. (5.4) have as many as 16 parameters, but some of them can be fixed by symmetry considerations.

The normalizations of the non-singlet distributions can be fixed imposing SU(3) symmetry. The proton and neutron NS distributions are related to the combinations of parton distributions a_3 and a_8 by the relation (independent of Q^2):

$$\Delta q_{NS}^{p,n} = \pm\frac{3}{4}a_3 + \frac{\sqrt{3}}{4}a_8 \ , \tag{5.9}$$

where ([90],[91]):

$$\begin{aligned} a_3 &= \frac{g_A}{g_V} = F + D = 1.2601 \pm 0.0025 \\ a_8 &= \frac{1}{\sqrt{3}}(3F - D) = \frac{1}{\sqrt{3}}(0.579 \pm 0.025) \end{aligned} \tag{5.10}$$

which gives

$$\eta_{NS}^{p} = 1.090 \pm 0.007 \ , \qquad \eta_{NS}^{n} = -0.8003 \pm 0.007 \ . \tag{5.11}$$

It was shown in Ref. [92] that SU(3) also constrains the high-x coefficient in the gluon parameterization to be equal to 4, so it was set to this value.

The analysis code has been run first by varying the mid-x coefficients γ and ρ, but no sensitivity was found for them for all the distributions except the singlet. So γ_Σ, $\gamma_{NS}^{p,n}$ were set to zero, and the same for the ρ coefficients, in agreement with the SMC publication. In this way the total number of free parameters is reduced to 10.

Table 5.2 shows the resulting best parameters from the QCD fit. With respect to the values published in the paper by the SMC collaboration in Ref.[84], the errors are in many cases one order of magnitude smaller. The gluon appears also much better constrained: the gluon coefficients of table 5.2 can be compared to the ones in Ref.[84] which are $\alpha_G = 0.33^{+2.05}_{-1.05}$ and $\eta_G = 0.25^{+0.29}_{-0.22}$.

$\Delta\Sigma$	α	-0.5173 ± 0.0030
	β	2.643 ± 0.040
	η	0.248 ± 0.020
	γ	-10.664 ± 0.072
Δq^p_{NS}	α	-0.517 ± 0.022
	β	2.95 ± 0.27
	η	1.090
	γ	0.
Δq^n_{NS}	α	0.935 ± 0.138
	β	3.48 ± 0.36
	η	-0.8003
	γ	0.
ΔG	α	1.337 ± 0.957
	β	4.0
	η	0.140 ± 0.136
	γ	0.
χ^2/NDF=539.95/463=1.17		

Table 5.2: Best fit parameter values and their statistical uncertainty at the input scale $Q^2 = 1$ GeV^2. The parameters with no error have been set to the values shown. The ρ coefficients, being all zero, are not shown in this table. The singlet distribution is very well constrained by data, while the gluon one has large uncertainties.

5.5 Statistical Error Bands

After the best fit has been found, each distribution is known in terms of parameters entering into the parameterization at the initial Q^2, and their errors, giving the 68% probability that a parameter is within the range given by the error. It is a common procedure ([87], [99]) to perform fits to structure functions and quote only the best values and the errors of the parameters, without showing how these affect the error on the distributions. This section will be devoted to the calculation of the statistical error bands, and it will be shown how they can be obtained in a straightforward way for both distributions and structure functions, at *any* Q^2 value.

The expression for the error of a distribution f is given by:

$$(\sigma_f)^2(x,Q^2) = \sum_{i,j} \frac{df}{dp_i}(x,Q^2)\frac{df}{dp_j}(x,Q^2)\mathrm{cov}(p_i,p_j) \;, \tag{5.12}$$

where p_i and p_j are the parameters on which f depends. The analytic form of the distributions is only known at the initial $Q^2 = Q_0^2$, in the form of Eq. (5.4), so that only at Q_0^2 it is possible to calculate analytically the errors on the distributions. To calculate $\frac{df}{dp_i}(x,Q^2)$, an expression for the Q^2 evolution of the derivatives of each distribution with respect to each one of the parameters entering in the initial parameterizations has to be found. In the following it will be assumed that the covariance matrix has no dependence on Q^2.

In a simplified notation, where all the Δ symbols indicating the polarizations have been dropped, and the splitting functions have been denoted with P_i, $i = 1,..,5$, the evolution equations take the form:

$$\begin{aligned}
\frac{d}{dt}q_{NS} &= P_1 \otimes q_{NS} \\
\frac{d}{dt}\Sigma &= P_2 \otimes \Sigma + P_3 \otimes G \\
\frac{d}{dt}G &= P_4 \otimes \Sigma + P_5 \otimes G \;,
\end{aligned} \tag{5.13}$$

At any Q^2 value the non-singlet distributions only depend on their own initial parameters and do not depend on the ones entering the initial parameterization of Σ, G, or the other NS distribution, since they are completely decoupled from them in the evolution equations (5.13). Singlet and gluon distributions instead depend on each other because of their evolution, so that to find the evolution of their derivatives will be a more complicated matter. For this reason the NS case will be considered first.

Non-singlet case. If p_i is one of the parameters α_{NS}, β_{NS}, η_{NS}, γ_{NS}, ρ_{NS}, then by applying the first derivative with respect to p_i to the first equation in (5.13), one gets:

$$\frac{d}{dp_i}\frac{d}{dt}q_{NS} = \frac{d}{dp_i}P_1 \otimes q_{NS} \;, \tag{5.14}$$

and, by exchanging the order of derivative:

$$\frac{d}{dt}\left(\frac{d}{dp_i}q_{NS}\right) = P_1 \otimes \left(\frac{d}{dp_i}q_{NS}\right) \;, \tag{5.15}$$

so that the derivatives of the NS distributions evolve according to the same equations as the distributions. When performing the Q^2 evolution, the initial values will be given by $\frac{d}{dp_i} q_{NS}(x, Q_0^2)$, whose analytical form will be shown later.

Gluon and singlet case. Let us now consider the evolution of the derivatives of G and Σ with respect to one of the parameters entering the initial distribution of Σ, say Σ_i. By interchanging the order of the derivatives, one gets:

$$\begin{aligned} \frac{d}{dt}\frac{d\Sigma}{d\Sigma_i} &= P_2 \otimes \frac{d\Sigma}{d\Sigma_i} + P_3 \otimes \frac{dG}{d\Sigma_i} \\ \frac{d}{dt}\frac{dG}{d\Sigma_i} &= P_4 \otimes \frac{d\Sigma}{d\Sigma_i} + P_5 \otimes \frac{dG}{d\Sigma_i} \,, \end{aligned} \tag{5.16}$$

which shows that $d\Sigma/d\Sigma_i$ evolves together with $dG/d\Sigma_i$, and they cannot be separated in the evolution.

To numerically evaluate these distributions one has to provide the initial values. The initial parameterization of $d\Sigma/d\Sigma_i$ is known, since the parameters have been calculated. The distribution $dG/d\Sigma_i$ is zero at the initial Q^2, since Σ_i only enters in the parameterization of Σ. To properly evaluate the evolution of a derivative of Σ (or G) one then has to evolve it with the other distribution set to zero at the starting Q^2.

Once the derivatives of each distribution with respect to the parameters it depends on are evaluated at the Q^2 value of interest, the errors σ on the distributions are calculated as:

$$\begin{aligned} (\sigma\Sigma)^2 &= \sum_{i,j}\left[\frac{d\Sigma}{d\Sigma_i}\frac{d\Sigma}{d\Sigma_j}\mathrm{cov}(\Sigma_i,\Sigma_j) + \frac{d\Sigma}{d\Sigma_i}\frac{d\Sigma}{dG_j}\mathrm{cov}(\Sigma_i,G_j) + \frac{d\Sigma}{dG_i}\frac{d\Sigma}{dG_j}\mathrm{cov}(G_i,G_j)\right] \\ (\sigma G)^2 &= \sum_{i,j}\left[\frac{dG}{d\Sigma_i}\frac{dG}{d\Sigma_j}\mathrm{cov}(\Sigma_i,\Sigma_j) + \frac{dG}{d\Sigma_i}\frac{dG}{dG_j}\mathrm{cov}(\Sigma_i,G_j) + \frac{dG}{dG_i}\frac{dG}{dG_j}\mathrm{cov}(G_i,G_j)\right] \\ (\sigma q_{NS}^{p,n})^2 &= \sum_{i,j}\left[\frac{dq_{NS}^{p,n}}{dp_i}\frac{dq_{NS}^{p,n}}{dp_j}\mathrm{cov}(p_i,p_j)\right] \,. \end{aligned} \tag{5.17}$$

The expressions for the derivatives of the distributions are quite lengthy but simplify considerably in the case of $\rho = 0$. The complete forms will nevertheless be reported. Given an initial parameterization with the form of Eq. (5.4), the derivatives with respect to each parameter are:

$$
\begin{aligned}
\frac{d\Delta f}{d\alpha} &= N_f\, \eta x^{\alpha}\,(1-x)^{\beta}\,(1+\gamma x+\rho\sqrt{x})\left(\ln x - N_f \frac{dN_f^{-1}}{d\alpha}\right)\\
\frac{d\Delta f}{d\beta} &= N_f\, \eta x^{\alpha}\,(1-x)^{\beta}\,(1+\gamma x+\rho\sqrt{x})\left(\ln(1-x) - N_f \frac{dN_f^{-1}}{d\beta}\right)\\
\frac{d\Delta f}{d\eta} &= N_f\, x^{\alpha}\,(1-x)^{\beta}\,(1+\gamma x+\rho\sqrt{x}) = \frac{\Delta f}{\eta}\\
\frac{d\Delta f}{d\gamma} &= N_f\, \eta\, x^{\alpha}\,(1-x)^{\beta}\left(x - N_f \frac{dN_f^{-1}}{d\gamma}\right)\\
\frac{d\Delta f}{d\rho} &= N_f\, \eta\, x^{\alpha}\,(1-x)^{\beta}\left(\sqrt{x} - N_f \frac{dN_f^{-1}}{d\rho}\right)\ ,
\end{aligned}
\tag{5.18}
$$

where the subscripts f in the parameters α, β, γ and ρ have been dropped for simplicity, and:

$$
\begin{aligned}
&N_f \frac{dN_f^{-1}}{d\alpha} = \frac{\Gamma(\alpha+1)\Gamma\left(\alpha+\beta+\frac{5}{2}\right)}{D(\alpha+\beta+2)} \times\\
&\quad \times \left[\gamma(\beta+1) + (\alpha+\beta+2)(\alpha+\beta+2+\gamma(\alpha+1))(\psi(\alpha+1)-\psi(\alpha+\beta+2))\right] +\\
&\quad + \frac{1}{D}\rho(\alpha+\beta+2)^2\Gamma\left(\alpha+\frac{3}{2}\right)\Gamma(\alpha+\beta+2)\left(\psi\left(\alpha+\frac{3}{2}\right)-\psi\left(\alpha+\beta+\frac{5}{2}\right)\right)\\
&N_f \frac{dN_f^{-1}}{d\beta} = \frac{\Gamma(\alpha+1)\Gamma\left(\alpha+\beta+\frac{5}{2}\right)}{D(\alpha+\beta+2)} \times\\
&\quad \times \left[-\gamma(\alpha+1) + (\alpha+\beta+2)(\alpha+\beta+2+\gamma(\alpha+1))(\psi(\beta+1)-\psi(\alpha+\beta+2))\right] +\\
&\quad + \frac{1}{D}\rho(\alpha+\beta+2)^2\Gamma\left(\alpha+\frac{3}{2}\right)\Gamma(\alpha+\beta+2)\left(\psi\left(\beta+1\right)-\psi\left(\alpha+\beta+\frac{5}{2}\right)\right)\\
&N_f \frac{dN_f^{-1}}{d\gamma} = \frac{1}{D}(\alpha+1)\Gamma(\alpha+1)\Gamma\left(\alpha+\beta+\frac{5}{2}\right)\\
&N_f \frac{dN_f^{-1}}{d\rho} = \frac{1}{D}(\alpha+\beta+2)\Gamma\left(\alpha+\frac{3}{2}\right)\Gamma(\alpha+\beta+2)\\
&D = (\alpha+\beta+2+\gamma(\alpha+1))\,\Gamma(\alpha+1)\Gamma\left(\alpha+\beta+\frac{5}{2}\right) +\\
&\quad + \rho(\alpha+\beta+2)\Gamma\left(\alpha+\frac{3}{2}\right)\Gamma(\alpha+\beta+2)\ ,
\end{aligned}
\tag{5.19}
$$

with $\psi(x) = \frac{d}{dx}\ln\Gamma(x)$. These quantities constitute the initial parameterizations in the calculation of the statistical error bands.

Results for the four combinations of polarized parton distributions are shown in Fig. 5.1, for different Q^2 values of 1, 4, 25 and 60 GeV^2. Each polarized distributions f must

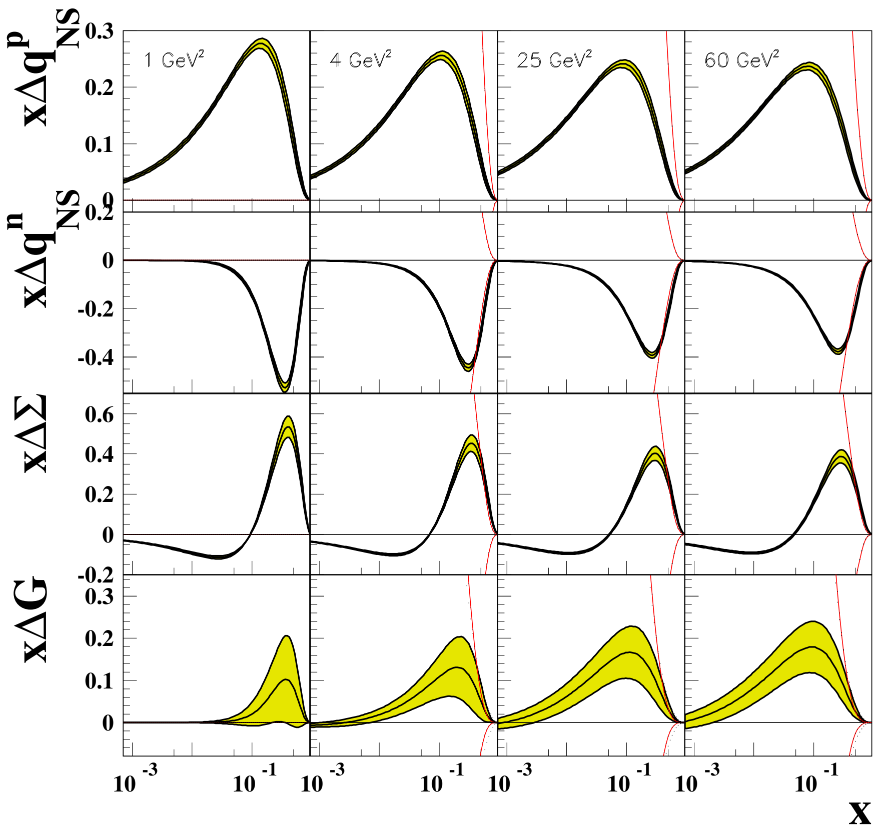

Figure 5.1: Central values and statistical error bands for $x\Delta q^{p,n}_{NS}(x,Q^2)$, $x\Delta\Sigma(x,Q^2)$ and $x\Delta G(x,Q^2)$, for the Q^2 values 1, 4, 25 and 60 GeV^2. The plots are superposed with the MRST2001 ([100], straight lines) and CTEQ6 ([101], dotted line), fits to unpolarized world data, which constitutes an upper limit to be satisfied by the polarized distributions. The two unpolarized parameterizations cannot be distinguished for the quark plots.

obey the positivity limit

$$|\Delta f| \leq f \; , \tag{5.20}$$

where f is the unpolarized distribution. In Fig. 5.1 the obtained polarized distributions are compared to the latest unpolarized MRST ([100]) and CTEQ ([101]) parameterizations, and it appears clear that these limits are well respected. These two unpolarized parameterizations are in agreement in the small x region shown in the plots, for all distributions except for the gluon, where they differ slightly.

The quark distributions appear to be very well determined by data, but the gluon distribution has still large uncertainties. Even within the large uncertainties, it is possible to see that the gluon distribution has a clear positive sign, becoming more definite at increasing Q^2 values.

The Q^2 behaviour of the distributions can be understood with the following reasoning. At small Q^2 the resolving power of the virtual photon is low, so it is not able to discriminate between a parton with momentum x and the system of a parton with lower momentum y plus an emitted gluon: the virtual photon will assign a momentum x to the system. At higher Q^2 the resolving power increases, and the virtual photon is able to discriminate among different kinds of partons. The distribution of partons at small x increases, since more partons carry smaller momentum fraction, and decrease at high x for the same reason. This is also the reason why unpolarized structure functions decrease at high x for increasing Q^2, and increase at small x. In the case of polarized structure functions, which describe spin, this reasoning still holds, and it is confirmed by data: the extracted quark polarized distributions have indeed a decreasing behaviour at high x with increasing Q^2. The gluon contribution instead increases with Q^2 since at higher Q^2 the photon is able to discriminate gluon-initiated processes.

Once the distributions are known, it is possible to evaluate g_1^p, g_1^d, g_1^n, using Eq. (5.1). The statistical error can be obtained in a similar way as for the distributions:

$$\sigma^2(g_1) = \sum_{i,j} \frac{\partial g_1}{\partial p_i} \frac{\partial g_1}{\partial p_j} \mathrm{cov}(p_i, p_j) \tag{5.21}$$

where now the sum is over all possible parameters p_i and p_j, including cross terms of gluon with NS, and singlet with NS. The results are shown in Figs.5.2, 5.3 and 5.4 for the four reference Q^2 values.

5.6 Systematic errors

Fig. 5.1 shows the statistical error bars alone, obtained by propagating the statistical errors on the measured $g_1^{p,n,d}$ values to the distributions. The measured values on the structure functions also have systematic errors, which should be propagated too. The procedure used to obtain the systematic bands consists in shifting the data points for each experimental data set by $\pm\sigma_{\text{syst}}$, while leaving the data from the other experiments

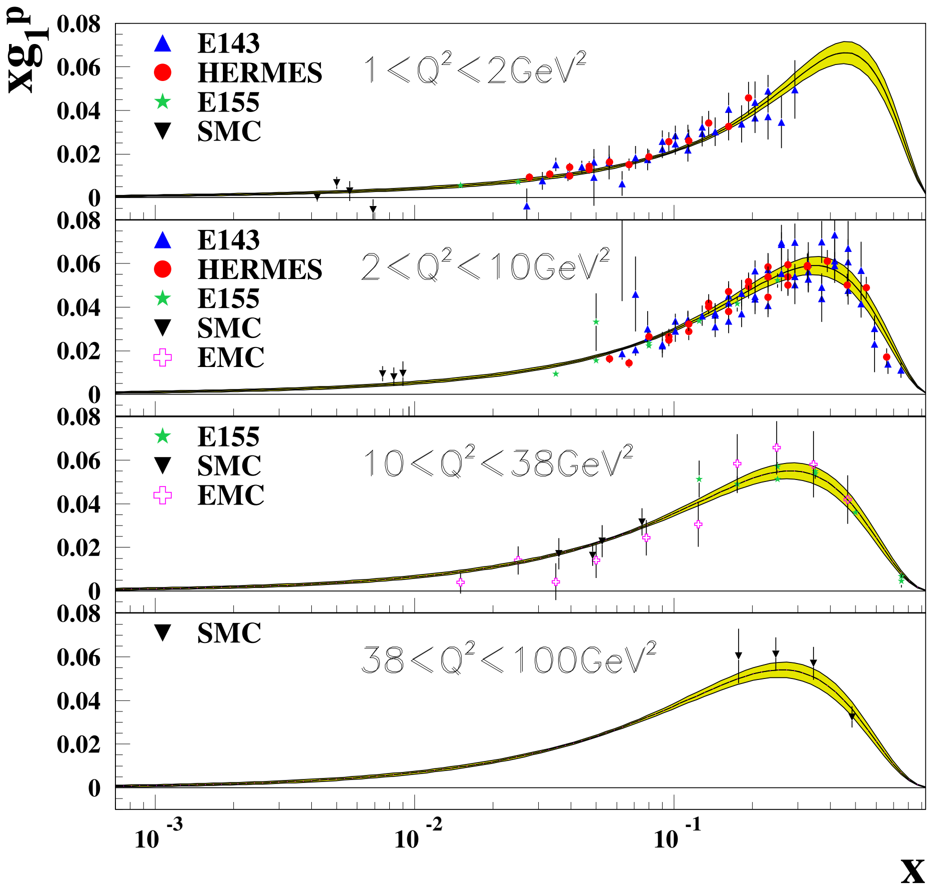

Figure 5.2: Central values and statistical error bands for xg_1^p for Q^2 values of 1, 4, 25 and 60 GeV^2. The bands are superposed with the data in each energy range.

at their central values, and looking at how the polarized distributions change. Since 12 data sets have been used, this means that 24 χ^2 minima have to be obtained. In this way the extreme values for the change in the distributions are obtained: the real central value will be within the systematic band thus obtained.

Some less precise experiments, like EMC, have very large systematic errors. Special attention has to be paid when shifting their central values, since this could be interpreted by the fitting routine as a high Q^2 dependence. For this reason the shifted data were weighted by the sum in quadrature of statistical and systematic errors, in the fitting pro-

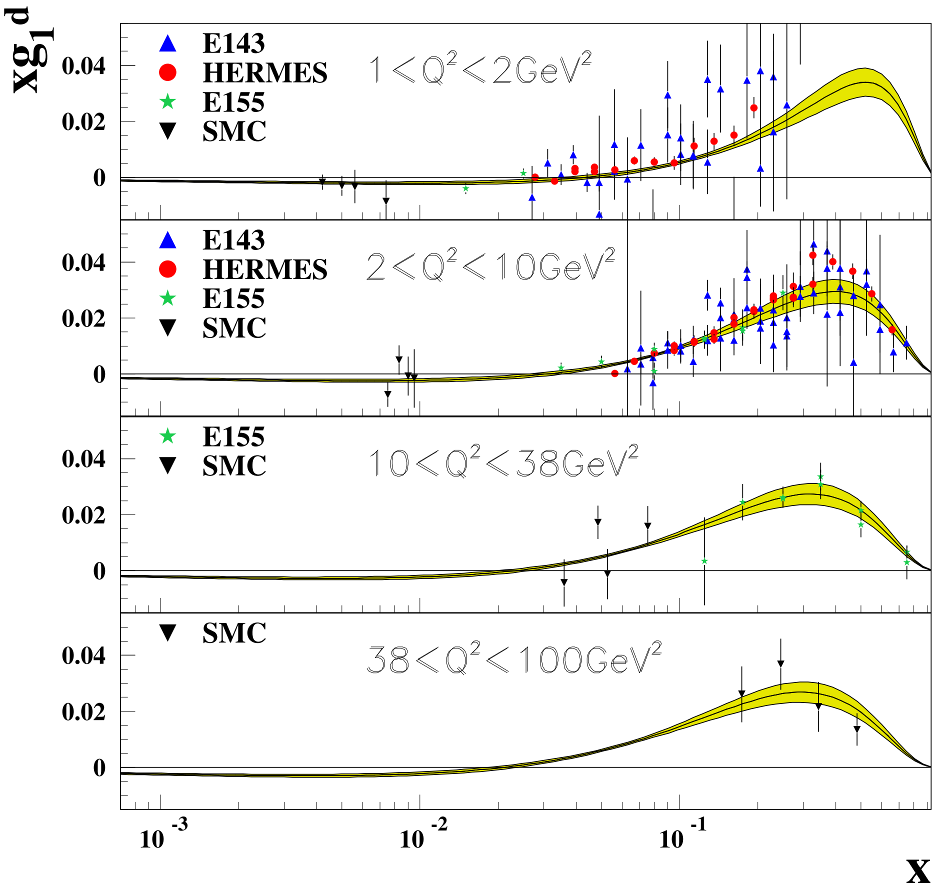

Figure 5.3: Central values and statistical error bands for xg_1^d for Q^2 values of 1, 4, 25 and 60 GeV^2. The bands are superposed with the data in each energy range.

cedure, to give them a lower weight.

Fig. 5.5 shows the bands within which the polarized distributions are contained when shifting the g_1 central values. Whenever the fits exceeded the unpolarized limit (shown in the figure) the bands were cut to respect such a limit. This could not be done for the points at 1 GeV^2, where no MRST2001 or CTEQ6 fits to unpolarized distributions are available.

Fig. 5.6 shows the final results for the fits to the polarized distributions $\Delta q_{NS}^{p,n}(x, Q^2)$, $\Delta\Sigma(x, Q^2)$ and $\Delta G(x, Q^2)$ for the reference values of 1, 4, 25 and 60 GeV^2, in the range

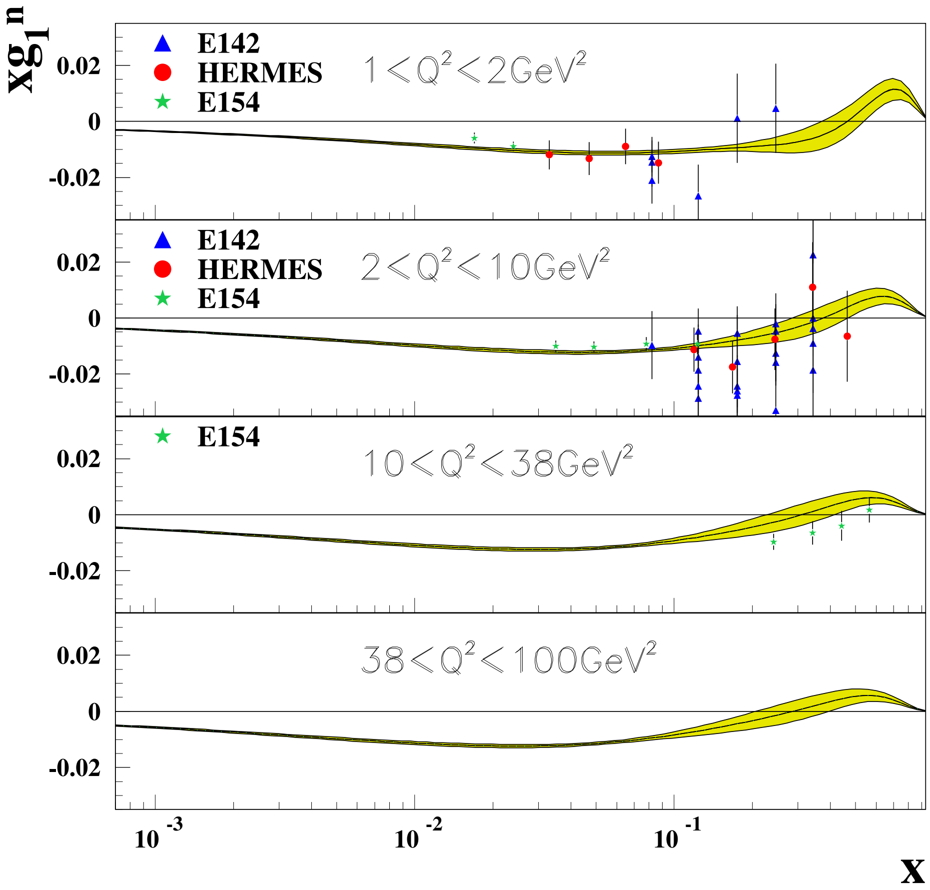

Figure 5.4: Central values and statistical error bands for xg_1^n for Q^2 values of 1, 4, 25 and 60 GeV^2. The bands are superposed with the data in each energy range.

$0.0007 \leq x \leq 0.93$, including statistical and systematic errors. The smaller error bands are the statistical errors, while the larger bands are the total errors $\sigma_{\text{tot}}(x, Q^2)$, calculated as the sum in quadrature of the statistical and systematic errors:

$$\sigma_{\text{tot}}(x, Q^2) = \sqrt{\sigma^2_{\text{stat}}(x, Q^2) + \sigma^2_{\text{syst}}(x, Q^2)}\ . \tag{5.22}$$

Singlet and non-singlet distributions are very well constrained by data, but large uncertainties still remain in the gluon sector. The gluon distribution is consistent with zero at the starting scale of 1 GeV^2, gaining a definite positive sign at increasing Q^2.

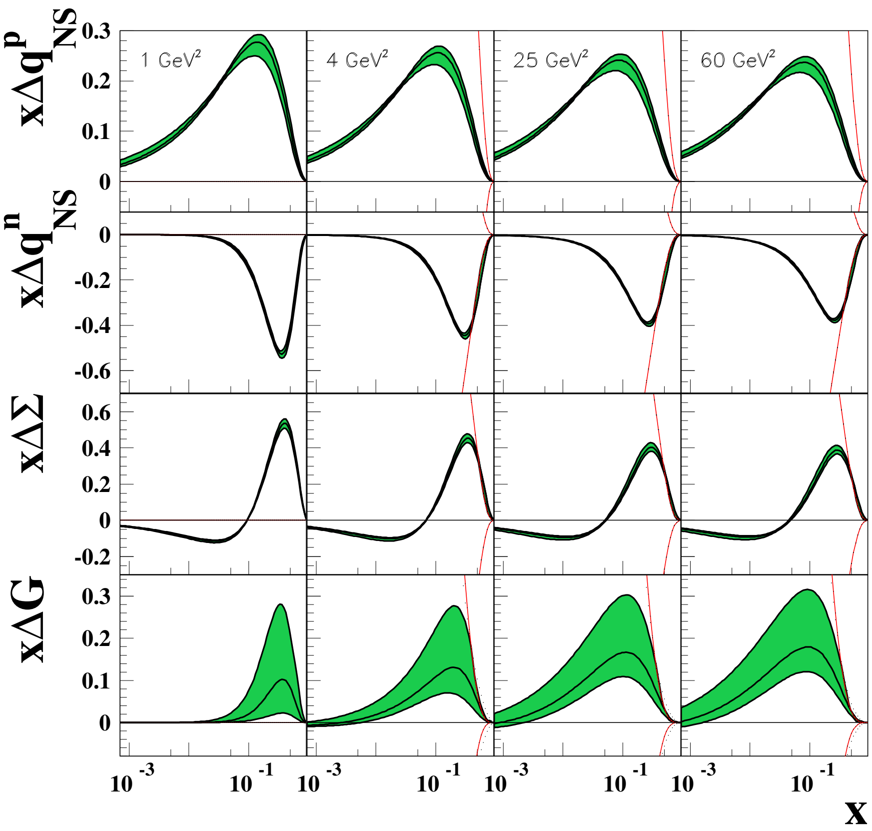

Figure 5.5: Central values and systematic error bands for Q^2 values of 1, 4, 25 and 60 GeV^2. The bands are superposed with MRST20011 (full lines) and CTEQ6 (dotted lines) fits to unpolarized world data, which constitutes a limit to be satisfied by the polarized distributions. A cut was applied to distributions that are exceeding the unpolarized limit.

5.7 Integrals

As discussed in ch.4, interesting quantities are the integrals of polarized parton distributions over the variable x. The polarized structure functions and distributions have thus been integrated over the range $0.0007 \leq x \leq 0.93$. The results are in Table 5.3, where statistical and systematic errors are shown. The error for each integral was obtained as the area between the best fit and the best fit plus or minus the errors. The error obtained from the statistical band is symmetric, while this is not the case for the areas of Fig. 5.5, so asymmetric systematic errors are obtained.

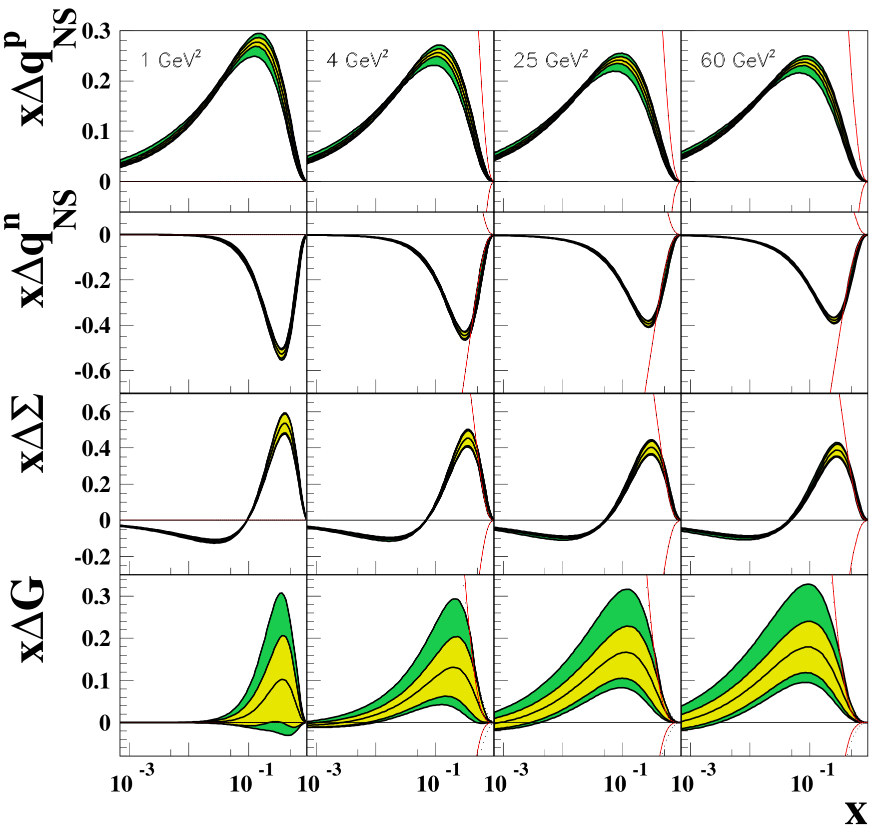

Figure 5.6: Final results for the fits of $x\Delta q^p_{NS}$, $x\Delta q^n_{NS}$, $x\Delta\Sigma$ and $x\Delta G$ for Q^2 reference values of 1, 4, 25 and 60 GeV^2. The fits are superposed with the statistical errors given by the internal band and the sum in quadrature of statistical and systematic errors given by the external band.

Integrals of $g_1^{p,d,n}(x, Q^2)$ have been calculated in different x ranges to compare them with published values, and such a comparison is reported in table 5.4, where only statistical errors are shown, in both published values and from this analysis. The fact that the errors obtained from the fit are in many cases larger than previously published ones does not lead to the conclusion that the fit does not represent an improvement with respect to the past. Results reported from other papers were obtained directly from integrating g_1 data on the measured x range from each experiment. The data points within each experiment are at different Q^2, and an ansatz has to be used in order to evolve the points to a common Q^2 value in order to be able to perform the integration. It is usually assumed

Q^2 (GeV^2)	$\int_{0.0007}^{0.93} dx\ \Delta q^p_{NS}(x,Q^2)$	$\int_{0.0007}^{0.93} dx\ \Delta q^n_{NS}(x,Q^2)$
1	$1.021 \pm 0.048\ ^{+0.072}_{-0.085}$	$-0.802 \pm 0.044\ ^{+0.043}_{-0.045}$
4	$1.003 \pm 0.043\ ^{+0.066}_{-0.079}$	$-0.800 \pm 0.036\ ^{+0.055}_{-0.026}$
25	$0.987 \pm 0.040\ ^{+0.060}_{-0.075}$	$-0.799 \pm 0.031\ ^{+0.047}_{-0.023}$
60	$0.982 \pm 0.039\ ^{+0.057}_{-0.074}$	$-0.798 \pm 0.030\ ^{+0.045}_{-0.023}$
	$\int_{0.0007}^{0.93} dx\ \Delta\Sigma(x,Q^2)$	$\int_{0.0007}^{0.93} dx\ \Delta G(x,Q^2)$
1	$0.309 \pm 0.088\ ^{+0.049}_{-0.068}$	$0.140 \pm 0.157\ ^{+0.282}_{-0.109}$
4	$0.310 \pm 0.073\ ^{+0.058}_{-0.095}$	$0.327 \pm 0.199\ ^{+0.387}_{-0.164}$
25	$0.318 \pm 0.069\ ^{+0.076}_{-0.102}$	$0.533 \pm 0.248\ ^{+0.512}_{-0.218}$
60	$0.324 \pm 0.070\ ^{+0.084}_{-0.105}$	$0.613 \pm 0.265\ ^{+0.556}_{-0.238}$

	$\int_{0.0007}^{0.93} dx\ \mathrm{g}_1^p(x,Q^2)$	$\int_{0.0007}^{0.93} dx\ \mathrm{g}_1^d(x,Q^2)$	$\int_{0.0007}^{0.93} dx\ \mathrm{g}_1^n(x,Q^2)$
1	0.125 ± 0.009	0.040 ± 0.008	-0.046 ± 0.009
4	0.131 ± 0.009	0.042 ± 0.008	-0.048 ± 0.008
25	0.135 ± 0.009	0.043 ± 0.008	-0.049 ± 0.008
60	0.136 ± 0.009	0.043 ± 0.008	-0.049 ± 0.008

Table 5.3: Top: integrals of polarized parton distributions Δq^p_{NS}, Δq^n_{NS}, $\Delta\Sigma$ and ΔG over the measured range $0.0007 \leq x \leq 0.93$. First quoted errors are statistical while second are systematic. Bottom: integrals of $\mathrm{g}_1^{p,d,n}$ over the same x range. Errors are statistical only.

that the ratio $\mathrm{g}_1(x,Q^2)/\mathrm{F}_1(x,Q^2)$ does not depend on Q^2, as world data suggest. By using a parameterization for F_1 obtained from world data, the values for g_1 at a different Q^2 can be obtained, making it possible to perform the integration. Results obtained in this way are more precise than those obtained from a QCD fit, since the purpose of the fit is also to accomodate data from different targets and experiments in a model valid over a wide Q^2 and x range, and to extract additional information such as the parton distributions. It is then understandable that precision may be lost in the process. It is then impressive that in many cases the precision of the integrals from the fit is comparable if not better than the results obtained from g_1 data alone.

x Range	Exp.	Q^2	Integral	Ref.
Proton				
$0.003 \leq x \leq 0.8$	SMC	5	0.130 ± 0.003	[84]
	T.A.	4	0.129 ± 0.008	
$0.03 \leq x \leq 0.8$	E143	3	0.121 ± 0.003	[93]
	E143	5	0.117 ± 0.003	[93]
	T.A.	4	0.115 ± 0.007	
$0.021 \leq x \leq 0.85$	HERMES	2.5	0.122 ± 0.003	[43]
	T.A.	4	0.119 ± 0.007	
Deuteron				
$0.003 \leq x \leq 0.8$	SMC	5	0.036 ± 0.004	[84]
	T.A.	4	0.044 ± 0.007	
$0.03 \leq x \leq 0.8$	E143	3	0.046 ± 0.003	[93]
	E143	5	0.043 ± 0.003	[93]
	T.A.	4	0.048 ± 0.006	
Neutron				
$0.003 \leq x \leq 0.8$	SMC	5	-0.054 ± 0.007	[84]
	T.A.	4	-0.041 ± 0.008	
$0.03 \leq x \leq 0.8$	E143	3	-0.023 ± 0.008	[93]
	E143	5	-0.025 ± 0.007	[93]
	T.A.	4	-0.019 ± 0.006	
$0.023 \leq x \leq 0.6$	HERMES	2.5	-0.034 ± 0.013	[42]
	T.A.	4	-0.024 ± 0.006	
$0.03 \leq x \leq 0.6$	E142	2	-0.028 ± 0.006	[59]
	T.A.	1	-0.021 ± 0.006	
	T.A.	4	-0.024 ± 0.006	

Table 5.4: Comparison of integrals $\int dx\ \mathrm{g}_1^{p,d,n}(x, Q^2)$ from other experiments and from this analysis (T.A.). The first column indicates the x range of integration, the second the experimental collaboration author of the analysis, the third is the Q^2 at which the integral is calculated. The fourth column gives the integral with its statistical error alone, and the fifth gives the reference to the article where the result is published. The results from this analysis are in good agreement with older results, having, in some cases, also smaller statistical errors.

Integrals from new HERMES $\mathbf{g}_1^d$ data. The results obtained in ch.3 can be used to obtain experimental values for the integral of g_1^d over the measured x range, in a more precise way than from the fits. Under the hypothesis that $\mathrm{g}_1^d(x, Q^2)/\mathrm{F}_1^d(x, Q^2)$ is independent of Q^2, the value of $\mathrm{g}_1^d(x, Q^2_{\mathrm{ref}})$ at a reference Q^2 value Q^2_{ref} is given by:

$$\frac{\mathrm{g}_1^d(x, Q^2_{\mathrm{meas}})}{\mathrm{F}_1^d(x, Q^2_{\mathrm{meas}})} \mathrm{F}_1^d(x, Q^2_{\mathrm{ref}}) \,, \tag{5.23}$$

where the fifteen parameter fit for F_1^d was used, introduced in ch.3. For a given x bin, up to three Q^2 bins exist. The g_1^d values have first been obtained in the 49 bins at the same $Q^2_{\rm ref}$ and then a weighted average has been performed over the different Q^2 bins that belong to the same x bin. The integral $\mathcal{I}$ has been calculated as

$$\mathcal{I} = \int_{0.0021}^{0.85} dx\ g_1^d(x, Q^2_{\rm ref}) = \sum_{i=1}^{49} (x_{i+1} - x_i)\, g_1^d(< x >_i, Q^2_{\rm ref})\ , \tag{5.24}$$

and the statistical error as:

$$\sigma^2_{\mathcal{I}} = \sum_{i=1}^{49}\ (x_{i+1} - x_i)^2\ \sigma^2(g_1^d(< x >_i, Q^2_{\rm ref})), \tag{5.25}$$

where $< x >_i$ is the average x in the i-th bin, with x values contained between x_i and x_{i+1}.

Given the systematic error of g_1^d/F_1^d in an x bin, the systematic error at $Q^2_{\rm ref}$ has been obtained in the same way as the value of g_1^d, i.e. according to Eq. (5.23). The values belonging to the same x bin have been averaged using a weighted average with weights given by the inverse squared of the statistical errors in each Q^2 bin. To obtain the systematic error on the integral, the values of g_1^d have been shifted by the systematic error in each x bin and $\mathcal{I}$ recalculated.

The values obtained for the integral of g_1^d over the measured x range are in table 5.5 and they are in very good agreement with the values of table 5.4 (the SMC results have a similar x range). The statistical errors, as previously discussed, are smaller than the ones obtained from the fits. The systematic errors are of the same order of magnitude as previous publications.

$Q^2_{\rm ref}$ (GeV^2)	$\int_{0.0021}^{0.85} dx\ g_1^d(x, Q^2_{\rm ref})$
1	$0.0400 \pm 0.0018 \pm 0.0052$
4	$0.0400 \pm 0.0023 \pm 0.0040$
5	$0.0398 \pm 0.0024 \pm 0.0036$

Table 5.5: Integrals of g_1^d over the measured x range for different $Q^2_{\rm ref}$ values, calculated from the new HERMES data alone. The first error is statistical and the second is systematic.

5.8 Conclusions

Fits to world data on the structure function g_1 for the extraction of polarized parton distributions describe the data well, and are able to provide good insight into the polarized distributions. The gluon polarization shows a definite positive sign explaining, at least in part, the *spin puzzle*.

The problem still remains that the fitting procedure is only valid in the kinematic x, Q^2 range of data, so that the fits cannot be trusted at lower x or higher Q^2 than existing data. This makes it difficult to give predictions on the behavior of the integrals of structure functions or polarized distributions over the whole x range between 0 and 1. However, even if one decides to trust the fits, and calculates the integrals from the fitted distributions over the whole range of x, the fact has to be taken into account that the errors on the distributions, and especially on the gluons, blow up at low x (note that the plots shown in this chapter are x times the distributions). This brings a large uncertainty in the estimation of the integral. More data is needed at lower x to be able to constrain the gluons before an integral of ΔG can provide an indication as to whether or not the spin puzzle has been solved. One could also try to get an estimate of the possible behavior of the structure functions at lower x by using theoretical predictions as those discussed in section 4.2.4; however as this thesis is mainly focused on the impact of data on the precision of the extraction of the polarised parton distributions, this would go beyond its scope.

There are nevertheless still some ways the fits could be improved with existing data, and are discussed here briefly.

Quality of data. The deuterium HERMES data used from the 1998 and 2000 production is missing the smearing corrections, coming from the finite resolution of the spectrometer. They have to be determined by a Monte Carlo simulation, and they are expected to contribute a 2-3% of g_1^d, but mostly at low x.

Normalizations. Each data set from each experiment has an intrinsic normalization uncertainty, coming from the uncertainties on target and beam polarizations, and on the luminosity measurement. This means that each data set should be properly normalized.

This can only be done in a comparison with other data sets, and usually by the inclusion of an additional term into the χ^2 definition [102]:

$$\chi^2 = \chi^2_{data} + \sum_{expts} \frac{N_i - 1}{\Delta N} \tag{5.26}$$

where ΔN is the normalization uncertainty quoted by the experiment, and N_i is a set of additional parameters to be inserted in the χ^2 definition at the beginning of the study. The minimization will provide a best value for the normalizations, that are then fixed for the fit.

Higher twist effects. Data at $Q^2 < 4$ GeV^2 are usually rejected in unpolarized analyses, because higher twist (non-perturbative) effects start having an important role. This is not yet possible to do in the polarized case because it would mean the loss of a large amount of data that is necessary to constrain the distributions at small x, since the small Q^2 region corresponds for fixed target experiments also to the small x region. In the absence of a clear theoretical calculation, alternatively these effects can be parameterized by the introduction of a Q^2 dependence in addition to the lower twist (LT) structure function of the form

$$\mathrm{g}_1^{HT}(x, Q^2) = \mathrm{g}_1^{LT}(x, Q^2) \times \left[1 + \frac{f(x)}{Q^2}\right] \tag{5.27}$$

where $\mathrm{g}_1^{HT}(x, Q^2)$ describes the higher twist form of the structure function and $f(x)$ is parameterized as a polynomial in x whose coefficients have to be determined from data. Recent studies ([102]) have shown that the application of these corrections affects the fits only at small x but still it is consistent with a simple NLO calculation, within the precision of the error bars.

Chapter 6

Conclusions

The most precise measurement yet made of the deuteron structure function g_1^d has been performed with almost 10 million DIS events collected by the HERMES experiment. Data covered the scattered lepton kinematic range $0.0041 < x < 0.81$ and $0.21 < Q^2 < 7.3$ GeV^2.

The results were used in combination with world data on g_1^p, g_1^d and g_1^n, some of which collected by HERMES in previous years, to extract the polarized parton distributions $\Delta q_{NS}^{p,n}(x, Q^2)$, $\Delta\Sigma(x, Q^2)$ and $\Delta G(x, Q^2)$. The method used the fact that each distribution has a different Q^2 dependence. Data collected at different Q^2 values can be used to extract these distributions. Both statistical and systematic errors on the measured g_1 values were propagated into the polarized distributions. A full treatment of statistical errors was developed, allowing the calculation of statistical error bands at *any* Q^2 value, and not only at the initial Q_0^2, where the analytical parameterization is known. The quark distributions are very well determined, and the resulting gluon distribution has a definite positive sign and increases with Q^2.

Integrals for the distributions and the structure functions were obtained from the fits in the range $0.0007 < x < 0.93$ and are in agreement with previous calculations ([84]). The integral of g_1^d has also been calculated over the measured x range, using HERMES data alone, obtaining a great improvement with respect to previously published results.

Although the measurement shown in this thesis is extremely precise, it does not cover the whole x range of g_1, and data are still needed especially at lower values of x and higher Q^2, where non-perturbative contributions can be safely neglected.

The model in which the total spin of the nucleon is carried only by quarks is no longer valid, as the pioneering EMC experiment showed. Nowadays the small EMC result is interpreted as the difference of quark and gluon spin, meaning that the quarks could still carry a significant portion of the nucleon's polarization, but at the same time also the gluons do. The results in this thesis are a clear indication that gluon polarization is positive, at least in the x, Q^2 range of measured data, supporting such an interpretation. As the total contribution of each distribution to the nucleon's spin involves an integral over x, which cannot be performed given the limited x range, these results are only indicative that the spin crisis no longer exists and that the real problem is now to get more data to cover a larger kinematic range and measure the gluon distribution more precisely.

Future measurements of longitudinally polarized parton distributions will be done mostly at RHIC, HERA, and CERN.

RHIC (at the Brookhaven National Laboratory) has a spin program that consists in producing polarized beams of protons, with the main goal of measuring ΔG through $\vec{p} - \vec{p}$ scattering. The main channel will be direct photon production. At tree level the direct photon can be produced by Compton scattering $qg \to q\gamma$ and by quark-antiquark annihilation $q\bar{q} \to \gamma g$, and, since the antiquark distribution inside the proton is small, the process is dominated by Compton scattering. In this way the gluon distribution inside the proton can be directly probed, by identifying photons with high transverse momentum. RHIC measurements are expected to provide one of the cleanest, and at lower x, measurements of ΔG of any existing experiments (see Fig. 6.1).

Proton-proton collisions at RHIC will also be used to produce $W^{\pm}$ bosons ([11]), originating from the interaction of $u\bar{d}$ or $\bar{u}d$ quarks in the proton which subsequently decay into charged leptons and can provide information on the ratios $\Delta u/u$ and $\Delta\bar{d}/\bar{d}$ from W^+ and on $\Delta\bar{u}/\bar{u}$ and $\Delta d/d$ from W^- ([104]).

The gluon distribution can be easily measured in processes where the gluon enters directly, like photon-gluon fusion ($\gamma^* g \to q\bar{q}$). In this process the $q\bar{q}$ pair creates two hadron jets, or at lower energies, single hadron pairs, with opposite large transverse momentum. Up to now, a single data point was obtained by the HERMES experiment ([105]) with a similar analysis, using high transverse momentum hadron pairs, indicating a positive gluon polarization $\Delta G/G = 0.41 \pm 0.18 \pm 0.03$ at an average $< x >= 0.17$ (see

Fig.6.1).

The COMPASS experiment was built at CERN with the goal of measuring the gluon polarization. Polarized muon beams are produced by pion decays, and their high energy ($\simeq$ 200 GeV) makes it possible to reach low x regions ($x < 0.01$). COMPASS is exploring the possibility to measure the gluon polarization through open charm events. The contribution coming from the charm quark to the structure function g_1 ([106]) can be expressed as a convolution of a known function and the gluon distribution. Given the x dependence of g_1, this can be de-convoluted to extract ΔG. The large acceptance of the detector and its full particle identification will allow a large sample of charmed particles to be collected.

Fig. 6.1 shows projections for the statistical accuracy of the COMPASS and RHIC results, compared to the projected accuracy of the HERMES result, and the x range for each experiment. According to expectations, the results from COMPASS and RHIC will be able to discriminate among different models for the gluon polarizations.

New and exciting results will come from these experiments, that will probably shed more light on the mystery of the nucleon spin. The future of spin physics is starting now.....so fasten your seat belts and enjoy the ride!

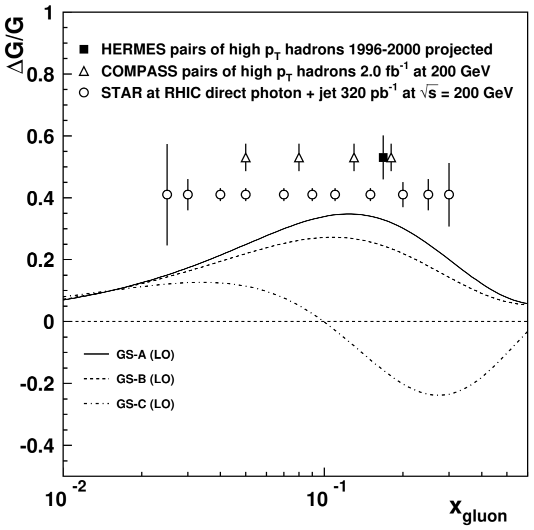

Figure 6.1: Projection for statistical accuracies of HERMES, COMPASS and RHIC spin physics experiments, superposed to three different QCD leading-order models for ΔG at Q^2 =10 GeV^2. The plot is based on projections shown in Ref. [107].

Bibliography

[1] F. Halzen and A.D. Martin, *Quarks and Leptons: An Introductory Course in Modern Particle Physics*, John Wiley & Sons, New York, 1984.

[2] H1 Collaboration, C. Adloff et al., Eur. Phys. J. C**21** (2001) 33.

[3] ZEUS Collaboration, J. Breitweg et al., Phys. Lett. B**487** (2000) 53.

[4] R.G. Roberts, *The structure of the proton*, Cambridge University Press, 1990.

[5] EMC Collaboration, J. Ashman et al., Phys. Lett. B**206** (1988) 364.

[6] HERMES Collaboration, K. Ackerstaff et al., Nuc. Instr. Meth. A**417** (1998) 230.

[7] HERMES Collaboration, K. Ackerstaff et al., Phys. Lett. B**464** (1999) 123.

[8] SMC Collaboration, B. Adeva et al., Phys. Lett. B**369** (1996) 93.

[9] SMC Collaboration, B. Adeva et al., Phys. Lett. B**420** (1998) 180.

[10] M. Beckman, *Proceedings from the Workshop on Testing QCD through Spin Observables in Nuclear Targets*, University of Virginia, Charlottesville, Virginia, USA, Apr 18 - 20, 2002.

[11] B. Bourrely and J. Soffer, Nucl. Phys. B**445** (1995) 341.

[12] T. Benisch et al., Nucl. Instr. Meth. A**471** (2001) 314.

[13] A. Solokov, I. Ternov, Sov. Phys. Doklady **8** (1964) 1203.

[14] M. Beckmann et al., Nucl. Instr. Meth. A**479**/2-3 (2002) 334.

[15] F. Menden, MSc. thesis, HERMES internal note 98/001.

[16] J. Wendland, MSc. thesis, HERMES internal note 99/016.

[17] J. Wendland, HERMES internal note 01/067.

[18] L. De Nardo, HERMES internal note 01/005.

[19] T. Ernst, PhD thesis, University of Freiburg, 1985.

[20] B. Lampe and E. Reya, Phys. Rept. **332** (2000) 1.

[21] M. Anselmino, A. Efremov and E. Leader, Phys. Rept. **261** (1995) 1.

[22] D.F. Geesaman, S. Saito and A.W. Thomas, Ann. Rev. Nucl. Part. Sci. **45** (1995) 337.

[23] M. Lacombe et al., Phys. Lett. B**101** (1981) 139.

[24] NMC Collaboration, P. Amaudruz et al., Nucl. Phys. B**371** (1992) 3.

[25] NMC Collaboration, P. Amaudruz et al., Phys. Lett. B**364** (1995) 107.

[26] L.W. Whitlow, S. Rock, A. Bodek, E.M. Riordan and S.Dasu, Phys.Lett. B**250** (1990) 193.

[27] L.W. Whitlow, PhD thesis, SLAC report 357.

[28] E155 Collaboration, P. L. Anthony et al., hep-ex/0204028.

[29] SMC Collaboration, B. Adeva et al., Phys. Lett. B**302** (1993) 533.

[30] E143 Collaboration, K. Abe et al., Phys. Rev. Lett. B**76** (1996) 587.

[31] E155 Collaboration, P. L. Anthony et al., Phys. Lett. B**458** (1999) 529.

[32] M. Stratmann, Z. Phys. C**60** (1993) 763.

[33] X. Song, Phys. Rev. D**54** (1996) 1995.

[34] H. Weigel and L. Gamberg, Nucl. Phys. A**680** (2000) 48.

[35] M. Wakamatsu, Phys. Lett. B**487** (2000) 118.

[36] H. Böttcher, Y. Gärber and U. Stößlein, HERMES internal note 99/053.

[37] L. De Nardo, A. Gute, U. Stößlein and C. Weiskopf, *Preliminary extraction of* g_1^d *from 98b4 data*, in preparation.

[38] S. Brandt, *Statistical and Computational Methods in Data Analysis*, North-Holland Publishing Company, 2nd edition, 1976.

[39] R.E. Kirk, *Elementary Statistics*, Brooks/Cole Publishing Company, Monterey, California, 2nd edition, 1984.

[40] C. Weiskopf, PhD thesis, in preparation.

[41] I.V. Akushevich et al., J. Phys. G**20** (1994) 513.

[42] HERMES Collaboration, K. Ackerstaff et al., Phys. Lett. B**404** (1997) 383.

[43] HERMES Collaboration, A. Airapetian et al., Phys. Lett. B**442** (1998) 484.

[44] SMC Collaboration, B. Adeva et al., Phys. Rev. D**58** (1998) 112001.

[45] N. Akopov et al., *Preliminary extraction of* g_1^d *from the 00b1 Data*, HERMES preliminary report.

[46] I. Akushevich, A. Ilyichev and N. Shumeiko, hep-ph/0106180.

[47] NMC Collaboration, P. Amaudruz et al., Nucl. Phys. B**483** (1997) 3.

[48] E665 Collaboration, M.R. Adams et al., Phys. Rev. D**54** (1996) 3006.

[49] E. Gotsman, E. Levin, U. Maor and E. Naftali, Nucl. Phys. B**539** (1999) 535.

[50] H. Abramowicz and A. Levy, hep-ph/9712415.

[51] U. Stößlein, private communications.

[52] S. Pokorski, *Gauge Field Theories*, Cambridge University Press, 1987.

[53] J. Collins, *Renormalization*, Cambridge University Press, 1984.

[54] A.V. Manohar, *Proceedings of the seventh Lake Louise Winter Institute : symmetry and spin in the standard model, Chateau Lake Louise, 23-29 February 1992*, editors B.A. Campbell et al., World Scientific Singapore, 1992. .

[55] J. Kodaira, S. Matsuda, K. Sasaki and T. Uematsu, Nucl. Phys. B**159** (1979) 99.

[56] D. Bailin, *Weak Interactions*, Sussex Univ. Press, 1982.

[57] EMC Collaboration, J. Ashman et al., Nucl. Phys. B**328** (1989) 1.

[58] E. Leader, A.V. Sidorov and D.B. Stamenov, Phys. Lett. B**488** (2000) 283.

[59] E142 Collaboration, P.L. Anthony et al., Phys. Rev. D**54** (1996) 6620.

[60] SMC Collaboration, B. Adeva et al., Phys. Lett. B**320** (1994) 400.

[61] J. Ellis and M. Karliner, Phys. Lett. B**213** (1988) 73.

[62] S.J. Brodsky, J. Ellis and M. Karliner, Phys. Lett. B**206** (1988) 309.

[63] A. Donnachie and P.V. Landshoff, Z. Phys. C**61** (1994) 139.

[64] S.D. Bass and P.V. Landshoff, Phys. Lett. B**336** (1994) 537.

[65] A.H. Mueller and T.L. Trueman, Phys. Rev. **160** (1967) 1306.

[66] L. Galfi, J. Kuti and A. Pathos, Phys. Lett. B**31** (1970) 465.

[67] F.E. Close and R.G. Roberts, Phys. Rev. Lett. **60** (1988) 1471.

[68] S.I. Adler, Phys. Rev. **177** (1969) 2426.

[69] J.S. Bell and R. Jackiw, N. C. A**51** (1969) 47.

[70] S.A. Larin, Phys. Lett. B**334** (1994) 192.

[71] J.D. Bjorken, Phys. Rep. **148** (1966) 1467.

[72] J. Ellis and R. Jaffe, Phys. Rev. D**9** (1974) 1444.

[73] G. Altarelli and G. Parisi, Nucl. Phys. B**126** (1977) 298.

[74] I.S. Gradshteyn and I.M. Ryzhik, *Tables of Integrals, Series, and Products*, Academic Press, San Diego, CA, 6th edition, 2000.

[75] R. Mertig and W.L. van Neerven, Z. Phys. C**70** (1996) 637.

[76] W. Vogelsang, Phys. Rev. D**54** (1996) 2023.

[77] G. t'Hooft and M. Veltman, Nucl. Phys. B**44** (1972) 189.

[78] M. Stratmann, A. Weber and W. Vogelsang, Phys. Rev. D**53** (1996) 138.

[79] E155 Collaboration, P.L. Anthony et al., Phys. Lett. B**493** (2000) 19.

[80] E143 Collaboration, K. Abe et al., Phys. Rev. D**58** (1998) 112003.

[81] W. Vogelsang, Nucl. Phys. B**475** (1996) 47.

[82] R.D. Ball, S. Forte and G. Ridolfi, Phys. Lett. B**378** (1996) 255.

[83] G. Altarelli, R.D. Ball, S. Forte and G. Ridolfi, Acta Phys. Polon. B**29** (1998) 1145.

[84] SMC Collaboration, B. Adeva et al., Phys. Rev. D**58** (1998) 112002.

[85] R. Windmolders, SMC internal note 98/02.

[86] D. Fashing, hep-ph/9610261.

[87] T. Gehrmann and W.T. Stirling, Phys. Rev. D**53** (1996) 6100.

[88] A.D. Martin, R.G. Roberts and W.J. Stirling, Phys. Lett. B**354** (1995) 155.

[89] F. James, CERN Program Library Long Writeup D506.

[90] Particle Data Group, R.M. Barnett et al., Phys. Rev. D**54**, 1 (1996).

[91] F.E. Close and R.G. Roberts, Phys. Lett. B**316**, (1993) 165.

[92] S.J. Brodsky, M. Burkardt and I. Schmidt, Nucl. Phys. B**441** (1995) 197.

[93] E143 Collaboration, K. Abe et al., Phy. Rev. D**58**. (1998) 112003.

[94] E154 Collaboration, K. Abe et al., Phys. Lett. B**405** (1997) 180.

[95] E154 Collaboration, K. Abe et al., Phys. Rev. Lett.**79** (1997) 26.

[96] E155 Collaboration, P.L. Anthony et al., Phys. Lett. B**463** (1999) 339.

[97] SMC Collaboration, B. Adeva et al., Phys. Rev. D**60** (1999) 072004.

[98] M. Schmelling, *Plenary talk given at the XXVIII Intern. Conf. on High Energy Physics, Warsaw, July 25-31, 1996*, hep-ex/9701002.

[99] AAC Collaboration, Y. Goto et al., Phys. Rev. D**62** (2000) 034017.

[100] A.D. Martin, R.G. Roberts, W.J. Stirling and R.S. Thorne, Eur. Phys. J. C**23** (2002) 73.

[101] J. Pumplin, D.R. Stump, J. Huston, H.L. Lai, P. Nadolsky and W.K. Tung, hep-ph/0201195.

[102] J. Blümlein and H. Böttcher, hep-ph/0203155.

[103] A. Deshpande, Proceedings of *The Workshop on Polarized Protons at High Energies - Accelerator Challenges and Physics Opportunities*, DESY, Hamburg, May 17-20, 1999, and hep-ex/9908051.

[104] B.W. Filippone and X. Ji, hep-ph/0101224.

[105] HERMES Collaboration, A. Airapetian et al., Phys. Rev. Lett. **84** (2000) 2584.

[106] M. Glück, E. Reya, and W. Vogelsan, Z. Phys. C**57** (1993) 309.

[107] TESLA Technical Report, DESY 2001-011, Part I, Executive Summary, ed.s F. Richards et al.

Appendix A

SU(3)

SU(3) is the set of unitary 3x3 U matrices with detU=1. The fundamental representation of the SU(3) group is given by the matrices

$$U = e^{\frac{1}{2}\boldsymbol{\lambda}_i \omega_i} \tag{A.1}$$

where ω_i are eight real parameters, and $\boldsymbol{\lambda}_i$ are called Gell-Mann matrices. They are the generators of this group, and there are 3^2-1=8 linearly dependent traceless hermitian 3x3 matrices ([1]):

$$\boldsymbol{\lambda}_i = \begin{pmatrix} \boldsymbol{\sigma}_i & 0 \\ 0 & 0 \end{pmatrix} \text{ with } i = 1,2,3 \ ; \ \boldsymbol{\lambda}_4 = \begin{pmatrix} 0 & 0 & 1 \\ 0 & 0 & 0 \\ 1 & 0 & 0 \end{pmatrix} \ ; \ \boldsymbol{\lambda}_5 = \begin{pmatrix} 0 & 0 & -i \\ 0 & 0 & 0 \\ i & 0 & 0 \end{pmatrix}$$

$$\boldsymbol{\lambda}_6 = \begin{pmatrix} 0 & 0 & 0 \\ 0 & 0 & 1 \\ 0 & 1 & 0 \end{pmatrix} \ ; \ \boldsymbol{\lambda}_7 = \begin{pmatrix} 0 & 0 & 0 \\ 0 & 0 & -i \\ 0 & i & 0 \end{pmatrix} \ ; \ \boldsymbol{\lambda}_8 = \frac{1}{\sqrt{3}} \begin{pmatrix} 1 & 0 & 0 \\ 0 & 1 & 0 \\ 0 & 0 & -2 \end{pmatrix}, \tag{A.2}$$

with the Pauli spin matrices

$$\boldsymbol{\sigma}_1 = \begin{pmatrix} 0 & 1 \\ 1 & 0 \end{pmatrix} \ ; \ \boldsymbol{\sigma}_2 = \begin{pmatrix} 0 & -i \\ i & 0 \end{pmatrix} \ ; \ \boldsymbol{\sigma}_3 = \begin{pmatrix} 1 & 0 \\ 0 & -1 \end{pmatrix}. \tag{A.3}$$

The Gell-Mann matrices satisfy the relations:

$$\begin{aligned} [\boldsymbol{\lambda}_i, \boldsymbol{\lambda}_j] &= 2i f_{ijk} \boldsymbol{\lambda}_k \\ \{\boldsymbol{\lambda}_i, \boldsymbol{\lambda}_j\} &= \frac{4}{3}\boldsymbol{\delta}_{ij} + 2 d_{ijk} \boldsymbol{\lambda}_k \end{aligned} \tag{A.4}$$

where f_{ijk} are fully antisymmetric under the interchange of any pair of indices, and d_{ijk} are fully symmetric. Also:

i	j	k	d_{ijk}	i	j	k	f_{ijk}
1	1	8	$1/\sqrt{3}$	1	2	3	1
1	4	6	1/2	1	4	7	1/2
1	5	7	1/2	1	5	6	-1/2
2	2	8	$1/\sqrt{3}$	2	4	6	1/2
2	4	7	-1/2	2	5	7	1/2
2	5	6	1/2	3	4	5	1/2
3	3	8	$1/\sqrt{3}$	3	6	7	-1/2
3	4	4	1/2	4	5	8	$\sqrt{3}/2$
3	5	5	1/2	6	7	8	$\sqrt{3}/2$
3	6	6	-1/2				
3	7	7	-1/2				
4	4	8	$-1/2\sqrt{3}$				
5	5	8	$-1/2\sqrt{3}$				
6	6	8	$-1/2\sqrt{3}$				
7	7	8	$-1/2\sqrt{3}$				
8	8	8	$-1/\sqrt{3}$				

The fundamental representation of SU(3) is a triplet. The three color charges of a quark and the u, d, s quarks (neglecting the different masses of these quarks) form the fundamental representation of a SU(3) symmetry group.

Appendix B

Renormalization Group and the Running of the Coupling Constant

One of the observable manifestations of vacuum fluctuations in QED is the potential screening of the electron charge. In order to measure its charge, the electron must be placed in an electromagnetic field, and then the reaction with the field must be studied. But on the way to the charge, a quantum probe can undergo virtual dissociation into an e^+e^- pair, which forms an effective dipole, leading to a screening effect.This process gives a contribution to the cross section proportional to α_{EM}, depending on the 4-momentum of the photon. Therefore the inclusion of vacuum effects transforms a constant (the charge) into a function, referred to as the *effective charge*.

In general, in any renormalizable theory, the quantum corrections cause the constant numerical value of the coupling constant to become a function of Q^2, i.e. the theory predicts only the Q^2 behaviour of the coupling constant, but not the actual value at any given Q^2. Experimentally the curve on which $\alpha(Q^2)$ lies is selected with the condition $\alpha(\mu^2) = \alpha_\mu$, as shown in Fig.B.1. In QED we have $\alpha_{EM}(0) = 1/137$. The physical curve can be represented as a function of two dimensionless arguments Q^2/μ^2 and α_μ, i.e. it can be written as $\bar{\alpha}(Q^2/\mu^2, \alpha)$. However the pair μ, α_μ can correspond to any physical point. *Renormalization invariance* means that any two parameterizations must lead to the same result:

$$\bar{\alpha}\left(\frac{Q^2}{\mu_1^2}, \alpha_1\right) = \bar{\alpha}\left(\frac{Q^2}{\mu_2^2}, \alpha_2\right) \ , \tag{B.1}$$

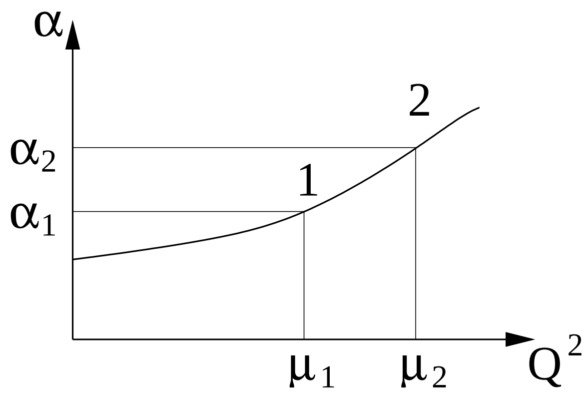

Figure B.1: The running coupling constant.

and obviously

$$\bar{\alpha}\left(\frac{\mu_2^2}{\mu_1^2}, \alpha_1\right) = \alpha_2 \qquad\qquad \bar{\alpha}\left(\frac{\mu_1^2}{\mu_2^2}, \alpha_2\right) = \alpha_1 \; . \tag{B.2}$$

By combining these two expressions we get the functional equation:

$$\bar{\alpha}(x, \alpha) = \bar{\alpha}\left(\frac{x}{t}, \bar{\alpha}(t, \alpha)\right) \; . \tag{B.3}$$

The *renormalization group* is the group of all transformations from one possible parameterization to the other. They form a continuous, one parameter group:

$$x \to x' = \frac{x}{t} \qquad\qquad \alpha \to \bar{\alpha}(t, \alpha) \; . \tag{B.4}$$

The renormalization group method is a systematic method of improving the results of ordinary perturbation theory. The point is that exact solutions of the quantum field equations must satisfy the condition of renormalization invariance. In practice we deal with pieces of Taylor series expansions in the coupling constant. The properties of these approximate solutions can differ significantly from those of the exact solutions because renormalization invariance is violated in perturbation theory. These differences can become important when the solution has a singularity, as occurs, for example, in the ultraviolet limit. The renormalization group method allows one to obtain from the approximate result a renormalization invariant expression which coincides with the original expression at lowest order in α. The group differential equations serve as a technical tool for realizing this program. By differentiating Eq. (B.3) one gets

$$x\frac{\partial \bar{\alpha}(x, \alpha)}{\partial x} = \beta(\bar{\alpha}(x, \alpha)) \; . \tag{B.5}$$

It is easy to show that any function $\beta(\alpha)$ exactly satisfies Eq. (B.3). The β function can be expressed as

$$\beta(\alpha) = \left.\frac{\partial\bar{\alpha}(x,\alpha)}{\partial x}\right|_{x=1} . \tag{B.6}$$

The renormalization group method amounts to obtaining the β function from a given approximate solution using Eq. (B.6). Then the solution to Eq. (B.5) gives an improved approximate solution, which, on the one hand, corresponds to the original solution to lowest order, and, on the other hand, is renormalization invariant. In QCD, the one-loop approximation for α_s is:

$$\alpha_s(Q^2) \sim \frac{4\pi}{\beta_0 \ln\frac{Q^2}{\Lambda^2}} , \qquad \beta_0 = 11 - \frac{2}{3}n_f , \tag{B.7}$$

and the 2-loop approximation is:

$$\alpha_s(Q^2) \sim \frac{4\pi}{\beta_0 \ln\frac{Q^2}{\Lambda^2}} \left[1 - \frac{\beta_1}{\beta_0^2}\frac{\ln\ln\frac{Q^2}{\Lambda^2}}{\ln\frac{Q^2}{\Lambda^2}}\right] \qquad \beta_1 = 102 - \frac{38}{3}n_f . \tag{B.8}$$

The renormalized coupling constant is:

$$\alpha_s(Q^2) = \frac{\alpha_s(\mu^2)}{1 + \frac{\alpha_s(\mu^2)}{12\pi}(33-2n_f)\ln\frac{Q^2}{\mu^2}} . \tag{B.9}$$

As Q^2 increases, it becomes infinitely small for short-distance interactions, and the theory is asymptotically free. From Eq. (B.9) we see that at sufficiently low Q^2 the effective coupling will become large. The scale at which this happens is usually denoted with Λ^2, where:

$$\Lambda^2 = \mu^2 e^{-\frac{12\pi}{(33-2n_f)\alpha_s(\mu^2)}} , \tag{B.10}$$

so that:

$$\alpha_s(Q^2) = \frac{12\pi}{(33-2n_f)\ln\frac{Q^2}{\Lambda^2}} . \tag{B.11}$$

For $Q^2 >> \Lambda^2$ the effective coupling is small and a perturbative approach in terms of quarks and gluons interacting weakly makes sense. For $Q^2 \sim \Lambda^2$ we cannot use such a picture any longer since quarks and gluons will arrange themselves into strongly bound clusters, namely hadrons. The value of Λ is not predicted by theory and it has to be experimentally determined: we can expect it to be of the order of a typical hadronic mass. It is experimentally measured to be $\Lambda \sim 0.2$ GeV. Thus for example, for experiments with

$Q^2 \sim (30 \text{ GeV})^2$ it follows that $\alpha_s \sim 0.2$ and perturbative theory can be used. In the large Q^2 limit the quark masses can be neglected and they contribute no mass scale to QCD. Nevertheless there is a mass scale Λ inherent to the theory, which enters through renormalization.

Appendix C

The Mellin Transform

C.1 LO case

The n-th moment of a function is defined as the Mellin transform ([74]) of f:

$$f_n(Q^2) = \int_0^1 f(x, Q^2)\, x^{n-1}\, dx \; . \tag{C.1}$$

The moment of a convolution of two functions f and g has the interesting property of being the product of the moments of the two functions:

$$\int_0^1 dx\, x^{n-1}\, f \otimes g = \int_0^1 dx\, x^{n-1} \int_x^1 \frac{dy}{y} f\left(\frac{x}{y}\right) g(y) = f_n g_n \; . \tag{C.2}$$

This makes it very convenient to work in the Mellin n-moment space, where the evolution equations can be solved analytically at a given order in α_s. In fact one has:

$$\begin{aligned}
\frac{d}{dt}\Delta q^n_{NS}(Q^2) &= \frac{\alpha_s(Q^2)}{2\pi} P^{(0)n}_{NS} \Delta q^n_{NS} \\
\frac{d}{dt}\begin{pmatrix} \Delta\Sigma^n(Q^2) \\ \Delta G^n(Q^2) \end{pmatrix} &= \frac{\alpha_s(Q^2)}{2\pi} \begin{pmatrix} P^{(0)n}_{qq} & 2n_f P^{(0)n}_{qG} \\ P^{(0)n}_{Gq} & P^{(0)n}_{GG} \end{pmatrix} \begin{pmatrix} \Delta\Sigma^n \\ \Delta G^n \end{pmatrix} \\
&= \frac{\alpha_s(Q^2)}{2\pi} \hat{P}^{(0)n} \begin{pmatrix} \Delta\Sigma^n \\ \Delta G^n \end{pmatrix}
\end{aligned} \tag{C.3}$$

where $P^{(0)n}_{ij}$ are the nth-moments of the splitting functions $P^{(0)}_{ij}$ and depend only on the number of flavours n_f and on n. They can be found in Ref.[20].

These momentum space evolution equations are usually called *LO renormalization group equations*, since they were originally derived from the operator product expansion for the unpolarized structure functions. The moments $P_{ij}^{(0)n}$ are called *anomalous dimensions* (there is actually a factor between the two) and they determine the logarithmic dependence on Q^2 for the parton distributions and so for g_1. The solution to Eq. (C.3) is very straightforward:

$$\begin{aligned} \Delta q_{NS}^n(Q^2) &= L^{-\frac{2}{\beta_0}P_{NS}^{(0)n}} \Delta q_{NS}^n \\ \begin{pmatrix} \Delta\Sigma^n(Q^2) \\ \Delta G^n(Q^2) \end{pmatrix} &= L^{-\frac{2}{\beta_0}\hat{P}^{(0)n}} \begin{pmatrix} \Delta\Sigma^n(Q_0^2) \\ \Delta G^n(Q_0^2) \end{pmatrix} , \end{aligned} \tag{C.4}$$

where $L = \alpha_s(Q^2)/\alpha_s(Q_0^2)$. One then just has to diagonalize the matrix $\hat{P}^{(0)}$ and find the two eigenvalues $\lambda_\pm$. This can be achieved with the help of the two projection matrices $\hat{P}_\pm$ that project the two eigenvalues $\lambda_\pm$:

$$\hat{P}_\pm = \pm\frac{\hat{P}^{(0)n} - \lambda_\mp^n \hat{I}}{\lambda_+^n - \lambda_-^n} \tag{C.5}$$

$$\lambda_\pm^n = \frac{1}{2}\left[P_{qq}^{(0)n} + P_{GG}^{(0)n} \pm \sqrt{(P_{qq}^{(0)n} - P_{GG}^{(0)n})^2 + 8n_f P_{qG}^{(0)n} P_{Gq}^{(0)n}}\right] , \tag{C.6}$$

where $\hat{I}$ is the identity matrix. The projection matrices have the usual properties $\hat{P}_\pm^2 = \hat{P}_\pm$, $\hat{P}_+\hat{P}_- = \hat{P}_-\hat{P}_+ = 0$, and $\hat{P}_+ + \hat{P}_- = \hat{I}$. The matrix $\hat{P}^{(0)n}$ can then be decomposed into:

$$\hat{P}^{(0)n} = \lambda_+^n \hat{P}_+ + \lambda_-^n \hat{P}_- , \tag{C.7}$$

and the matrix expression in Eq. (C.4) becomes:

$$L^{-\frac{2}{\beta_0}\hat{P}^{(0)n}} = L^{-\frac{2}{\beta_0}\lambda_+^n}\hat{P}_+ + L^{-\frac{2}{\beta_0}\lambda_-^n}\hat{P}_- . \tag{C.8}$$

The solutions to the evolution equations for the n-moments are:

$$\begin{aligned} \Delta\Sigma^n(Q^2) &= L^{-\frac{2}{\beta_0}\lambda_-^n}\left[\alpha_n\Delta\Sigma^n(Q_0^2) + \beta_n\Delta G^n(Q_0^2)\right] \\ &+ L^{-\frac{2}{\beta_0}\lambda_+^n}\left[(1-\alpha_n)\Delta\Sigma^n(Q_0^2) - \beta_n\Delta G^n(Q_0^2)\right] \\ \Delta G^n(Q^2) &= L^{-\frac{2}{\beta_0}\lambda_-^n}\left[(1-\alpha_n)\Delta G^n(Q_0^2) + \frac{\alpha_n(1-\alpha_n)}{\beta_n}\Delta\Sigma^n(Q_0^2)\right] \\ &+ L^{-\frac{2}{\beta_0}\lambda_+^n}\left[\alpha_n\Delta G^n(Q_0^2) - \frac{\alpha_n(1-\alpha_n)}{\beta_n}\Delta\Sigma^n(Q_0^2)\right] , \end{aligned} \tag{C.9}$$

where

$$\alpha_n = \frac{P_{qq}^{(0)n} - \lambda_+^n}{\lambda_-^n - \lambda_+^n}$$

$$\beta_n = \frac{2n_f P_{qG}^{(0)n}}{\lambda_-^n - \lambda_+^n}\,. \tag{C.10}$$

Once the distributions are fixed at a particular scale Q_0^2 (by experiment or theoretical assumptions) their evolution is determined by the QCD dynamics of the anomalous dimensions at leading order in α_s. After obtaining the n-moments one has to invert them to obtain the parton distributions. This can be achieved by a numerical integration, by using the formula:

$$f(x,Q^2) = \frac{1}{\pi}\int_0^\infty dz\ \mathrm{Im}\left[e^{i\phi}e^{-(c+ze^{i\phi})}\ f^{n=c+ze^{i\phi}}(Q^2)\right] \tag{C.11}$$

C.2 NLO case

In momentum space the evolution equations are simply given by:

$$\begin{aligned}
\frac{d}{dt}\Delta q^n_{NS\pm}(Q^2) &= \left[\frac{\alpha_s(Q^2)}{2\pi}P^{(0)n}_{NS} + \left(\frac{\alpha_s(Q^2)}{2\pi}\right)^2 P^{(1)n}_{NS\pm}\right]\Delta q^n_{NS\pm}(Q_0^2)\\
\frac{d}{dt}\begin{pmatrix}\Delta\Sigma^n(Q^2)\\ \Delta G^n(Q^2)\end{pmatrix} &= \left[\frac{\alpha_s(Q^2)}{2\pi}\begin{pmatrix}P^{(0)n}_{qq} & 2n_f P^{(0)n}_{qG}\\ P^{(0)n}_{Gq} & P^{(0)n}_{GG}\end{pmatrix} + \right.\\
&+ \left.\left(\frac{\alpha_s(Q^2)}{2\pi}\right)^2\begin{pmatrix}P^{(1)n}_{qq} & 2n_f P^{(1)n}_{qG}\\ P^{(1)n}_{Gq} & P^{(1)n}_{GG}\end{pmatrix}\right]\otimes\begin{pmatrix}\Delta\Sigma^n(Q_0^2)\\ \Delta G^n(Q_0^2)\end{pmatrix}\\
&= \left[\frac{\alpha_s(Q^2)}{2\pi}\hat{P}^{(0)n} + \left(\frac{\alpha_s(Q^2)}{2\pi}\right)^2\hat{P}^{(1)n}\right]\otimes\begin{pmatrix}\Delta\Sigma^n(Q_0^2)\\ \Delta G^n(Q_0^2)\end{pmatrix}\,.
\end{aligned} \tag{C.12}$$

The solutions to these equations are a generalization of Eq. (C.4):

$$\begin{aligned}
\Delta q^n_{NS\pm}(Q^2) &= \left\{1 - \frac{2}{\beta_0}\frac{\alpha_s(Q^2)-\alpha_s(Q_0^2)}{2\pi}\left(P^{(1)n}_{NS\pm} - \frac{\beta_1}{2\beta_0}P^{(0)n}_{NS}\right)\right\}\times\\
&\times\ L^{-\frac{2}{\beta_0}P^{(0)n}_{NS}}\Delta q^n_{NS\pm}(Q_0^2)\\
\begin{pmatrix}\Delta\Sigma^n(Q^2)\\ \Delta G^n(Q^2)\end{pmatrix} &= \left\{L^{-\frac{2}{\beta_0}\hat{P}^{(0)n}} + \frac{\alpha_s(Q^2)}{2\pi}\hat{U}L^{-\frac{2}{\beta_0}\hat{P}^{(0)n}} - \frac{\alpha_s(Q_0^2)}{2\pi}L^{-\frac{2}{\beta_0}\hat{P}^{(0)n}}\hat{U}\right\}\times\\
&\times\ \begin{pmatrix}\Delta\Sigma^n(Q_0^2)\\ \Delta G^n(Q_0^2)\end{pmatrix}
\end{aligned} \tag{C.13}$$

where, as before, $L = \alpha_s(Q^2)/\alpha_s(Q_0^2)$. Also,

$$\begin{aligned}
\hat{U} &= -\frac{2}{\beta_0}(\hat{P}_+\hat{R}\hat{P}_+ + \hat{P}_-\hat{R}\hat{P}_-) + \frac{\hat{P}_-\hat{R}\hat{P}_+}{\lambda_+^n - \lambda_-^n - \frac{1}{2}\beta_0} + \frac{\hat{P}_+\hat{R}\hat{P}_-}{\lambda_-^n - \lambda_+^n - \frac{1}{2}\beta_0} \\
\hat{R} &= \hat{P}^{(1)n} - \frac{\beta_1}{2\beta_0}\hat{P}^{(0)n}
\end{aligned} \tag{C.14}$$

and $\hat{P}_\pm$ are the matrices that project the two eigenvalues $\lambda_\pm$, already defined in Eq. (C.5). The explicit form of the solution in Eq. (C.13) can be found ([20]) by using the property given in Eq. (C.8).

The solutions for the nth moment of the quark distributions can be inverted to get Δq, or they can be used to get the n-th moments of g_1:

$$\mathrm{g}_1^n(Q^2) = \frac{1}{2}\sum_{q,\bar{q}} e_q^2 \left[\left(1 + \frac{\alpha_s}{2\pi}C_q^n\right)\Delta q^n + \frac{\alpha_s}{2\pi}2C_G^n\Delta G^n(Q^2)\right] . \tag{C.15}$$

By comparing Eq. (4.32) and Eq. (C.15) it appears clear that the Wilson coefficient functions C_i^n are the first order approximation in α_s of the coefficients E_i^q introduced in section 4.1:

$$\begin{aligned}
E_q^n &= 1 + \frac{\alpha_s}{2\pi}C_q^n \\
E_G^n &= 0 + \frac{\alpha_s}{2\pi}C_G^n.
\end{aligned} \tag{C.16}$$

In any NLO (and beyond) treatment Wilson coefficients and splitting functions are not uniquely defined, but the measurable quantity g_1 has to be independent of the scheme convention. The requirements of convention independence can be easily derived, using eqs(C.13) and (C.15). Let us suppose that we choose a different factorization scheme in the NS sector:

$$C_{NS}^n \to C_{NS}'^n = C_{NS}^n + \Delta_{NS}^n . \tag{C.17}$$

Up to order $\mathcal{O}(\alpha_s^2)$ also the splitting functions $P_{NS}^{(1)}$ need to be redefined:

$$P_{NS}^{(1)n} \to P_{NS}'^{(1)n} = P_{NS}^{(1)n} + \frac{\beta_0}{2}\Delta_{NS}^n . \tag{C.18}$$

Similarly, in the singlet sector, a change in the factorization scheme brings a change in the matrix $\hat{P}^{(1)}$:

$$\begin{aligned}
\hat{C}^n &\to \hat{C}'^n = \hat{C}^n + \hat{\Delta}^n \\
\hat{P}^{(1)n} &\to \hat{P}'^{(1)n} = \hat{P}^{(1)n} + \frac{\beta_0}{2}\hat{\Delta}^n - [\hat{\Delta}^n, \hat{P}^{(0)}] ,
\end{aligned} \tag{C.19}$$

where the upper row in the $\hat{C}$ matrix corresponds to the quark $C_q = C_{qq}$ and gluon $C_G = C_{qG}$ Wilson coefficients, while the second row is introduced to keep the treatment as symmetric as possible, and it does not bring any contribution. It is worth noting that the transformations of the splitting functions in Eq. (C.19) are not fixed by the change in the first row of the coefficient functions alone, since the lower row in $\hat{\Delta}$ remains undetermined. From all these results, it is clear that a consistent (factorization scheme independent) analysis of g_1 requires the knowledge of *all* splitting functions $P^{(1)}$ and coefficient functions $C_{q,G}$. Such an analysis has been performed in very few schemes.

Appendix D

χ^2 distribution and z^2 test

D.1 χ^2 distribution

Let us consider a quantity x taken from a gaussian distribution with true mean equal to zero and variance $\sigma^2 = 1$. The probability of measuring a value of x between a and b is ([38]):

$$P(a < x < b) = \frac{1}{\sqrt{2\pi}} \int_a^b e^{-x^2/2} dx \; . \tag{D.1}$$

Given N measurements of x, let us define the χ^2 as the sum of the squares of the measured values:

$$\chi^2 = x_1^2 + x_2^2 + ... + x_N^2 \; . \tag{D.2}$$

The probability distribution of χ^2 is:

$$\begin{aligned} P(\chi^2) &= P(x_1^2 + x_2^2 + ... + x_N^2 < \chi^2) = \\ &= \left(\frac{1}{\sqrt{2\pi}}\right)^{N/2} \int_{x_1^2+x_2^2+...+x_N^2<\chi^2} e^{-(x_1^2+x_2^2+...+x_N^2)/2} dx_1 ... dx_N \\ &= \left(\frac{1}{\sqrt{2\pi}}\right)^{N/2} \int_{r^2<\chi^2} e^{-r^2/2} dV_N \\ &= \frac{1}{2^{N/2}\Gamma\left(\frac{N}{2}\right)} \int_0^{\chi^2} e^{-u/2} u^{N/2-1} du \; , \end{aligned} \tag{D.3}$$

where dV_N is the element of volume of a N-dimensional sphere:

$$dV_N = \frac{N\pi^{N/2} r^{N-1}}{\Gamma(1 + N/2)} \, dr \; , \tag{D.4}$$

with $r^2 = x_1^2 + x_2^2 + ... + x_N^2$, and $u = r^2$. The probability density $f(\chi^2)$ is the derivative of the probability distribution $P(\chi^2)$:

$$f(\chi^2) = \frac{1}{2^{N/2}\Gamma\left(\frac{N}{2}\right)} e^{-\chi^2/2}(\chi^2)^{N/2-1} \; . \tag{D.5}$$

The expectation value of χ^2 is*:

$$E(\chi^2) = \frac{1}{2^{N/2}\Gamma\left(\frac{N}{2}\right)} \int_0^\infty \chi^2 e^{-\chi^2/2}(\chi^2)^{N/2-1} d\chi^2 = N \; , \tag{D.6}$$

where we used the fact that $\Gamma(x) = \int_0^\infty e^{-t} t^{x-1} dt$.

The variance of the distribution is

$$\sigma_{\chi^2}^2 = E((\chi^2)^2) - (E(\chi^2))^2 = N(N+2) - N^2 = 2N \; . \tag{D.7}$$

In the general case of a distribution with measured mean $\bar{x}$ and variance σ^2 the χ^2 is defined as:

$$\chi^2 = \sum_{i=1}^{N} \frac{(x_i - \bar{x})^2}{\sigma^2} \; . \tag{D.8}$$

In this case it's important to notice that the expectation value of χ^2 will not be N but $N-1$, since the meaning of N in eqs.(D.6) and (D.7) is that of total degrees of freedom, and in Eq. (D.8) the total degrees of freedom are $N-1$, because of the condition on the average: $\sum x_i/N = \bar{x}$.

Fig. D.1 shows the probability density $f(\chi^2)$ for different values of N, compared to the gaussian distribution with same variance and mean value. The two distributions tend to overlap for large N.

D.2 z^2 test

Let us consider the general case of measuring x_i with different accuracies σ_i. Let us also suppose that the errors are randomly distributed around zero, i.e.:

$$x_i = x + \varepsilon_i \quad \text{with} \quad E(\varepsilon_i) = 0, \quad E(\varepsilon_i^2) = \sigma_i^2 \; . \tag{D.9}$$

*The expectation value $E(x)$ of a quantity x can be obtained from its probability density f as $E(x) = \int x f(x) dx$

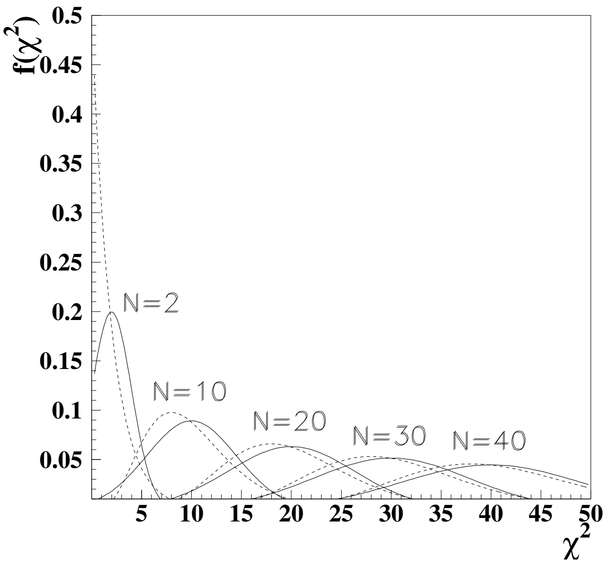

Figure D.1: χ^2 distributions (dashed) and gaussian distributions (solid) having same variance $2N$ and mean value N. As N increases the two distributions tend to overlap.

The weighted average $\bar{x}$ is given by $\bar{x} = \sum_i \frac{x_i}{\sigma_i^2} / \sum_i \frac{1}{\sigma_i^2}$, which gives a best estimate for the errors ε_i given by:

$$\bar{\varepsilon}_i = x_i - \bar{x} \; . \tag{D.10}$$

We expect, in absence of any bias on the measurement, that these quantities are normally distributed around zero with variance σ_i^2, so that $\bar{\varepsilon}_i/\sigma_i$ are expected to follow a gaussian distribution with mean equal to zero, and unit variance. In this case, the sum

$$z^2 = \frac{1}{N-1} \sum_{i=1}^{N} \left(\frac{\bar{\varepsilon}_i}{\sigma_i} \right)^2 \tag{D.11}$$

follows a χ^2 distribution with expectation value equal to 1 and variance equal to $2(N-1)$. Using normal propagation of errors, we get, for the expectation value of z and its 68% confidence limit, the values:

$$z = 1 \pm \frac{1}{\sqrt{2(N-1)}} \; . \tag{D.12}$$

Appendix E

Statistical errors

E.1 Independent variables

Given M independent measurements E_i of the same quantity E with different standard deviations σ_i, the best estimate for E is given by the weighted mean:

$$E = \frac{\sum_{i=1}^{M} \frac{E_i}{\sigma_i^2}}{\sum_{i=1}^{M} \frac{1}{\sigma_i^2}} \quad , \quad \frac{1}{\sigma^2} = \sum_{i=1}^{M} \frac{1}{\sigma_i^2} \ , \tag{E.1}$$

where σ is the standard deviation in the weighted mean. For example, if two quantities $E_A \pm \sigma_A$ and $E_B \pm \sigma_B$ are calculated from different data sets, namely A and B, with $A \cap B = \varnothing$, then they are independent, and the best estimate of E, over the whole data set A+B is given by the weighted mean.

The error of any function $f(E_A, E_B)$ has the form:

$$\sigma_f = \sqrt{\left(\frac{\partial f}{\partial E_A}\sigma_A\right)^2 + \left(\frac{\partial f}{\partial E_B}\sigma_B\right)^2} \ . \tag{E.2}$$

E.2 Correlated variables

When the statistics involved in calculating E_A and E_B are not independent, the error for a function $f(E_A, E_B)$ has the expression:

$$\sigma_f = \sqrt{\left(\frac{\partial f}{\partial E_A}\sigma_A\right)^2 + \left(\frac{\partial f}{\partial E_B}\sigma_B\right)^2 + 2\frac{\partial f}{\partial E_A}\frac{\partial f}{\partial E_B}\mathrm{cov}(E_A, E_B)} \ , \tag{E.3}$$

where the last term takes care of the correlations between E_A and E_B.

Given a large number N of measurements E_{A_i}, the standard deviation σ_A is empirically defined as:

$$\sigma_A^2 = \frac{1}{N-1}\sum_{i=1}^{N}(E_{A_i} - E_A)^2 \;, \tag{E.4}$$

while the covariance between E_A and E_B is given by:

$$\mathrm{cov}(E_A, E_B) = \frac{1}{N-1}\sum_{i=1}^{N}(E_{A_i} - E_A)(E_{B_i} - E_B) \;, \tag{E.5}$$

where E_A and E_B are the averages of E_{A_i} and E_{B_i}*. When E_A and E_B are independent, over a large number N of measurements they will fluctuate around their average in an uncorrelated way, so that the covariance is zero and one recovers the usual formula for the propagation of errors in a function of independent variables. From Eq. (E.4) it follows that

$$\mathrm{cov}(E_A, E_A) = \sigma_A^2 \;, \tag{E.6}$$

while the linearity properties of the covariance follow from Eq. (E.5):

$$\mathrm{cov}(aE_A + bE_B, E_c) = a\,\mathrm{cov}(E_A, E_c) + b\,\mathrm{cov}(E_B, E_c) \tag{E.7}$$

that will prove to be useful later (here a and b are constants).

It is worth noting that the covariance is a property only of E_A and E_B, and not of the specific form of the function f.

E.2.1 Totally correlated variables

In this case in which the set A is divided into M disjunct samples, the relation

$$\frac{E_A}{\sigma_A^2} = \sum_{i=1}^{M}\frac{E_i}{\sigma_i^2} \tag{E.8}$$

holds (see Eq. (E.1)), where the indices i indicate the independent subsets of A. If B is a subset of A, then for a particular bin corresponding to set B, the relation between E_A and E_B is given by the weighted mean:

$$E_A = \frac{\sigma_A^2}{\sigma_B^2}E_B + \frac{\sigma_A^2}{\sigma_{A-B}^2}E_{A-B} \;, \tag{E.9}$$

*The averaged value of E is supposed to be a good approximation of the *true* value, so they are assumed to be equal, and no distinction is going to be made between the two.

where the remaining terms containing the values of E_i in the other bins i have gone into $A-B$. The relation between E_A and E_B is then linear and one can apply eqs.(E.6) and (E.7) to get the covariance $\mathrm{cov}(E_A, E_B)$:

$$\mathrm{cov}(E_A, E_B) = \frac{\sigma_A^2}{\sigma_B^2}\mathrm{cov}(E_B, E_B) + \frac{\sigma_A^2}{\sigma_{A-B}^2}\mathrm{cov}(E_{A-B}, E_B) = \frac{\sigma_A^2}{\sigma_B^2}\sigma_B^2 = \sigma_A^2\ , \tag{E.10}$$

where the independence of E_{A-B} and E_B was used, giving $\mathrm{cov}(E_{A-B}, E_B) = 0$.

The standard deviation in f is then:

$$\sigma_f = \sqrt{\left(\frac{\partial f}{\partial E_A}\right)^2 \sigma_A^2 + \left(\frac{\partial f}{\partial E_B}\right)^2 \sigma_B^2 + 2\frac{\partial f}{\partial E_A}\frac{\partial f}{\partial E_B}\sigma_A^2} \qquad B \subseteq A\ . \tag{E.11}$$

E.2.2 Partially correlated variables

A more difficult case is when the two quantities E_A and E_B under consideration are calculated using two data sets that have a non zero intersection. In this case the two quantities are said to be only partially correlated.

To calculate the covariance two sets A' and B' are introduced, such that $A = A' + A \cap B$ and $B = B' + A \cap B$. It must be:

$$\begin{aligned} \frac{E_A}{\sigma_A^2} &= \frac{E_{A'}}{\sigma_{A'}^2} + \frac{E_{A\cap B}}{\sigma_{A\cap B}^2} \\ \frac{E_B}{\sigma_B^2} &= \frac{E_{B'}}{\sigma_{B'}^2} + \frac{E_{A\cap B}}{\sigma_{A\cap B}^2}\ , \end{aligned} \tag{E.12}$$

so that

$$E_A = \frac{\sigma_A^2}{\sigma_{A'}^2}E_{A'} + \frac{\sigma_A^2}{\sigma_B^2}E_B - \frac{\sigma_A^2}{\sigma_{B'}^2}E_{B'}\ . \tag{E.13}$$

The covariance $\mathrm{cov}(E_A, E_B)$ is:

$$\begin{aligned} \mathrm{cov}(E_A, E_B) &= \frac{\sigma_A^2}{\sigma_{A'}^2}\mathrm{cov}(E_{A'}, E_B) + \frac{\sigma_A^2}{\sigma_B^2}\mathrm{cov}(E_B, E_B) - \frac{\sigma_A^2}{\sigma_{B'}^2}\mathrm{cov}(E_{B'}, E_B) \\ &= \sigma_A^2 - \frac{\sigma_A^2}{\sigma_{B'}^2}\mathrm{cov}(E_{B'}, E_B) \\ &= \sigma_A^2 - \frac{\sigma_A^2}{\sigma_{B'}^2}\sigma_B^2\ , \end{aligned} \tag{E.14}$$

where the fact that $\text{cov}(E_{A'}, E_B) = 0$ was used (A' and B are independent) together with $\text{cov}(E_B, E_{B'}) = \sigma_B^2$ as follows from Eq. (E.10), since $B' \subseteq B$. Using the relation $\frac{1}{\sigma_B^2} = \frac{1}{\sigma_{B'}^2} + \frac{1}{\sigma_{A\cap B}^2}$, one gets the covariance in the case of partially correlated variables:

$$\text{cov}(E_A, E_B) = \frac{\sigma_A^2 \sigma_B^2}{\sigma_{A\cap B}^2} \,. \tag{E.15}$$

This expression recovers both the errors for the case of independent variables and the one for totally correlated, in the two limits of $\sigma_{A\cap B} = \infty$ and $\sigma_B = \sigma_{A\cap B}$. In this case however the knowledge of $E_A \pm \sigma_A$ and $E_B \pm \sigma_B$ alone is not enough to calculate the error in any expression including A and B, since one also needs the error in the intersection $A \cap B$.

Table E.1 contains a compilation of errors for some functions, for the three cases of independent, completely and partially correlated quantities.

Independent		Completely Correlated		Partially Correlated	
f	σ_f	f	σ_f	f	σ_f
$E_A - E_B$	$\sqrt{\sigma_A^2 + \sigma_B^2}$	$E_A - E_B$	$\sqrt{\lvert\sigma_A^2 - \sigma_B^2\rvert}$	$E_A - E_B$	$\sqrt{\sigma_A^2 + \sigma_B^2 - 2\frac{\sigma_A^2\sigma_B^2}{\sigma_{A\cap B}^2}}$
$\frac{E_A - E_B}{\sqrt{\sigma_A^2 + \sigma_B^2}}$	1	$\frac{E_A - E_B}{\sqrt{\lvert\sigma_A^2 - \sigma_B^2\rvert}}$	1	$\frac{E_A - E_B}{\sqrt{\sigma_A^2 + \sigma_B^2 - 2\frac{\sigma_A^2\sigma_B^2}{\sigma_{A\cap B}^2}}}$	1
$\frac{E_A}{E_B}$	$\frac{E_A}{E_B}\sqrt{\frac{\sigma_A^2}{{E_A}^2} + \frac{\sigma_B^2}{{E_B}^2}}$	$\frac{E_A}{E_B}$	$\frac{E_A}{E_B}\sqrt{\frac{\sigma_A^2}{{E_A}^2} + \frac{\sigma_B^2}{{E_B}^2} - \frac{2}{E_A E_B}\sigma_A^2}$	$\frac{E_A}{E_B}$	$\frac{E_A}{E_B}\sqrt{\frac{\sigma_A^2}{{E_A}^2} + \frac{\sigma_B^2}{{E_B}^2} - \frac{2}{E_A E_B}\frac{\sigma_A^2\sigma_B^2}{\sigma_{A\cap B}^2}}$

Table E.1: This table shows the errors for some simple functions, useful to check the agreement between two quantities E_A and E_B. The cases of complete independence, complete and partial correlation (that is one of the two, either E_A or E_B, is calculated over a data set that is included in the other) are considered.

Appendix F

Tables with numerical results

			TOP				BOTTOM			
bin	y bin	x bin	$N_{\mathrm{cs}}^{\stackrel{\Rightarrow}{\rightarrow}}$	$N_{\mathrm{dis}}^{\stackrel{\Rightarrow}{\rightarrow}}$	$N_{\mathrm{cs}}^{\stackrel{\Leftarrow}{\rightarrow}}$	$N_{\mathrm{dis}}^{\stackrel{\Leftarrow}{\rightarrow}}$	$N_{\mathrm{cs}}^{\stackrel{\Rightarrow}{\rightarrow}}$	$N_{\mathrm{dis}}^{\stackrel{\Rightarrow}{\rightarrow}}$	$N_{\mathrm{cs}}^{\stackrel{\Leftarrow}{\rightarrow}}$	$N_{\mathrm{dis}}^{\stackrel{\Leftarrow}{\rightarrow}}$
1	1	1	20619	21845	20219	21362	4244	13449	4281	13045
2	1	2	4317	9593	4214	9626	1928	7878	1890	7724
3	1	3	3540	10895	3481	10480	2077	9517	2132	9111
4	1	4	3299	11984	3187	11715	2393	11046	2251	10875
5	1	5	3091	13832	3005	13493	2615	12570	2486	12500
6	1	6	2922	14920	2760	14457	2585	13681	2539	13565
7	1	7	2630	15563	2513	15335	2435	14717	2374	14690
8	1	8	2283	15473	2227	15311	2280	14867	2224	14829
9	1	9	74	9792	76	9407	72	9550	88	9287
10	2	9	2023	7118	1968	6866	2022	6726	1968	6497
11	1	10	40	10149	36	9923	62	9986	37	9749
12	2	10	1724	7751	1701	7536	1851	7296	1779	7098
13	1	11	22	9946	17	9935	23	9706	19	9758
14	2	11	1278	8147	1216	8204	1380	7770	1364	7837
15	1	12	19	10971	16	10812	15	10727	9	10442
16	2	12	971	8159	934	8082	997	7747	991	7610
17	1	13	13	11610	14	11741	8	11355	13	11052
18	2	13	612	8060	598	7735	697	7513	664	7443
19	1	14	7	12606	7	12258	12	11975	12	11922
20	2	14	343	7187	355	7320	399	7112	371	7124
21	1	15	2	13305	2	12963	3	12491	6	12512
22	2	15	193	6793	182	6990	212	6775	219	6704
23	1	16	1	9925	2	9606	0	9101	1	9036
24	2	16	4	6348	5	6332	1	6046	5	6201
25	3	16	86	4034	83	4066	83	3891	92	3884
26	1	17	0	10024	1	10003	2	9527	2	9396
27	2	17	1	5675	3	5879	1	5707	5	5724
28	3	17	42	3762	32	3993	48	3796	36	3871
29	1	18	1	10741	1	10928	4	9820	1	9881
30	2	18	1	5219	1	5205	2	4961	2	4996
31	3	18	15	3581	11	3534	19	3498	17	3674
32	1	19	2	10731	2	10909	1	9829	1	9650
33	2	19	1	4939	2	5229	1	4834	3	4883
34	3	19	6	3155	8	3295	8	3022	8	3285
35	1	20	0	10483	1	10801	1	9792	0	9619
36	2	20	2	4332	2	4351	0	3936	2	4137
37	3	20	2	2655	6	2764	7	2609	2	2710
38	1	21	0	10153	0	10166	0	9187	2	9103
39	2	21	0	3311	1	3431	0	3037	0	3140
40	3	21	2	2173	3	2374	1	2200	1	2342
41	1	22	0	8563	1	8548	0	7744	1	7540
42	2	22	0	2670	0	2788	1	2457	0	2564
43	3	22	2	1816	0	2048	1	1755	1	1880
44	1	23	0	8045	0	8299	1	7473	1	7703
45	2	23	0	1391	1	1562	0	1332	1	1440
46	1	24	0	6551	0	6828	0	5997	1	6295
47	1	25	0	4106	0	4223	1	3766	0	3841
48	1	26	0	2030	0	2114	1	1825	1	1998
49	1	27	0	680	1	778	0	657	1	649

Table F.1: Events selected from the 98b4 production

			TOP				BOTTOM			
x bin	y bin	bin	$N_{\mathrm{cs}}^{\overset{\Rightarrow}{\rightarrow}}$	$N_{\mathrm{dis}}^{\overset{\Rightarrow}{\rightarrow}}$	$N_{\mathrm{cs}}^{\overset{\Leftarrow}{\rightarrow}}$	$N_{\mathrm{dis}}^{\overset{\Leftarrow}{\rightarrow}}$	$N_{\mathrm{cs}}^{\overset{\Rightarrow}{\rightarrow}}$	$N_{\mathrm{dis}}^{\overset{\Rightarrow}{\rightarrow}}$	$N_{\mathrm{cs}}^{\overset{\Leftarrow}{\rightarrow}}$	$N_{\mathrm{dis}}^{\overset{\Leftarrow}{\rightarrow}}$
1	1	1	23230	78801	23594	79541	23296	84283	23314	84198
2	1	2	10088	47367	10070	47859	10243	50478	9941	51030
3	1	3	11310	56497	11382	56755	11387	60243	11291	60690
4	1	4	12335	66716	12327	67361	12548	70069	12439	70714
5	1	5	13361	76912	13511	77147	13648	80974	13615	81944
6	1	6	13770	84854	13506	86535	13793	88766	13658	88879
7	1	7	13237	91006	13322	92107	13396	93955	12953	95161
8	1	8	12149	91307	12146	93457	12065	95820	12219	96179
9	1	9	474	58056	461	58735	425	61259	413	61829
10	2	9	10859	41958	11148	42439	10884	42567	10899	43493
11	1	10	255	61416	266	62015	239	64525	285	65351
12	2	10	9804	45792	9970	46399	9656	47015	9790	47360
13	1	11	136	60941	155	61644	157	64228	135	65104
14	2	11	7706	49595	7767	50413	7630	51057	7458	52798
15	1	12	91	66918	102	68192	94	70155	108	71665
16	2	12	5682	49596	5651	50826	5624	51323	5661	52401
17	1	13	57	72984	71	74343	75	76957	72	77825
18	2	13	3751	48826	3784	49942	3549	50750	3647	51277
19	1	14	49	76179	38	77755	57	80643	59	82647
20	2	14	2206	46350	2205	47325	2161	47380	2141	49241
21	1	15	22	80783	35	82053	26	85372	42	87324
22	2	15	1112	43736	1131	45482	1048	45562	1101	47347
23	1	16	12	59504	10	61061	13	64340	19	64836
24	2	16	29	39688	31	41181	33	42041	32	43092
25	3	16	545	25801	563	27029	578	26056	532	27702
26	1	17	11	61833	16	63308	10	66481	11	67771
27	2	17	21	36717	11	38255	16	39129	17	40218
28	3	17	227	24760	240	26205	224	25830	256	27081
29	1	18	8	66058	7	67282	7	71099	7	72723
30	2	18	5	33132	4	34551	14	35086	19	36681
31	3	18	94	22388	95	23667	108	23409	115	24825
32	1	19	9	65959	3	67854	5	71846	4	73127
33	2	19	5	31790	6	33768	9	34218	7	35434
34	3	19	51	20094	38	21572	49	20915	44	22393
35	1	20	4	64185	6	66216	6	70704	3	72427
36	2	20	4	27335	5	28721	6	28899	1	30547
37	3	20	19	17116	21	18721	17	17749	30	19397
38	1	21	4	61484	7	63267	2	68317	2	70583
39	2	21	3	20453	3	22078	1	22153	1	23169
40	3	21	9	14389	11	15986	9	15001	6	16594
41	1	22	4	51270	5	53097	4	57686	1	59718
42	2	22	3	16940	1	18144	4	18524	4	19267
43	3	22	6	12117	8	13390	8	12707	3	14042
44	1	23	1	49063	3	52015	2	56091	3	58639
45	2	23	1	9276	3	10260	0	9563	3	10956
46	1	24	3	39718	3	42746	3	44475	4	47472
47	1	25	3	24015	2	26041	2	27116	1	29102
48	1	26	2	12033	3	13197	1	13622	1	14547
49	1	27	0	4146	1	4527	1	4131	2	4627

Table F.2: Events selected from the 00b1 production

				1998		2000	
bin	$< x >$	$< y >$	$< Q^2 >$	g_1/F_1	$\sigma_{stat}(g_1/F_1)$	g_1/F_1	$\sigma_{stat}(g_1/F_1)$
1	0.0041	0.8842	0.2107	-0.03438	0.04486	-0.00538	0.01305
2	0.0070	0.8612	0.3033	0.01962	0.03926	0.00417	0.01306
3	0.0085	0.8451	0.3720	-0.05434	0.03190	-0.00641	0.01100
4	0.0105	0.8264	0.4494	-0.00520	0.02749	-0.00031	0.00964
5	0.0130	0.8036	0.5369	-0.00110	0.02416	-0.00542	0.00866
6	0.0160	0.7785	0.6411	-0.00662	0.02238	-0.00314	0.00806
7	0.0190	0.7511	0.7508	0.01795	0.02109	0.00346	0.00770
8	0.0234	0.7227	0.8684	0.02229	0.02076	0.00370	0.00761
9	0.0278	0.6008	0.8619	-0.04130	0.02626	0.00392	0.00988
10	0.0278	0.8161	1.1708	-0.04768	0.03230	0.00712	0.01168
11	0.0330	0.5566	0.9542	-0.01889	0.02724	0.00697	0.01020
12	0.0330	0.7923	1.3583	-0.02722	0.02912	-0.00787	0.01061
13	0.0395	0.5085	1.0403	0.06593	0.02959	0.00994	0.01107
14	0.0395	0.7595	1.5538	0.04178	0.02616	0.02147	0.00961
15	0.0470	0.4709	1.1463	-0.01333	0.03034	0.03470	0.01129
16	0.0470	0.7352	1.7897	-0.00104	0.02523	0.01725	0.00925
17	0.0562	0.4335	1.2618	0.03447	0.03161	0.01826	0.01164
18	0.0562	0.7104	2.0678	-0.02604	0.02462	0.00523	0.00901
19	0.0670	0.3974	1.3790	0.01285	0.03308	0.04894	0.01226
20	0.0670	0.6808	2.3624	0.04661	0.02485	0.02964	0.00909
21	0.0800	0.3629	1.5018	0.01638	0.03490	0.04209	0.01292
22	0.0800	0.6508	2.6932	0.05217	0.02532	0.05135	0.00921
23	0.0954	0.2908	1.4368	0.01016	0.05117	0.03974	0.01880
24	0.0954	0.4646	2.2956	0.07554	0.03630	0.05487	0.01332
25	0.0954	0.6817	3.3683	0.03286	0.03042	0.07172	0.01109
26	0.1137	0.2608	1.5358	0.06751	0.05531	0.07843	0.02028
27	0.1137	0.4292	2.5275	0.11449	0.04016	0.07424	0.01467
28	0.1137	0.6423	3.7824	0.10270	0.03099	0.07064	0.01130
29	0.1356	0.2362	1.6589	0.14979	0.05801	0.07643	0.02120
30	0.1356	0.4047	2.8422	0.06241	0.04392	0.10224	0.01590
31	0.1356	0.6121	4.2988	0.06120	0.03223	0.08232	0.01188
32	0.1620	0.2095	1.7578	0.12938	0.06394	0.09091	0.02326
33	0.1620	0.3737	3.1355	0.18180	0.04662	0.12323	0.01692
34	0.1620	0.5800	4.8664	0.15808	0.03442	0.10847	0.01264
35	0.1930	0.1882	1.8842	0.21856	0.06922	0.14304	0.02526
36	0.1930	0.3487	3.4910	0.14384	0.05212	0.14278	0.01879
37	0.1930	0.5475	5.4813	0.11297	0.03822	0.15276	0.01388
38	0.2300	0.1730	2.0608	0.11450	0.07400	0.16634	0.02680
39	0.2300	0.3306	3.9382	0.19025	0.06026	0.16791	0.02189
40	0.2300	0.5120	6.0991	0.18789	0.04288	0.18407	0.01555
41	0.2740	0.1614	2.2896	0.03998	0.08206	0.19944	0.02968
42	0.2740	0.3062	4.3438	0.24074	0.06925	0.17399	0.02491
43	0.2740	0.4779	6.7795	0.25243	0.04882	0.18294	0.01756
44	0.3267	0.1849	3.1286	0.32244	0.06713	0.26050	0.02429
45	0.3267	0.4423	7.4840	0.26307	0.05850	0.24719	0.02094
46	0.3890	0.2113	4.2593	0.31645	0.06042	0.29640	0.02195
47	0.4640	0.2003	4.8115	0.22510	0.07637	0.34914	0.02804
48	0.5500	0.1937	5.5227	0.44695	0.10576	0.34747	0.03870
49	0.6600	0.2143	7.3221	0.34912	0.15105	0.38987	0.05706

Table F.3: The values g_1/F_1 and its statistical error, for each kinematic bin.

bin	RC	Align.	A_2	R
1	0.013079	0.000500	0.000019	0.001538
2	0.010240	0.000756	0.000032	0.001270
3	0.008581	0.000572	0.000033	0.001056
4	0.007066	0.000474	0.000035	0.000952
5	0.005711	0.000587	0.000035	0.001007
6	0.004447	0.001043	0.000032	0.000978
7	0.003407	0.000333	0.000026	0.000862
8	0.002133	0.000411	0.000016	0.000480
9	0.001566	0.001318	0.000001	0.000519
10	0.002086	0.000406	0.000006	0.000285
11	0.001672	0.001199	0.000020	0.000395
12	0.001426	0.000248	0.000014	0.000212
13	0.001973	0.000843	0.000049	0.000289
14	0.001289	0.000262	0.000043	0.000154
15	0.002238	0.000836	0.000085	0.000651
16	0.001469	0.000544	0.000080	0.000335
17	0.002337	0.002050	0.000132	0.001055
18	0.001731	0.000355	0.000130	0.000547
19	0.002246	0.001283	0.000191	0.001465
20	0.001789	0.000509	0.000192	0.000877
21	0.002069	0.000387	0.000265	0.001885
22	0.001834	0.000466	0.000269	0.001471
23	0.002243	0.002160	0.000354	0.002432
24	0.002013	0.001308	0.000344	0.002172
25	0.002182	0.000269	0.000363	0.002153
26	0.002195	0.002832	0.000452	0.002338
27	0.001712	0.002322	0.000435	0.002800
28	0.001806	0.000531	0.000450	0.002656
29	0.002944	0.003890	0.000555	0.002719
30	0.002201	0.001396	0.000526	0.003917
31	0.001900	0.000548	0.000532	0.003093
32	0.004459	0.002526	0.000659	0.003534
33	0.003390	0.001667	0.000604	0.004833
34	0.002855	0.000365	0.000598	0.003625
35	0.006417	0.003484	0.000735	0.004572
36	0.004979	0.002239	0.000648	0.005423
37	0.004103	0.001192	0.000631	0.004348
38	0.008282	0.001679	0.000793	0.005484
39	0.006105	0.001067	0.000659	0.005970
40	0.005031	0.000627	0.000624	0.005304
41	0.010004	0.002272	0.000790	0.006168
42	0.007093	0.003450	0.000613	0.006760
43	0.005852	0.000520	0.000552	0.006452
44	0.010298	0.003567	0.000634	0.007212
45	0.006398	0.000786	0.000399	0.007773
46	0.010566	0.004979	0.000369	0.008608
47	0.009563	0.003461	0.000052	0.010243
48	0.006677	0.006457	0.000421	0.012096
49	0.003846	0.005059	0.001255	0.015004

Table F.4: Systematic errors on g_1/F_1, for each kinematic bin, common to 1998 and 2000 data.

bin	Background	Target	Beam	Normalization	TSF	Total
1	0.000048	0.002063	0.000877	0.004892	0.002037	0.014380
2	0.000068	0.001830	0.000778	0.000724	0.000810	0.010592
3	0.000222	0.001710	0.000727	0.001506	0.000992	0.009046
4	0.000023	0.001550	0.000659	0.000036	0.000051	0.007342
5	0.000005	0.001350	0.000574	0.000289	0.000057	0.006018
6	0.000029	0.001111	0.000472	0.000072	0.000011	0.004825
7	0.000073	0.000873	0.000371	0.000043	0.000020	0.003656
8	0.000084	0.000524	0.000223	0.000155	0.000006	0.002303
9	0.000142	0.000178	0.000076	0.000144	0.000000	0.002130
10	0.000164	0.000178	0.000076	0.000090	0.000000	0.002161
11	0.000058	0.000230	0.000098	0.000290	0.000000	0.002130
12	0.000083	0.000230	0.000098	0.000186	0.000000	0.001498
13	0.000176	0.000737	0.000313	0.000794	0.000000	0.002448
14	0.000111	0.000737	0.000313	0.000531	0.000000	0.001640
15	0.000031	0.001317	0.000560	0.000393	0.000000	0.002888
16	0.000002	0.001317	0.000560	0.000325	0.000000	0.002174
17	0.000067	0.002024	0.000860	0.000707	0.000000	0.004016
18	0.000050	0.002024	0.000860	0.000198	0.000000	0.002884
19	0.000021	0.002844	0.001209	0.000635	0.000000	0.004339
20	0.000076	0.002844	0.001209	0.000607	0.000000	0.003767
21	0.000023	0.003820	0.001623	0.000712	0.000000	0.005078
22	0.000072	0.003820	0.001623	0.000655	0.000000	0.004845
23	0.000009	0.004958	0.002107	0.000830	0.000000	0.006742
24	0.000070	0.004958	0.002107	0.000925	0.000000	0.006363
25	0.000030	0.004958	0.002107	0.000540	0.000000	0.006239
26	0.000031	0.006287	0.002672	0.001266	0.000000	0.008172
27	0.000053	0.006287	0.002672	0.001204	0.000000	0.008030
28	0.000047	0.006287	0.002672	0.000969	0.000000	0.007643
29	0.000000	0.007844	0.003334	0.001868	0.000000	0.010374
30	0.000000	0.007844	0.003334	0.000909	0.000000	0.009791
31	0.000000	0.007844	0.003334	0.000730	0.000000	0.009323
32	0.000000	0.009670	0.004110	0.001853	0.000000	0.012370
33	0.000000	0.009670	0.004110	0.001704	0.000000	0.012300
34	0.000000	0.009670	0.004110	0.001353	0.000000	0.011576
35	0.000000	0.011744	0.004991	0.002517	0.000000	0.015618
36	0.000000	0.011744	0.004991	0.001493	0.000000	0.014990
37	0.000000	0.011744	0.004991	0.001077	0.000000	0.014197
38	0.000000	0.014122	0.006002	0.001915	0.000000	0.018473
39	0.000000	0.014122	0.006002	0.001810	0.000000	0.017698
40	0.000000	0.014122	0.006002	0.001581	0.000000	0.017093
41	0.000000	0.016811	0.007145	0.001446	0.000000	0.021901
42	0.000000	0.016811	0.007145	0.002177	0.000000	0.021135
43	0.000000	0.016811	0.007145	0.002032	0.000000	0.020353
44	0.000000	0.019832	0.008429	0.003119	0.000000	0.025402
45	0.000000	0.019832	0.008429	0.002123	0.000000	0.023895
46	0.000000	0.023124	0.009828	0.002912	0.000000	0.029162
47	0.000000	0.026684	0.011341	0.002261	0.000000	0.032467
48	0.000000	0.030226	0.012846	0.003803	0.000000	0.036412
49	0.000000	0.033914	0.014413	0.002954	0.000000	0.040419

Table F.5: Systematic errors on g_1/F_1, for each kinematic bin, for 1998 data.

bin	Background	Target	Beam	Normalization	Total
1	0.000008	0.000215	0.000108	0.000927	0.013213
2	0.000014	0.000167	0.000083	0.000947	0.010391
3	0.000026	0.000257	0.000128	0.000963	0.008723
4	0.000001	0.000012	0.000006	0.000991	0.007214
5	0.000024	0.000217	0.000108	0.001027	0.005924
6	0.000014	0.000126	0.000063	0.001069	0.004794
7	0.000014	0.000138	0.000069	0.001117	0.003706
8	0.000014	0.000148	0.000074	0.001170	0.002519
9	0.000013	0.000157	0.000078	0.001449	0.002567
10	0.000024	0.000285	0.000142	0.001027	0.002399
11	0.000021	0.000279	0.000139	0.001589	0.002648
12	0.000024	0.000315	0.000157	0.001058	0.001840
13	0.000026	0.000397	0.000199	0.001770	0.002832
14	0.000057	0.000859	0.000429	0.001104	0.001975
15	0.000080	0.001388	0.000694	0.001935	0.003507
16	0.000040	0.000690	0.000345	0.001141	0.002114
17	0.000035	0.000730	0.000365	0.002123	0.003996
18	0.000010	0.000209	0.000105	0.001181	0.002211
19	0.000080	0.001958	0.000979	0.002336	0.004374
20	0.000048	0.001186	0.000593	0.001231	0.002746
21	0.000058	0.001684	0.000842	0.002578	0.004271
22	0.000071	0.002054	0.001027	0.001285	0.003570
23	0.000037	0.001590	0.000795	0.003285	0.005449
24	0.000051	0.002195	0.001097	0.001898	0.004497
25	0.000066	0.002869	0.001434	0.001201	0.004619
26	0.000036	0.003137	0.001569	0.003667	0.006653
27	0.000034	0.002969	0.001485	0.002054	0.005621
28	0.000033	0.002826	0.001413	0.001262	0.004730
29	0.000000	0.003057	0.001529	0.004024	0.007706
30	0.000000	0.004090	0.002045	0.002153	0.006925
31	0.000000	0.003293	0.001646	0.001300	0.005385
32	0.000000	0.003636	0.001818	0.004495	0.008713
33	0.000000	0.004929	0.002465	0.002302	0.008583
34	0.000000	0.004339	0.002169	0.001348	0.006865
35	0.000000	0.005722	0.002861	0.004915	0.011826
36	0.000000	0.005711	0.002856	0.002412	0.010307
37	0.000000	0.006110	0.003055	0.001405	0.009285
38	0.000000	0.006654	0.003327	0.005197	0.013582
39	0.000000	0.006716	0.003358	0.002482	0.011706
40	0.000000	0.007363	0.003681	0.001480	0.011143
41	0.000000	0.007977	0.003989	0.005363	0.015881
42	0.000000	0.006960	0.003480	0.002619	0.013255
43	0.000000	0.007317	0.003659	0.001563	0.012076
44	0.000000	0.010420	0.005210	0.004433	0.018071
45	0.000000	0.009887	0.004944	0.001663	0.015070
46	0.000000	0.011856	0.005928	0.003670	0.019996
47	0.000000	0.013966	0.006983	0.003714	0.021586
48	0.000000	0.013899	0.006949	0.003683	0.022086
49	0.000000	0.015595	0.007797	0.003173	0.024107

Table F.6: Systematic errors on g_1/F_1, for each kinematic bin, for 2000 data.

Appendix G

I joined the HERMES collaboration in January 1999. I spent the summer of 1999 in Hamburg, where I became acquainted with the detector, the data analysis and the life in a big collaboration. TRD maintainance and data quality were among my duties in that period, and whenever I was in Hamburg. In that period I started building a code that could perform the g_1 analysis. I first worked on data from 1997, to obtain results in agreement with the published g_1^p paper. I then started analyzing data from 1998. The analysis was done in conjunction with another PhD student, Christoph Weiskopf. Independent analysis codes were developed to extract the measured asymmetry. The agreement of the two analyses on the measured asymmetry was the starting point for further studies we both made separately: I worked on tests on the stability of the asymmetry and he worked mainly on the PID and systematic errors. Uta Stösslein was the coordinator of the g_1 group, and she focused on yet other aspects of the analysis, such as the radiative corrections. In order to be able to extend the kinematic region to low x I determined the trigger efficiencies which I have studied for all productions from 1998 to 2000. Results on g_1^d from 1998 data were released in Zeuthen in July 2001 by the HERMES collaboration.

In 2001 I started to work on the next-to-leading order QCD fits, on a code used by the SMC Collaboration in a published paper. HERMES g_1^d results based on 2000 data were released in February 2002. Once the results on g_1^d with the high precision of 2000 data were obtained, new QCD fits could be performed. I developed a method to obtain the statistical error bands, and in June 2002 obtained the results shown in this thesis.